Università degli Studi di Ferrara

DOTTORATO DI RICERCA IN FISICA

COORDINATORE PROF. FILIPPO FRONTERA

TRANSVERSE SPIN EFFECTS IN POLARIZED SEMI INCLUSIVE DEEP INELASTIC SCATTERING

DOTTORANDO
DOTT. LUCIANO LIBERO PAPPALARDO

TUTORE
PROF.SSA PAOLA FERRETTI DALPIAZ

CO - TUTORE
DOTT. MARCO CONTALBRIGO

XX° CICLO

ANNI 2005 - 2007

Contents

Chapter 1

Introduction

1.1 Towards the inner structure of matter

Since the beginning of atomic physics, scattering experiments have proven to be a powerful tool to probe the inner structure of matter. Among the best examples is the discovery of the atomic nucleus, achieved in 1909 by Rutherford, Geiger and Marsden by scattering α particles off a gold foil [Gei09, Rut11]. The increased performances of the particle accelerators over the past decades enabled to dramatically increase the energy of the projectiles and thus their spatial resolution power. As a result the nucleon and its substructures were eventually been resolved adopting a similar approach, though with an enormously greater experimental complexity.

By the end of the 60's, the first inclusive Deep Inelastic Scattering $(e+p \rightarrow e'+X)$ experiments at SLAC showed that the *structure functions* of the nucleons were to a large extent independent on the squared momentum transfer Q^2. This *scaling behavior* of the structure functions was eventually interpreted by Bjørken and Feynman as the evidence of the existence of point-like sub-nucleonic particles, called *partons* [Bjo69a, Bjo69b, Fey69]. These objects were later identified with the *quarks*, spin $1/2$ particles with fractional electric charge and a new degree of freedom called *flavour*, whose existence had been earlier predicted by Gell-Mann and Zweig on the basis of the symmetry properties of the mesons and baryons multiplets [Gel64, Zwe64].

The *Quark Parton Model*, developed in the late 60's, has proven to be particularly successful in the prediction of a number of "macroscopic" observables of the hadrons such as the mass, the charge and the spin. According to this model, the proton is made of three quarks, each carrying approximately a third of the proton mass. Two quarks have flavour *up* and charge $+\frac{2}{3}e$ and one has flavour *down* and charge $-\frac{1}{3}e$, thus resulting in a total charge $+e$ (i.e. the same of the electron but with opposite sign). Furthermore, in a proton with spin along a certain direction, two of the quarks have spin in the same direction and one in the opposite direction, thus resulting in a total spin equal to $1/2$.

Though this model represented a major step toward the understanding of the inner structure of the nucleon, it was soon found to be not enough appropriate for a comprehensive interpretation of the experimental data. Indeed, experimental results showed that only roughly 50% of the nucleon's momentum is carried by quarks [Per72]. The missing momentum could only be

explained a few years later within the framework of the quantum chromodynamics (QCD), the gauge theory of strong interactions (see Appendix A). According to this theory, which requires the existence of the *color* as an additional degree of freedom of the quarks, the missing momentum of the nucleon is carried by the *gluons*, the gauge bosons of the strong interaction. These particles do not show up in the electro-weak scattering processes as they carry no electro-weak charge. The first evidence for the existence of gluons was the observation of three-jet events at the electron-positron collider PETRA at DESY in 1979 [Bar79].

Among the most surprising consequences of QCD is *confinement*, which causes a quark subjected to a high momentum transfer during a scattering process, to fragment into a colorless bunch of hadrons (jet) along its way to escape the nucleon. Since the momentum, the charge, the flavour and the spin orientation of the struck quark can be indirectly accessed through the analysis of the composition of the hadron jet, the experimental investigation of the hadronic final state in deep inelastic scattering experiments allows a deeper insight into the sub-nuclear processes than inclusive measurements alone.

1.2   The internal spin distribution of the nucleon

With the evidence that the proton and the neutron are not elementary particles, physicists were challenged with the task of explaining the nucleon's spin in terms of its constituents. This created a new frontier in hadron physics phenomenology which is still very active and has had a crucial impact in our understanding of the internal structure of the nucleon.

The internal dynamic spin structure of the nucleon can be probed by scattering polarized beams off polarized targets. As it is non-trivial to produce polarized nuclear targets and high energy polarized beams, the spin distribution of quarks inside the nucleon remained experimentally inaccessible for many years.

The first measurements of polarized electron-proton scattering were performed at SLAC by the E80 and E130 collaborations in the mid '70s [Alg76, Bau83]. Though affected by large experimental uncertainties, the spin-dependent structure functions of the proton were founf to be in reasonable agreement with the theoretical predictions. A break-through occurred in the late '80s, when the EMC collaboration repeated these measurements at CERN with higher precision and in a wider kinematic range using a polarized muon beam with an energy 10 times higher than at SLAC. The reported results for the spin-dependent structure function of the proton were found to be in strong disagreement with the predictions of the Ellis-Jaffe sum rule [Ell74, Ash88]. When used in combination with $SU(3)$ symmetry arguments to calculate the fraction of the nucleon's spin carried by the *up*, *down* and *sea* quarks, this result implies that the majority of the spin of the nucleon is not carried by the quarks, a major surprise that came soon to be known as the 'spin crisis'. This unexpected result, which caused a lot of excitement in the high energy physics community, was especially surprising since the extraction of the static magnetic moments of the nucleons, based on similar symmetry arguments, was in perfect agreement with the quark model predictions. The EMC results were substantially confirmed for both the proton and the neutron by the SMC experiment at CERN and the E142 experiment at SLAC

in the following years. The SMC experiment also provided another important result: the first determination of the separate contributions of the valence and the sea quarks to the nucleon spin in Semi-Inclusive Deep Inelastic Scattering measurements [Ade98]. In such measurements, the scattered lepton is required to be detected in coincidence with at least one of the hadrons produced in the fragmentation of the struck quark ($e + p \rightarrow e + h + X$).

The immediate consequence of all these results was that there ought to be additional sources of spin within the nucleon besides the quarks. The most natural candidates are the spin of the gluons (ΔG) and the orbital angular momentum of quarks (L_z^q) and gluons (L_z^G):

$$s_z^N = \frac{1}{2} = \frac{1}{2}\Delta\Sigma + \Delta G + L_z^q + L_z^G \qquad (1.1)$$

where:

$$\Delta\Sigma = (\Delta u_v + \Delta d_v + \Delta q_s) \qquad (1.2)$$

is the contribution carried by the valence and sea quark spins. Precision measurements from the HERMES and the COMPASS experiments have recently established that this contribution is of the order of 30%.

A variety of experiments have been realized, since the publication of the EMC results, to investigate the nucleon's spin structure with unprecedented precision. The main goal of the these experiments was to provide high precision measurements of all the various spin contributions listed in eqn. (1.1). Furthermore, thanks to the different experimental setups (beam energies, targets, detectors, etc), these experiments covered complementary kinematic regions, thus providing all together a wide coverage in x and Q^2 (see Figure 1.1). An overview of past and present experiments with polarized beam and target is reported in Table 1.1.
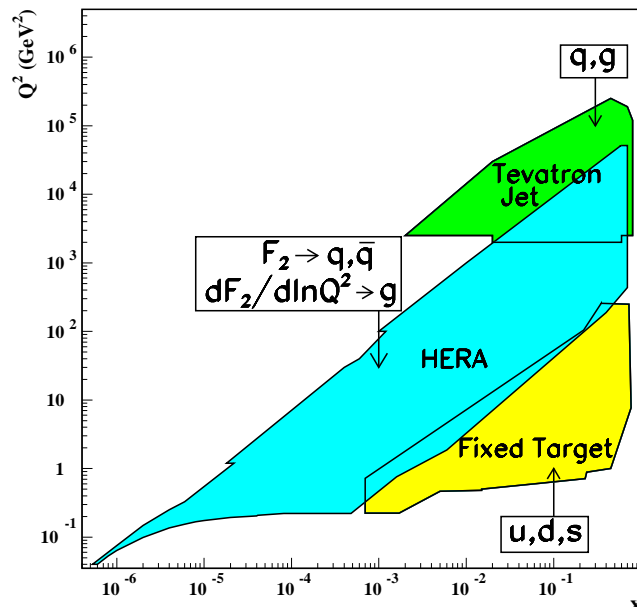
Figure 1.1: Kinematic domains in x and Q^2 probed by fixed-target and collider experiments [Yao06].

Exp.	Y	Beam [GeV]	Target	f	$\langle P_T \rangle$	$\langle P_B \rangle$	Q^2 range	x range	Ref.
SLAC									
E80	75	$10–13\ e^-$	H-butanol	0.11	40%	51%	1.4–2.7	0.20–0.33	[Alg76]
	77	$10–16\ e^-$	H-butanol	0.13	50%	85%	1.0–4.1	0.1–0.5	[Alg78]
E130	79	$16–23\ e^-$	H-butanol	0.15	58%	81%	3.5–10	0.18–0.7	[Bau83]
E142	92	$19–25\ e^-$	^3He	0.35	33%	36%	1.3–6.5	0.03–0.6	[Ant96]
E143	93	$10–29\ e^-$	$^{15}NH_3$	0.17	67%	87%	0.3–10	0.02–0.85	[Abe98]
	95		$^{15}ND_3$	0.24	24%				[Abe98]
E154	95	$48.3\ e^-$	^3He	0.55	38%	82%	1.2–15	0.014–0.7	[Abe97]
E155	97	$48.3\ e^-$	$^{15}NH_3$	0.15	80%	81%	1.0–40	0.014–0.9	[Ant00]
			^6LiD	0.36	22%				[Ant99]
E155x	99	$29–32\ e^-$	$^{15}NH_3$	0.13	70%	83%	0.7–20	0.02-0.8	[Ant02]
			^6LiD	0.18	22%				[Ant02]
CERN									
EMC	85	$100–200\ \mu^+$	$^{15}NH_3$	0.17	78%	79%	1.0–60	0.01–0.7	[Ash89]
SMC	92	$100\ \mu^+$	D-butanol	0.19	35%	82%	1.0–30	0.006–0.6	[Ade93]
	93	$190\ \mu^+$	H-butanol	0.12	86%	80%	1.0–60	0.003–0.7	[Ada94]
	94		D-butanol	0.20	51%	81%			[Ada95]
	96		$^{15}NH_3$	0.16	89%	77%	0.2–100	0.0008–0.7	[Ade97]
COMPASS	02	$160\ \mu^+$	^6LiD	0.50	50%	76%	1.0–100	0.004–0.7	[Age05]
	06	$160\ \mu^+$	$^{15}NH_3$	0.20	85%		–	–	[Bra06]
DESY									
HERMES	95	$27.5\ e^+$	$^3He\ \parallel$	1.00	46%	55%	1.0–15	0.023–0.6	[Ack97]
	96		H $\parallel$		80%	53%	0.8–20	0.021–0.85	[Air98]
	98	$27.5\ e^{+/-}$	D $\parallel$		84%		1.0–15	0.023–0.4	[Air03]
	02		H $\perp$		71%	–			[Els06]
JLAB									
CLAS	98	$2.5\ e^-$	$^{15}ND_3$	–	14%	72%	0.3–1.3	0.05–0.8	[Yun03]
		$2.6–4.3\ e^-$	$^{15}NH_3$		51%	70%	0.1–1.6	0.05–0.8	[Fat03]
E94-010	98	$0.9–5.1\ e^-$	^3He		35%	70%	0.1–0.9	–	[Ama02]
E99-117	00	$5.8\ e^-$	^3He		40%	80%	2.7–4.8	0.33–0.6	[Zhe04]
E01-006	02		$^{15}NH_3$		80%	68%	0.8–1.8	–	[Mck02]
			$^{15}ND_3$		20%				[Ron03]
BNL									
STAR	02	100 P–P	P–P Coll	1.00	16%	16%	–	–	[Ada04]
PHENIX	02				27%	27%			[Adl04]
	04				45%	45%			[Adl06]

Table 1.1: A selection of past and present experiments with both polarized beam and target is presented together with some of their main features. $\langle P_T \rangle$ ($\langle P_B \rangle$) is the Target (Beam) average polarization and f is the target dilution factor.

1.3 Transversity and Sivers distribution functions at HERMES

After averaging over the quark transverse momentum p_T, three parton distribution functions are needed at leading twist[1] for a complete description of the momentum and spin distributions of the quarks within the nucleon. Two of them have been widely measured in various experiments: the well known momentum (or spin-independent) distribution function $q(x, Q^2)$, which reflects the probability to find quarks within the nucleon carrying a fraction x of the nucleon momentum at photon virtuality Q^2, and the helicity distribution $\Delta q(x, Q^2)$, which reflects, in the helicity basis, the difference in probabilities to find quarks in a longitudinally polarized nucleon with their spin aligned and anti aligned to the spin of the nucleon [Lam00]. In a basis of transverse spin eigenstates, the third distribution function $\delta q(x, Q^2)$, known as *transversity* [Ral79, Art90, Jaf92], reflects the difference in probabilities to find, in a transversely polarized nucleon, quarks with their spin aligned and anti-aligned to the spin of the nucleon. This quantity has no probabilistic interpretation in the helicity basis, where it is related to a forward scattering amplitude involving helicity flip of both the quark and the target nucleon ($N^{\Rightarrow} q^{\Leftarrow} \rightarrow N^{\Leftarrow} q^{\Rightarrow}$). Since strong and electromagnetic interactions conserve chirality, transversity has so far remained unmeasured in inclusive processes due to its chiral-odd nature. At the HERMES experiment, the so called *Collins moments*, in which the transversity is convoluted with the chiral-odd Collins fragmentation function, are accessible through azimuthal single-spin asymmetries (SSA) in semi-inclusive deep inelastic scattering (DIS) on a transversely polarized proton target. The Collins function describes the correlation between the transverse spin of the struck quark and the transverse momentum $P_{h\perp}$ of the produced hadron [Col93]. The transverse polarization of the struck quark can indeed influence the transverse (with respect to the virtual photon direction) component of the hadron momentum, leading to a left-right asymmetry in the momentum distribution of the produced hadrons in the direction transverse to the nucleon spin (*Collins mechanism*) [Ant99].

In the last few years, a rapidly increasing attention is being devoted, from both the theoretical and the experimental point of view, to the non-collinear phenomena in the nucleon. It was indeed realized that many important new aspects of the nucleon structure can be accessed through the so-called Transverse Momentum Dependent (TMD) distribution functions. These distribution functions arise when the quark transverse momentum p_T is not integrated over. Among them the Sivers function is particularly interesting since its existence requires a non-zero orbital angular momenta of the quarks and has been linked to the spatial distribution of partons inside the nucleon [Bro02, Bur02]. The Sivers function describes the correlation between the transverse polarization of the target nucleon and the transverse momentum p_T of quarks (*Sivers mechanism*) [Siv90]. The Sivers function appears together with the well known spin-independent fragmentation function (*Sivers moments*) in the cross section for a transversely polarized nucleon and produces a different left-right asymmetry.

From 2002 to 2005 the HERMES experiment has operated with a hydrogen target polarized transversely to the direction of the HERA lepton beam. The data collected during this period

---

[1] A leading-twist or twist-two term is a leading-order term in a $1/Q$ expansion.

allowed the study of transverse target Single Spin Asymmetries (SSA). In particular, the extraction of the Collins and Sivers moments from the full HERMES transverse data set is presented in this thesis. A preliminary extraction of the Sivers function in combination with the momentum distribution function (*Sivers polarization*) is also presented.

1.4   Outlook of the thesis

The theoretical framework for the inclusive and semi-inclusive deep inelastic scattering is provided in Chapters 2 and 3, respectively. While a phenomenological and historical perspective is adopted in Chapter 2 for the description of the inclusive processes, a detailed treatment of the formalism concerning the physics of the transverse degrees of freedom of the nucleon is presented in Chapter 3. In Chapter 4 the main components of the HERMES experimental apparatus are presented. The extraction of the Collins and Sivers moments is discussed in Chapter 5 after a brief overview of the main steps of the data analysis. A selection of systematic studies is also reported at the end of the chapter. Chapter 6 is completely devoted to the estimate of the acceptance and smearing effects on the extracted azimuthal moments. A crucial role in the studies presented is played by a newly developed Monte Carlo generator which simulates azimuthal asymmetries arising from intrinsic quark momenta. A novel approach for the estimate of the acceptance effects is presented at the end of the chapter. The extracted Collins and Sivers moments, corrected for the acceptance effects, are shown in Chapter 7. The discussion and the interpretation of the results, together with a preliminary extraction of the Sivers polarization, are also treated in Chapter 7. Final conclusions and a brief summary are reported in Chapter 8.

Chapter 2

The Deep Inelastic Scattering

2.1 The non-perturbative regime of QCD and the structure of hadrons

The nucleon, as all baryons and mesons, is a system of confined quarks and gluons. Therefore only non-perturbative methods can describe its properties. In the non-perturbative (or long-distance) regime of QCD (see Appendix A), predictions of the physical observables related to the structure of the hadrons cannot be formulated from first principles but only within the framework of effective theories or phenomenological models [Bha88]. Non-perturbative methods have proved to be notoriously difficult in quantum field theory and often provide only partial descriptions of the structure of the hadrons. For instance, the Chiral Quark Soliton Model [Chr96, Dia98, Wak01, Efr05], which is one of the most sophisticated models for the nucleon, lacks any gluonic degree of freedom, thus making only predictions for the quark content of the nucleon. On the other hand, in the popular MIT bag model [Cho74a, Cho74b] quarks are treated as massless particles inside a bag of finite dimension and the confinement results from the balance of the pressure on the bag walls from the outside (vacuum pressure) and the pressure resulting from the kinetic energy of the quarks inside the bag.

More realistic non-perturbative predictions on the low-energy features of the hadron world are provided by the lattice-QCD, which allows for exact QCD solutions in a discretized space-time lattice. However, despite the noteworthy successes achieved in selected subjects and the increasing performances of the computers available, lattice-QCD is still heavily limited by the available computational power.

Experimental results are thus required to constrain models and to provide reliable information about the hadron inner structure. Among the most promising processes to be explored experimentally are the e^+e^- and $p\bar{p}$ annihilation and the lepton-hadron scattering. In particular, the study of deeply inelastic electron-nucleon scattering is of great historical importance because it led to the first clear evidence for scattering from individual point-like constituents confined within the nucleon.

2.2 The elastic electron-nucleon scattering

The elastic scattering of electrons (or muons [1]) off protons is the simplest process one can think of in order to extract information on the properties of the proton. In this case, indeed, the target protons stay intact and there is no creation of new particles:

$$l + p \rightarrow l + p \qquad (l = e, \mu) . \tag{2.1}$$

Due to the low energies involved, this reaction is dominated by the single-photon exchange mechanisms, as depicted in Figure 2.1.
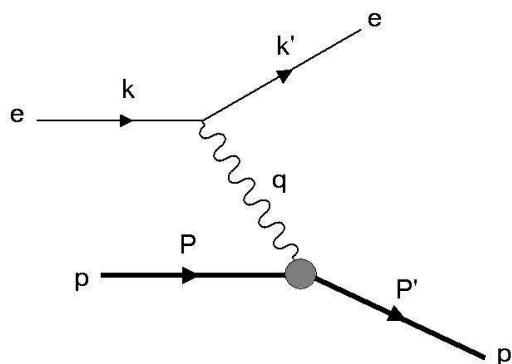
Figure 2.1: Feynman diagram of elastic electron-proton scattering.

Here k and P are the four-momenta of the incoming electron and proton, respectively, and k' and P' those of the scattered particles. The four-momentum q of the exchanged virtual photon is given by the difference between the initial and final state four-momenta:

$$q = k - k' = P' - P . \tag{2.2}$$

Averaging over all possible spin states and using the standard Feynman rules for QED, the squared amplitude of this process can be written in the following compact form:

$$\langle |\mathcal{A}|^2 \rangle = \frac{\alpha^2}{q^4} L_{\mu\nu} K_{\mu\nu} , \tag{2.3}$$

where $\alpha = \frac{e^2}{4\pi}$ is the electromagnetic coupling and $L_{\mu\nu}$ and $K_{\mu\nu}$ are the leptonic and the hadronic tensors describing the interaction at the leptonic and hadronic vertices, respectively. In particular the leptonic tensor can be expressed in the form

$$L_{\mu\nu} = 2(k^\mu k'^\nu + k^\nu k'^\mu + g^{\mu\nu}(m^2 - k^\sigma k'_\sigma)) , \tag{2.4}$$

---

[1]The same arguments apply to electrons and muons since they have identical electro-weak interactions.

where $g^{\mu\nu}$ is the metric tensor and m the mass of the lepton. It describes the emission of a virtual photon by a lepton and is calculable in Quantum Electrodynamics.

Unlike the lepton tensor, the hadronic tensor $K_{\mu\nu}$, which describes the absorption of the virtual photon by the proton, cannot be perturbatively derived from first principles. However a simple parametrization is possible in terms of the so-called *elastic proton form factors* K_1 and K_2:

$$K^{\mu\nu} = K_1\Big(- g^{\mu\nu} + \frac{q^\mu q^\nu}{q^2} \Big) + \frac{K_2}{M^2}\Big(P^\mu + \frac{1}{2}q^\mu \Big)\Big(P^\nu + \frac{1}{2}q^\nu \Big) , \qquad (2.5)$$

where M is the mass of the proton.

Since the proton stays intact during the process, its constituents can only contribute coherently to the scattering. As a consequence the two proton form factors contain very limited information about the substructure of the proton itself. These form factors, which only depend on q^2, can be redefined in terms of the electric (G_E) and magnetic (G_M) proton form factors. The former is associated with the charge distribution and the latter with the magnetic moment distribution of the proton. The elastic electron-proton scattering cross section can thus be written in the form:

$$\frac{d\sigma}{d\Omega} = \frac{4\alpha^2 E^2 \cos^2(\theta/2)}{q^4[1 + (2E/M)\sin^2(\theta/2)]}\left(\frac{G_E^2 + \tau G_M^2}{1 + \tau} + 2\tau G_M^2 \tan^2(\theta/2) \right) , \qquad (2.6)$$

known as the Rosenbluth formula [Ros50], where θ is the scattering angle and $\tau = -q^2/4M^2$. As in classical Rutherford scattering, a typical $1/q^4$ dependence is observed.

The measurement of the cross section and the subsequent extraction of G_E through the Rosenbluth formula allowed to extract the root-mean-square charge radius r_E of the proton [Mur74]:

$$r_E^2 = \int d^3x r^2 \rho(r) = -6\frac{dG_E(q^2)}{dq^2}\Bigg|_{q^2=0} = (0.81 \pm 0.04 \times 10^-13\,\text{cm})^2 . \qquad (2.7)$$

The same radius of about 0.8 fm was also obtained for the magnetic moment distribution.

2.3 The kinematics of the Deep Inelastic Scattering

While the elastic lepton-nucleon scattering led to the first measurements of the size of the proton, deep inelastic lepton-nucleon scattering experiments have proven to be particularly suitable to probe the partonic structure of the nucleon, allowing the measurement of a variety of parton distributions and related observables.

The deep-inelastic lepton-nucleon scattering (DIS) is a process in which a lepton l scatters off a nucleon N via the exchange of a virtual boson. In contrast to the elastic lepton-nucleon scattering, where the nucleon recoils but stays intact, in DIS processes the momentum transfer involved is so large that the nucleon breaks up and forms a hadronic final state X:

$$l + N \rightarrow l' + X. \tag{2.8}$$

In lowest order perturbation theory this interaction is described as the exchange of a neutral boson (γ or Z^0) between the lepton and the charged constituents inside the nucleon.

Since the HERMES center of mass energy is well below the mass of the neutral weak boson ($\sqrt{s} \approx 7\,GeV \ll m_{Z^0} = 91$ GeV), the Z^0 exchange is completely negligible at HERMES and only the single photon exchange mechanism, which is the dominant mechanism at HERMES energies, will be considered in the following.

Figure 2.2 shows a sketch of the DIS process in the one-photon exchange approximation. The incoming lepton interacts with the target proton via the exchange of a virtual photon with squared four-momentum $q^2 = -(k - k')^2$. In contrast to real photons, the exchanged photon, due to its virtuality, can be either longitudinally or transversely polarized. The quantities P and P_X, appearing in Figure 2.2, represent the target proton and the hadronic final X state four-momenta, respectively, while k and k' are the four-momenta of the incoming and the scattered lepton, respectively. In fixed target experiments, like HERMES, the laboratory frame coincides with the target (proton) rest frame so that $P = (M, \vec{0})$, with M the proton mass. In this frame, the incoming lepton scatters at an angle θ.
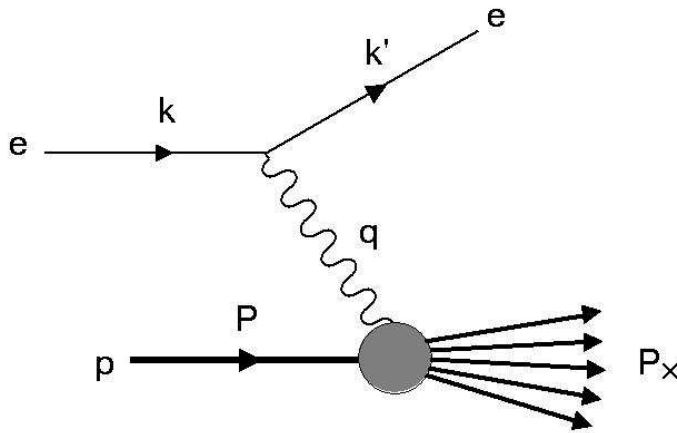
Figure 2.2: Feynman diagram of deep inelastic scattering on a proton.

The kinematics of the process can be characterized by the following Lorentz invariant quantities:

- The negative squared four momentum of the virtual photon

$$Q^2 \equiv -q^2 = (k - k')^2 \overset{lab}{=} 4EE'sin^2(\theta/2) \,, \tag{2.9}$$

where E and E' are the energies of the incident and scattered lepton, respectively. The quantity Q^2 is positive and represents a measure of the spatial scale that can be resolved by a virtual photon with wavelength $\lambda = 1/|q|$.

- The energy carried by the virtual photon (i.e. the energy transferred in the reaction)

$$\nu \equiv \frac{P \cdot q}{M} \stackrel{lab}{=} E - E' \tag{2.10}$$

- The squared invariant mass of the target-nucleon – virtual-photon system, which corresponds to the invariant mass of the system of hadrons produced in the final state:

$$W^2 \equiv (P + q)^2 \stackrel{lab}{=} M^2 + 2M\nu - Q^2 \tag{2.11}$$

- The Bjørken variable

$$x \equiv \frac{-q^2}{2P \cdot q} \stackrel{lab}{=} \frac{Q^2}{2M\nu} \qquad (0 \leq x \leq 1) \,, \tag{2.12}$$

which can be understood as a measure of the inelasticity of the scattering process. Combining the last two equations one obtains the relation $W^2 = M^2 + 2M\nu(1-x)$. Therefore, the limit $x = 1$ corresponds to elastic scattering regime, with $W^2 = M^2$, while $x < 1$ corresponds to the inelastic regime, in which $W^2 > M^2$.

- The fractional energy-transfer from the lepton to the nucleon

$$y \equiv \frac{P \cdot q}{P \cdot k} \stackrel{lab}{=} \frac{\nu}{E} \,. \tag{2.13}$$

The deep-inelastic scattering regime is usually defined by $Q^2 > 1 \ GeV^2$ and $W^2 > 4 \ GeV^2$. These conditions ensure a high enough resolution to probe the internal structure of the nucleon. Furthermore, the W^2 requirement excludes the elastic scattering region as well as inelastic scattering in resonance regions with $W^2 = M_R$, where M_R is the mass of the resonance. Being, in this regime, the energies of the incident and scattered leptons much larger than the lepton mass, the latter has been neglected in the definition of all the kinematical variables introduced above.

In the *inclusive* measurements only the outgoing lepton is detected and the corresponding cross section can be expressed in terms of two independent variables. It is usually convenient to express the cross section in terms of (E', θ) or alternatively (x, Q^2).

In *semi-inclusive* measurements one or more hadrons produced in the final X state are detected in coincidence with the outgoing lepton. If only one hadron is detected, the kinematics of this hadron is completely defined by three independent variables:

- The fractional (relative to the virtual photon) energy

$$z \equiv \frac{P \cdot P_h}{P \cdot q} \overset{lab}{=} \frac{E_h}{\nu} \ , \tag{2.14}$$

where $P_h = (E_h, \vec{p}_h)$ is four-momentum of the hadron

- The transverse (relative to the direction of the virtual photon) momentum

$$P_{h\perp} \equiv \frac{|\vec{P}_h \times \vec{q}|}{|\vec{q}|} \tag{2.15}$$

- The azimuthal angle ϕ_h, relative to the scattering plane.

The spin-averaged semi-inclusive DIS cross section thus depends on five independent variables: two inclusive variables (eg. x and Q^2) and three semi-inclusive ones (z, $P_{h\perp}$ and ϕ_h).

The kinematical variables introduced in this section are summarized in Table 2.1.

$k = (E, \vec{k})$; $k' = (E', \vec{k'})$;	$4-$momenta of incoming and outgoing lepton
$P \overset{lab}{=} (M, \vec{0})$	$4-$momenta of the target nucleon
θ, ϕ	polar and azimuthal scattering angles
$q = (\nu, \vec{q})$	$4-$momenta of the virtual photon
$Q^2 = -q^2 \overset{lab}{=} 4EE'sin^2(\theta/2)$	negative squared $4-$momentum transfer
$\nu = \frac{P \cdot q}{M} \overset{lab}{=} E - E'$	energy transfer from the incoming lepton to the target nucleon
$x = \frac{Q^2}{2P \cdot q} \overset{lab}{=} \frac{Q^2}{2M\nu}$	Bjørken variable
$y = \frac{P \cdot q}{P \cdot k} \overset{lab}{=} \frac{\nu}{E}$	fractional energy of the virtual photon
$W^2 = (P + q)^2 \overset{lab}{=} M^2 + 2M\nu - Q^2$	squared invariant mass of the hadronic final state
$P_h = (E_h, \vec{P}_h)$	$4-$momentum of a final state hadron
$z = \frac{P \cdot p}{P \cdot q} \overset{lab}{=} \frac{E_h}{\nu}$	fractional energy of the final state hadron
$P_{h\perp} \equiv \frac{|\vec{P}_h \times \vec{q}|}{|\vec{q}|}$	transverse momentum of the hadron
ϕ_h	azimuthal angle of the hadron w.r.t. scattering plane

Table 2.1: Definition of the most important kinematic variables used in deep-inelastic scattering.

2.4 The DIS cross section

The inclusive DIS differential cross section can be written in the form

$$\frac{d^2\sigma}{dE'd\Omega} = \frac{1}{2M}\frac{E'}{E}|\mathcal{A}|^2 \, , \tag{2.16}$$

where

$$|\mathcal{A}|^2 = \frac{\alpha^2}{Q^4}L_{\mu\nu}W_{\mu\nu} \tag{2.17}$$

is the squared amplitude for electron-hadron scattering, expressed in terms of the leptonic ($L_{\mu\nu}$) and the hadronic ($W^{\mu\nu}$) tensors. As depicted in Figure 2.3, the former describes the interaction at the leptonic vertex and the latter at the hadronic vertex.
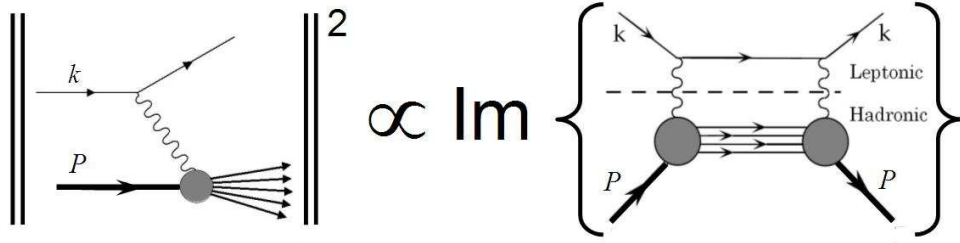
Figure 2.3: The optical theorem (see Appendix C) relates the squared amplitude $|\mathcal{A}|^2$ of the DIS process (left) with the imaginary part of forward scattering amplitude (right). The latter is here explicitly divided into the leptonic tensor (upper part) and the hadronic tensor (lower part).

After summation over all possible spin states s' of the final state lepton, the leptonic tensor can be split into a symmetric (S) and an antisymmetric (A) (under interchange of the Lorentz indices μ and ν), part:

$$L_{\mu,\nu}(k,s;k') = \sum_{s'} L_{\mu,\nu}(k,s;k',s') = L_{\mu,\nu}^{(S)}(k;k') + iL_{\mu,\nu}^{(A)}(k,s;k'). \tag{2.18}$$

The symmetric part

$$L_{\mu\nu}^{(S)}(k;k') = 2(k^\mu k'^\nu + k^\nu k'^\mu + g^{\mu\nu}(m^2 - k^\sigma k'_\sigma)) \tag{2.19}$$

is spin-independent while the antisymmetric part

$$L_{\mu\nu}^{(A)}(k,s;k') = 2m\epsilon_{\mu\nu\alpha\beta}s^\alpha(k^\beta - k'^\beta), \tag{2.20}$$

depends on the spin s of the incoming lepton. Here $\epsilon_{\mu\nu\alpha\beta}$ is the totally-antisymmetric Levi-Civita tensor (with $\epsilon_{0123} = +1$) and m is the lepton mass.

Also the hadronic tensor can be decomposed into a symmetric and an antisymmetric part, the former being spin-independent and the latter dependent on the target nucleon spin S:

$$W_{\mu,\nu}(q; P, S) = W_{\mu,\nu}^{(S)}(q; P) + i W_{\mu,\nu}^{(A)}(q; P, S). \tag{2.21}$$

The symmetric part can be parameterized in terms of two spin-independent inelastic form factors, W_1 and W_2, while the antisymmetric part in terms of two spin-dependent ones, G_1 and G_2:

$$\frac{1}{2M} W_{\mu\nu}^{(S)}(q; P) = \left(-g_{\mu\nu} + \frac{q_\mu q_\nu}{q^2} \right) W_1(P \cdot q, q^2) \tag{2.22}$$
$$+ \frac{1}{M^2} \left(P_\mu - \frac{P \cdot q}{q^2} q_\mu \right) \left(P_\nu - \frac{P \cdot q}{q^2} q_\nu \right) W_2(P \cdot q, q^2),$$

$$\frac{1}{2M} W_{\mu\nu}^{(A)}(q; P, S) = \epsilon_{\mu\nu\alpha\beta} q^\alpha \{ M S^\beta G_1(P \cdot q, q^2) \tag{2.23}$$
$$+ \frac{1}{M} [(P \cdot q) S^\beta - (S \cdot q) P^\beta] G_2(P \cdot q, q^2) \}.$$

The inelastic form factors W_1, W_2, G_1 and G_2 are Lorentz-invariant scalars and are usually substituted by four dimensionless quantities dependent on the two DIS variables x and Q^2:

$$F_1(x, Q^2) \equiv M W_1(P \cdot q, q^2) \tag{2.24}$$

$$F_2(x, Q^2) \equiv \nu W_2(P \cdot q, q^2) \tag{2.25}$$

$$g_1(x, Q^2) \equiv \frac{(P \cdot q)^2}{\nu} G_1(P \cdot q, q^2) \tag{2.26}$$

$$g_2(x, Q^2) \equiv \nu (P \cdot q) G_2(P \cdot q, q^2). \tag{2.27}$$

Being spin-independent, F_1 and F_2 are usually referred to as *unpolarized structure functions*. On the other hand g_1 and g_2, which dependent on spin, are known as *polarized structure functions*. Owing to the pQCD regime, all these structure functions cannot be predicted from first principles and can thus only be determined experimentally.

The symmetric and antisymmetric parts of the hadronic tensor can be rewritten in terms of these four structure functions according to:

$$W_{\mu\nu}^{(S)}(q; P) = 2 \left(-g_{\mu\nu} + \frac{q_\mu q_\nu}{q^2} \right) F_1(x, Q^2) +$$
$$\frac{2}{P \cdot q} \left(P_\mu - \frac{P \cdot q}{q^2} q_\mu \right) \left(P_\nu - \frac{P \cdot q}{q^2} q_\nu \right) F_2(x, Q^2) \tag{2.28}$$

$$W_{\mu\nu}^{(A)}(q; P, S) = \epsilon_{\mu\nu\alpha\beta} \frac{2M q^\alpha}{P.q} \left[S^\beta g_1(x, Q^2) + \left(S^\beta - \frac{S \cdot q}{P \cdot q} P^\beta \right) g_2(x, Q^2) \right] \tag{2.29}$$

Since the electromagnetic interaction conserves parity, only terms with the same symmetry can contribute to the cross section. Therefore substituting eqns. (2.18) and (2.21) into the expression of the differential cross section one obtains:

$$\frac{d^2\sigma}{dE'd\Omega} = \frac{\alpha^2}{2MQ^4}\frac{E'}{E}[L_{\mu\nu}^{(S)}W^{\mu\nu(S)} - L_{\mu\nu}^{(A)}W^{\mu\nu(A)}]. \tag{2.30}$$

2.4.1 The spin-independent cross section

Averaging over all spins in the initial state of the scattering process and summing over the spins in the final state, only the spin-independent symmetric parts of the leptonic and hadronic tensors contribute to the cross section. Expliciting the symmetric part of the leptonic and hadronic tensors, one can express the unpolarized cross section in terms of the spin-independent structure functions F_1 and F_2:

$$\frac{d^2\sigma^{unpol}}{dE'd\Omega} = \frac{\alpha^2}{2MQ^4}\frac{E'}{E}L_{\mu\nu}^{(S)}W^{\mu\nu(S)} =$$

$$\left(\frac{d^2\sigma}{dE'd\Omega}\right)_{Mott} \cdot \left[\frac{2}{M}F_1(x,Q^2)\tan^2(\theta/2) + \frac{1}{\nu}F_2(x,Q^2)\right], \tag{2.31}$$

where

$$\left(\frac{d^2\sigma}{dE'd\Omega}\right)_{Mott} = \frac{4\alpha^2 E'^2}{Q^4}\cos^2(\theta/2) \tag{2.32}$$

is the Mott cross section, which describes the elastic scattering of a relativistic spin-1/2 particle off a spinless point-like particle. As a result, the second term of eqn. (2.31), which contains the unpolarized structure functions, represents the deviation, due to the composite nature of the nucleon, of the observed DIS cross section from the Mott cross section. A selection of world data for the structure function F_2 as a function of Q^2 for different x is reported in Figure 2.4. The spin-independent DIS cross section (2.31) can be alternatively represented in terms of the inclusive variables x and Q^2:

$$\frac{d^2\sigma}{dxdQ^2} = \frac{4\pi\alpha^2}{xQ^4}\left[y^2 x F_1(x,Q^2) + (1-y)F_2(x,Q^2)\right] \tag{2.33}$$

or with respect to x and y:

$$\frac{d^2\sigma}{dxdy} = \frac{4\pi\alpha^2}{sx^2y^2}\left[xy^2 F_1(x,Q^2) + \left(1 - y - \frac{\gamma^2 y^2}{4}\right)F_2(x,Q^2)\right], \tag{2.34}$$

where $s = (P+k)^2$ denotes the squared center-of-mass energy and $\gamma = (2Mx)/Q$.
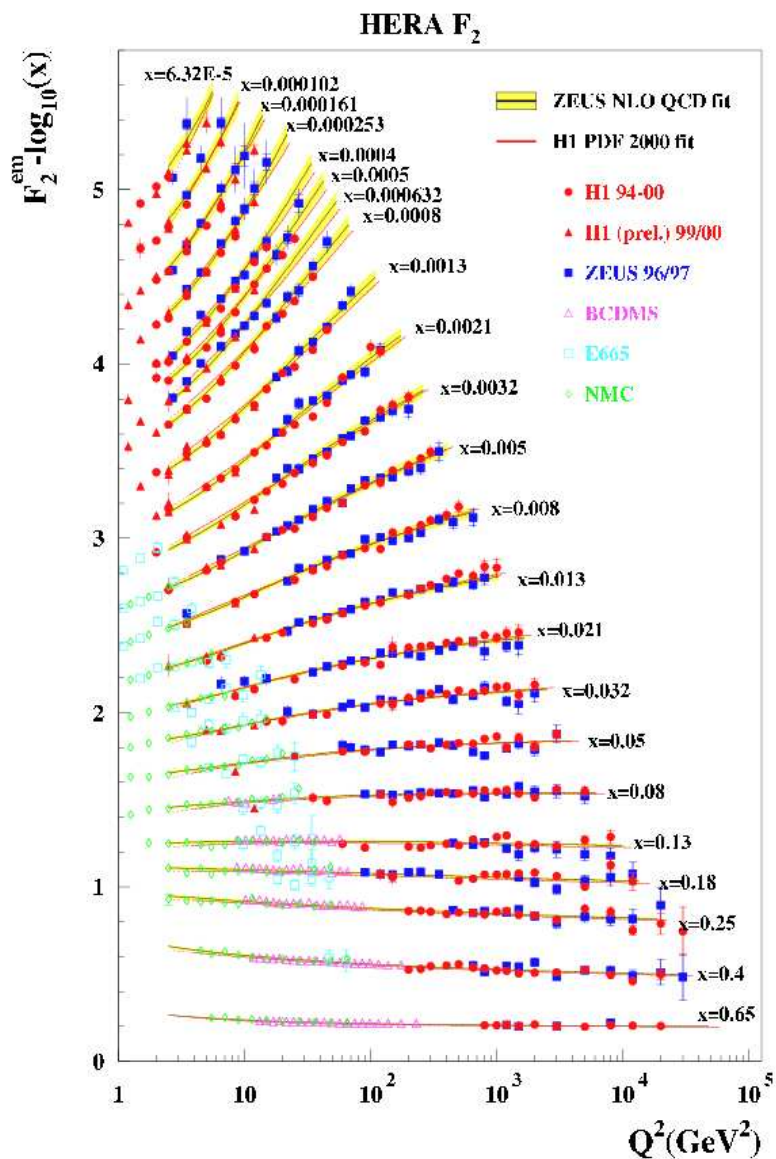
Figure 2.4: World data on $F_2(x, Q^2)$ from H1, ZEUS, NMC, E665 and the BCDMS collaborations.

2.4.2 The spin-dependent cross section

If both the incident lepton beam and the target protons are longitudinally polarized, the anti-symmetric (spin-dependent) parts of the leptonic and hadronic tensors contributes to the cross section. Since in this case both the spin-independent and the spin-dependent parts of the cross section are non-vanishing, the only way to isolate the spin-dependent component consists in measuring the difference of the cross sections obtained with two opposite target spin states. In the difference the unpolarized components cancel and one obtains the bare spin-dependent cross section:

$$\frac{d^3\sigma^{\overset{\Leftarrow}{\rightarrow}}}{dxdy} - \frac{d^3\sigma^{\overset{\Rightarrow}{\rightarrow}}}{dxdy} = \frac{4\alpha^2}{sxy}\left[\left(2 - y - \frac{\gamma^2 y^2}{2}\right)g_1(x,Q^2) - \gamma^2 y g_2(x,Q^2)\right], \qquad (2.35)$$

where $\rightarrow$ indicates the spin orientation of the incoming lepton and $\Leftarrow, \Rightarrow$ the two different spin states of the target nucleon.

Since $\gamma^2 \sim 1/Q^2$ and $g_2(x,Q^2)$ is small by itself, the cross section is dominated by the first term, containing the structure function $g_1(x,Q^2)$. In particular, if the target spin is collinear with the direction of the virtual photon the contribution of $g_2(x,Q^2)$ vanishes completely. However, since it is not possible to polarize the target nucleons with respect to the virtual photon direction, the non-vanishing contribution of the $g_2(x,Q^2)$ structure function, which arises from the fact that the virtual photon direction has a transverse component with respect to the target spin, is usually taken into account through a parametrization of the world data.

Figure 2.5 reports the $g_1(x)$ world results for protons, neutrons and deuterons as a function of the Bjørken variable x. Since it is not possible to build neutron targets, the $g_1(x)$ results on neutrons have been obtained using a polarized ^3He target, which basically behaves like a polarized neutron target since the spins of the two protons are opposite and result in a vanishing contribution, or alternatively from the difference of the results from the deuteron and the proton. If the target polarization is transverse to the incoming lepton direction, the expression of the polarized cross section becomes:

$$\frac{d^3\sigma^{\rightarrow\Downarrow}}{dxdyd\phi_S^l} - \frac{d^3\sigma^{\rightarrow\Uparrow}}{dxdyd\phi_S^l} = \frac{4\alpha^2}{sxy}\gamma\sqrt{1 - y - \frac{\gamma^2 y^2}{4}}\left[\gamma g_1(x,Q^2) + 2g_2(x,Q^2)\right]\cos\phi_S^l, \qquad (2.36)$$

where ϕ_S^l is the azimuthal angle of the target spin vector $\vec{S}$ with respect to the lepton beam direction. Due to the γ pre-factor, also the term containing $g_1(x,Q^2)$ is partially suppressed.

A precise measurement of $g_2(x,Q^2)$ was recently obtained by the E155 Collaboration by scattering longitudinally polarized electrons off transversely polarized NH_3 and ^6LiD targets [Ant02].

2.5 The Bjørken scaling

The early deep-inelastic scattering experiments performed at SLAC showed that the unpolarized structure function F_1 and F_2 are approximately Q^2-independent in the large momentum transfer
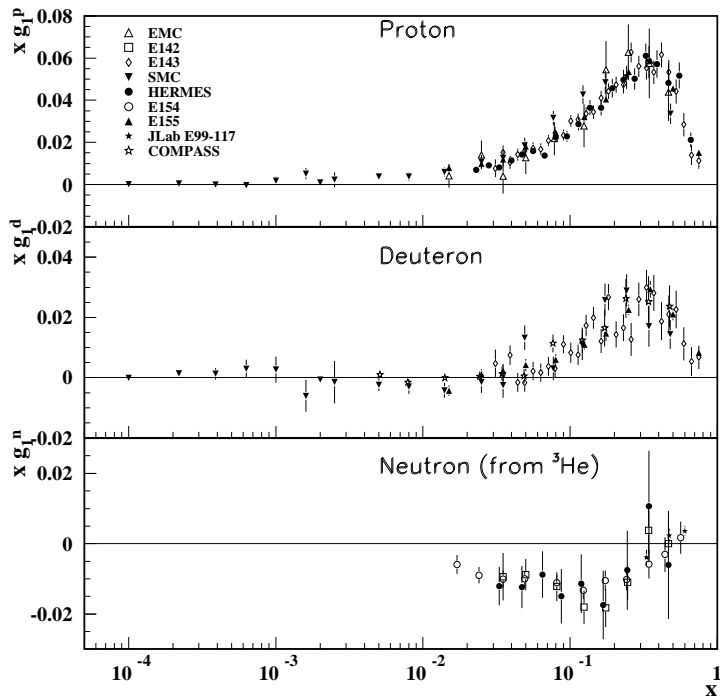
Figure 2.5: World results for the spin-dependent structure function $g_1(x)$ of the proton, deuteron and neutron (from ^3He target) measured in deep-inelastic scattering of polarized electrons/positrons [Yao06].

region:

$$F_{1,2}(x, Q^2) \approx F_{1,2}(x) \qquad (Q^2 \gg M^2) \, . \qquad (2.37)$$

This phenomenon, predicted by the Quark Parton Model (cf. Section 2.6), became known as *Bjørken scaling* or *scale invariance* because, in the so-called Bjørken limit

$$\lim_{Bj} = \left\{ \begin{array}{l} Q^2 \rightarrow \infty \\ \nu \rightarrow \infty \\ x \; fixed \end{array} \right. , \qquad (2.38)$$

the structure functions are left unchanged by a scale transformation, i.e. by a transformation in which Q^2 and ν are multiplied by an arbitrary scale factor k, so that x remains unchanged.

A Q^2-independence of the structure functions would imply that the electromagnetic probe (incoming lepton) "sees" the same proton structure no matter how big the spatial resolution is. This behavior is in clear contrast with the strong Q^2-dependence of the elastic form factors, which implies a inner structure of the proton[2]. The observed scaling behavior could be successfully accounted for by considering scattering from point-like constituents within the proton, rather then from the proton as a whole. This was historically the first dynamical evidence of

---

[2]If the proton were a point-like particle, the elastic form factors would also be independent of Q^2.

the quarks, whose existence had been previously inferred solely on the basis of static quantities, like the masses and quantum numbers of the hadrons.

With the increased accuracy of the next generation DIS experiments and the broadening of the kinematic regions explored, a noticeable Q^2-dependence of the structure functions appeared (cf. Figure 2.4). This violation of the Bjørken scaling, interpreted as the evidence of the dynamical structure of the proton (quarks can radiate gluons, gluons can split into $q\bar{q}$ pairs and gluons can couple with other gluons) represented one of the earliest triumphs of QCD (see Section 2.7).

2.6 The Quark Parton Model

The Quark Parton Model (QPM), developed by Bjørken and Feynman in the late 1960's [Bjo69a, Bjo69b, Fey69], provided an intuitive explanation for the observed Bjørken scaling. In this model, deep-inelastic lepton-nucleon scattering at high enough energies is interpreted as the incoherent elastic scattering of the lepton off the free point-like spin-$1/2$ charged constituents of the nucleon. These constituents, called *partons*, were later recognized to be the quarks, whose existence had been proposed a few years earlier by Gell-Mann and Zweig on the basis of the symmetry properties of the mesons and baryons multiplets [Gel64, Zwe64].

The QPM is conveniently formulated in a reference frame (see Figure 2.6) where the nucleon moves with very high momentum (*infinite-momentum frame* or *Breit frame*), such that the transverse momentum components and the rest mass of the constituents and the nucleon itself can be neglected [3]. In this special frame the scattering can be viewed as the absorption of a virtual photon by one of the collinearly moving partons inside the nucleon. The struck parton, which carries a fraction $p_q = \xi P$ of the total momentum of the nucleon, recoils with its original momentum reversed, as shown in the right-hand panel of Figure 2.6.

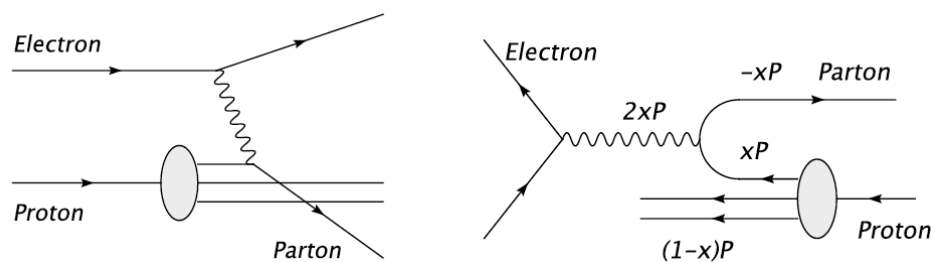Figure 2.6: Feynman diagram of the DIS process in the laboratory frame (left) and in the Breit frame (right).

After the absorption of the virtual photon, the mass-shell relation for the struck parton yields:

$$\left(\xi P + q\right)^2 = \xi^2 P^2 + 2\xi P \cdot q - Q^2 = 0 \,, \tag{2.39}$$

---

[3]Since the structure functions are Lorentz invariant, their description in the Breit frame is valid in any other frame as well.

where $q \equiv (\nu, \vec{q})$ is the four-momentum of the virtual photon and $Q^2 = -q^2$. Being a Lorentz invariant quantity, eqn. (2.39) also holds in the laboratory frame, where $P \equiv (M, 0)$:

$$\xi^2 M^2 + 2\xi M\nu - Q^2 = 0, \tag{2.40}$$

In the scaling limit $Q^2 \gg M^2$, the term $\xi^2 M^2$ becomes negligible and eqn. (2.40) yields $\xi \approx Q^2/(2M\nu)$, which is the definition of the Bjørken x variable (cf. Section 2.3). In the QPM the Bjørken x variable can thus be interpreted as the fractional momentum of the nucleon carried by the struck quark, and the DIS process consists in the incoherent sum of elastic scattering off the partons carrying a momentum fraction x of the nucleon momentum. The model, however, requires that the interaction between the individual partons is weak on short distances. This circumstance is satisfied if the scattering occurs on sufficiently short time scales, i.e. much shorter that the typical time scales of the interactions between partons. In this approximation, known as the *Impulse Approximation* (IA), the partons can be regarded as a gas of quasi-free particles.

In the QPM the nucleon is described in terms of the parton distribution functions (p.d.f.) $q_f(x)$, which represent the probability density to find in the nucleon a quark of flavour f and fractional momentum x. The quantity $q_f(x)dx$ thus represents the number of quarks with flavour f and fractional momentum in the range $[x, x + dx]$. Using the notations $q_f^{\overrightarrow{\Rightarrow}}(x)$ and $q_f^{\overrightarrow{\Leftarrow}}(x)$ for the probability densities to find a quark of flavour f with momentum fraction x and spin parallel or antiparallel, respectively, to the nucleon spin, one can define the spin-independent and spin-dependent parton distribution functions as:

$$q_f(x) = q_f^{\overrightarrow{\Rightarrow}}(x) + q_f^{\overrightarrow{\Leftarrow}}(x) \tag{2.41}$$

$$\Delta q_f(x) = q_f^{\overrightarrow{\Rightarrow}}(x) - q_f^{\overrightarrow{\Leftarrow}}(x) \, , \tag{2.42}$$

where $q_f(x)$ represents the distribution of the partons summed over the spin degrees of freedom and $\Delta q_f(x)$, given by the difference of the distributions of the partons with different helicity states, represents the helicity distribution within the nucleon.

The spin-independent and spin-dependent structure functions described in Section 2.4 can now be interpreted within the QPM as the charge-weighted sums over the quark flavours f (including anti-quarks)[4] of the corresponding parton distribution functions:

$$F_1(x) = \frac{1}{2} \sum_f e_f^2 q_f(x) \, , \tag{2.43}$$

$$g_1(x) = \frac{1}{2} \sum_f e_f^2 \Delta q_f(x) \, , \tag{2.44}$$

$$g_2(x) = 0 \, , \tag{2.45}$$

---

[4]Because of the large mass of c, b and t quarks, in practice only the three lightest quarks flavours u, d and s are considered.

where e_f is the fractional charge carried by the quarks. SInce the structure function g_2 is related to the transverse degrees of freedom of the quarks within the nucleon, it has no interpretation and vanishes in the QPM, where all the partons are assumed to move collinearly to the nucleon. The spin-independent structure function F_1 is related to F_2 by the ratio of the photo-absorption cross sections of longitudinally (L) and transversely (T) polarized virtual photons:

$$R(x, Q^2) = \frac{\sigma_L(x, Q^2)}{\sigma_T(x, Q^2)} = \frac{(1 + \gamma^2)F_2(x) - 2xF_1(x)}{2xF_1(x)} \ . \tag{2.46}$$

In the Bjørken limit the kinematic factor $\gamma = (2Mx)/Q$ becomes negligible (cf. eqn. (2.38)). In addition, the photo-absorption cross section σ_L for longitudinally polarized photons with helicity 0 vanishes due to helicity conservation at the virtual photon–parton scattering vertex. Thus $R(x, Q^2) \rightarrow 0$ and eqn. (2.46) yields:

$$F_2(x) = 2xF_1(x) \ , \tag{2.47}$$

known as the Callan-Gross relation [Cal69]. Since this relation only holds for spin-$1/2$ point-like partons, its experimental fulfillment represented the proof for the spin-$1/2$ nature of quarks.

Expliciting the various quark flavours and using the notation $q_u(x) \equiv u(x)$, $q_d(x) \equiv d(x)$, etc, the structure function F_2 can be written separately for the proton and the neutron as

$$\frac{1}{x}F_2^p = \left[\frac{4}{9}(u_v^p + u_s + \overline{u}_s) + \frac{1}{9}(d_v^p + d_s + \overline{d}_s) + \frac{1}{9}(s_s + \overline{s}_s)\right] \tag{2.48}$$

$$\frac{1}{x}F_2^n = \left[\frac{4}{9}(u_v^n + u_s + \overline{u}_s) + \frac{1}{9}(d_v^n + d_s + \overline{d}_s) + \frac{1}{9}(s_s + \overline{s}_s)\right] \ , \tag{2.49}$$

where the sub-indexes v and s denote the *valence quarks* and the *sea quarks* (cf. Section 2.7) distributions, respectively. In addition, since the proton and the neutron are partners of an isospin doublet ($I = 1/2$), their quark distributions are subject to the following relations:

$$u_v^p(x) = d_v^n(x) = u_v(x) \qquad d_v^p(x) = u_v^n(x) = d_v(x) \tag{2.50}$$

Using relations (2.50) we can rewrite eqns. (2.48) and (2.49) in the compact form:

$$\frac{1}{x}F_2^p = \frac{1}{9}\left[4u_v + d_v\right] + \frac{4}{3}S \tag{2.51}$$

$$\frac{1}{x}F_2^n = \frac{1}{9}\left[u_v + 4d_v\right] + \frac{4}{3}S \ , \tag{2.52}$$

where we have used the assumption:

$$u_s(x) = \bar{u}_s(x) = d_s(x) = \bar{d}_s(x) = s_s(x) = \bar{s}_s(x) = S(x) \ . \tag{2.53}$$

Further constraints on the quark structure functions result from the fact that the quantum numbers of the proton (neutron) should correspond to those of the uud (udd) combination of valence quarks: baryon number 1, strangeness 0, charge 1 (0). Therefore, by summing over all contributing partons, the following sum rules have to be fulfilled:

$$\int_0^1 dx[u(x) - \overline{u}(x)] = \int_0^1 dx u_v(x) = 2 \quad (1) \tag{2.54}$$

$$\int_0^1 dx[d(x) - \overline{d}(x)] = \int_0^1 dx d_v(x) = 1 \quad (2) \tag{2.55}$$

$$\int_0^1 dx[s(x) - \overline{s}(x)] = 0 \ . \tag{2.56}$$

2.7 The QCD-improved Quark Parton Model

As anticipated in Section 2.5, the scaling of the unpolarized structure functions, predicted by the quark parton model, is only approximately valid. As clearly visible in Figure 2.4, the structure function F_2 significantly increases at small x and slowly decreases at large x as a function of Q^2. This behavior cannot be explained in the framework of the QPM. In addition neutrino-nucleon DIS results showed that only about half of the nucleon momentum is carried by quarks:

$$\int_0^1 F_2^{\nu,N}(x)dx = \int_0^1 x \left[u(x) + \bar{u}(x) + d(x) + \bar{d}(x) + s(x) + \bar{s}(x) \right] dx \approx 0.5. \tag{2.57}$$

Both these observations can be explained without having to abandon the successful QPM, provided interactions among the partons, which were not accounted for in the early version of the model, are introduced. Such interactions, which are well described in the framework of QCD (see Appendix A), give rise to high order corrections to the QPM. At NLO in the strong coupling ($\mathcal{O}(\alpha_S)$), photon-gluon-fusion (PGF) and QCD Compton scattering, depicted in Figure 2.7, contribute to the DIS cross section. All these higher order corrections are taken into account in the so-called QCD-improved Quark Parton Model. According to this extended version of the QPM, quarks in the nucleons are dressed with a cloud of gluons and virtual quark-antiquark pairs, the so-called sea-quarks introduced in Section 2.6.

The question about the missing momentum (cf. eqn. (2.57)) is trivially solved ones the gluons, which cannot be directly probed by the incoming lepton since they do not carry electric charge, are take into account, providing the remaining 50% of the total momentum of the nucleon.

The interactions among the partons together with the Q^2-dependence of the strong (running) coupling constant α_S can in addition explain the violation of the Bjørken scaling observed in the structure functions: A photon with a larger four-momentum probes the nucleon with a higher resolution. At higher resolution the nucleon appears to be composed by a larger number of resolved quarks and gluons, all sharing the total nucleon momentum. As a consequence the probability of finding partons with large x decreases with increasing Q^2 while, accordingly,
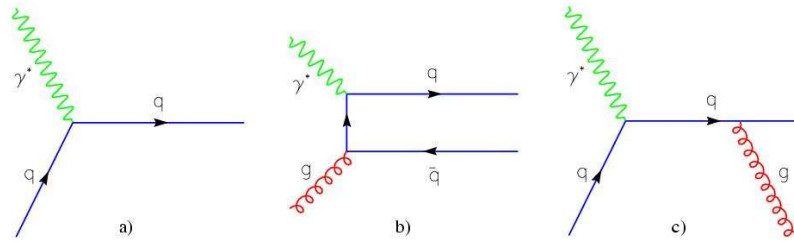
Figure 2.7: Feynman diagrams for the leading order DIS process (a) and the two NLO processes Photon-Gluon-Fusion (b) and QCD Compton scattering (c).

the probability of probing partons with low x substantially increases, explaining the results in Figure 2.4. A sketch of the Q^2-dependence of the nucleon structure is reported in Figure 2.8.
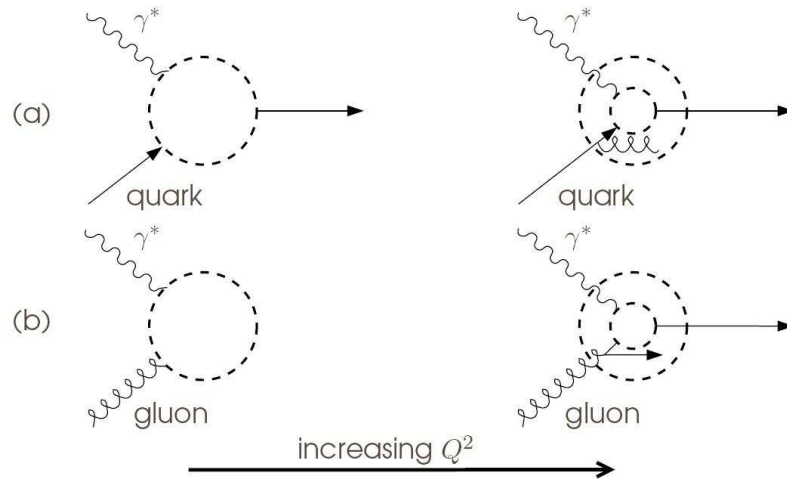
Figure 2.8: Increasing Q^2, the spatial resolution improves and a larger number of partons is resolved.

The Q^2-dependence (or Q^2-evolution) of the parton (quarks and gluons) distribution functions is described by the Dokshitzer-Gribov-Lipatov-Altarelli-Parisi (DGLAP) equations ([Dok77], [Gri72], [Lip75], [Alt77])

$$\frac{dq(x,Q^2)}{d\ln Q^2} = \int_x^1 \frac{dx'}{x'} \left[q(x',Q^2) \cdot P_{qq}\left(\frac{x}{x'}\right) + g(x',Q^2) \cdot P_{qg}\left(\frac{x}{x'}\right) \right] \tag{2.58}$$

$$\frac{dg(x,Q^2)}{d\ln Q^2} = \int_x^1 \frac{dx'}{x'} \left[g(x',Q^2) \cdot P_{gg}\left(\frac{x}{x'}\right) + \sum_q q(x',Q^2) \cdot P_{gq}\left(\frac{x}{x'}\right) \right] \tag{2.59}$$

Once the parton distribution functions are known at some scale Q_0^2, the DGLAP equations allow to calculate them at any other scale Q^2 where perturbation theory holds.

Chapter 3

The transverse degrees of freedom of the nucleon

3.1 The quark-quark correlation matrix

According to the Quark Parton Model, one can describe the DIS process as the incoherent sum of elastic scattering on quasi-free constituents (quarks and antiquarks) of the nucleon (cf. Section 2.6). In this perspective, if we consider a DIS process in which an initial state nucleon with momentum P and spin S is probed by a virtual photon carrying four momentum q, leading to a (not observed) final hadronic state X with momentum P_X and energy E_X, it is possible to rewrite the hadronic tensor $W_{\mu\nu}$ using a quantum field approach [BDR02]:

$$W^{\mu\nu} = \frac{1}{2\pi} \sum_q e_q^2 \sum_X \int \frac{d^3 P_X}{(2\pi)^3 2E_X} \int \frac{d^4 p}{(2\pi)^4} \int \frac{d^4 k}{(2\pi)^4} \delta(k^2)$$

$$\times [\bar{u}(k)\gamma^\mu \phi(p; P, S)]^* [\bar{u}(k)\gamma^\nu \phi(p; P, S)]$$

$$\times (2\pi)^4 \delta^4(P - q - P_X)(2\pi)^4 \delta^4(p + q - k) \,. \tag{3.1}$$

Here p and e_q are the four-momentum and the fractional electric charge of the soft quark struck by the virtual photon, $u(\bar{u})$ is the spinor of the scattered quasi-free quark, carrying four momentum $k = p + q$, and γ_μ are the Dirac matrices. The matrix elements

$$\phi_i(p; P, S) = \langle X | \psi_i(0) | P, S \rangle \,, \tag{3.2}$$

of the quark fields ψ_i between the nucleon $|P, S\rangle$ and its remnant $|X\rangle$, describe the emission of the soft quark from the nucleon. The Dirac delta functions ensure momentum conservation. In this formalism the struck quark and the nucleon remnant appear as two intermediate physical states of a forward scattering and the hadronic tensor can be represented by the handbag diagram reported in Figure 3.1. Eqn. (3.1) can be rewritten in the more synthetic form

$$W_{\mu\nu} = \sum_q e_q^2 \int \frac{d^4 p}{(2\pi)^4} \, \delta((p + q)^2) \text{Tr}[\Phi \gamma_\mu (\slashed{p} + \slashed{q}) \gamma_\nu] \,, \tag{3.3}$$
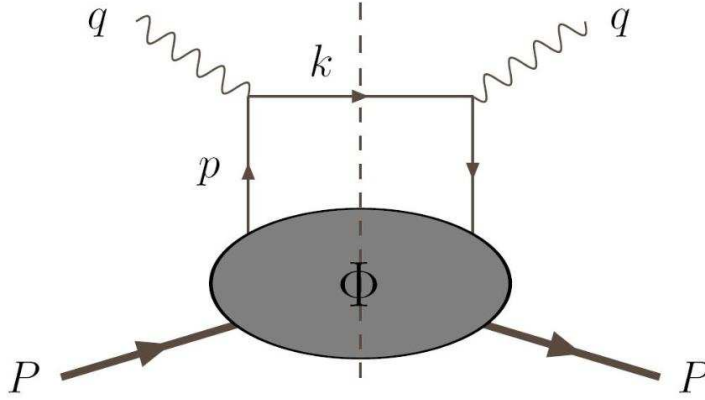
Figure 3.1: Handbag diagram for inclusive DIS.

where we have introduced the *quark-quark correlation matrix* (or *quark-quark correlator*)

$$\Phi_{i,j}(p, P, S) = \sum_X \int \frac{d^3 P_X}{(2\pi)^3 2E_X} (2\pi)^4 \delta^4(P - p - P_X) \langle P, S | \psi_j(0) | X \rangle \langle X | \psi_i(0) | P, S \rangle . \quad (3.4)$$

Here i and j are Dirac indices and summation over quark color is implicit.
Using translational invariance, the completeness relation $\sum_X |X\rangle\langle X| = \mathbb{1}$ and the identity

$$(2\pi)^4 \delta^4(P - p - P_X) \equiv \int d^4\xi e^{i(P-p-P_X)\cdot\xi} , \quad (3.5)$$

it is possible to rewrite the correlation matrix as a bilocal, bilinear operator acting on the initial nucleon state $|P, S\rangle$, integrated over all possible separations ξ of the second quark spinor:

$$\Phi_{i,j}(p, P, S) = \int d^4\xi e^{ip\cdot\xi} \langle P, S | \bar{\psi}_j(0) \psi_i(\xi) | P, S \rangle. \quad (3.6)$$

The correlation matrix can be decomposed in a basis of Dirac matrices:

$$\Gamma = \left\{ \mathbb{1}, \gamma^\mu, \gamma^\mu\gamma_5, i\gamma_5, i\sigma^{\mu\nu}\gamma_5 \right\} , \quad (3.7)$$

where $\sigma^{\mu\nu} = i/2[\gamma^\mu, \gamma^\nu]$, each selecting a different aspect of the nucleon inner structure [BDR02]:

$$\Phi(p, P, S) = \frac{1}{2} \left\{ \mathcal{S}\mathbb{1} + \mathcal{V}_\mu\gamma^\mu + \mathcal{A}_\mu\gamma_5\gamma^\mu + i\mathcal{P}_5\gamma_5 + i\mathcal{T}_{\mu\nu}\sigma^{\mu\nu}\gamma_5 \right\} . \quad (3.8)$$

Here $\mathcal{S}$, $\mathcal{V}_\mu$, $\mathcal{A}_\mu$, $\mathcal{P}_5$ and $\mathcal{T}_{\mu\nu}$ are scalar, vector, axial-vector, pseudo-scalar and tensor parameters, respectively, all depending on combinations of the momenta p, P and the nucleon spin S. Imposing hermiticity, parity invariance and time-reversal invariance of the correlation matrix Φ, these quantities are given by:

$$\mathcal{S} = \frac{1}{2}\text{Tr}(\mathbb{1}\Phi) = C_1 \ , \tag{3.9}$$

$$\mathcal{V}^\mu = \frac{1}{2}\text{Tr}(\gamma^\mu \Phi) = C_2 P^\mu + C_3 p^\mu \ , \tag{3.10}$$

$$\mathcal{A}^\mu = \frac{1}{2}\text{Tr}(\gamma^\mu \gamma_5 \Phi) = C_4 S^\mu + C_5 p \cdot S P^\mu + C_6 p \cdot S p^\mu \ , \tag{3.11}$$

$$\mathcal{P}_5 = \frac{1}{2i}\text{Tr}(\gamma_5 \Phi) = 0 \ , \tag{3.12}$$

$$\mathcal{T}^{\mu\nu} = \frac{1}{2i}\text{Tr}(\sigma^{\mu\nu}\gamma_5 \Phi) = C_7 P^{[\mu}S^{\nu]} + C_8 p^{[\mu}S^{\nu]} + C_9 p \cdot S P^{[\mu}p^{\nu]} \ , \tag{3.13}$$

where the coefficients $C_i = C_i(p^2, p \cdot P)$ are real functions.

The quantities above can be ordered according to powers of $1/P^+$, where the leading order term is $(1/P^+)^{-1} = P^+$ and the next-to-leading term is $(1/P^+)^0 = 1$ (see Appendix B for the light-cone formalism). The different powers correspond to the twist expansion according to [Jaf96], where the leading term is twist-two.

If we neglect, for the moment, the transverse momentum of the quarks in the nucleon, only the vector, axial-vector and tensor terms survive at leading-order in P^+ and the five eqns. (3.9)–(3.13) reduce to the following three equations.

$$\mathcal{V}^\mu = \frac{1}{2}\int d^4\xi e^{ip\cdot\xi}\langle P,S|\bar{\psi}(0)\gamma^\mu\psi(\xi)|P,S\rangle = A_1 P^\mu \ , \tag{3.14}$$

$$\mathcal{A}^\mu = \frac{1}{2}\int d^4\xi e^{ip\cdot\xi}\langle P,S|\bar{\psi}(0)\gamma^\mu\gamma_5\psi(\xi)|P,S\rangle = \lambda_N A_2 P^\mu \ , \tag{3.15}$$

$$\mathcal{T}^{\mu\nu} = \frac{1}{2i}\int d^4\xi e^{ip\cdot\xi}\langle P,S|\bar{\psi}(0)\sigma^{\mu\nu}\gamma_5\psi(\xi)|P,S\rangle = A_3 P^{[\mu}S_T^{\nu]} \ , \tag{3.16}$$

where λ_N denotes the nucleon helicity and

$$A_1 = \frac{1}{2P^+}\text{Tr}(\gamma^+ \Phi) \ , \tag{3.17}$$

$$\lambda_N A_2 = \frac{1}{2P^+}\text{Tr}(\gamma^+ \gamma_5 \Phi) \ , \tag{3.18}$$

$$S_T^i A_3 = \frac{1}{2P^+}\text{Tr}(\gamma^+ \gamma^i \gamma_5 \Phi) \ . \tag{3.19}$$

In the derivation of eqns. (3.14)–(3.16) the approximate relation $S^\mu \approx \lambda_N P^\mu/M + S_T^\mu$ was tacitely used.

Integrating the amplitudes A_i over p with the constraint $x = \frac{p^+}{P^+}$, three leading-twist parton distribution functions are obtained:

$$q(x) = \int \frac{d^4 p}{(2\pi)^4} A_1(p^2, p \cdot P) \delta \left(x - \frac{p^+}{P^+} \right) , \qquad (3.20)$$

$$\Delta q(x) = \int \frac{d^4 p}{(2\pi)^4} A_2(p^2, p \cdot P) \delta \left(x - \frac{p^+}{P^+} \right) , \qquad (3.21)$$

$$\delta q(x) = \int \frac{d^4 p}{(2\pi)^4} A_3(p^2, p \cdot P) \delta \left(x - \frac{p^+}{P^+} \right) . \qquad (3.22)$$

These parton distribution functions provide, together, a complete description of the momentum and spin distributions of the quarks within the nucleon at leading-twist level. The first two were already introduced in Section 2.6: the spin-independent (or momentum) distribution $q(x)$ and the helicity distribution $\Delta q(x)$. These quantities have been measured with high accuracy by a number of experiments in the past decades. In particular the HERMES experiment has played a crucial role in the extraction of the helicity distribution, providing the most precise measurement available to date [Air05b, Air07]. The third p.d.f. ($\delta q(x)$), called *trasversity*, has so far remained unmeasured due to its chiral-odd nature (see next section). A first extraction of $\delta q(x)$, based on a global fit of the data from HERMES, COMPASS and BELLE, has very recently been reported by [Ans07]. Integrating eqns. (3.20) – (3.22) over x yields:

$$q = \int_0^1 [q(x) - \bar{q}(x)] \, dx = g_V , \qquad (3.23)$$

$$\Delta q = \int_0^1 [\Delta q(x) + \Delta \bar{q}(x)] \, dx = g_A , \qquad (3.24)$$

$$\delta q = \int_0^1 [\delta q(x) - \delta \bar{q}(x)] \, dx = g_T , \qquad (3.25)$$

i.e. the first moments of the three leading-twist parton distribution functions correspond to the vector, axial and tensor charge of the nucleon, respectively. In particular, containing the difference between quark and antiquark momentum distributions, the vector charge of the nucleon is simply the valence number (2 for u quarks and 1 for d quarks for the proton and viceversa for the neutron).

In terms of the three leading-twist parton distribution functions the quark-quark correlator reads:

$$\Phi(p, P, S) = \frac{1}{2} \left\{ q(x) \not{P} + \lambda_N \Delta q(x) \gamma_5 \not{P} + \delta q(x) \not{P} \gamma_5 \not{S}_T \right\} . \qquad (3.26)$$

3.2 Interpretation of the three leading-twist parton distribution functions

In the basis of helicity eigenstates $(|+\rangle, |-\rangle)$ (*helicity basis*) it is possible to define 16 different quark-nucleon forward amplitudes $\mathcal{A}_{\Lambda\lambda,\Lambda'\lambda'}$, where $\lambda\lambda'(\Lambda\Lambda')$ represent quark (nucleon) helicity states. However, imposing helicity conservation and parity and time-reversal invariance, only three independent amplitudes survive:

$$\mathcal{A}_{++,++}, \quad \mathcal{A}_{+-,+-}, \quad \mathcal{A}_{+-,-+} \,. \tag{3.27}$$

The first two are diagonal in the helicity basis, while the third is off diagonal, i.e. requires the helicity flip of the quark $(\lambda = -\lambda')$

The optical theorem (see Appendix C) allows to relate these forward quark-nucleon amplitudes to the three leading-twist parton distribution functions derived in Section 3.1:

$$q(x) = q^{\vec{\Rightarrow}}(x) + q^{\vec{\Leftarrow}}(x) \equiv q^+(x) + q^-(x) \sim \mathrm{Im}(\mathcal{A}_{++,++} + \mathcal{A}_{+-,+-}) \,, \tag{3.28}$$

$$\Delta q(x) = q^{\vec{\Rightarrow}}(x) - q^{\vec{\Leftarrow}}(x) \equiv q^+(x) - q^-(x) \sim \mathrm{Im}(\mathcal{A}_{++,++} - \mathcal{A}_{+-,+-}) \,, \tag{3.29}$$

$$\delta q(x) \sim \mathrm{Im}(\mathcal{A}_{+-,-+}) \,. \tag{3.30}$$

The first two are related to the two quark helicity conserving amplitudes and can therefore be diagonalized in the helicity basis. As a consequence they have a precise probabilistic interpretation in this basis: $q(x)$ reflects the probability to find quarks, within an unpolarized nucleon, carrying a fraction x of its total longitudinal momentum irrespectively to the spin orientation, and $\Delta q(x)$ reflects the difference in probabilities to find, in a longitudinally polarized nucleon, quarks with their spin aligned or anti-aligned to the spin of the nucleon.

Unlike $q(x)$ and $\Delta q(x)$, $\delta q(x)$, being related to a quark helicity-odd amplitude, cannot be diagonalized in the helicity basis and therefore has no probabilistic interpretation in this basis. In particular, since helicity and chirality coincide in the infinite momentum frame, since all masses can be neglected, transversity is a *chiral-odd* function. Therefore, since electromagnetic and strong interactions conserve chirality, transversity is not measurable in inclusive DIS processes. This can be understood since helicity is a conserved quantity for nearly massless particles and therefore a helicity flip is suppressed by a factor of $\frac{m}{Q^2}$, as displayed in Figure 3.2 (c). In addition no direct relation between $\delta q(x)$ and the polarized structure function $g_2(x)$ exists, which can be accessed in inclusive DIS on a transversely polarized target.

However, in a basis of transverse spin eigenstates, which are defined as linear combinations of the helicity eigenstates

$$| \uparrow \rangle = \frac{1}{2} \left(|+\rangle + i|-\rangle \right) \,, \qquad | \downarrow \rangle = \frac{1}{2} \left(|+\rangle - i|-\rangle \right) \,, \tag{3.31}$$

$\delta q(x)$ acquires a probabilistic interpretation and becomes a number density reflecting the difference in probabilities to find, in a transversely polarized nucleon, quarks with their spin aligned or anti-alligned to the spin of the nucleon:

$$\delta q(x) = q^{\Uparrow\uparrow}(x) - q^{\Uparrow\downarrow}(x) \equiv q^\uparrow(x) - q^\downarrow(x) \sim \mathrm{Im}(\mathcal{A}_{\uparrow\uparrow,\uparrow\uparrow} - \mathcal{A}_{\uparrow\downarrow,\uparrow\downarrow}) \,. \tag{3.32}$$
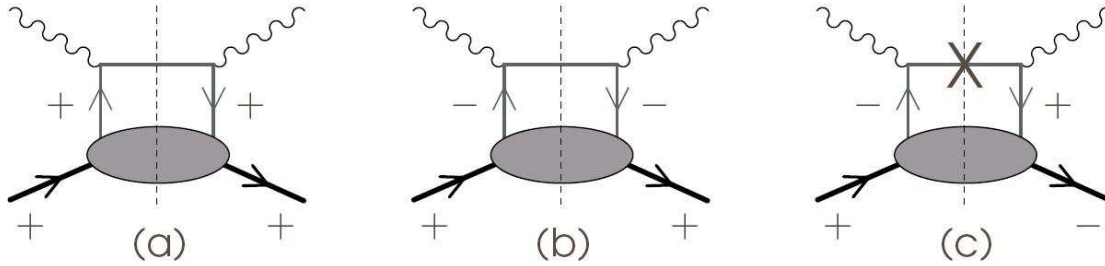
Figure 3.2: Handbag diagrams of the three independent configurations of quark and nucleon helicities in inclusive DIS. The configurations (a) and (b) are proportional to $q(x)$ and $\Delta q(x)$, respectively. The configuration (c), which includes helicity flips of quark and nucleon, is proportional to $\delta q(x)$ and forbidden by helicity conservation.

Since the basis of transverse spin eigenstates can be transformed into the helicity basis through a simple rotation, only in relativistic regimes, where Lorentz boost and rotation do not commute, differences between $\Delta q(x)$ and $\delta q(x)$ are expected. In addition, unlike the helicity distribution, transversity does not exist for gluons in the nucleon since a hypothetical $\delta g(x)$ would be related to an helicity flip gluon-nucleon amplitude, which implies an impossible helicity flip of 2 for a spin-half target. As a consequence, the transversity is a pure valence object. This of course heavily differentiates the Q^2 evolution of the transversity and helicity distributions. So, even if at some scale Q_0^2 transversity and helicity distribution would coincide, this is not necessarily the case at a different Q^2 scale, as shown in Figure 3.3.

The three leading-twist parton distribution functions, which are equally important for a complete description of the momentum and spin distribution of the nucleon at leading-twist level, are related by three important bounds. From the definitions of $q(x)$, $\Delta q(x)$ and $\delta q(x)$, the relation $q(x) = q^+(x) + q^-(x) = q^\uparrow(x) + q^\downarrow(x)$ follows which immediately leads to the first two bounds:

$$|\Delta q(x)| \leqslant q(x) \,, \qquad |\delta q(x)| \leqslant q(x) \,. \tag{3.33}$$

The third, more subtle, bound, which simultaneously involves the three leading-twist parton distribution functions, is known as the Soffer inequality [Sof95]:

$$q(x) + \Delta q(x) \geqslant 2|\delta q(x)| \,. \tag{3.34}$$

A graphical representation of this inequality is reported in Figure 3.4. Its derivation is more complicated as it involves three quantities that are not diagonal in the same basis. Similar inequalities hold for the antiquark distributions.
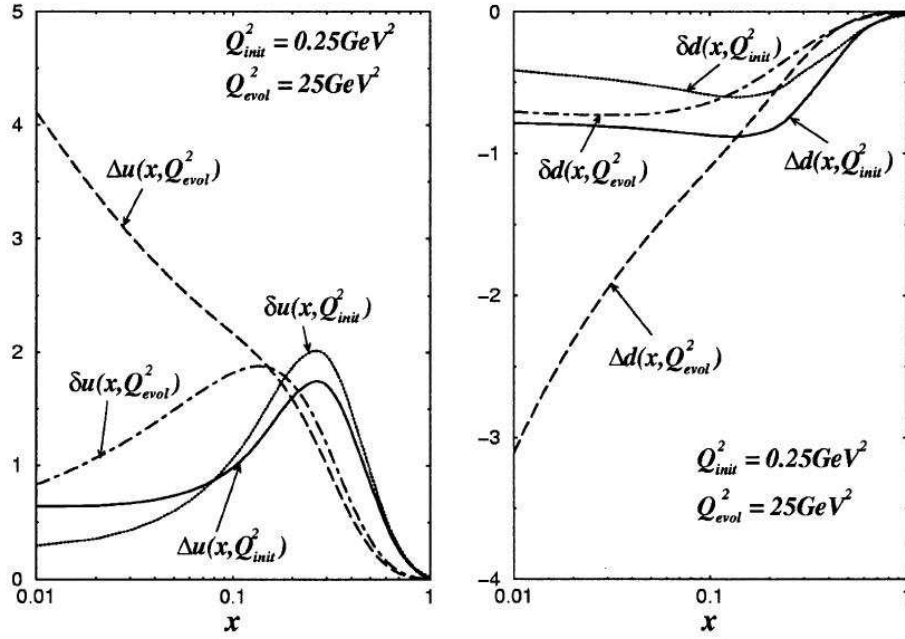
Figure 3.3: Chiral Quark Soliton Model calculation of $\Delta q(x)$ and $\delta q(x)$ for *up* and *down* quarks. While the two distributions are very similar at the scale of the model ($Q_0^2 = 0.25$ GeV^2), they differ substantially, especially in the low x region, after a perturbative evolution at ($Q^2 = 25$ GeV^2) [BDR02, Wak99].

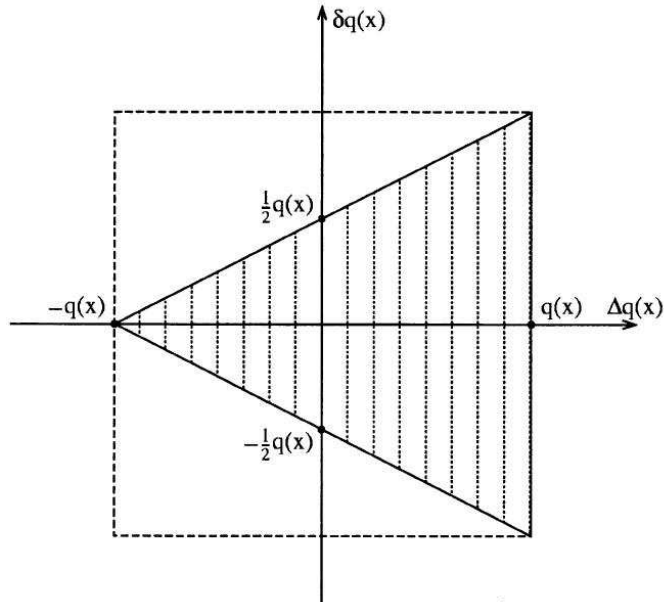Figure 3.4: The Soffer bound on the leading-twist parton distribution functions (source [BDR02]).

3.3   Transverse Momentum Dependent parton distribution functions

Intrinsic transverse momentum $\vec{p}_T$ can originate from partonic confinement and from basic QCD evolution [Arr04]. So far it has been neglected because it is small compared to the longitudinal component. However, as it influences the final momenta of the produced hadrons, it becomes important in the description of the Semi-Inclusive DIS (see section 3.7). More in general, it cannot be ignored in perturbative QCD hard processes and in soft non perturbative physics since it becomes crucial for the explanation of many single spin effects recently observed in several ongoing experiments.

Taking into account the transverse component, which is suppressed by one power of P^+ with respect to the longitudinal one, the quark four-momentum reads:

$$p^\mu = xP^\mu + p_T^\mu \,, \tag{3.35}$$

where P^μ is, as usual, the nucleon total longitudinal momentum. Furthermore, additional amplitudes now appear in the axial-vector and tensor component of the quark-quark correlator:

$$\mathcal{A}^\mu = \lambda_N A_2 P^\mu + \frac{1}{M}\tilde{A}_1\, p_T \cdot S_T P^\mu \,, \tag{3.36}$$

$$\mathcal{T}^{\mu\nu} = A_3 P^{[\mu}S_T^{\nu]} + \frac{\lambda_N}{M}\tilde{A}_2 P^{[\mu}p_T^{\nu]} + \frac{1}{M^2}\tilde{A}_3 p_T \cdot S_T P^{[\mu}p_T^{\nu]} \,, \tag{3.37}$$

where we have defined the new real functions $\tilde{A}_i(p^2, p \cdot P)$ and introduced powers of M so that all coefficients have the same dimension. As a consequence, if we do not integrate over the transverse momentum p_T, we obtain six p_T-dependent distribution functions. Four of them, called $q(x, p_T^2)$, $\Delta q(x, p_T^2)$, $h_{1T}(x, p_T^2)$ and $h_{1T}^\perp(x, p_T^2)$, reduce to the three leading-twist parton distribution functions $q(x)$, $\Delta q(x)$ and $\delta q(x)$ after integration over p_T:

$$q(x) = \int d^2\vec{p}_T\, q(x, p_T^2) \,, \tag{3.38}$$

$$\Delta q(x) = \int d^2\vec{p}_T\, \Delta q(x, p_T^2) \,, \tag{3.39}$$

$$\delta q(x) = \int d^2\vec{p}_T \left\{ h_{1T}^q(x, p_T^2) + \frac{p_T^2}{2M} h_{1T}^{\perp q}(x, p_T^2) \right\} \equiv \int d^2 p_T^2\, \delta q(x, p_T^2) \,. \tag{3.40}$$

The other two, called $g_{1T}(x, p_T^2)$ and $h_{1L}^\perp(x, p_T^2)$, are completely new and are related, together with $h_{1T}^\perp(x, p_T^2)$, to the terms of the correlation matrix containing the $\tilde{A}_i$ functions.

If the target nucleon is unpolarized, the only measurable quantity is $q(x, p_T^2)$, which represents the number density of quarks with longitudinal momentum fraction x and squared transverse momentum p_T^2. If the target nucleon is longitudinally polarized there is some probability to find the quarks polarized along the same direction as the nucleon, $\Delta q(x, p_T^2)$, or along a different direction, $h_{1L}^\perp(x, p_T^2)$. If, on the other hand, the target nucleon is transversely polarized, there is some probability to find the quarks polarized along the same direction as the nucleon, $\delta q(x, p_T^2)$,

along a different direction, $h_{1T}^{\perp}(x, p_T^2)$, or longitudinally polarized, $g_{1T}^{\perp}(x, p_T^2)$. This variety of situations is allowed by the presence of a non-vanishing quark transverse momentum p_T. After the integration over p_T, only the cases of quark polarization parallel (or antiparallel) to that of the nucleon, $\Delta q(x)$ and $\delta q(x)$, survive.

Relaxing the time-reversal invariance condition (see Section 3.4), which was retained in the derivation of the parton distribution functions in Section 3.1, two additional terms in the vector and tensor components of Φ arise:

$$\mathcal{A}^{\mu} = \cdots + \frac{1}{M} A_1' \epsilon^{\mu\nu\rho\sigma} P_{\nu} p_{T\rho} S_{\perp\sigma} \,, \tag{3.41}$$

$$\mathcal{T}^{\mu\nu} = \cdots + \frac{1}{M} A_2' \epsilon^{\mu\nu\rho\sigma} P_{\rho} p_{T\sigma} \,, \tag{3.42}$$

which give rise to two p_T-dependent T-odd distribution functions. The first of them, $f_{1T}^{\perp}$, known as the *Sivers function* is related to the number density of unpolarized quarks in a transversely polarized nucleon. The second, $h_1^{\perp}$, known as the *Boer-Mulders function*, measures the quark transverse polarization in an unpolarized hadron.

The Sivers function $f_{1T}^{\perp}$ was first proposed by Sivers [Siv90] to explain single-spin asymmetries observed in pion production in proton-proton scattering. The interest on this function has greatly grown over the past years after a theoretical work [Bro02, Bur02] has demonstrated that a non-zero Sivers function requires a non-vanishing orbital angular momentum of the quarks within the nucleon, which is one of the still missing pieces of the nucleon spin puzzle (cf. eqn. (1.1)).

The p_T-dependent parton distribution functions introduced in this section are reported in Figure 3.5 together with a schematic illustration of their probabilistic interpretations. Nucleon and quarks are represented by yellow (big) and red (small) circles, respectively. The arrows indicate the spin orientation relative to a virtual photon entering from the left, and U, L and T stand for Unpolarized, Longitudinal polarized and Transversely polarized quarks and nucleons.

For future applications it is convenient to define the following moments of the generic parton distribution function $d^q(x, p_T^2)$:

$$d^{(1/2)q}(x) \equiv \int d^2\vec{p}_T d^{(1/2)q}(x, p_T^2) \equiv \int d^2\vec{p}_T \frac{|\vec{p}_T|}{2M} d^q(x, p_T^2) \,, \tag{3.43}$$

$$d^{(n)q}(x) \equiv \int d^2\vec{p}_T d^{(n)q}(x, p_T^2) \equiv \int d^2\vec{p}_T \left(\frac{\vec{p}_T^2}{2M^2} \right)^n d^q(x, p_T^2) \,, \tag{3.44}$$

where n is an integer.

Positivity bounds similar to those reported in eqn. (3.33) hold for the two T-odd parton distribution functions $f_{1T}^{\perp}$ and $h_1^{\perp}$. Using the formalism of eqns. (3.43) and (3.44) yields [Bac00]:

$$|f_{1T}^{\perp(1)q}(x, p_T^2)| \leqslant q^{(1/2)}(x, p_T^2) \,, \tag{3.45}$$

$$|h_1^{\perp(1)q}(x, p_T^2)| \leqslant q^{(1/2)}(x, p_T^2) \,. \tag{3.46}$$

Figure 3.5: Leading-twist transverse momentum dependent quark distribution functions.

3.4   Naïve time-reversal quantities

In order to justify the existence of the T-odd (i.e. time-reversal violating) Sivers ($f_{1T}^{\perp}$) and Boer-Mulders ($h_1^{\perp}$) functions introduced in the previous section, a short digression is here necessary.

Invariance under a time-reversal operation which transforms initial states into final states, implies the following constraint on the quark-quark correlation matrix Φ [BDR02]:

$$\Phi^*(p, P, S) = \gamma_5 C \Phi(\tilde{p}, \tilde{P}, \tilde{S}) C^\dagger \gamma_5 \ , \qquad (3.47)$$

where $C = i\gamma^2\gamma^0$ and the tilde four-vectors are defined as $\tilde{p}^\mu = (p^0, -\vec{p})$. Normally, T-odd terms in Φ would change the sign of the l.h.s. of eqn. (3.47) and would therefore be forbidden. However, it has been proved [Bro02] that the insertion of a gauge link operator $\mathcal{L}$ in Φ (see Appendix D), which is required for the gauge invariance of Φ itself, allows for the existence of T-odd parton distribution functions. In the simplest case, indeed, the gauge link acts through a soft gluon exchange, which causes final state interactions between the struck quark and the nucleon remnant (see Figure 3.6). As a consequence, since the transformation of interacting final states into initial states is not as simple as for non-interacting final states, time-reversal invariance cannot be implemented by simply imposing the condition (3.47). Therefore, in the presence of final state interactions, the violation of condition (3.47) does not mean that time-reversal is violated. This circumstance is often referred to as naïve T-odd.

While standard time-reversal changes the nucleon state $|P, S\rangle$ into $|-P, -S\rangle$, naïve time-reversal, due to the final state interactions, only changes the initial state $|P, S\rangle$ into $|P, -S\rangle$. Therefore a violated naïve time-reversal can also be interpreted as a violation of a time-reversal without interchange of initial and final states. Naïve T-odd distribution functions are thus not fully T-odd functions and can, therefore, be non-zero. If, on the other hand, one neglects the

gauge link, naïve T-odd functions like the Sivers function would transform, under standard time-reversal, into their negative, and, thus, would vanish. In the following the adjective "naïve" will be omitted and naïve T-odd quantities will simply be referred to as T-odd.
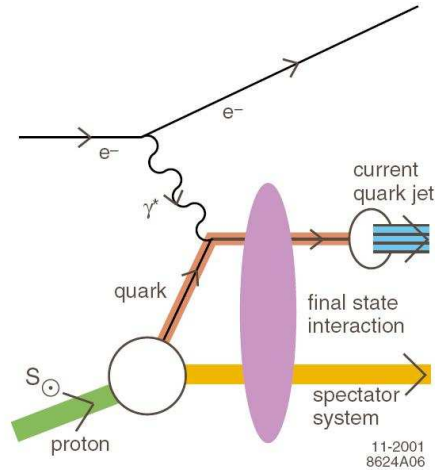
Figure 3.6: Final state interaction in semi-inclusive deep inelastic scattering (source [Bro02]).

3.5 Subleading-twist Distribution Functions

Taking into account also terms of order of $(1/P^+)^0$, six new (*twist-three*) distribution functions enter the p_T-integrated quark-quark correlation matrix [Mul96]: three T-even functions, $e^q(x)$, $h_L^q(x)$ and $g_T^q(x)$, and three T-odd functions, $h^q(x)$, $e_L^q(x)$ and $f_T^q(x)$, where L and T indicate a Longitudinally and a Transversely polarized nucleon, respectively (see Table 3.1).

Since various kinematical and dynamical effects like the quark masses, the intrinsic transverse motion and the gluon interactions enter the definition of these functions, their probabilistic interpretation in terms of partonic distributions is not trivial. However, it can be shown [Mul96] that twist-three distribution functions can be decomposed into three parts: a quark mass term, a term which is related to a leading-twist parton distribution function and a genuine interaction-dependent twist-three term, which arises from non-handbag diagrams like the one shown in Figure 3.7. The latter (interaction-dependent) term, which may differ for different processes, requires the contribution of the quark-quark-gluon correlation function.

Among the twist-three distribution functions, $g_T^q(x)$ is particularly interesting since it is related to the polarized structure function $g_2(x)$:

$$g_1(x) + g_2(x) = \frac{1}{2} \sum_{q,\bar{q}} e_q^2 g_T^q(x) \ . \tag{3.48}$$

Furthermore, the decomposition of $g_T^q(x)$ contains, together with other terms, the transversity distribution, although suppressed by the m_q/M ratio:
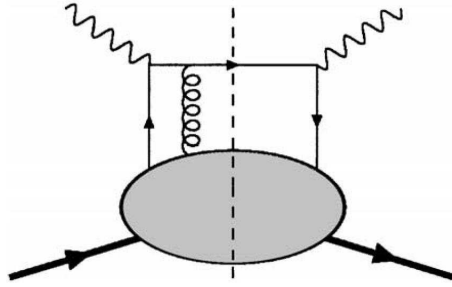
Figure 3.7: Higher-twist contribution to DIS involving quark-quark-gluon correlation.

Quark Distribution Functions			
Twist	U	L	T
2	$q(x)$	$\Delta q(x)$	$\delta q(x)$
3 (T-even)	$e(x)$	$h_L(x)$	$g_T(x)$
3 (T-odd)	$h(x)$	$e_L(x)$	$f_T(x)$

Table 3.1: Leading-twist and twist-three quark transverse momentum independent distribution functions. U, L and T stand for Unpolarized, Longitudinal polarized and Transversely polarized nucleon.

$$g_T^q(x) = \frac{m_q}{M}\delta q(x) + \frac{1}{x}g_{1T}^{(1)q}(x) + \tilde{g}_T^q(x) \,, \tag{3.49}$$

where the interaction dependent term is indicated by a tilde. Eqn. (3.49) shows that only an indirect relation between $g_2(x)$ and $\delta q(x)$ exists, which means that it is not possible to extract one of the two from the measurement of the other.

3.6 The polarized Drell-Yan

As anticipated in Section 3.2, helicity conservation prevents transversity to be measured in inclusive DIS processes. However transversity can in principle be measured in processes that involve another chiral-odd object. Such processes will indeed have an overall chiral-even cross section and ensure helicity conservation.

As an example, transversity can be measured in transversely-polarized Drell-Yan processes in proton-proton scattering. Here the transversity distribution of the quarks from one of the two colliding protons can be measured in combination with that of the anti-quarks from the other proton. Polarized Drell-Yan in proton-proton scattering is part of the RHIC Spin Program.

The PAX experiment [PAX05], proposed for the High Energy antiproton Storage Ring (HESR) facility at FAIR (GSI) aims to measure transversity in polarized proton-antiproton scattering.

Since the gluons, which split up into sea quark-antiquark pairs, do not exhibit a transversity distribution in the nucleon, the valence-quark transversity distributions are expected to be much larger than the sea-quarks ones. As a consequence larger cross section asymmetries (analyzing powers) are predicted in the proton-antiproton scattering than in the proton-proton scattering. In the former case, indeed, the product of two valence-quark distributions, δq in the proton and $\delta \bar{q}$ in the antiproton, which are equal due to charge conjugation symmetry, enters the cross section, while in the latter case only the product of a valence-quark times a sea-quark transversity distribution enters the cross section.

3.7 The Semi-Inclusive Deep Inelastic Scattering

The Semi-Inclusive DIS (SIDIS) measurements, in which one or more final state hadrons are detected together with the scattered lepton, represent an alternative way to access transversity. Here, indeed, transversity enters the cross section in combination with a chiral-odd *fragmentation function* (see Section 3.7.3). By identifying the produced hadrons, one is able to gain valuable information about the parent quarks. This allows, for instance, to measure the flavour decomposition of the parton distribution functions [Air05b]. Thanks to their highly efficient discrimination power between leptons and hadrons and among different hadron types, the HERMES and the COMPASS experiments are particularly suited for such measurements.

The formalism described so far for the inclusive DIS can be easily extended to include also Semi-Inclusive measurements. For the one-hadron case one has:

$$l(\ell) + N(P) \rightarrow l(\ell') + h(P_h) + X(P_X) \,, \tag{3.50}$$

where l, N, h and X denote the lepton, the nucleon target, the produced hadron and the undetected hadronic final state, respectively, and the quantities in parentheses denote their four-momenta (see Figure 3.8).
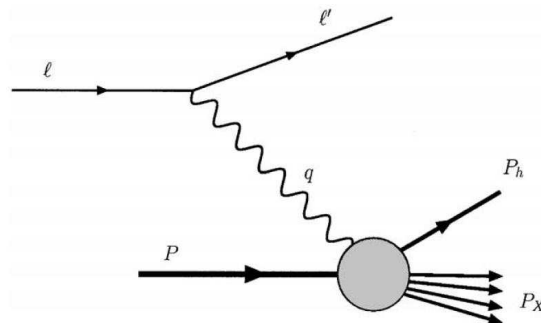
Figure 3.8: Feynman diagram for Semi-Inclusive Deep Inelastic Scattering.

This extension requires, as a new ingredient, a description of the transition from the partonic (i.e. quarks and gluons) to the hadronic degrees of freedoms.

The process in which the final hadrons emerge from the deep inelastic scattering is called *fragmentation* (or *hadronization*) and cannot be treated using perturbative QCD since the strong coupling constant α_s becomes too large at low energy, which is exactly where fragmentation occurs.

However, a variety of phenomenological models has been developed for the description of the fragmentation process. A very successful model is the LUND string-fragmentation model [And83, And97]. In this model, the color field connecting the initial quarks is assumed to produce a potential which increases linearly with the distance between the quarks (color string). After one of the quarks is struck by the virtual photon and moves away, the energy stored in the string rises linearly with the increasing separation. As soon as this energy exceeds the rest mass of a quark-antiquark pair, the string breaks up and leads to the creation of such a pair. The partners of this pair are then connected to the initial quarks by two new strings. The process (breaking of the string and formation of new quark-antiquark pairs) continues until a quark-antiquark pair is formed which is close to the mass shell of a hadron. The LUND model is widely implemented in the Monte Carlo codes used by the high energy physics community.

3.7.1   Factorization theorem and fragmentation functions

An essential concept for the description of semi-inclusive DIS is the so-called *factorization theorem*, which states that the scattering process of the virtual photon off a nucleon can be divided into three parts: the hard scattering of the photon off one of the nucleon's constituents, the selection of these constituents according to their distribution within the nucleon and the hadronization of the struck parton into the final state hadrons. The cross section for a lepto-production of a hadron h can thus be factorized as:

$$\frac{d^3\sigma^h}{dxdQ^2dz} = \sum_{a,b=q,\bar{q},g} d_a(x,Q^2) \otimes \sigma_{ab}(x,Q^2) \otimes F_b^h(z,Q^2) \,, \qquad (3.51)$$

where $d_a(x,Q^2)$ is a parton distribution function, describing the distribution of the initial state partons a in the nucleon, σ_{ab} is the hard-scattering cross section (calculable from perturbation theory) for the process $la \rightarrow l'b$ and $F_b^h(z,Q^2)$ is a *fragmentation function* (FF), i.e. a function that describes the transition (fragmentation) from the final state parton b into a hadron h carrying a fractional energy z.

More in general, QCD factorization has been established for three classes of semi-inclusive processes: di-hadron production in e^+e^- annihilation, semi-inclusive DIS, and Drell-Yan (cf. Section 3.6). It still remains to be proven whether factorization also holds for more complicated processes in hadronic scattering.

If we consider only the three lightest quark flavours (u, d, s), the FFs can be divided into three categories: favorite (fav), unfavorite ($unfav$) and strange (s), depending on the flavour of the fragmenting quark and on the quark content of the produced hadron, according to [1]:

---

[1]Since this argument is of general valence, F represents here a generic fragmentation function.

$$F_{fav}(z, Q^2) = F_u^{\pi^+}(z, Q^2) = F_{\bar{u}}^{\pi^-}(z, Q^2) = F_{\bar{d}}^{\pi^+}(z, Q^2) = F_d^{\pi^-}(z, Q^2) \,, \tag{3.52}$$

$$F_{unfav}(z, Q^2) = F_u^{\pi^-}(z, Q^2) = F_{\bar{u}}^{\pi^+}(z, Q^2) = F_{\bar{d}}^{\pi^-}(z, Q^2) = F_d^{\pi^+}(z, Q^2) \,, \tag{3.53}$$

$$F_s(z, Q^2) = F_s^{\pi^+}(z, Q^2) = F_{\bar{s}}^{\pi^-}(z, Q^2) = F_{\bar{s}}^{\pi^+}(z, Q^2) = F_s^{\pi^-}(z, Q^2) \,. \tag{3.54}$$

Similar expressions hold for the charged kaons. The fragmentation functions are not calculable from first principles and have been historically derived from fits of data from e^+e^- experiments [Kre00]. Parameterizations for the fragmentation functions for charged hadrons have been recently obtained for the first time in a global NLO QCD analysis of e^+e^- annihilations data and of single-inclusive hadron production from proton-proton collisions (RHIC) and deep inelastic lepton-hadron scattering (HERMES) [Flo07].

3.7.2 The hadronic tensor

Since the leptonic vertex of the Feynman diagram which describes the SIDIS process is identical to that for the DIS process (cf. Figures 2.2 and 3.8), the leptonic tensor is unchanged:

$$L_{\mu,\nu} = 2(\ell^\mu \ell'^\nu + \ell^\nu \ell'^\mu + g^{\mu\nu}(m^2 - \ell^\sigma \ell'_\sigma)) + 2im\epsilon_{\mu\nu\alpha\beta}s^\alpha(\ell^\beta - \ell'^\beta). \tag{3.55}$$

In contrast, the hadronic tensor has now to include the fragmentation of the struck quark. If we limit ourselves to the leading and first subleading (twist-three) terms, the hadronic tensor takes the form [Bac07]:

$$2MW^{\mu\nu} = 2z \sum_{q\bar{q}} e_q^2 \int d^2 p_T d^2 K_T \delta(p_T + q_T - K_T) \operatorname{Tr} \Bigg\{ \Phi^q(x, p_T)\gamma^\mu \Delta^q(z, K_T)\gamma^\nu$$

$$-\frac{1}{Q\sqrt{2}} \Big[\gamma^\alpha \slashed{n}_+ \gamma^\nu \tilde{\Phi}_{A\alpha}^q(x, p_T)\gamma^\mu \Delta^q(z, K_T) + \gamma^\alpha \slashed{n}_- \gamma^\nu \tilde{\Delta}_{A\alpha}^q(z, K_T)\gamma^n u \Phi^q(x, p_T) + h.c. \Big] \Bigg\} \,, \tag{3.56}$$

where $n_+ = [0, 1, 0_T]$ and $n_- = [1, 0, 0_T]$ are light-like vectors, p_T is the quark transverse momentum and K_T denotes the transverse component of the final state hadron momentum with respect to the direction of the fragmenting quark. Φ and Δ are the correlation functions for the quark distribution (lower blob of Figure 3.9 a) and for the quark fragmentation (upper blob of Figure 3.9 a), respectively, while the tilde functions $\tilde{\Phi}$ and $\tilde{\Delta}$ are their analogs with an additional gluon leg (see Figure 3.9 b and c) and are usually referred to as *quark-gluon-quark distribution correlation function* and *quark-gluon-quark fragmentation correlation function*.

A complete parametrization of the correlation functions $\Phi(x, p_T)$, $\Delta(z, K_T)$, $\tilde{\Phi}(x, p_T)$ and $\Delta(z, \tilde{K_T})$ up to twist-three level and their decomposition in the basis of the Dirac matrices (eqn. (3.7)) is reported in [Bac07]. In particular, the decomposition of the correlation matrix $\Delta(z, K_T)$ yields eight leading-twist fragmentation functions dependent on z and on K_T^2. After summation over the spin of the produced hadron S_h, only two fragmentation functions remain at leading twist: the spin-independent fragmentation function $D_1^q(z, K_T^2)$ and the so-called *Collins function* $H_1^{\perp q}(z, K_T^2)$ [Col93].
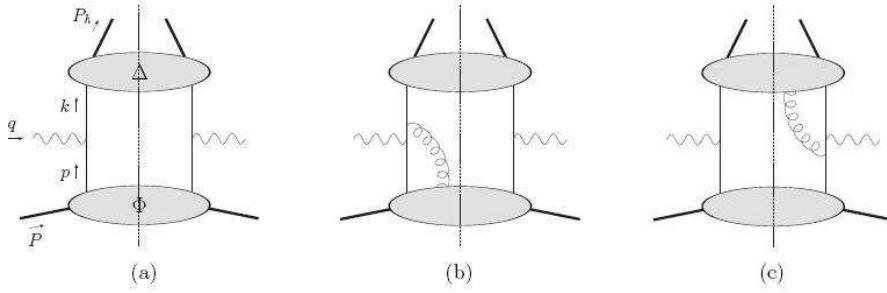
Figure 3.9: Extended handbag diagrams for semi-inclusive DIS.

3.7.3 The $D_1^q(z, K_T^2)$ and $H_1^{\perp q}(z, K_T^2)$ fragmentation functions

Similarly to the leading-twist parton distribution functions, the leading-twist fragmentation functions $D_1^q(z, K_T^2)$ and $H_1^{\perp q}(z, K_T^2)$ have a probabilistic interpretation: the first one represents the probability density that a struck quark of flavour q fragments into a hadron h with energy fraction z and transverse momentum K_T with respect to the direction of the fragmenting quark. The second, known as the *Collins function*, represents the correlation between the transverse spin of the fragmenting quark and the transverse momentum of the produced hadron. It can thus be viewed as a quark spin analyzer. From a probabilistic point of view, it expresses the difference of probability densities for quarks with opposite transverse spin states to fragment into a hadron h with transverse momentum K_T with respect to the direction of the fragmenting quark. A positive Collins function then corresponds to a preference of the hadron to move to the left for fragmenting quark moving into the page and quark spin pointing upwards. Like the Sivers function it vanishes when integrated over the intrinsic transverse momentum. The probabilistic interpretation of these two fragmentation functions is represented in Figure 3.10.

Figure 3.10: The leading-twist transverse momentum dependent fragmentation functions. The struck quark (produced hadron) is represented as a small red (big yellow) circle.

While D_1^q does not change sign under chirality and time-reversal operations, the Collins function $H_1^{\perp q}$ is a chiral-odd and T-odd quantity. In contrast to the T-odd parton distribution functions described in Section 3.4, T-odd fragmentation functions are not constrained by time-reversal invariance because of the unknown hadronic final state X accompanying the detected hadron h. In particular it has been shown [Bac01, Bac02a] that the exchange of a soft gluon between the initial quark and the fragmentation correlator is not necessary since final-state interactions, which occur solely in the upper soft part of the extended handbag diagram shown in Figure 3.9, are sufficient for the existence of T-odd FFs.

As for the parton distribution functions, also for the fragmentation functions it is convenient to introduce of the moments (the relation $\vec{K}_T = -z\vec{k}_T$, where $\vec{k}_T$ denotes the intrinsic transverse momentum of the fragmenting quark, is used below):

$$F^{(1/2)}(z) \equiv z^2 \int d^2\vec{k}_T F^{(1/2)}(z, z^2 k_T^2) \equiv z^2 \int d^2\vec{k}_T \frac{|\vec{k}_T|}{2M_h} F(z, z^2 k_T^2) \,, \qquad (3.57)$$

$$F^{(n)}(z) \equiv z^2 \int d^2\vec{k}_T F^n(z, z^2 k_T^2) \equiv z^2 \int d^2\vec{k}_T \Big(\frac{\vec{k}_T^2}{2M_h} \Big)^n F(z, z^2 k_T^2) \,, \qquad (3.58)$$

where n is an integer and F represents the generic (spin-independent or Collins) transverse momentum dependent fragmentation function. In particular, the positivity constraint leads to the following inequality between the moments of the two fragmentation functions [Bac02b]:

$$|H_1^{\perp(1)}(z, z^2 k_T^2)| \leq D_1^{(1/2)}(z, z^2 k_T^2) \,. \qquad (3.59)$$

3.7.4 The SIDIS cross section

The cross section of the one-hadron semi-inclusive electron-nucleon scattering is six-fold differential :

$$d^6\sigma \equiv \frac{d^6\sigma}{dx\,dy\,dz\,d\phi\,d\phi_S\,dP_{h\perp}^2} = \frac{\alpha^2 y}{8zQ^4} 2M W^{\mu\nu} L_{\mu\nu} \,. \qquad (3.60)$$

Here ϕ_S is the azimuthal angle, around the virtual photon direction, between the transverse component of the target spin vector $\vec{S}_T$ and the scattering plane, and ϕ is the azimuthal angle between the scattering plane and the hadron-production plane, as depicted in Figure 3.11. As will be discussed in Section 3.7.5, these two angles play a crucial role in the interpretation of the cross section asymmetries.
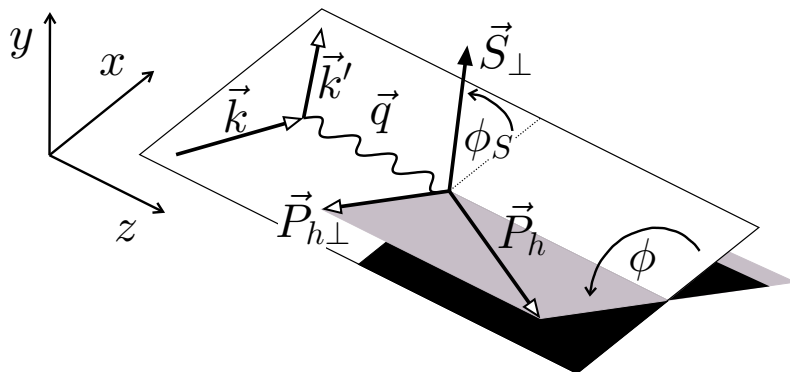
Figure 3.11: Definition of the azimuthal angles ϕ and ϕ_S between the scattering plane (white), the hadron-production plane (grey) and the transverse component of the nucleon spin vector $\vec{S}_\perp$ (or $\vec{S}_T$).

Assuming single photon exchange, the lepton-hadron cross section can be expressed in a model independent way through a set of structure functions, which in general depend on x, Q^2, z and $P_{h\perp}^2$, according to [Bac07]:

$$
\frac{d^6\sigma}{dxdydzd\phi d\phi_S dP_{h\perp}^2} = \frac{\alpha^2}{xyQ^2}\frac{y^2}{2(1-\epsilon)}\left(1+\frac{\gamma^2}{2x}\right)\left\{F_{UU,T}+\epsilon F_{UU,L}\right.
$$

$$
+\sqrt{2\epsilon(1+\epsilon)}\,\cos\phi\,F_{UU}^{\cos\phi}+\epsilon\cos(2\phi)\,F_{UU}^{\cos(2\phi)}+\lambda_e\sqrt{2\epsilon(1-\epsilon)}\,\sin\phi\,F_{LU}^{\sin\phi}
$$

$$
+S_L\left[\sqrt{2\epsilon(1+\epsilon)}\,\sin\phi\,F_{UL}^{\sin\phi}+\epsilon\sin(2\phi)\,F_{UL}^{\sin(2\phi)}\right]
$$

$$
+S_L\lambda_e\left[\sqrt{1-\epsilon^2}\,F_{LL}+\sqrt{2\epsilon(1-\epsilon)}\,\cos\phi\,F_{LL}^{\cos\phi}\right]
$$

$$
+|S_T|\left[\sin(\phi-\phi_S)\left(F_{UT,T}^{\sin(\phi-\phi_S)}+\epsilon F_{UT,L}^{\sin(\phi-\phi_S)}\right)\right.
$$

$$
+\epsilon\sin(\phi+\phi_S)\,F_{UT}^{\sin(\phi+\phi_S)}+\epsilon\sin(3\phi-\phi_S)\,F_{UT}^{\sin(3\phi-\phi_S)}
$$

$$
\left.+\sqrt{2\epsilon(1+\epsilon)}\,\sin\phi_S\,F_{UT}^{\sin\phi_S}+\sqrt{2\epsilon(1+\epsilon)}\,\sin(2\phi-\phi_S)\,F_{UT}^{\sin(2\phi-\phi_S)}\right]
$$

$$
+|S_T|\lambda_e\left[\sqrt{1-\epsilon^2}\,\cos(\phi-\phi_S)\,F_{LT}^{\cos(\phi-\phi_S)}+\sqrt{2\epsilon(1-\epsilon)}\,\cos\phi_S\,F_{LT}^{\cos\phi_S}\right.
$$

$$
\left.\left.+\sqrt{2\epsilon(1-\epsilon)}\,\cos(2\phi-\phi_S)\,F_{LT}^{\cos(2\phi-\phi_S)}\right]\right\}. \tag{3.61}
$$

The first and second subscript in the structure functions above indicate the polarization[2], with respect to the photon direction, of beam and target, respectively, whereas the third subscript in $F_{UU,T}$, $F_{UU,L}$, $F_{UU,T}^{\sin(\phi-\phi_S)}$ and $F_{UU,L}^{\sin(\phi-\phi_S)}$ specifies the polarization of the virtual photon. In addition, λ_e denotes the helicity state of the lepton beam and

$$
\epsilon = \frac{1-y-\frac{\gamma^2 y^2}{4}}{1-y+\frac{y^2}{2}+\frac{\gamma^2 y^2}{4}} \tag{3.62}
$$

is the ratio of the longitudinal and the transverse photon fluxes.

By comparing eqn. (3.61) with the expression of the cross section which results from eqn. (3.60) after substituting the full expressions of the leptonic and hadronic tensors, one can eventually extract the various structure functions.

If we introduce the unit vector $\hat{P}_{h\perp}=P_{h\perp}/|P_{h\perp}|$ and the notation

---

[2]U=Unpolarized; L=Longitudinally polarized, T=Transversely polarized.

$$\mathcal{C}[\mathcal{W} \, d \, F] = x \sum_{q,\bar{q}} e_q^2 \, \mathcal{I}[\mathcal{W} \, d \, F] \, , \tag{3.63}$$

where

$$\mathcal{I}[\mathcal{W} \, d \, F] = \int d^2\vec{p}_T d^2\vec{k}_T \, \delta^2\Big(\vec{p}_T - \vec{k}_T - \frac{\vec{P}_{h\perp}}{z}\Big) \mathcal{W}(\vec{p}_T, \vec{k}_T) \, d_q(x, p_T^2) \, F_q(z, z^2 k_T^2) \tag{3.64}$$

is a convolution integral over the quark transverse momenta $\vec{p}_T$ and $\vec{k}_T$, defined for any combination of a parton distribution function $d(x, p_T)$ and a fragmentation function $F(z, z^2 k_T^2)$ multiplied by a weight $\mathcal{W}$, one obtains for instance [3]:

$$F_{UU,T} = \mathcal{C}[q \, D_1] \, , \tag{3.65}$$

where q and D_1 are the spin-independent distribution and fragmentation function, respectively;

$$F_{UU}^{\cos\phi} = \frac{2M}{Q} \, \mathcal{C}\left[-\frac{\hat{P}_{h\perp} \cdot \vec{k}_T}{M_h}\Big(xhH_1^\perp + \frac{M_h}{Mz}q\tilde{D}^\perp \Big) - \frac{\hat{P}_{h\perp} \cdot \vec{p}_T}{M}\Big(xf^\perp D_1 + \frac{M_h}{Mz}h_1^\perp \tilde{H} \Big) \right] \tag{3.66}$$

and

$$F_{UU}^{\cos 2\phi} = \mathcal{C}\left[-\frac{2(\hat{P}_{h\perp} \cdot \vec{k}_T)(\hat{P}_{h\perp} \cdot \vec{p}_T) - \vec{k}_T \cdot \vec{p}_T}{MM_h}h_1^\perp H_1^\perp \right] \, , \tag{3.67}$$

which include, the Boer-Mulders function $h_1^\perp$, (see Section 3.3), and the Collins function $H_1^\perp$, and contribute to the spin-independent part of the cross section;

$$F_{UT}^{\sin(\phi+\phi_S)} = \mathcal{C}\left[-\frac{\hat{P}_{h\perp} \cdot \vec{k}_T}{M_h} \delta q \, H_1^\perp \right] \, , \tag{3.68}$$

and

$$F_{UT,T}^{\sin(\phi-\phi_S)} = \mathcal{C}\left[-\frac{\hat{P}_{h\perp} \cdot \vec{p}_T}{M} f_{1T}^\perp \, D_1 \right] \, , \tag{3.69}$$

which contain the product of the transversity times the Collins function and the product of the Sivers function times the spin-independent fragmentation function, respectively, and are the two of main interest for the analysis presented in this thesis;

$$F_{UT}^{\sin(3\phi-\phi_S)} = \mathcal{C}\left[\frac{2(\hat{P}_{h\perp} \cdot \vec{p}_T)(\vec{p}_T \cdot \vec{k}_T) + p_T^2(\hat{P}_{h\perp} \cdot \vec{k}_T) - 4(\hat{P}_{h\perp} \cdot \vec{p}_T)^2(\hat{P}_{h\perp} \cdot \vec{k}_T)}{2M^2 M_h}h_{1T}^\perp H_1^\perp \right] \, , \tag{3.70}$$

$$F_{UT}^{\sin\phi_S} = \frac{2M}{Q} \, \mathcal{C}\left\{ xf_T D_1 - \frac{M_h}{Mz}\delta q\tilde{H} - \frac{\vec{p}_T \cdot \vec{k}_T}{2MM_h}\left[\Big(xh_T + xh_T^\perp \Big)H_1^\perp + \frac{M_h}{Mz}\Big(f_{1T}^\perp \tilde{D}^\perp - g_{1T}\tilde{G}^\perp \Big) \right] \right\} \, ,$$

---

[3]The full list of structure functions, including those depending on the longitudinal polarization of the beam and/or the target, is reported in [Bac07].

and

$$(3.71)$$

$$
F_{UT}^{\sin(2\phi-\phi_S)} = \frac{2M}{Q}\,\mathcal{C}\bigg\{ \frac{2(\hat{P}_{h\perp}\cdot\vec{p}_T)^2 - p_T^2}{2M^2}\left(xf_T^\perp D_1 - \frac{M_h}{Mz}h_{1T}^\perp \tilde{H}\right) -
$$

$$
\frac{2(\hat{P}_{h\perp}\cdot\vec{p}_T)(\hat{P}_{h\perp}\cdot\vec{k}_T) - \vec{p}_T\cdot\vec{k}_T}{2MM_h}\left[\left(xh_T + xh_T^\perp\right)H_1^\perp - \frac{M_h}{Mz}\left(f_{1T}^\perp \tilde{D}^\perp - g_{1T}\tilde{G}^\perp\right)\right]\bigg\} ,
$$

$$(3.72)$$

which, although suppressed, also contribute to the transverse-spin dependent part of the cross section (cf. Section 5.5.1).

Part of the distribution functions that appear in the expressions above have already been introduced in the previous sections and are reported in Table 3.5. The remaining functions (xh, $xf^\perp$, xf_T, xh_T, $xh_T^\perp$ and $xf_T^\perp$) can be expressed in terms of combinations of quantities already defined (cf. Table 3.5) plus higher order objects [Bac07]. The tilde functions originate from the decomposition of the distribution and fragmentation quark-gluon-quark correlators in the basis of the Dirac matrices.

For our purposes it is convenient to split the differential cross section according to the polarization state of beam and target:

$$
d^6\sigma = d^6\sigma_{UU} + d^6\sigma_{LU} + d^6\sigma_{UL} + d^6\sigma_{LL} + d^6\sigma_{UT} + d^6\sigma_{LT} , \tag{3.73}
$$

where each of the terms has the following general structure:

$$
d^6\sigma_{BeamTarget} = \frac{2\alpha^2}{sxy^2}\otimes K(y)\otimes \mathcal{A}(\phi,\phi_S)\otimes \sum_{q\bar{q}} e_q^2\,\mathcal{I}[\mathcal{W}\cdot d\cdot F] . \tag{3.74}
$$

Here $K(y)$ is a kinematic factor proportional to one of the following quantities [Bac07]:

$$
A(y) = \left(1 - y + \frac{y^2}{2} - \frac{y^2\gamma^2}{4}\right)\frac{1}{1+\gamma^2} , \tag{3.75}
$$

$$
B(y) = \left(1 - y - \frac{y^2\gamma^2}{4}\right)\frac{1}{1+\gamma^2} , \tag{3.76}
$$

$$
C(y) = \frac{1}{\sqrt{1+\gamma^2}}y\left(1 - \frac{y}{2}\right) , \tag{3.77}
$$

$$
D(y) = \frac{2(2-y)}{1+\gamma^2}\sqrt{1 - y - \frac{y^2\gamma^2}{4}} , \tag{3.78}
$$

and $\mathcal{A}(\phi,\phi_S)$ is an azimuthal modulation consisting of the *sine* or the *cosine* of a proper combination of the azimuthal angles ϕ and ϕ_S, defined in Figure 3.11.

Among all these terms, we are mainly interested in the following two, corresponding to the structure functions (3.68) and (3.69):

$$d^6\sigma_{UT} = -\frac{2\alpha^2}{sxy^2}|\vec{S}_T|B(y)\sin(\phi+\phi_S)\sum_{q\bar{q}}e_q^2\mathcal{I}\left[\frac{\vec{k}_T\cdot\hat{P}_{h\perp}}{M_h}\delta q(x,p_T^2)H_1^{\perp q}(z,z^2k_T^2)\right] \ , \quad (3.79)$$

in which the convolution integral of the product of the transversity distribution and the Collins fragmentation function is modulated by $\sin(\phi+\phi_S)$, and

$$d^6\sigma_{UT} = -\frac{2\alpha^2}{sxy^2}|\vec{S}_T|A(y)\sin(\phi-\phi_S)\sum_{q\bar{q}}e_q^2\mathcal{I}\left[\frac{\vec{p}_T\cdot\hat{P}_{h\perp}}{M}f_{1T}^{\perp q}(x,p_T^2)D_1^q(z,z^2k_T^2)\right] \ , \quad (3.80)$$

in which the convolution integral of the product of the Sivers distribution function and the spin-independent fragmentation function is modulated by $\sin(\phi-\phi_S)$.

3.7.5 The Collins and Sivers azimuthal moments

In order to extract the distribution and fragmentation functions of interest it is convenient to measure the so-called *azimuthal moments*:

$$\langle\sin(n\phi+m\phi_S)\rangle_{beam\ target}^h \equiv \frac{\int d\phi_S d^2P_{h\perp}\sin(n\phi+m\phi_S)d^6\sigma_{beam\ target}}{\int d\phi_S d^2P_{h\perp}d^6\sigma_{UU}} \ , \quad (3.81)$$

$$\langle\cos(n\phi+m\phi_S)\rangle_{beam\ target}^h \equiv \frac{\int d\phi_S d^2P_{h\perp}\cos(n\phi+m\phi_S)d^6\sigma_{beam\ target}}{\int d\phi_S d^2P_{h\perp}d^6\sigma_{UU}} \ , \quad (3.82)$$

where n and m are positive or negative integers.

To separate the individual terms of the spin-dependent part of the cross section, cross section differences of opposite spin states are formed. In particular, if we limit ourselves to the UT case, we can select the d_{UT}^6 term through the difference

$$d^6\sigma_{UT} \equiv \frac{1}{2}\left(d^6\sigma_{U\uparrow}-d^6\sigma_{U\downarrow}\right) \ , \quad (3.83)$$

where $\uparrow$ ($\downarrow$) indicates the spin orientation parallel (antiparallel) to the direction specified by the angle ϕ_S. Since, by definition, the spin averaged cross sections yields the spin-independent part of the cross section:

$$d^6\sigma_{UU} \equiv \frac{1}{2}\left(d^6\sigma_{U\uparrow}+d^6\sigma_{U\downarrow}\right) \ , \quad (3.84)$$

the azimuthal moments assume the structure of cross section asymmetries. In particular if one considers only the target (or the beam) polarization, as for in the UT case, these asymmetries are usually referred to as Single Spin Asymmetries (SSA). Therefore, for instance, eqn. (3.81) for the UT case can be written in the form:

$$\langle \sin(n\phi + m\phi_S) \rangle_{UT}^h \approx \frac{\int d\phi_S d^2 P_{h\perp} \sin(n\phi + m\phi_S)(d^6\sigma_{U\uparrow} - d^6\sigma_{U\downarrow})}{\int d\phi_S d^2 P_{h\perp}(d^6\sigma_{U\uparrow} + d^6\sigma_{U\downarrow})} \ . \tag{3.85}$$

From the experimental point of view, the main advantage of this approach is that many systematic uncertainties that would affect the absolute cross sections cancel in the measurement of the asymmetry.

The so-called Collins ($n = 1,\ m = 1$) and Sivers ($n = 1,\ m = -1$) moments, which are derived from the cross sections (3.79) and (3.80), respectively, can be written in the form:

$$\langle \sin(\phi + \phi_S) \rangle_{UT}^h = -|\vec{S}_T| \frac{\frac{1}{xy^2}B(y)\sum_{q\bar{q}} e_q^2 \int d^2\vec{P}_{h\perp}\, \mathcal{I}\left[\frac{\vec{k}_T \cdot \hat{P}_{h\perp}}{M_h}\delta q(x, p_T^2)H_1^{\perp q}(z, z^2 k_T^2)\right]}{2\frac{1}{xy^2}A(y)\sum_{q\bar{q}} e_q^2 q(x)D_1^q(z)} \ , \tag{3.86}$$

$$\langle \sin(\phi - \phi_S) \rangle_{UT}^h = -|\vec{S}_T| \frac{\frac{1}{xy^2}A(y)\sum_{q\bar{q}} e_q^2 \int d^2\vec{P}_{h\perp}\, \mathcal{I}\left[\frac{\vec{p}_T \cdot \hat{P}_{h\perp}}{M}f_{1T}^{\perp q}(x, p_T^2)D_1^q(z, z^2 k_T^2)\right]}{2\frac{1}{xy^2}A(y)\sum_{q\bar{q}} e_q^2 q(x)D_1^q(z)} \ . \tag{3.87}$$

The experimental observation of non-zero Collins and Sivers moments is often referred to as the Collins and the Sivers effect, respectively.

The Collins moments (3.86) give access to the product of the transversity distribution and Collins fragmentation function, whereas the Sivers moment (3.87) gives access to the product of the Sivers function and the spin-independent fragmentation function. Unfortunately these products are embedded in the convolution integral (3.64), which cannot be factorized because of the weights $\mathcal{W} = \frac{\vec{k}_T \cdot \vec{P}_{h\perp}}{M_h}$ (for Collins) and $\mathcal{W} = \frac{\vec{p}_T \cdot \vec{P}_{h\perp}}{M}$ (for Sivers). To solve these integrals one has to make an assumption on the transverse momentum dependence of the distribution and fragmentation functions involved.

The simplest assumption one can think of is that there is no intrinsic transverse momentum of the quarks inside the target. For instance, if we consider the transversity and the Collins function, and use the relation $\vec{K}_T = -z\vec{k}_T$ between the transverse momentum of the hadron with respect to the quark direction and the transverse momentum of the quark itself, we get

$$\delta(x, p_T^2) \approx \delta q(x)\delta(p_T^2) \qquad\qquad H_{1T}^{\perp}(z, K_T^2) \approx H_{1T}^{\perp}(z)\delta(K_T^2) \ . \tag{3.88}$$

A more realistic assumption is the so-called *Gaussian ansatz* [Bac02b], according to which the transverse momenta p_T and K_T follow a Gaussian distribution:

$$\delta q(x, p_T^2) \approx \frac{\delta q(x)}{\pi\langle p_T^2(x)\rangle}e^{-\frac{p_T^2}{\langle p_T^2(x)\rangle}} \qquad\qquad H_{1T}^{\perp}(z, K_T^2) \approx \frac{H_{1T}^{\perp}(z)}{\pi\langle K_T^2(z)\rangle}e^{-\frac{K_T^2}{\langle K_T^2(z)\rangle}} \ , \tag{3.89}$$

where $\quad \langle p_T^2(x)\rangle = \frac{\int d^2\vec{p}_T\, p_T^2 q(x, p_T^2)}{q(x)} \quad$ and $\quad \langle K_T^2(x)\rangle = \frac{\int d^2\vec{K}_T\, K_T^2 D_1(z, K_T^2)}{D_1(z)}.$

Under this assumption the distribution and the fragmentation functions factorize and the integral can be calculated analytically. One then obtains:

$$\langle \sin(\phi + \phi_S)\rangle_{UT}^h = -\frac{|\vec{S}_T|}{\sqrt{1 + z^2 \langle p_T^2\rangle / \langle K_T^2\rangle}} \frac{\frac{1}{xy^2} B(y) \sum_{q\bar{q}} e_q^2 \delta q(x) H_1^{\perp(1/2)q}(z)}{\frac{1}{xy^2} A(y) \sum_{q\bar{q}} e_q^2 q(x) D_1^q(z)} , \qquad (3.90)$$

$$\langle \sin(\phi - \phi_S)\rangle_{UT}^h = -\frac{|\vec{S}_T|}{\sqrt{1 + \langle K_T^2\rangle / (z^2 \langle p_T^2\rangle)}} \frac{\frac{1}{xy^2} A(y) \sum_{q\bar{q}} e_q^2 f_{1T}^{\perp(1/2)q}(x) D_1^q(z)}{\frac{1}{xy^2} A(y) \sum_{q\bar{q}} e_q^2 q(x) D_1^q(z)} . \qquad (3.91)$$

In order to avoid any assumption on the transverse momentum distributions one can construct the so-called $P_{h\perp}$-weighted asymmetries, in which the convolution integral is weighted with the magnitude of the hadron transverse momentum $P_{h\perp}$ divided by z. This approach yields to the following expressions for the $P_{h\perp}$-weighted Collins and Sivers moments:

$$\left\langle \frac{P_{h\perp}}{zM_h} \sin(\phi + \phi_S)\right\rangle_{UT}^h \equiv \frac{\int d\phi_S d^2 \vec{P}_{h\perp} \frac{P_{h\perp}}{zM_h} \sin(\phi + \phi_S) \, d^6\sigma_{UT}}{\int d\phi_S d^2 \vec{P}_{h\perp} \, d^6\sigma_{UU}}$$

$$= |\vec{S}_T| \frac{\frac{1}{xy^2} B(y) \sum_{q\bar{q}} e_q^2 \delta q(x) H_1^{\perp(1)q}(z)}{\frac{1}{xy^2} A(y) \sum_{q\bar{q}} e_q^2 q(x) D_1^q(z)} \qquad (3.92)$$

$$\left\langle \frac{P_{h\perp}}{zM} \sin(\phi - \phi_S)\right\rangle_{UT}^h \equiv \frac{\int d\phi_S d^2 \vec{P}_{h\perp} \frac{P_{h\perp}}{zM} \sin(\phi - \phi_S) \, d^6\sigma_{UT}}{\int d\phi_S d^2 \vec{P}_{h\perp} \, d^6\sigma_{UU}}$$

$$= -|\vec{S}_T| \frac{\frac{1}{xy^2} A(y) \sum_{q\bar{q}} e_q^2 f_{1T}^{\perp(1)q}(x) D_1^q(z)}{\frac{1}{xy^2} A(y) \sum_{q\bar{q}} e_q^2 q(x) D_1^q(z)} \qquad (3.93)$$

The factor $\frac{1}{xy^2} A(y)$ in eqn. (3.93) may not cancel because numerator and denominator are integrated separately over certain x and y ranges in a measurement.

For the extraction of the Sivers function from the measured azimuthal moments, it is convenient to define the *purities*

$$\mathcal{P}_q^h(x, z) \equiv \frac{e_q^2 \, q(x) D_1^{q\to h}(z)}{\sum_{q'\bar{q}'} e_{q'}^2 q'(x) D_1^{q'\to h}(z)} , \qquad (3.94)$$

constructed from known spin-independent distribution and fragmentation functions.
Using the definition of the purities, the $P_{h\perp}$-weighted Sivers moments can be rewritten as:

$$\left\langle \frac{P_{h\perp}}{zM} \sin(\phi - \phi_S)\right\rangle_{UT}^h \equiv -|\vec{S}_T| \frac{\frac{1}{xy^2} A(y)}{\frac{1}{xy^2} A(y)} \sum_{q,\bar{q}} \mathcal{P}_q^h(x, z) \frac{f_{1T}^{\perp(1)q}(x)}{q(x)} , \qquad (3.95)$$

where the ratio $f_{1T}^{\perp(1)q}(x)/q(x)$ between the Sivers and the spin-independent distribution function is called *Sivers polarization*. A similar expression can be written for the unweighted Sivers moments once the Gaussian ansatz has been applied:

$$\langle\, \sin(\phi - \phi_S)\rangle_{UT}^h \equiv -\frac{|\vec{S}_T|}{\sqrt{1 + \langle K_T^2\rangle/(z^2\langle p_T^2\rangle)}} \frac{\frac{1}{xy^2}A(y)}{\frac{1}{xy^2}A(y)} \sum_{q,\bar{q}} \mathcal{P}_q^h(x,z) \frac{f_{1T}^{\perp(1/2)q}(x)}{q(x)} \ . \qquad (3.96)$$

Results from a large number of high precision unpolarized DIS experiments are available for the spin-independent distribution functions. The second ingredient of the purities, the spin-independent fragmentation functions, are usually obtained at HERMES from parameterizations based on the LUND string fragmentation model tuned in such a way to reproduce the HERMES multiplicities [Lie04].

For the extraction of the trasversity distribution function from the measured Collins moments, a similar approach can be adopted, in principle. In this case, however, a new type of purities has to be defined which includes the Collins fragmentation function. This has represented an intrinsic limit for years since no measurements were available for the Collins FF. However a preliminary extraction of the Collins FF has been very recently obtained in e^+e^- annihilations at the Belle experiment [Sei06].

Chapter 4

The HERMES experiment at HERA

In order to study the inner spin structure of the nucleon in polarized deep inelastic scattering, the HERMES experiment exploited three major ingredients: a high-energy highly polarized lepton beam, a highly polarized nucleon target and a spectrometer with a good particle identification power, a reasonable tracking resolution and a relatively large geometrical acceptance. In this chapter the various components used in the HERMES experiment during the 2002-2005 period, in which a transversely polarized hydrogen target was employed, are described in details.

4.1   The Hadron Electron Ring Accelerator (HERA)

HERMES is one of the four experiments at the HERA lepton-proton collider at DESY, in Hamburg. HERA was built between May 1984 and November 1990 and saw the first electron-proton collision at the end of 1991. Until its final shut-down, in June 2007, it was the only lepton-proton collider existing in the world.

HERA basically consists of two concentric rings accommodated in a tunnel with a circumference of 6.3 km. One of the rings provides a 27.5 GeV lepton (electron or positron) beam and the other a 920 GeV proton beam. The two beams were brought into collision in two distinct interaction points in correspondence of the North and the South experimental Halls, where the two collider experiments H1 and the ZEUS are located. In contrast, the HERMES experiment, which is located in the East Hall, has an internal gas target and made use of the lepton beam only. The fourth experiment, HERA-B, which operated in the West Hall during the limited period 1999-2003, was also a fixed target experiment and used the proton beam only.

Before entering the HERA rings, the particles pass through a complex chain of pre-accelerators, as depicted in Figure 4.1. The proton beam is produced by strip injection of H^- beams produced by LINAC III into DESY III, followed by the injection into PETRA, which is the HERA's main pre-accelerator. Lepton beams are produced and accelerated by Linac II, and then accumulated in the Positron Intensity Accumulator PIA before being injected into DESY II. The lepton beams are then injected into DORIS or PETRA with an energy of 7 GeV, and finally injected at 12 GeV into the HERA storage ring, where they are eventually ramped up to the nominal beam energy of 27.5 GeV.
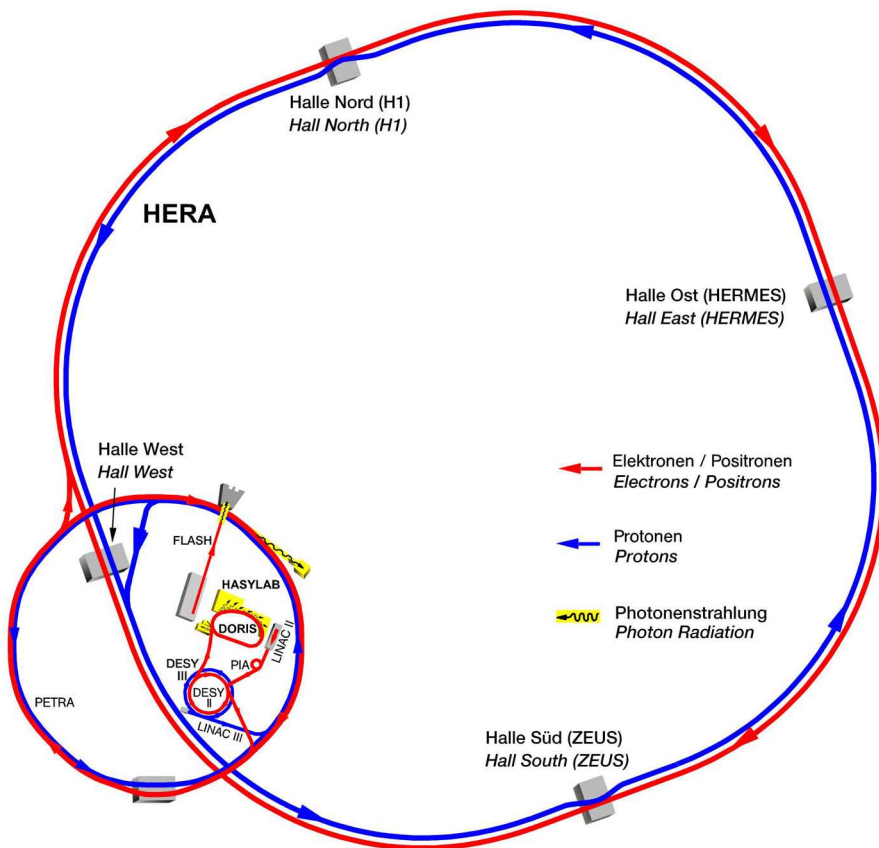
Figure 4.1: Sketch of the HERA accelerator facility at DESY showing the two HERA rings, the location of the four experiments (HERMES, ZEUS, H1 and HERA-B) and the chain of pre-accelerators.

The HERA lepton beam consists of up to 220 bunches with a length of 27 ps separated by 96 ns and a lifetime in the range 12-16 hours[1]. A typical plot reporting the current of the beams (in mA) as a function of time (in hours) is shown in Figure 4.2.

During the 2001-2002 shut-down, HERA was upgraded with an improved focusing at the collider interaction points and a more efficient transfer line between the different pre-accelerators. The facility, as it was after 2002, is often referred to as HERA II.

4.1.1 The Lepton Beam Polarization

It is well known that an external magnetic field, pointing to a certain direction y, causes the spin of a particle passing through to be oriented either parallel or anti-parallel to the field itself. In a storage ring, such as HERA, the rotating particles will thus have their spin oriented orthogonally to the orbit plane. At the beginning the beam results unpolarized since, for statistical reasons, there will be approximately the same amount of particles with spin up and spin down. However

---

[1] The proton beam lifetime is much longer.
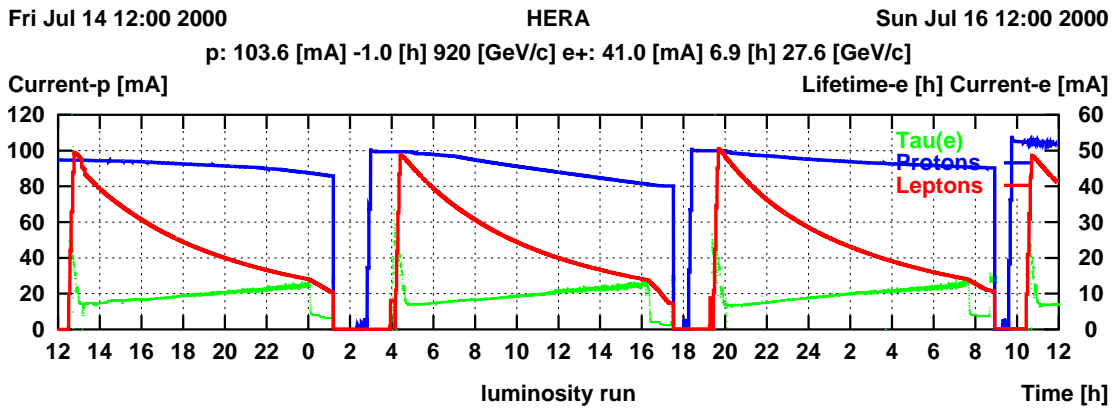
Figure 4.2: Current of the beams (in mA) as a function of time (in hours) for three consecutive fills. For each fill, the upper curve represents the proton beam current, the curve in the middle represents the lepton beam current and the lower curve shows the electron beam lifetime. During each fill the lepton beam current decreases exponentially and the beam is dumped when the current has reached ~ 13 mA. The sudden drop of the lepton beam lifetime from about 15 hours to about 2 hours in the very last part of the fill is due to the injection of high density gas in the HERMES target cell (High Density Runs).

the synchrotron radiation, emitted by the rotating particles, is known to cause a spin flip whose probability $\mathcal{P}$ depends on the actual spin orientation of the particle, i.e.:

$$\mathcal{P}(\text{up} \rightarrow \text{down}) \neq \mathcal{P}(\text{down} \rightarrow \text{up}) \ . \tag{4.1}$$

As a consequence, after a certain number of revolutions, the number of particles with spin up are different from the number of particles with spin down and the beam acquires a net transverse polarization:

$$P = \frac{N(\text{up}) - N(\text{down})}{N(\text{up}) + N(\text{down})} \neq 0 \ . \tag{4.2}$$

This mechanism is known as the *Sokolov-Ternov* (ST) *effect* [Sol64]. The beam polarization built up from an initially unpolarized beam in a circular machine with a perfectly flat orbit is described by the empirical formula:

$$P_{ST}(t) = \frac{8}{5\sqrt{3}} \left(1 - e^{-\frac{t}{\tau_{ST}}} \right) \ , \tag{4.3}$$

where

$$\tau_{ST} = \frac{8}{5\sqrt{3}} \frac{m_e^2 c^2 \rho^3}{e^2 \hbar \gamma^5} \tag{4.4}$$

is the Sokolov-Ternov rise-time constant. Here γ is the Lorentz factor, ρ is the bending radius of the orbit, m_e and e are the electron mass and charge, c is the speed of light, $\hbar$ is the Planck constant and E is the lepton (electron or positron) energy.

Depolarizing effects, which can be caused either by beam-beam interactions or imperfections and misalignment of the magnets, compete with the ST effect and have to be taken into account in the evaluation of the polarization. The strength of these depolarization effects, which cause a reduction of the polarization degree of the beam, can be parameterized in terms of a single-time depolarizing time constant τ_{dep}, such that the effective polarization can be written as:

$$P_{eff} = \frac{8}{5\sqrt{3}} \frac{\tau_{dep}}{\tau_{dep} + \tau_{ST}} \quad . \tag{4.5}$$

As a result, the maximum achievable polarization becomes smaller and the rise time shorter. Efforts taken at HERA in the mid '90s to optimize the lepton beam orbit allowed to achieve polarization values in the range $50\% - 60\%$ (see Figure 4.3).
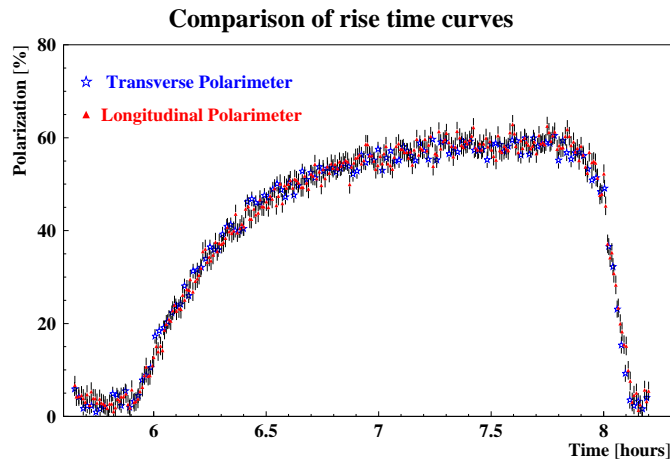
Figure 4.3: Polarization build-up through the Sokolov-Ternov effect. Within a rise time of about 22 minutes polarizations between 50% and 60% are typically reached.

Though the lepton beam is naturally polarized in the transverse direction, most of the interesting physical observables at HERMES require a longitudinally polarized beam. The *longitudinal* polarization can be achieved by rotating the spin of the beam particles from the transverse direction to a direction parallel to the beam orbit. This is done by means of the so-called spin rotators. These devices consist of six interleaved horizontal and vertical dipole magnets generating a pattern of vertical and horizontal orbit deflections. After passing through a spin rotator, the trajectory of an electron (or positron) beam will not be affected, but the orbit kicks will cause a series of rotations of the spin vector such that it is finally turned by $90°$ (see Figure 4.4). Two sets of spin rotators have been installed before and after the experimental North, East and West Halls[2], as depicted in Figure 4.5. The reason for using pairs of spin rotators is that the polarization needs to be turned back to the transverse direction in order to take advantage of the *Sokolov-Ternov effect*.

---

[2]The spin rotators close to H1 and ZEUS were only installed after the upgrade to HERA II.
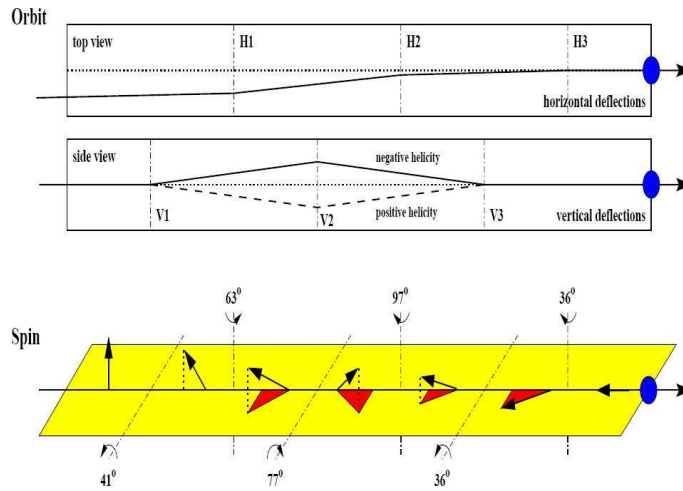
Figure 4.4: A schematic diagram showing the operation principle of one spin rotator. A sequence of vertical and horizontal magnetic fields move the beam orbit (top) and rotate the particle polarization direction (bottom). The sequence is chosen such that the vertical position of the orbit is unchanged by the rotator, but the spin receives a net rotation to the longitudinal direction.

4.1.2 The Transverse and Longitudinal Polarimeters

The uncertainty in the beam polarization degree constitutes an important part of the systematic uncertainty for precision measurements of polarized cross section, asymmetries etc. Therefore it is essential to provide precise and frequent measurements of the beam polarization. At HERA, two polarimeters are in operation. Both polarimeters make use of a cross section asymmetry in the Compton back scattering of circularly polarized photons off polarized electrons/positrons. The Transverse Polarimeter (TPOL) was installed in the HERA east hall in 1992 and measures the transverse polarization [Bar93]. Circularly polarized light, with its helicity being switched with a frequency of 83.8 Hz, is sent from a continuous Argon ion laser against the lepton beam at a shallow angle. The backscattered photons are detected with a tungsten-scintillator sandwich calorimeter consisting of two identical halves separated along the beam plane. If the beam polarization is in the y direction (i.e. perpendicular to the orbit plane), the Compton scattered photons are distributed asymmetrically along the y direction. The asymmetry is proportional to the beam polarization along the y-direction [Bec00]. By measuring the asymmetry in the energy deposition of backscattered photons between the top and the bottom halves of the calorimeter, the mean average vertical position $\langle y \rangle$ of the energy deposition can be inferred. The transverse polarization P_y of the beam can be derived from the difference of the mean values $\langle y \rangle$ measured with right (R) and left (L) circularly polarized light.

The Longitudinal Polarimeter (LPOL), installed in 1995-1996 in the East Right straight section of the HERA lepton ring, measures the longitudinal polarization behind the HERMES interaction point. The setup is similar to that of the TPOL: it consists of a pulsed laser generating polarized light with alternating helicity at each pulse. The light crosses the beam 53
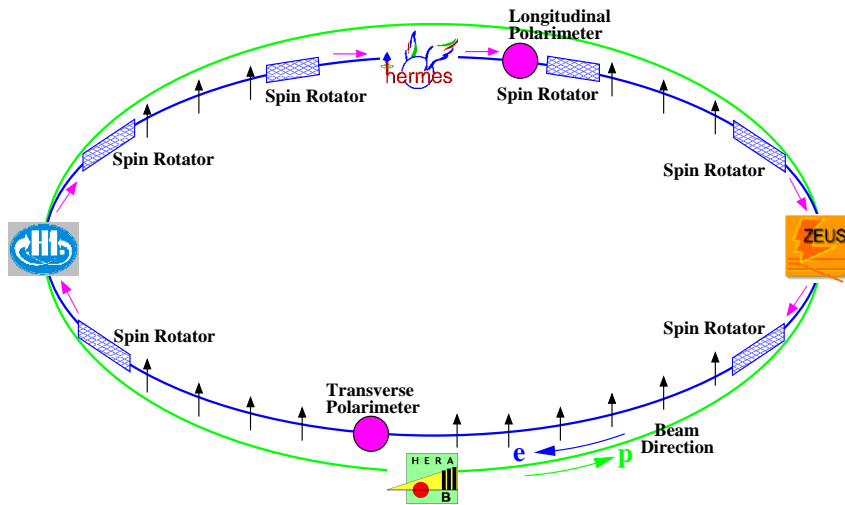
Figure 4.5: Schematic representation of HERA with the four experiments and the three pairs of spin rotators. The longitudinal and transverse polarimeters are also shown.

m downstream of the HERMES target at an angle of about 9 mrad. Several thousand photons are backscattered when the laser pulse crosses a electron/positron bunch. Their energy sum is measured by a radiation hard calorimeter consisting of an array of four 20 cm long NaBi(W0)$_2$ crystals. For a longitudinal lepton polarization the Compton cross section is independent of the azimuthal scattering angle, but switching the laser helicity will modify the energy spectrum. The asymmetry, generated by the different laser helicity states, of the energy weighted sums of backscattered photons ζ along the y direction, determines the longitudinal polarization P_z of the beam. A detailed description of the setup of the LPOL can be found in [Bec02].

4.2 The HERMES target

Among the primary goals of the HERMES experiment were the measurement of *Double Spin Asymmetries* (DSA), which require both the beam and the target to be polarized, and of *Single Spin Asymmetries* (SSA), which require either a polarized beam or a polarized target. The use of a gas target was found to be the optimal solution for HERMES since, due to its relatively low density, it ensures a reasonable life time of the beam. In addition a gas target is highly polarizable and has virtually no dilution from unpolarized material. This, together with the fact that polarity of the gas can easily be flipped, constitutes a major advantage with respect to the use of liquid or solid state targets.

Due to its purity, its high polarization degree and its position internal to the beam pipe (so that the lepton beam does not encounter any unpolarized material before colliding with the target atoms), the HERMES target [Ack98, Air05] is unique and represents one of the strengths of the experiment.

The target system consists of three main components (all shown in Figure 4.6):

- an Atomic Beam Source (ABS), which produces polarized hydrogen or deuterium atoms

- a storage cell around the central axis of the lepton beam line

- two diagnostic devices: a Breit-Rabi Polarimeter (BRP), to measure the atomic polarization, and a Target Gas Analyzer (TGA), to measure the atomic fraction of the gas.

In 1995 HERMES started data taking with a longitudinal polarized ^3He target followed by longitudinally polarized hydrogen in 1996 and 1997 and longitudinally polarized deuterium from 1998 to 2000. During the shutdown in 2001 the longitudinal target magnet was replaced by a transverse target magnet, and from 2002 to 2005 a transversely polarized hydrogen target was used. At the end of 2005 the ABS, the BRP and the TGA were removed to allow the installation of a Recoil Detector around the target cell. Since then, only unpolarized H and D targets were used till the final shutdown, in July 2007. A schematic view of the HERMES polarized target region is shown in Figure 4.7.
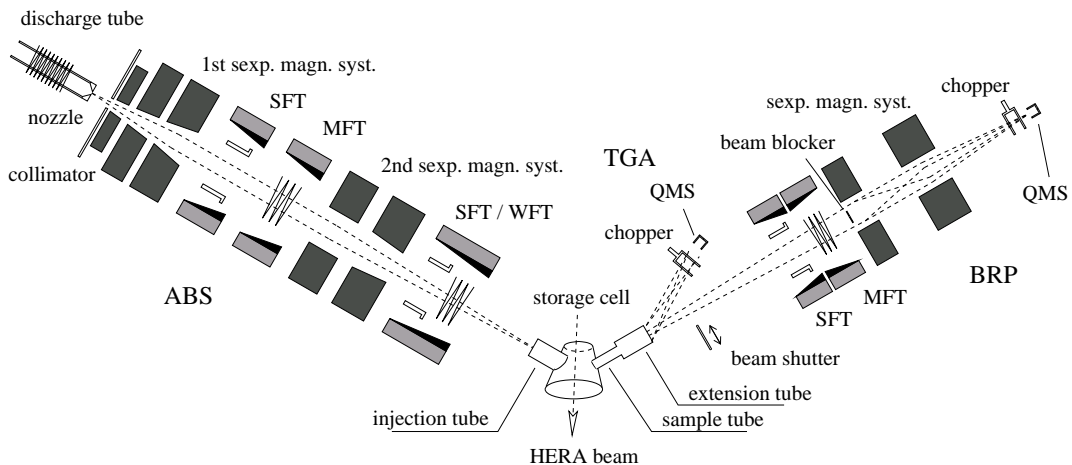
Figure 4.6: Representation of the Atomic Beam Source (ABS), Breit-Rabi Polarimeter (BRP) and Target Gas Analyzer (TGA) with the storage cell in the center.

4.2.1 The Atomic Beam Source

The ABS [Nas03] is a device which makes use of the Stern-Gerlach effect [Ger21] to generate atomic polarization of hydrogen or deuterium. First, the molecular (H_2 or D_2) gas is dissociated by means of a radio frequency dissociator (until 2000) or a microwave dissociator (from 2000 on). The hydrogen (deuterium) atoms flow through a cooled nozzle with a temperature of 100 K. A thin layer of frozen water on the nozzle surface helps to prevent recombination [Bau03a]. The atomic gas, with all hyperfine states $|n\rangle \equiv |m_s, m_I\rangle$ (see Figure 4.8) equally populated, then enters a beam forming system followed by a system of sextupole magnets with a radial
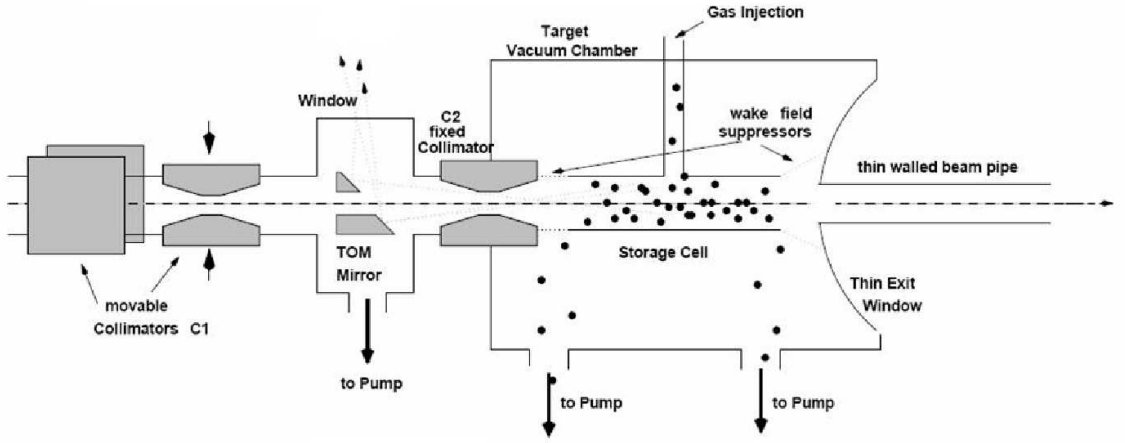
Figure 4.7: Side view of the HERMES polarized target region before the installation of the Recoil Detector.

field dependence for the hyperfine states selection. Due to the Stern-Gerlach effect, hydrogen atoms in the two spin states $|1\rangle = |+\frac{1}{2}, +\frac{1}{2}\rangle$ and $|2\rangle = |+\frac{1}{2}, -\frac{1}{2}\rangle$, which have the same electron spin $|m_s\rangle$ but opposite nuclear spin $|m_I\rangle$, are focused by the sextupole magnets, while the other two states $|3\rangle = |-\frac{1}{2}, -\frac{1}{2}\rangle$ and $|4\rangle = |-\frac{1}{2}, +\frac{1}{2}\rangle$ are defocused and thus pumped out by the pump system. In order to obtain nuclear polarization, transitions between hyperfine states $|1\rangle \rightarrow |3\rangle$ and $|2\rangle \rightarrow |4\rangle$ are induced respectively by two independent RF-transitions: a strong (SFT) and a weak (WFT) field transitions (see Figure 4.6). In this way it is possible to populate the two states with the same nuclear spin orientation. Similar arguments hold for the six hyperfine states of the deuterium atoms.
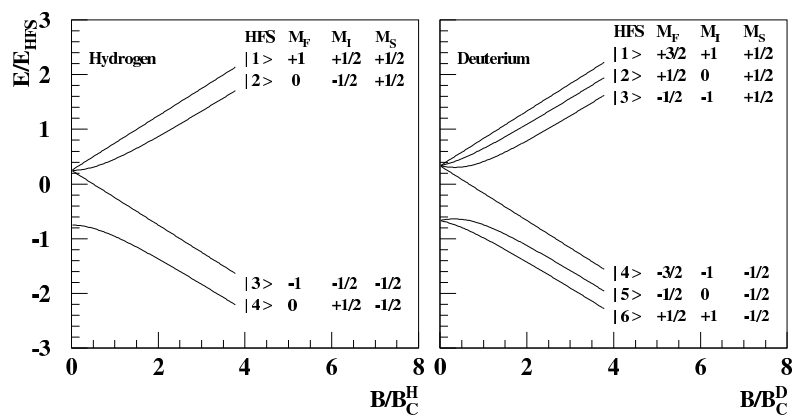
Figure 4.8: Hyperfine splitting of hydrogen (left) and deuterium (right) atomic energy levels as a function of the magnetic holding field B relative to the critical field B_c. The energy is given relative to the hyperfine splitting at $B = 0$.

Since switching on one transition and off the other only requires a very short time, it is possible to invert the nuclear polarization every 60 s[3]. The switching of the target polarization is fast enough to reduce the possibility of systematic time-dependent errors in the measurements of the asymmetries and is slow enough to avoid synchronization problems in the data acquisition.

4.2.2 The Storage Cell

After the selection of the hyperfine states, the gas is fed into a storage cell [Bau03b], which allows to increase the areal target density by about two orders of magnitude compared to a free jet target. The areal target density obtained at HERMES is of the order of 10^{14} atoms/cm^2. The storage cell is an open ended elliptical tube (40 cm long, 29 mm wide and 9.8 mm high) made of thin (75 μm) ultra pure aluminum. It is embedded in a 0.3 mm thick stainless steel target chamber inside the ultra high vacuum of the HERA lepton beam pipe. In order to reduce the amount of synchrotron light entering the target chamber and sequentially the spectrometer, a number of beam collimators were placed in front of the HERMES target (see Figure 4.7). The feed tube, through which the polarized gas atoms are injected into the cell with fluxes of up to $6.5 \cdot 10^{16}$ atoms/s, is installed perpendicular to the beam axis at the center of the cell (as depicted in Figure 4.7). As a result, the target density has a triangular shape with the maximum in correspondence of the position of the injection tube. In addition to the injection tube a smaller sampling tube exists which extracts about 5% of the gas for analysis in the TGA and BRP. This sampling tube is installed opposite to the injection tube at an angle of 120°. This angle avoids a direct injection into the sampling tube, thus allowing to analyze the gas only after the thermalization with the cell wall has occurred. In front of the storage cell and behind its extension so-called wake-field suppressors provide a gradual electrical transition between the storage cell and the beam pipe. Without the wake-field suppressors the bunched lepton beam in HERA would cause strong radio frequency fields to be emitted at the discontinuity of the beam pipe impedance. These wake-field would not only heat up the target cell but also destabilize the beam orbit. The wake-field suppressor also prevent thermal conduction between the cell and the beam pipe, which is operated at room temperature. A schematic view of the target cell is shown in Figure 4.9.

During the 2002–2005 period, the temperature of the cell was kept at 100K in order to reduce the thermal velocities of the gas atoms inside. In addition this temperature ensures low recombination and depolarization effects. In order to reduce depolarization and recombination of atoms due to wall collisions the cell is coated with a radiation hard hydrophobic silicon based polymer called Dryfilm. After a number of wall collisions the atoms diffuse along the cell axis towards both ends. During the diffusion process the atoms cross the lepton beam many times, significantly enhancing the probability of beam-target collisions. The ultra high vacuum of the HERA lepton beam line is preserved thanks to a powerful pumping system.

---

[3]For the transversely polarized target the spin flip interval was increased to 90s.
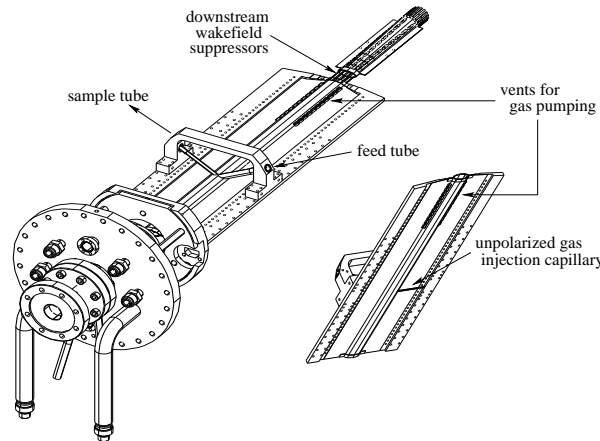
Figure 4.9: Sketch of the HERMES target cell and its support structure.

4.2.3 The Target Gas Analyzer TGA

In order to measure the atomic and molecular content of the gas extracted from the center of the storage cell, a special device, called Target Gas Analyzer (TGA) [Bau03b], was installed. The main component of the TGA is a $90°$ off-axis Quadrupole Mass Spectrometer (QMS) with a beam ionizer and a Channel Electron Multiplier (CEM) for single ion detection. As a first step particles (both atoms and molecules) are ionized by a 70 eV electron beam. The ions are then pulled by an electric field toward the QMS, where they are mass filtered, and finally detected by the CEM. In front of the QMS a chopper with a frequency of 5.5 Hz periodically stops the sample beam to allow the subtraction of the signal of the residual gas in the chopper chamber. In order to avoid interference with the BRP measurement, the TGA is tilted by $7°$ with respect to the sampling tube (see right-hand side of Figure 4.6).

The degree of dissociation α_{TGA} of the sample beam is extracted roughly once per minute from the measurements of the flow rates for atoms (ϕ_a) and molecules (ϕ_m):

$$\alpha_{TGA} = \frac{\phi_a}{\phi_a + \phi_m} \ . \tag{4.6}$$

The degree of dissociation in the storage cell is then obtained by applying a sampling correction factor C_α. Dissociation degrees up to 92% for hydrogen and 95% for deuterium have been achieved. Together with calibration measurements, which are performed during the breaks between fills, two quantities can be calculated: the degree of dissociation in the absence of recombination within the cell, α_0, and the fraction of atoms surviving recombination in the cell, α_r. Both quantities are necessary for the determination of the density-averaged nuclear polarization P_T in the cell.

4.2.4 The Breit-Rabi Polarimeter

The gas extracted by the sampling tube also allows the measurement of the polarization degree of the target. This measurement is performed by a Breit-Rabi Polarimeter (BRP) [Bau02]. The BRP consists of a pair of radio frequency transitions - a strong (SFT) and a medium field transition (MFT) - which can be tuned for different hyperfine state transitions (see right-hand side of Figure 4.6). A sextupole magnet system focuses atoms with $m_s = +\frac{1}{2}$ towards the detector unit and defocuses atoms with $m_s = -\frac{1}{2}$. As in the TGA, a QMS together with a chopper for background subtraction is used for the detection. The atomic polarization P_a can be deduced from the measurement of the relative populations of the hyperfine states of hydrogen or deuterium atoms. This quantity, however, represents the polarization at the center of the storage cell. The polarization averaged along the cell, P_{BRP}, is obtained by applying a sampling corrections c_P, provided by a Monte Carlo simulations of the ballistic flow of the target gas atoms in the storage cell [Air05c]:

$$P_{BRP} = c_P \cdot P_a . \tag{4.7}$$

Combining the BRP and the TGA measurements, the averaged target polarization P_T as seen by the electron beam can be calculated as:

$$P_T = \alpha_0[\alpha_r + (1 - \alpha_r)\beta] \cdot P_{BRP} . \tag{4.8}$$

Here β is the ratio of the nuclear polarization of molecules produced by recombination and the nuclear polarization of the atoms. A direct measurement of the remnant polarization contained in the recombined molecules is not possible at HERMES as the BRP is capable only of atomic polarization measurements. In dedicated measurements at higher storage cell temperature of 260 K, with enhanced recombination, the range of β could be restricted to the interval $[0.45, 0.83]$. The uncertainty on β is part of the systematic uncertainty of the target polarization value.

4.2.5 The Target Magnet

The target magnet surrounding the storage cell provides a holding field which defines the polarization axis. While a holding field parallel to the lepton beam has no effect on the beam and a marginal effect on the scattered particle trajectories, for a transverse holding field different effects have to be taken into account. The deflection of the beam requires compensation by correction coils and limits the strength of the magnetic field due to the amount of synchrotron radiation generated by the beam. Since not only the beam but also the scattered particles are deflected, the reconstructed vertex position and scattering angles must be corrected for the deflection. At HERMES two alternative offline Transverse Magnet Correction (TMC) methods have been developed (see Section 4.3.2).
In addition to the influence on the particle trajectories, depolarizations effects occur due to the

bunched structure of the HERA lepton beam. The time period of 96.1 ns between two adjacent lepton bunches corresponds to a bunch frequency of 10.41 MHz. The induced magnetic high frequency field around the lepton beam contains a large number of harmonics because of the short bunch length of 30 ps. The energy splitting between the hyperfine states of the target atoms depends on the strength of the magnetic holding field. If a harmonic of the beam induced field matches a transition frequency, transitions will occur between the hyperfine states resulting in a change in the relative populations. As a result the net target polarization decreases. Therefore, both the longitudinal and the transverse holding fields have been set in such a way to avoid these resonances, with a good homogeneity over the full length of the storage cell. The setup for the transverse magnet, installed in 2002, was improved in 2003 with the addition of a correction coil which further reduced the inhomogeneities of the holding field in the transverse directions x and y to the level of 10^{-4} [Wan04].

4.2.6 The average target polarization

From 1997 to 2003, the target polarization values provided by the target group were averaged over each of the data taking periods. These periods were typically of the order of one year, between main shut-downs of HERA for maintenance[4]. However, after the first three months of 2004 the performances of the polarized target became unstable and a similar behavior was registered throughout the 2005. As a consequence, the target polarization needed to be averaged over much shorter periods. Since the ABS was removed at the end of 2005, the data collected during the last two years, 2006 and 2007, were unpolarized. The average target polarization values obtained with transversely polarized hydrogen from 2002 to 2005 are reported in Table 4.1. The estimated systematic uncertainty on the target polarization is of the order of 5%.

Period	polarization
Apr 2002 - Mar 2003	0.783 ± 0.041
Sep 2003 - Dec 2003	0.795 ± 0.033
Jan 2004 - Mar 2004	0.777 ± 0.039
Apr 2004 - Aug 2004	$0.648 \pm 0.090 \ ... \ 0.775 \pm 0.044$
Nov 2004 - Nov 2005	$0.579 \pm 0.112 \ ... \ 0.761 \pm 0.050$

Table 4.1: Target polarization values for the different data taking periods with transversely polarized hydrogen. Due to the unstable conditions of the target, only the smallest and the highest polarization values are reported for the last two periods. The statistical uncertainties are negligible compared to the listed systematic uncertainties.

---

[4]During the commissioning of the target in 1996 the TGA was not available for most of the time and the measurement of the target polarization suffered from a large systematic uncertainty.

4.2.7 The Unpolarized Gas Feed System (UGFS)

Besides the injection of polarized hydrogen and deuterium atoms, whose density was intrinsically limited by the performances of the ABS, the storage cell was also periodically filled with unpolarized gas by means of the so-called *Unpolarized Gas Feed System* (UGFS). After the removal of the ABS, at the end of 2005, the UGFS was the only device used to feed the storage cell. The UGFS allowed not only the injection of unpolarized hydrogen and deuterium, but also of heavier gasses like krypton, xenon, neon and nitrogen. However, during the last two years (2006 and 2007) only unpolarized hydrogen and deuterium were used.

The densities of the unpolarized gases provided by the UGFS were adjustable acting on a dosing valve and only limited by the requirement to provide less than a maximum contribution τ_H^{max} to the reduction of the lepton beam life time. The beam life time contribution τ_H is given by the ratio $(\tau_0\tau_G)/(\tau_0 - \tau_G)$, where τ_G (τ_0) is the beam lifetime with (without) gas in the target cell. The normal density runs (or Low Density Runs) usually provided a 45-hour beam life time contribution. Exceptions were represented by the so called 'end of fill' runs, executed during the very last part of the HERA fills, when the lepton beam current was below ~ 13 mA. During these runs a high density unpolarized gas was injected into the storage cell providing a beam life time contribution of only 2 hours. The target density was then only limited by the detector rates, and densities up to two orders of magnitude larger than that with the ABS could be achieved. The possibility to change the gas density and to inject the gas also into the target chamber allowed various calibration measurements.

4.3 The HERMES Spectrometer

The HERMES experiment uses an open forward magnetic spectrometer for the detection of the scattered lepton and a large fraction of the hadronic final states. The spectrometer is capable of particle detection in a broad kinematic interval with a good angular and momentum resolution. It allows to detect particles with scattering angles between ± 170 mrad in the horizontal direction and between 40 and 140 mrad in the vertical direction [Dur95] and consists of two identical halves placed above and below the HERA beam pipe. The spectrometer consists of four main components:

- a spectrometer magnet

- a tracking system

- a particle identification (PID) system.

- a triggering system

The spectrometer magnet, which allows the determination of the momentum of charged particles, is a standard dipole magnet with a relatively high angular acceptance. The tracking system basically consists of three sets of tracking chambers placed in front, inside and behind the spectrometer magnet, respectively. The particle identification system consists of four main

components: a RICH, a transition radiation detector (TRD), a preshower detector and an Electromagnetic Calorimeter, and allows a very good separation between leptons and hadrons and a good identification of the various hadron types (pions, kaons and protons). Finally, the triggering system, which allows to separate useful physics events from background contributions, consists of a combination of three hodoscopes built out of scintillating material in combination with PMTs. The location of the various detectors is shown in Figure 4.10 and a detailed description of the detector components can be found in [Ack98].
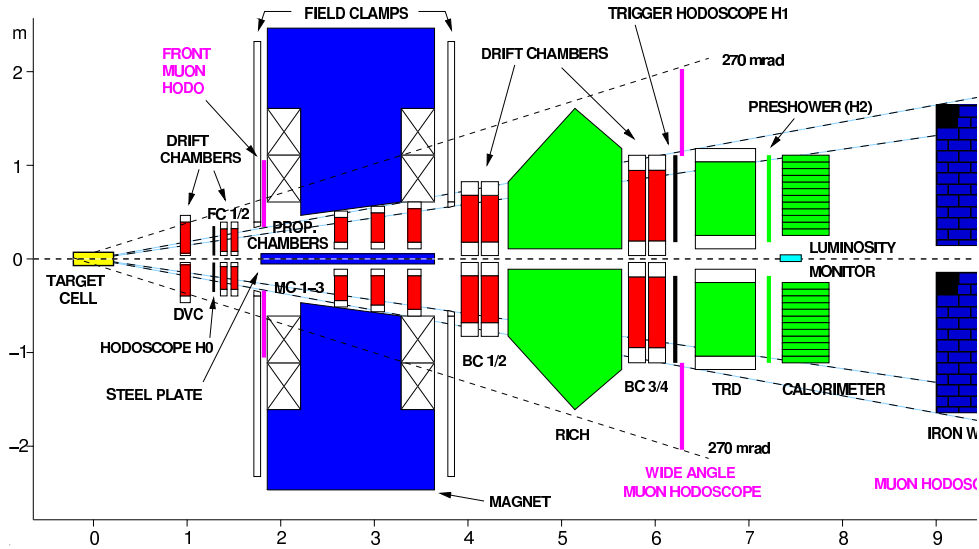
Figure 4.10: A two dimensional, vertical cut of the HERMES spectrometer. Until 1997 a threshold Čerenkov detector was in place of the Ring Imaging Čerenkov (RICH), the silicon detector was not installed until 2001

For the description of the HERMES spectrometer it is necessary to introduce the so-called HERMES coordinate system. The origin of this reference system is located at the center of the target cell. The axes are defined such that the z direction is along the incident lepton momentum, pointing upstream, x points towards the center of the HERA ring and y points upward.

4.3.1 The spectrometer Magnet

During data taking the spectrometer magnet is operated at a deflecting power of $\int Bdl = 1.3$ Tm. The magnetic dipole field is oriented in the vertical direction, deflecting charged particles horizontally. A 11 cm thick iron plate (septum plate), located in the symmetry plane between the two spectrometer halves, shields both the lepton and the proton beam from the magnetic field[5]. The remaining effects are compensated by a correction coil. Field clamps in front and behind the magnet reduce fringe fields in the adjacent detectors. The aperture of the magnet limits the geometrical acceptance of the spectrometer to ± 140 mrad in the vertical and ± 170

---

[5]The proton beam pipe passes in between the spectrometer halves at a distance of 72 cm from the lepton beam.

mrad in the horizontal direction. The lower limit on the vertical acceptance of ± 40 mrad is given by the septum plate.

4.3.2 The Tracking system

The main purpose of the tracking system is the 3-dimensional reconstruction of the tracks of the charged particles and the determination of the particles momenta through the definition of the angle of deflection due to the magnetic field.

All HERMES tracking devices can be divided into two categories depending on their spatial acceptance: main tracking is provided by the drift chambers, identified as the Drift Vertex Chambers (DVCs), Front Chambers (FCs) and Back Chambers (BCs), depending on their position, while extended tracking is achieved by wire chambers, located inside the dipole, called Magnet Chambers (MCs) and a silicon tracker referred to as Lambda Wheel (LW). Except for the silicon detector, which is located right next to the target, all tracking devices are wire chambers, each consisting of several planes.

The Drift Chambers

The core of the HERMES tracking system is represented by the Front Chambers (FC) [Bra01], located at about 1.6 m from the target center, just in front of the magnet, and the Back Chambers (BC) [Ber98], that are combined into two groups in front and behind the RICH detector. They are conventional horizontal drift chambers. Each of their modules consists of six layers of drift cells, each made of a plane of alternating anode and cathode wires between a pair of cathode foils. The cathode foils and wires are at high voltage while the anode wires are at ground. The cells are organized in three pairs, a vertical pair (X-plane), and two staggered planed (U and V planes), which are at an angle of $\pm 30^o$ with respect to the vertical plane to help resolve left-right ambiguities. They are filled with a mixture of 90% Ar, 5% CO_2 and 5% CF_4. The choice of this particular mixture results from three requirements: non-flammability, fast electron drift velocities, small aging effects (assured by the CF_4 component).

When charged particles traverse the chambers, they ionize the gas molecules encountered along their paths. While accelerated toward the anode wires, electrons stripped from the gas molecules ionize other gas molecules. This process results in an avalanche of positive ions which are attracted to the cathode wires. Due to the high mobility of the electrons, their drift time across the cell can be used to determine where in the cell a particle has passed.

The two modules of the FC have drift cells of 7 mm width and 8 mm depth. The resolution per plane is 225 μm, while the single plane efficiency ranges from 97% to 99%, depending on the position in the cell. The BCs have a drift cell size of 15×16 mm. The resolutions are 275 μm for BC1/2 and 300 μm for BC3/4. For leptons (electron or positrons), the BC plane efficiency was found to be well above 99%, while it is somewhat smaller for hadrons (about 97%) because of their reduced ionization density.

Readout cards, responsible for amplification, pulse shaping and discrimination, are mounted on the drift chambers. The signals are transported to Fast-Bus TDCs in the Electronic Trailer (ET),

which is located 30 m away. A draw of a BC module is shown in Figure 4.11 together with a schematic view of the field lines.
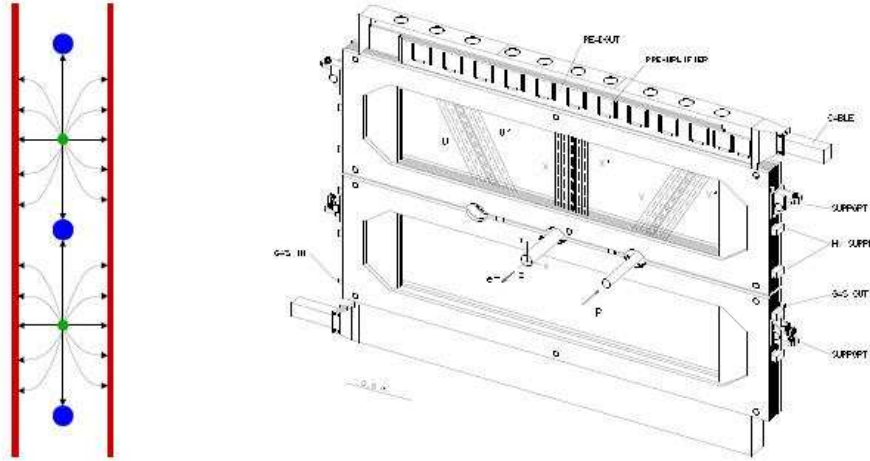
Figure 4.11: Left: The thin anode wires, the thick cathode wires and the cathode planes are visible together with the field lines. Right: a schematic drawing of a BC module.

A set of Drift Vertex Chambers (DVC) was installed 1.1 m downstream of the target between the 1996 and 1997 data taking periods. The DVCs were installed later since redundancy in the front region was desired. Furthermore the loss of a single FC plane could have had a large impact on HERMES tracking. These chambers consist of six planes of conventional drift chambers with a design similar to that of the FCs, albeit smaller, and the same gas mixture as the FCs. The acceptance is somewhat larger though, extending vertically from ± 35 to ± 270 mrad and horizontally to ± 220 mrad. The planes have a wire spacing of 6 mm and a resolution of 220 μm per plane.

The Magnet Chambers

The three Magnet Chambers (MC) [And01] are located in the gap of the magnet. Initially they were intended to help resolve multiple tracks in case of high track occupancies. This turned out not to be necessary because of the low background. Still, they are helpful in determining the momentum of low energy particles (for instance from Λ decays) that do not reach the back part of the detector due to the large deflection in the magnet (see Figure 4.12). These tracks are called *short tracks* or *magnet tracks*.
The MCs are multi-wire proportional chambers (MWPC) able to operate in a strong magnetic field and to deal with high multiplicities. Each chamber has three planes with a cell width of 2 mm, providing a resolution of 700 μm. The positioning of the MCs is shown in Figure 4.13. The MCs gas mixture is the same as for the drift chambers, but the mixing ratios have been
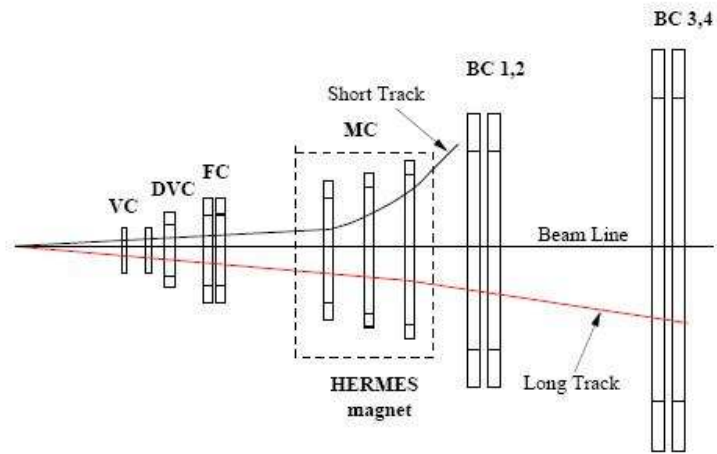
Figure 4.12: A 'short' and a 'long' track in the HERMES spectrometer (top view). Although removed long time ago, the Vertex Chambers (VC) still appear in the picture.
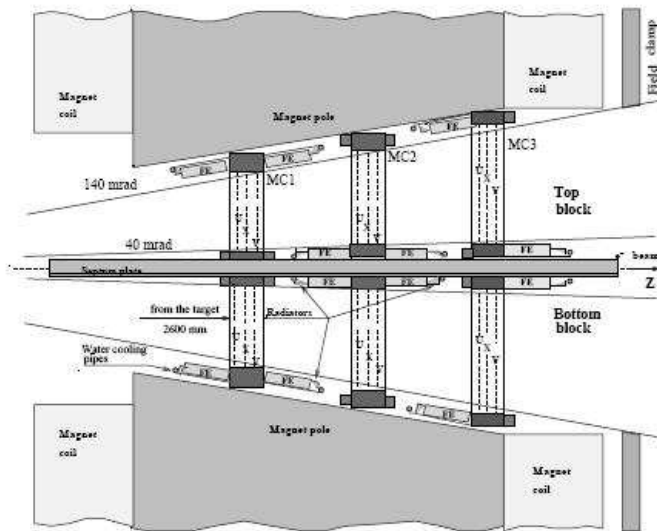
Figure 4.13: The positioning of the six MCs inside the spectrometer magnet.

optimized: 65% Ar, 30% CO_2 and 5% CF_4. A digital single bit-per-wire readout was chosen to accommodate the readout electronics for a large number of channels (5504) within a very restricted space volume.

The Lambda Weel

After the 2000 shutdown, an additional tracking device, the Lambda Weel [Ste00], was installed. The main goal of this detector was to increase the acceptance for longer living particles such as Λ, Λ_c, K_s that decay outside the target region, allowing the reconstruction of the secondary vertex. As the Λ-decay length ($\tau/c$) is about 7.9 cm, the position of the Lambda Weel was chosen to be between 45 and 50 cm downstream of the target cell. Furthermore, since pions from Λ-decay have small momenta, the detector needed to be placed inside the beam vacuum. The Lambda-Wheel consists of two sets of disk-shaped silicon detectors. Each set is divided into 12 modules, each consisting of two trapezoidal double sided 300 μm thick silicon strip sensors. The disk has an external diameter of 33.6 cm and a inner diameter of 9 cm leaving space for the beam pipe and wake field suppressors. As the Wheel is placed close to the accelerator, special care needed to be taken to screen the detector from the RF filed generated by the beam.

The Tracking algorithms

The combined information of many tracking detectors is needed for an unambiguous track reconstruction. At HERMES, a tree-search algorithm is applied for fast and efficient track finding. The principle of this method is to look at the whole hit pattern of the detectors in several iterative steps, doubling the resolution at each step. For a given resolution, the algorithm checks if the hit pattern contains a subpattern consistent with an allowed track, by comparing with all sets of allowed patterns stored in a database. If this is the case, the procedure is repeated at increased resolution, otherwise the pattern is rejected. The HERMES reconstruction program (HRC) needs about 11 iterations to find a track. This is done independently for the hits in the front and back part of the detector, resulting in a set of front and back partial tracks. In a next step, all combinations of front and back partial tracks are tested to match spatially in the x - y plane within a defined tolerance. Matching combinations are refitted to form a full track. The track momentum is determined by comparing the position of the track in front and its slope in front and behind the magnet with numbers in a look-up table. This look-up table contains the momentum of a given track as a function of the relevant track parameters. The overall momentum resolution in the track reconstruction was estimated to be $\Delta p/p = 2.6\%$. In many of the data productions the information of the DVCs was not used. Instead, a slightly different method was developed to reconstruct tracks using only the FC and BC hits. The matching of the front and back partial tracks is first done with a larger tolerance. Then, by fixing the matching point to the position of the higher quality back track extrapolated in the middle of the magnet, the front track parameters are recalculated. This method is called force bridging, i.e. the front track is forced to match the back track in the center of the magnet.

In 1998 the threshold Čerenkov detector in between BC1/2 and BC3/4 was replaced by the

RICH. The RICH material has a considerably larger radiation length than that of the Čerenkov. As a consequence, the momentum resolution of the data taken with the RICH decreased by up to a factor of 2 with respect to data taken with the Čerenkov counter.

When analyzing the data collected during the 2002-2005 running period, in which a transversely polarized target has been used, the vertex and scattering angle reconstruction have to be corrected for the deflection operated by the target transverse magnet (see Section 4.2.5). To do this, the transverse magnet field has been carefully mapped in 2003. The measured field map has been used for the 2003-2005 data productions while for the 2002 production a theoretical field map was calculated with the help of the magnetostatic program MAFIA [Wei97]. A survey of the magnet field along the z-axis and at certain positions along the x-direction served as input for this calculation.
Two different methods for the target magnet correction (TMC) are available, both using the track position information from the DVC and the FCs [Aug07].

In **method 1** the correction on the particle track is applied based on reference tracks from a data base. In a detailed tracking calculation a grid of trajectories covering the HERMES acceptance is computed in small steps of momentum, z-vertex and vertical and horizontal angles. From this set the trajectory closest to a measured particle track is selected, based on the tracking information from the DVC and FCs. The remaining deviations from the reference track in the data base are used in a linear interpolation to yield the corrected z-vertex and vertical scattering angle of the measured track. The true horizontal angle can then be computed from the position of FC2.

Method 2 is based on a ray tracing procedure. Using the reasonable assumption that a trajectory which is in the beginning close to a reference trajectory will also be close to the reference trajectory at the end, a Taylor expansion for the final position in terms of the initial position can be performed. The coefficients provide a quick way to relate the initial position of a track to its final position with the help of a transfer function. For the determination of these transfer coefficients several reference particles had to be tracked through the magnet field using the MIT-Raytrace program [Kow87]. In order to correct the z-vertex position and the scattering angles the right transfer function, which depends on the particle momentum and the z-position from which the particle is assumed to originate, has to be found iteratively until convergence is achieved.

4.3.3 The Particle Identification (PID) Devices

The HERMES PID system consists of four different particle identification detectors: an electromagnetic calorimeter, a preshower detector, a transition radiation detector (TRD) and a threshold Čerenkov detector, that was replaced by a dual radiator Ring Imaging Čerenkov detector (RICH) in 1998. A probabilistic algorithm which uses the responses of these detectors provides a very clean ($> 98\%$) separation of the scattered leptons from the hadrons. The particle identification is achieved in two steps: first leptons and hadrons are separated with the TRD,

the preshower detector and the calorimeter, then pions, kaons and protons are identified by the response of the RICH. Although the main task of the RICH detector is the identification of the various hadron types, it helps to identify leptons as well. Typical PID detector responses are plotted in Figure 4.14.
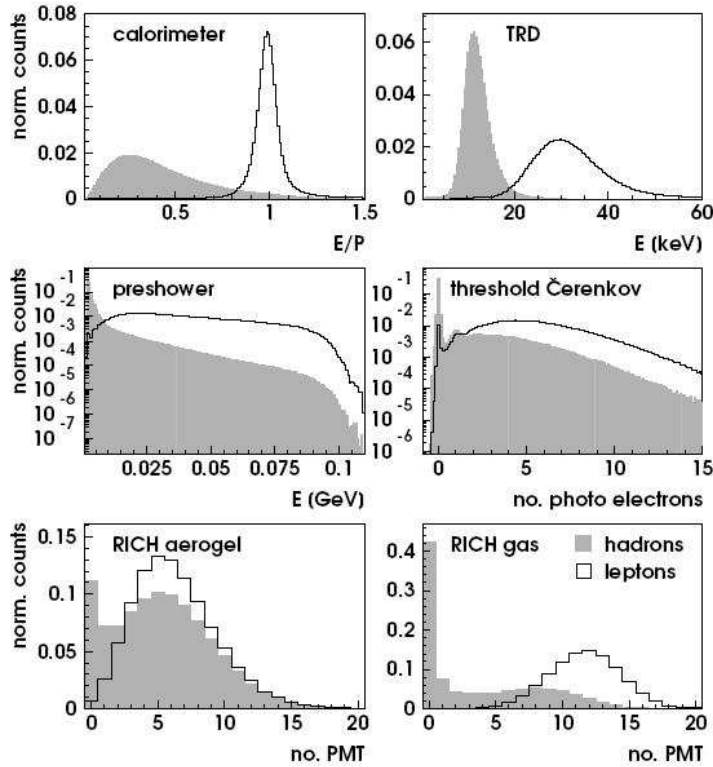
Figure 4.14: The responses of the different PID detectors for hadrons and leptons. In order to plot the responses for a given detector, the particles were identified with cuts on the responses of the remaining PID detectors (source [Els06]).

The Electromagnetic Calorimeter

The HERMES calorimeter [Ava98] was designed to perform an electron-pion separation of at least 10 at first level trigger, and > 100 in the offline analysis. It consists of 420 radiation hard F101 lead glass blocks [Ava96] per each detector half and is located at the downstream end of the spectrometer. The main properties of F101 lead glass are listed in Table 4.2. The frontal area of each block is $9 \times 9 \text{ cm}^2$. The length is 50 cm and corresponds to 18 radiation lengths[6]. Each block is viewed from the rear by a PhotoMultiplier Tube (PMT). The gain of the PMTs is monitored continuously by a dye laser sending light pulses through glass fibers to every PMT

---

[6]The radiation length X_0 indicates the length after which an electron still has $1/e \approx 37\%$ of its initial energy. It can be approximated by $X_0 \sim 180 \cdot (A/Z^2)$.

as well as to a reference photo diode. A comparison of the PMT signals to that of the reference diode measures the relative gain of the PMTs.

F101 Lead Glass		
Chemical composition:	PB_3O_4	(51.23 %)
	SiO_2	(41.53 %)
	K_2O	(7.00 %)
	Ce	(0.20 %)
Radiation Length:	2.78 cm	
Critical Energy (E_c):	17.97 MeV	
Refraction index:	1.65	
Molire Radius:	3.28 cm	

Table 4.2: Chemical composition and calorimetric properties of F101 Lead Glass. The addition of 0.2% of Cerium significantly improves the radiation hardness of the material.

An electron with an energy larger than the critical energy E_c, at which radiative processes start to dominate the energy loss in the material, will lose its energy primarily via emission of Bremsstralhung photons. If these photons have a sufficiently high energy they convert into electron-positron pairs, which, in turn, emit Bremsstralhung photons. The process evolves until the energy of the electrons and positrons falls below the critical energy E_c, generating a so-called electromagnetic shower. The energy of electrons and positrons in the shower is sufficiently high to create Čerenkov light in the lead glass blocks of the calorimeter. The block size was chosen in order to contain 99% of an electromagnetic shower inside a matrix of 3×3 blocks. The amount of Čerenkov photons, detected by the PMTs, then provides a measure of the shower and, to a good approximation, of the energy of the primary electron (positron). The spatial resolution of the impact point is $\sigma \approx 0.7$ cm. The energy resolution of the calorimeter can be parameterized as [Ava98]:

$$\frac{\sigma(E)}{E} = \frac{5.1 \pm 1.1}{\sqrt{E(GeV)}} + (2.0 \pm 0.5) + \frac{10.0 \pm 2.0}{E} \ . \tag{4.9}$$

The energy response was measured to be linear within 1% in the range from 1 to 30 GeV [Ava96]. For particle identification the ratio E/p of the deposited energy to the momentum of the particle is considered. In contrast to leptons (positrons or electrons) which produce electromagnetic showers depositing almost all their energy, hadrons only deposit a fraction of their energy due to ionization losses and nuclear interactions. The top-left panel of Figure 4.14 shows the probability distributions for hadrons and leptons to deposit a fraction E/p of their energy in the calorimeter. The leptons have a distinct peak at $E/p \simeq 1$, while the hadron distribution is much wider and mostly to lower values. If leptons with high momentum radiate bremsstrahlung photons in the detector material in front or inside the magnet, the photons will travel along the lepton path and may hit the same calorimeter cluster as the original lepton. Thus the detected energy in the calorimeter can be larger than the lepton momentum determined by

the magnet after the photon emission (this explain the large tail at $E/p > 1$).

The hadron rejection factor[7] of the HERMES calorimeter was measured to be between 10 and 100 depending on the electron (positron) energy and the calorimeter threshold. The rejection factor increases to values between 50 and 160 in the off-line analysis.

The calorimeter is also used for detection and energy determination of photons. This is, for instance, of crucial importance for the identification of neutral pions. In addition the calorimeter is part of the first level trigger.

The Preshower Detector

Electron-hadron separating power of an electromagnetic calorimeter can be substantially improved if the calorimeter is preceded by a material with a large mean free path length for hadrons[8]. By doing so, indeed, charge exchange reactions such as $\pi^- p \rightarrow \pi^0 n$ are suppressed. For this reason a $\sim 2X_0$ thick preshower detector, consisting of a wall of 42 vertically oriented plastic scintillator paddles behind an 11 mm thick lead plate, was installed right in front of the calorimeter. A schematic drawing of the preshower-calorimeter setup is shown in Figure 4.15.
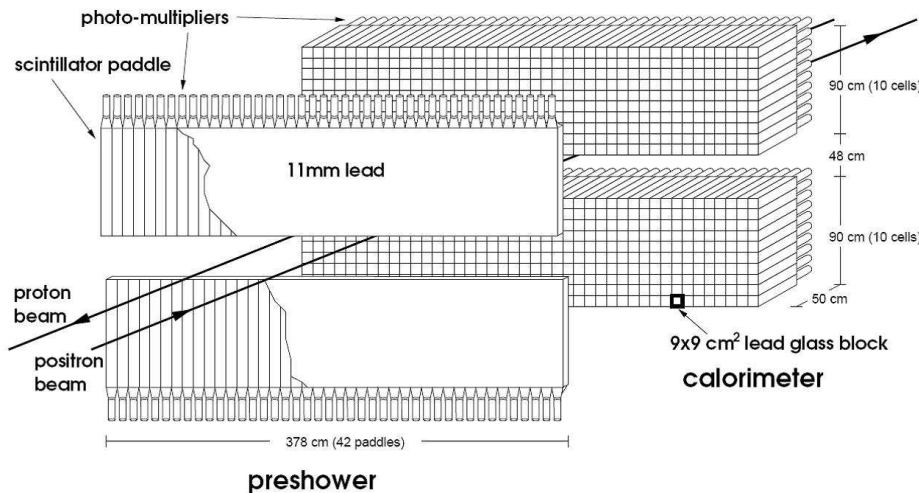
Figure 4.15: Three dimensional view of the preshower detector and the electromagnetic calorimeter.

The paddles have an area of 9.3×91 cm^2 and overlap by $2-3$ mm for maximum efficiency. Each paddle is read out individually by a PMT. Leptons may initiate electromagnetic showers in the lead plate and deposit energy with a mean of $20-40$ MeV in the scintillators whereas hadrons only produce a minimum ionizing signal of 2 MeV. The probability distribution for the preshower signal is also shown in Figure 4.14.

---

[7]The hadron rejection factor is defined as the ratio of the total number of hadrons to the number of hadrons misidentified as leptons, for a given energy cut.

[8]The mean free path length for hadrons can be approximated as $\lambda \sim 35 \cdot A^{1/3}$ and is measured in [g/cm^2].

The Transition Radiation Detector (TRD)

In order to achieve a sufficiently large electron-hadron separation, the installation of a detector with a pion rejection factor of about 100 was required. Because of the limited available space, a transition radiation detector (TRD) was chosen to this purpose.

When a relativistic particle passes through the interface between two dielectric media with different dielectric constants it emits radiation in a narrow cone with an opening angle θ inversely proportional to the Lorentz factor $\gamma = 1/\sqrt{1 - \beta^2}$. This phenomenon is a consequence of the requirement of continuity of the Coulomb field at the boundary between the two media.

The transition radiation (TR) for ultra-relativistic particles is in the X-ray region (several keV). In the passage from vacuum to a medium with electron density n_e, the probability of emission of a transition radiation photon in the ultra-relativistic regime is given by:

$$W_{TR} = \frac{8\pi\alpha^2\gamma n_e}{3m_e} \, , \tag{4.10}$$

where α is the fine structure constant and m_e is the electron mass. The linear dependence of W_{TR} on γ enables a separation of highly relativistic ($\beta \simeq 1$) particles in a way that would require a much longer Čerenkov detector for the same separation power.

At HERMES energies only electrons (positrons) emit such transition radiation in the X-ray region. For instance a 5 GeV electron has a $\gamma = 10000$ while for a pion $\gamma = 35$, so that the probability that the electron emits a TR photon will be 300 times larger than for the pion. The detection of an X-ray in coincidence with a charged particle thus allows to discriminate between electrons (positrons) and hadrons. Figure 4.16 shows how the measurements of the TR improves the separation of electrons from pions.
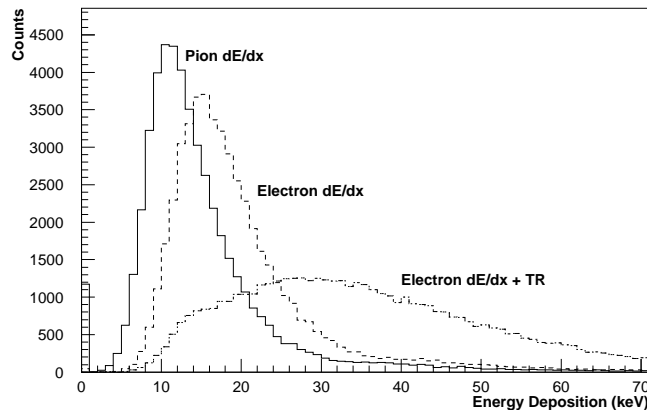
Figure 4.16: Response of a single TRD module. The energy dE/dx deposited in the TRD due to ionization is not able to provide a clear separation between pions and electrons. When the transition radiation is included, the electron peak moves to higher energies and the separation significantly improves.

The dependence of W_{TR} on the square of $\alpha = 1/137$ implies that in order to achieve a considerable probability for the emission of a TR photon, many radiator layers are needed, and the

dependence on n_e implies the use of a material with high electron density. The radiator also needs to be highly transparent to X rays, in order to avoid self-absorption. A polypropylene fiber radiator satisfies all requirements, while the last problem is solved by building a sandwich structure of radiators and X-rays detectors.

The HERMES TRD consists of a sequence of 6 modules per detector half, arranged as shown in Figure 4.17. Figure 4.17 also shows the different impact of the detector on an electron track and a pion track.
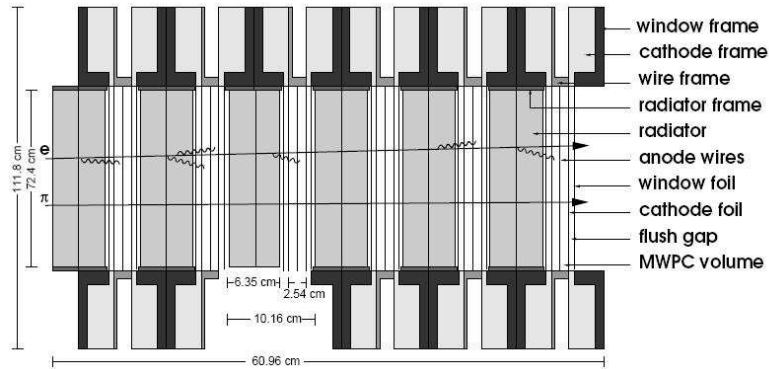
Figure 4.17: Schematic overview of the 6 modules of the HERMES TRD. Each module consists of a radiator and a multi-wire proportional chamber.

Each of these modules consists of a radiator material and a multiwire proportional chamber (MWPC), separated by a flush-gap where CO_2 circulates in order to avoid the diffusion of oxygen and nitrogen into the chambers. The structure of a single module is shown in Figure 4.18.
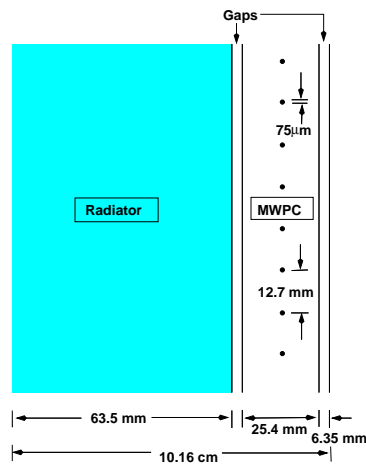
Figure 4.18: Top view of a single TRD module.

The radiator is a loosely packed array of polypropylene fibers with a diameter of $17 - 20$ μm,

arranged in roughly 300 two-dimensional layers, with a total thickness of 6.35 cm. The gas in the wire chambers needs to have high atomic number, in order to achieve best X-ray absorption, thus a mixture of 90% Xenon and 10% Methane, the latter acting as a quencher to avoid the creation of electron avalanches in the chamber, is used. The MWPC consists of 256 vertical wires . Signals from the wires are amplified and transmitted to Fast-Bus ADCs.

In order to obtain a good hadron rejection factor, data from several modules need to be combined. A functional combination based on the 'truncated mean' method was adopted. According to this method the largest signal from the six modules is rejected while the average of the other five is considered. The improvement obtained with this method, which yields a pion rejection factor above 100, is illustrated in Figure4.19. By using a probability based approach, this factor is further increases.
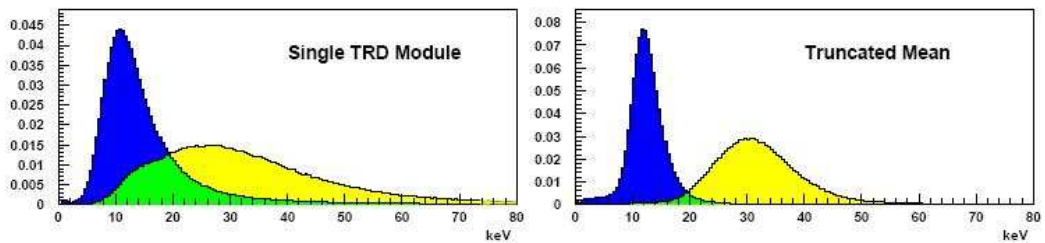
Figure 4.19: Left: the response of a single TRD module. Right: the truncated mean of all 6 modules significantly improves the lepton-hadron separation.

The Čerenkov Detector and the RICH

If a particle passes through a material with a velocity larger than the phase velocity of light in the material, it emits Čerenkov radiation on a cone with a characteristic opening angle θ_c given by:

$$\cos \theta_c = \frac{1}{\beta n} \ , \tag{4.11}$$

where n is the refractive index of the material and $\beta = v/c$ is the ratio of the velocity v of the particle and the speed of light in vacuum c. On the other hand, particles with $\beta < \beta_{thresh} = \frac{1}{n}$ or, equivalently, with momentum

$$P < P_{thresh} = \beta_{th}\gamma_{th}m_0 = \frac{m_0}{\sqrt{n^2 - 1}} \tag{4.12}$$

do not emit Čerenkov light. The fact that in a given material different particles have different threshold momenta provides a way to discriminate between them. This is the working principle of the Čerenkov detectors.

Until the end of 1997 a threshold Čerenkov counter was used to provide lepton identification below the threshold momentum for pions. Each of the counters in top and bottom consisted of a

glass radiator, a system of 20 spherical mirrors and 20 matching photomultiplier tubes mounted on the outside of the aluminum enclosure containing the mirrors and the gas. The radiator gas was a mixture of 70% N_2 and 30% C_4F_{10}, resulting in a P_{thresh} of 20.9 MeV for $e^{\pm}$, 3.8 GeV for pions and 13.9 GeV for kaons. For tracks classified as hadrons by the other PID detectors, the Čerenkov detector could be used to identify pions in a momentum range from 3.9 to 13.9 GeV.

During the shutdown break in the Spring of 1998, the Čerenkov counter was replaced by a dual radiator Ring Imaging Čerenkov detector [Ako02] in order to improve the discrimination between pions, kaons and protons. The RICH uses the same support structure as the Čerenkov counter. Two radiators with rather significantly different refractive indices are used, enabling the identification of the different hadron types over a momentum range from 1 to 15 GeV. The first radiator is a wall of 10.5×10.5 cm^2 aerogel tiles with an entire thickness of 5.5 cm, installed right behind the entrance window [Miy03]. The tiles are stacked in 5 layers with 5 horizontal rows and 17 vertical columns. Aerogel is a silica gel foam, i.e. containing air, with refractive index 1.0304. The second radiator is a heavy gas, C_4F_{10} with a refractive index of 1.0014, filling the volume of the detector. Dry nitrogen is constantly flushed through the aerogel layer to prevent degradation by the C_4F_{10}. Čerenkov photons are reflected from a spherical mirror array onto a photon detector in the focal plane above the gas radiator. The mirror array consists of eight spherical mirror segment with a radius of curvature of 2.20 m and a reflectivity of 85%. The photon detector is an array of 1934 PMTs with a diameter of 18.6 mm, arranged in a hexagonal closed packed matrix. Conventional PMTs sensitive to the visible light region were chosen to detect Čerenkov light. Each of the PMTs is surrounded by an aluminized plastic foil funnel to maximize light collection. A sketch of the top RICH detector is shown in Figure 4.20.
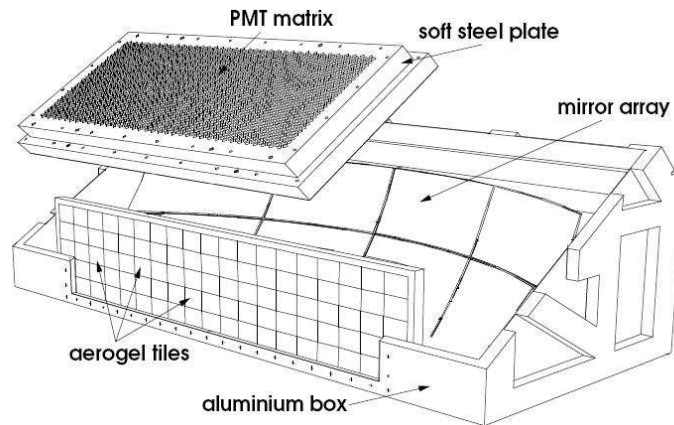
Figure 4.20: Schematic drawing of the upper half of the HERMES RICH detector.

The expected Čerenkov angles for pions, kaons and protons, due to the passage through the two radiators, are plotted as a function of the momentum in Figure 4.21. The two radiators have a different momentum window in which they give a good separation between pions, kaons and protons: momenta lower than approximately 10 GeV are below the threshold for Čerenkov

radiation with a gas radiator, while in this range the aerogel has its greatest discriminating power. At higher momenta the curves for aerogel saturate and it is not possible anymore to distinguish among hadrons based on aerogel information, and the gas is used instead.
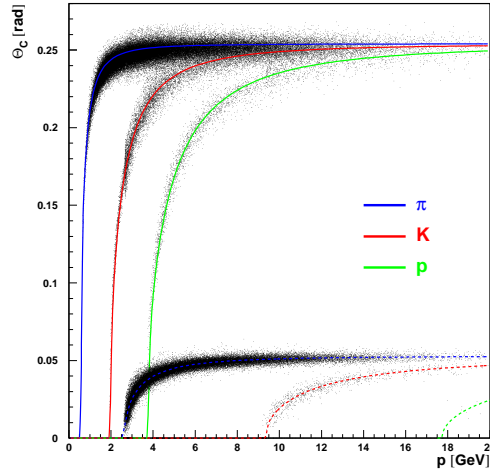
Figure 4.21: Čerenkov angle versus momentum for aerogel (top curves) and C_4F_{10} (bottom curves) radiators. Pions, kaons and protons are clearly separated by combining the signal from both radiators.

The detected 'rings' are not circular, but rather distorted ellipses, as the photon detector is not exactly in the mirror's phocal surface. The aerogel rings are rather difficult to detect, since only a few photons are produced in the aerogel layer. A typical event with a kaon in the upper and an electron and a pion in the lower detector half is depicted in Figure 4.22: A 14.6 GeV electron leaves an aerogel and a gas ring while a 1.5 GeV π^- and a 5.5 GeV K^+ only leave an aerogel ring. The particle associated with the 1.5 GeV track is clearly a pion since a 1.5 GeV kaon is below the Čerenkov threshold. Moreover a pion of 5.5 GeV would have an additional gas ring, while the radius in case of a proton would be much smaller. The figure is an indication of the particle identification power of the RICH detector.
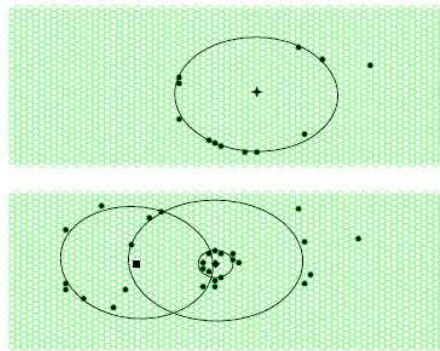
Figure 4.22: A typical RICH event with a 14.6 GeV electron in the lower half, yielding two rings, a 15 GeV π^- in the lower half and a 5.5 GeV K^+ in the upper half.

In HERMES two reconstruction methods are used: Indirect Ray Tracing (IRT) and Direct Ray Tracing (DRT). The RICH PID Scheduler (RPS) combines the best features of both tracing methods by defining which method should be used. More information about the RICH PID reconstruction can be found in [Hom03].

Although the reconstruction is not always simple, the RICH detector is certainly a powerful PID instrument. Furthermore, though the RICH was optimized to provide a good hadron separation, it is also used, together with the other PID detectors, for the separation of leptons and hadrons.

4.3.4 The trigger system

The trigger system selects events interesting for physics analysis from background events. The HERMES trigger working principle is rather straightforward: if a combination of signals of certain detectors are above a predefined threshold, all detector responses are read out.

The first level trigger decision is made within about 400 nsec after the event occurred, using proper combinations of signals from the wire chambers, the calorimeter and three hodoscopes: H0, H1 and H2. H1 and H2 are located in the back part of the spectrometer (see Figure 4.10) and consist of 42 paddles of $9.3 \times 91 \times 1$ cm^3 scintillating material, a 25 cm long light-guide and a PMT at the outer end of each paddle. In particular H2 coincides with the preshower detector described above. During 1995 only the backward region was used for triggering, leading to a large background originating from the HERA proton beam. In 1996 the third hodoscope (H0) was installed in the front region to improve trigger efficiencies. H0 has a different structure than the other two hodoscopes. It consists of a 3.2 mm thick plastic scintillator plate read out by a couple of PMTs.

Various first-level triggers are used at HERMES for DIS events, photoproduction events and for calibration and monitoring of the detectors. The main trigger selects candidates for the scattered lepton in DIS by requiring coincident signals in the three hodoscopes in one detector half and a minimum energy deposited in two adjacent calorimeter columns in the same half, all in coincidence with the HERA beam bunch signal. The threshold energy of the calorimeter is set to 1.4 GeV for data taking with polarized target and 3.5 GeV for the unpolarized target. Only around 13% of the DIS trigger events have at least one identified lepton and approximately 5% of the recorded events are identified as DIS events in the offline analysis.

Not all the generated triggers can be accepted by the HERMES Data Acquisition system (DAQ). Indeed, during the time needed for readout, no new events can be recorded, resulting in a dead time of the data acquisition. The dead time is defined as the ratio of trigger requests which had to be rejected and the total number of readout requests. During standard running the HERMES DAQ is capable of reading out the detector information at rates up to 500 Hz with dead time below 10%.

4.3.5 Luminosity Measurement

In order to do absolute measurements of cross sections and to be able to compare data set of different years it is crucial that the luminosity is determined precisely. In general this is done

either by counting the number of DIS events in a data set or by using a luminosity monitor which makes use of a well known physics process. In case of positron beam, the HERMES luminosity monitor is particularly sensitive to Bhabha scattering ($e^+e^- \rightarrow e^+e^-$) and annihilation processes ($e^+e^- \rightarrow \gamma\gamma$) between beam positrons and the shell electrons of the target atoms. For electron beam the measurable process is Moller scattering ($e^-e^- \rightarrow e^-e^-$). All these reactions have small scattering angles and leave both particles with a similar amount of energy.

The luminosity monitor consists of two small calorimeters, located on both sides of the beam pipe in the horizontal plane, about 7.2 m downstream of the target. The calorimeters consist of 3×4 arrays of radiation resistant $\mathrm{NaBi(WO_4)_2}$ crystals. Each crystal is 20 cm long and has a cross section of $2.2 \times 2.2 \ \mathrm{cm}^2$. At the back side a PMT is coupled to each crystal for the read out of the signal. A schematic drawing of the luminosity monitor and its readout scheme is shown in Figure 4.23.
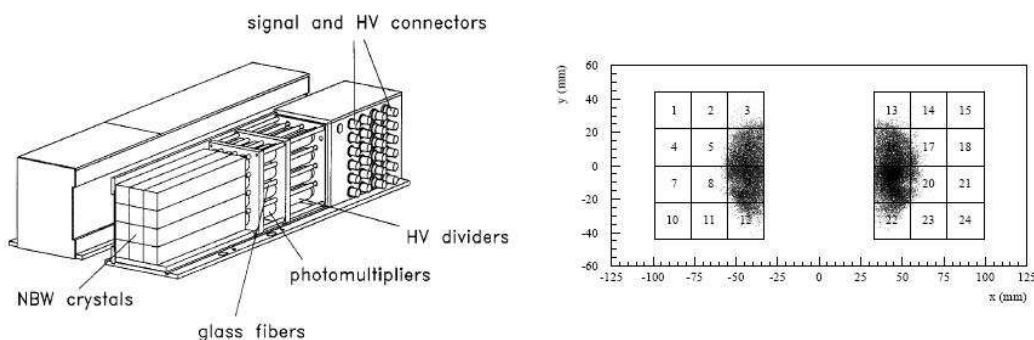
Figure 4.23: Left: Schematic drawing of the luminosity monitor and its readout scheme. Right: Front view showing the reconstructed impact points.

Since the luminosity monitor is positioned outside of the standard HERMES acceptance, it requires its own dedicated trigger in order to select the desired process. Triggering occurs when signals in both luminosity detector halves exceed a 4.5 GeV threshold. The very well known cross section of the scattering and annihilation processes is integrated and folded with the detector acceptance and efficiency. From this and the coincidence rate the luminosity can be determined with an accuracy of $\Delta L/L \simeq 6\%$. For asymmetry measurements only the relative luminosity of data with two different spin configurations is relevant. In this case the uncertainty is much smaller, $\Delta R/R \simeq 0.9 - 1.5\%$. In [Ben01] a detailed description of the luminosity monitor and the contribution of systematic uncertainties to the luminosity measurement is given.

4.3.6 The Data Acquisition and processing

Different time scales are used in the HERMES data acquisition system. The shortest time interval is the *event*, containing all reconstructed tracks which are observed when a trigger is generated. All events recorded within approximately 10 sec are grouped into a *burst*. Bursts are

then combined into a *run* with a size of about 450 MB. Dependent on the luminosity, a run lasts around 10 min. The longest time scale, the fill, is determined by the $8 - 12$ h storage time of the HERA lepton beam.

Apart from event-based information, also monitoring and calibration data like information from the luminosity monitor, the polarimeters, the target, detector temperatures, pressure gauges, voltage settings, etc. needs to be read out from the various detectors. This so-called *slow control* data is read out once every ~ 10 sec, independently on the triggers from the spectrometer. After the acceptance of a certain trigger, all detector responses are read out by the Data Acquisition (DAQ) chain according to their 'equipment number'. The DAQ system digitizes the analog and timing information for an accepted trigger in the ADC and TDC modules located in Fastbus crates. The data from the FastBus crates are bundled by event builder modules and sent over fast opticals links cluster, where they are stored on staging disks and on data tapes.

All raw data is buffered in Experimental Physics Input Output (EPIO) format on hard disks in the Linux cluster and backed up regularly on data tapes. After the end of each HERA fill all collected data is transferred to a taping robot at DESY main site using a Fast Distributed Data Interface (FDDI).

Information contained in the detector signals like the hit positions, energy depositions, etc., are determined with the HERMES decoder (HDC) using mapping, geometry and calibration of the individual detectors. All required information is stored in an ADAMO [Cer93] database. In a next step the HERMES reconstruction (HRC) program finds tracks in the spectrometer. Using a timing signal that is written to the event data and slow control data streams, both data streams can be synchronized. All synchronized data which is useful for physics analyses, is stored in data summary tables, the so-called μDST files.

For Monte Carlo data a very similar production chain is applied. Instead of the DAQ and HDC, a generator of DIS events, GMC, based on LEPTO [Ier97] and JETSET [Sjo95] is used. The simulation of the detector responses and its material is performed by HMC, containing a GEANT3 [Bru84] implementation of all detector components. The Monte Carlo data are reconstructed and compressed with HRC and the μDST-writer, just like real data, although some tables for the generated values are added. Further details are given in Section 6.1. The two chains, for real data and Monte Carlo data, are displayed in Figure 4.24.
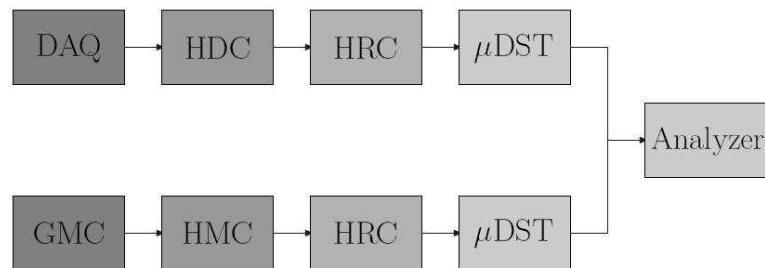
Figure 4.24: The HERMES data production chains for detector data (top raw) and for Monte Carlo data (bottom row).

Chapter 5

The extraction of the Azimuthal Moments

The Collins and Sivers azimuthal moments, discussed in Chapter 3, have been extracted in the analysis of the HERMES data collected during the 2002-2005 running period, in which a transversely polarized hydrogen target was used. To this purpose several checks were applied in order to ensure a high quality of the data before selecting Inclusive and Semi-Inclusive Deep-Inelastic Scattering events. The yields of the selected events were used to construct a single-spin asymmetry (SSA) dependent on the two azimuthal angles ϕ and ϕ_S, as reported in Section 3.7.5. The Collins and Sivers sine modulations were then extracted in a two-dimensional fit using two different fit methods: a standard least square fit and an unbinned maximum likelihood fit. In addition, several tests on the extraction method were performed to estimate the impact of different sources of systematic errors on the final results.

5.1   The HERMES data productions

The starting point of all the analyses performed at HERMES is represented by the so-called μDST files, in which the data, after being precessed through the chain described in Section 4.3.6, is stored. The μDST files are labeled by the last two digits of the corresponding year of data taking, a letter to indicate the production, and a cypher. In the first production of μDST files for a new data taking period (*a*-production), detector calibrations based on the data of the preceding period are used. The *a*-production allows detailed detector calibrations which serve as input for a re-production of the μDST files (*b*-production). In the subsequent *c*-production, additional corrections which rely on proper calibrations are taken into account. The cypher, which completes the production name, is increased for further fast re-productions which do not require the track reconstruction. Such re-productions are usually carried out when improved slow control information such as beam or target polarization values becomes available.

The analysis presented here is based on the HERMES full transverse data set, achieved during the 2002-2005 data taking period, in which a transversely polarized hydrogen target was used. The data productions used in the present analysis are: $02c0$, $03c0$, $04c0$ and $05c0$.

5.2 Data quality

Since, depending on the argument/type of the analysis, not all the information from the entire experimental set-up is needed, the μDST files also contain events collected when one or more detectors were not working properly. The first step of each analysis consists in the selection of those events for which all needed parts of the experimental set-up were properly operating. All information about the performance of the detectors, which is stored at the *burst* level, is combined, by the data-quality group, into the so-called *burst lists*. These lists contain bit patterns of 32 bits for each burst for both detector halves. Each bit corresponds to a certain detector (or part of the experiment) and is set to "1" if the detector was operating properly and to "0" in the opposite case. For the present analysis all bits were required to be set to "1", with the only exception of the first bit, which requires a beam polarization above 20%. This requirement is left out since the present analysis deals with single spin asymmetries in which only the target (and not the beam) needs to be polarized. In general, all PMTs are required to work properly. However, one single PMT, out of all those connected to the calorimeter blocks, is allowed to be dead in the year 2002, when several failures occurred as a consequence of ageing. This was shown not to influence the SSAs of charged hadrons in SIDIS [Has03].

The most important data quality requirements are:

- good performance of the PID detectors and the tracking detectors

- good target performances

- reasonable beam current and luminosity

- reasonable luminosity rate $(1\ Hz \leq\ L\ \leq 50\ Hz)$

- DAQ dead time smaller than $50\ \%$.

Details about the data quality checks can be found in [Wen03] and on the HERMES data quality web page [HDQb].

5.3 The event selection

Once the 'good' bursts of a certain data production are selected according to the data quality criteria, several requirements have to be imposed at the event level. Indeed, a number of cuts and constraints have to be applied on the recorded tracks in order to correctly identify Inclusive and Semi-Inclusive Deep Inelastic Scattering events. The events that pass all requirements constitute the data set that is used in the physical analysis. In this section the various selection criteria are discussed in the same order as they are applied in the analysis chain.

5.3.1 The geometrical cuts

As a first step, several geometrical cuts are applied in order to suppress the background and to exclude those tracks that might be affected by edge effects of the spectrometer. For instance, the longitudinal vertex coordinate z_{vertex} at which the scattering occurs is restricted to the longitudinal dimension of the target cell. Furthermore the tracks have to be fully contained within the effective volume of the spectrometer, the so-called *fiducial volume*. Differently from the charged particles, the photons identification is exclusively based on the calorimeter signal. In order to avoid transverse shower leakages, which would result in a partial loss of the original photon energy, photons are required to hit a smaller section of the effective calorimeter front area. All geometric cuts are listed in Table 5.1.

	charged particles	photons
vertex position	$-18 \text{ cm} \leq z_{vertex} \leq 18 \text{ cm}$	
calorimeter position	$|x_{calo}| \leq 175 \text{ cm}$	$|x_{calo}| \leq 125 \text{ cm}$
	$30 \text{ cm} \leq y_{calo} \leq 108 \text{ cm}$	$33 \text{ cm} \leq y_{calo} \leq 105 \text{ cm}$
front field clamp position	$|x_{ffc}| \leq 31 \text{ cm}$	
rear field clamp position	$|y_{rfc}| \leq 54 \text{ cm}$	
rear clamp position	$|x_{rc}| \leq 100 \text{ cm}$	
	$|y_{rc}| \leq 54 \text{ cm}$	
septum plate position	$|y_{sp}| \geq 7 \text{ cm}$	

Table 5.1: The geometrical cuts applied to the detected charged particles and photons.

5.3.2 The Particle Identification

Lepton-Hadron discrimination

Combining the responses of the four PID detectors a very good separation between leptons (electrons and positrons) and hadrons is achievable at HERMES. From the response of the particle identification detectors it is possible to generate a likelihood function, PID, that is related to the probability of a particle to be a hadron or a lepton. In particular, given the energy E deposited in the detector and the momentum p of the particle, the issue is to find the probability $P(l(h)|Ep)$ that the particle is a lepton l or a hadron h. Bayes theorem relates such a probability to the observable probabilities $P(l(h)|p)$ that a particle with momentum p is a lepton (hadron), and $P(E|l(h)p)$ that a lepton (hadron) with a momentum p deposits an energy E in the detector:

$$P(l(h)|Ep) = \frac{P(l(h)|p)P(E|l(h)p)}{P(l|p)P(E|lp) + P(h|p)P(E|hp)} \ . \tag{5.1}$$

The probability distributions $P(E|lp)$ and $P(E|hp)$, called *parent distributions*, can be estimated in a test beam facility by measuring the response of the detectors to a beam of leptons

or hadrons. A different approach, which is commonly used at HERMES, consists in measuring the response of a given PID detector for a certain type of particle which is selected by the other PID detectors. This method has the advantage of taking into account possible ageing effects of the detectors. The cuts have to be hard enough to define a clean sample but, at the same time, have to ensure a reasonable statistics. As a consequence the cut ranges vary for each data production, being tighter for the productions with higher statistics and less tight for those with a lower statistics. From the ratio between the probabilities $P(l|Ep)$ and $P(h|Ep)$, defined in eqn. (5.1), one can define the quantity:

$$\text{PID}' = \text{PID} - \log_{10} \phi \,, \tag{5.2}$$

where

$$\text{PID} = \log_{10} \frac{P(E|lp)}{P(E|hp)} \tag{5.3}$$

and

$$\phi = \frac{\phi_h}{\phi_l} = \frac{P(h|p)}{P(l|p)} \,. \tag{5.4}$$

The hadron and lepton fluxes ϕ_h and ϕ_l are calculated with an iterative procedure. In general the combined PID for more then one detector D is given by:

$$\text{PID} = \log_{10} \prod_D \frac{P_D(E|lp)}{P_D(E|hp)} = \sum_D \text{PID}_D \,. \tag{5.5}$$

The most common PID combinations used in HERMES are:

$$\text{PID}_3 = \text{PID}_{\text{CALO}} + \text{PID}_{\text{PRE}} + \text{PID}_{\text{CER}} \tag{5.6}$$

$$\text{PID}_5 = \text{PID}_{\text{TRD}} = \sum_{i=1}^{6} \text{PID}_{\text{TRD}_i} \,, \tag{5.7}$$

where 'CALO', 'PRE', 'CER' and 'TRD' stand for the electromagnetic calorimeter, the preshower detector, the Čerenkov detector and the transition radiation detector, respectively. The sum in eqn. (5.7) runs over the 6 TRD modules per detector half. In 1998 the Čerenkov detector was replaced by the RICH, and the product of the conditional probabilities for gas and aerogel radiators is used. PID_3 and PID_5 values are assigned to each detected particle and a cut is applied on the quantity:

$$\text{PID}' = \text{PID}_3 + \text{PID}_5 - \log_{10} \phi = \log_{10} \frac{\mathcal{P}_l}{\mathcal{P}_h} \,, \tag{5.8}$$

which represents the logarithm of the probability ratio that a given particle is a lepton or a hadron. By definition, the quantity PID' is positive if the probability of being a lepton is higher than that of being a hadron, and negative in the opposite case. This provides a simple way to

separate leptons from hadrons (see Figure 5.1). In the analysis reported in this thesis, leptons and hadrons are identified with the following PID cuts:

$$\mathrm{PID}_3 + \mathrm{PID}_5 - \log_{10}\phi > 2.0 \quad \text{(leptons)} \tag{5.9}$$

$$\mathrm{PID}_3 + \mathrm{PID}_5 - \log_{10}\phi < 0.0 \quad \text{(hadrons)} . \tag{5.10}$$
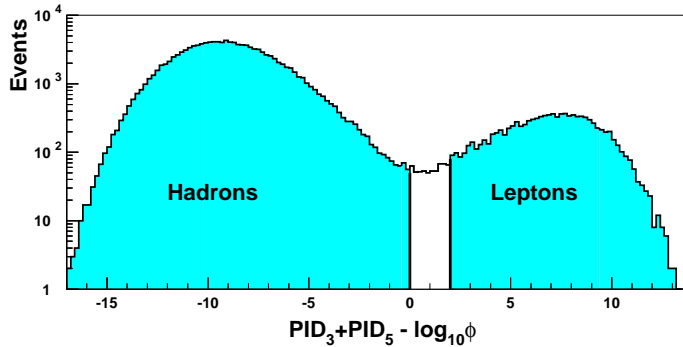
Figure 5.1: Typical distribution of $\mathrm{PID}_3 + \mathrm{PID}_5$. The applied PID cuts are also represented.

Charged Hadrons identification

When passing through the two RICH radiators, charged particles emit a certain pattern of Čerenkov photons (see, for instance, Figure 4.22), allowing the separation of the various charged hadron types (pions, kaons and protons). The photon pattern, which is focused on the PMT matrix by the spherical mirror array, is associated with a track in the spectrometer using an inverse ray tracing algorithm [Jun00]. Combining all measured Čerenkov angles in a range around the theoretical expected angle, average Čerenkov angles are computed for the two radiators, aerogel (a) and gas (g), for each of the three hadron hypothesis, $h = \pi, K, p$. Two likelihoods, $\mathcal{L}_h^a$ and $\mathcal{L}_h^g$, can be calculated and combined to the total likelihood $\mathcal{L}_h^{tot} = \mathcal{L}_h^a \cdot \mathcal{L}_h^g$. The hadron type hypothesis with the largest total likelihood is assigned to the track. The correctness of the identification is assured by requiring the condition

$$Q_p = \log_{10}\frac{\mathcal{L}_{h_1}^{tot}}{\mathcal{L}_{h_2}^{tot}} > 0 , \tag{5.11}$$

where h_1 and h_2 are the most and the second most likely hadron type, respectively. If the identification algorithm could not find a most probable hadron type, the quality parameter Q_p is set to zero.
The efficiency and the contamination degree of the hadron identification are estimated using a Monte Carlo simulation of the RICH detector. The analysis of the Monte Carlo data allows the determination of the conditional probability $P(h_{id}|h_{true})$ that a given hadron of the true

type h_{true} is identified as particle of type h_{id}. The conditional probability is equivalent to the efficiency of the identification if $h_{true} = h_{id}$. However, for the interpretation of $P(h_{id}|h_{true})$ as a contamination in case of $h_{true} \neq h_{id}$, the relative hadron fluxes must be taken into account. These conditional probabilities, which depend on the track momentum and the topology of the photon pattern on the PMT matrix, are combined into a matrix [Hom03]

$$\mathcal{P} = \begin{pmatrix} P(\pi_{id}|\pi_{true}) & P(\pi_{id}|K_{true}) & P(\pi_{id}|p_{true}) \\ P(K_{id}|\pi_{true}) & P(K_{id}|K_{true}) & P(K_{id}|p_{true}) \\ P(p_{id}|\pi_{true}) & P(p_{id}|K_{true}) & P(p_{id}|p_{true}) \end{pmatrix} . \tag{5.12}$$

The $\mathcal{P}$-matrix elements are extracted in 1 GeV momentum bins. Furthermore, since the more tracks are detected in one detector half (top or bottom), the higher is the probability for patterns to overlap, the $\mathcal{P}$-matrix elements are extracted separately for one, two and more than two tracks in a given detector half. The results are plotted in Figure 5.2.
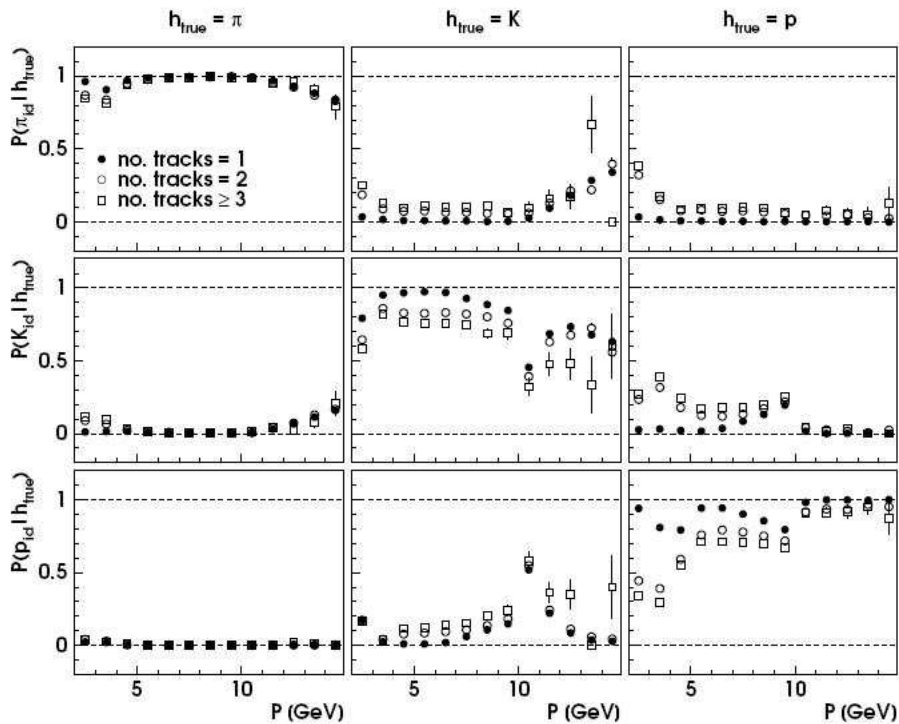
Figure 5.2: The $\mathcal{P}$-matrix elements as a function of the particle momentum. The plot shows the conditional probabilities that a given hadron of true type h_{true} is identified as a pion, kaon, or proton, respectively. The different symbols represent the different number of charged particle tracks per detector half.

The RICH pion identification has a large efficiency and the probability to misidentify a kaon or a proton as a pion is small over almost the entire momentum range. For kaons the momentum threshold of the gas radiator is visible as a discontinuity at around 10 GeV.

The $\mathcal{P}$-matrix relates the flux of identified hadrons $\vec{I} = (N_\pi^{id}, N_K^{id}, N_p^{id})$, to the true flux of 'true' hadrons, $\vec{N} = (N_\pi^{true}, N_K^{true}, N_p^{true})$, through the linear relation $\vec{I} = \mathcal{P} \cdot \vec{N}$. In order to obtain the true flux from the measured flux of identified hadrons, the $\mathcal{P}$-matrix has to be inverted:

$$\vec{N} = \mathcal{P}^{-1} \cdot \vec{I}. \tag{5.13}$$

In the analysis of semi-inclusive events, a weight w_i dependent on the identified hadron type is assigned to each particle track according to the inverse $\mathcal{P}$-matrix. For instance, a track identified as h_{id} is weighted by $(\mathcal{P}^{-1})_{\pi_{true}, h_{id}}$ in the true pion count rate and by $(\mathcal{P}^{-1})_{K_{true}, h_{id}}$ in the true kaon count rate. The sum of these weights over all tracks with identified hadron type $(h_{id})_i$ yields the number of true hadrons

$$N_h^{true} = \sum_i (\mathcal{P}^{-1})_{h_{true}, (h_{id})_i} = \sum_i w_{h,i} \tag{5.14}$$

used in the analysis.

Neutral pions Identification

Due to their short mean life $[(8.4 \pm 0.6) \times 10^{-17}\,\mathrm{s} \rightarrow c\tau = 25.1\,\mathrm{nm}]$, the identification of the neutral pions is obtained through the detection of pairs of correlated photons, which represent the dominant decay mode, with a branching ratio of almost 99%. As described in Section 4.3.3, at HERMES the energies and positions of photons are measured by the electromagnetic calorimeter. The calculation of the photon 4-momentum is then achieved by connecting the photon position on the calorimeter front to the z-coordinate of the electon/positron scattering vertex with a straight line. The next step for the identification of the neutral pions consists in the computation of the invariant mass $M_{\gamma\gamma}$. For this purpose pairs of photons with energy above 1 GeV are considered. For events with more than two photons (and less than nine), all possible combinations are taken into account. Events with more than nine photons are considered as background and rejected in order to limit the combinatorial background.

Figure 5.3 shows the invariant mass distribution of all photon pair combinations after applying the geometrical cuts (see Table 5.1) and the kinematic cuts (see Section 5.3.3). In order to estimate the mean value and the width of the experimental π^0 mass distribution as well as the background/signal ratio, the invariant mass distribution spectrum has been fitted with a normalized Gaussian plus a modified second order polynomial. The fit results are listed in Table 5.2. The obtained π^0 mass is reasonably close to the value quoted by the Particle Data Group (134.29 ± 0.06 MeV) [Yao06]. The 5σ deviation is mainly caused by the energy calibration of the calorimeter and the fact that the position reconstruction of the photons is solely based on the calorimeter signals. In the data production used in this analysis, the energy calibration of the calorimeter yielded a constant correction factor for the measured photon energies. An energy calibration dependent on the signal in the preshower detector, which will improve the resolution of the calorimeter and, consequently, the reconstruction of the π^0 mass, is currently under study and not yet implemented in this analysis. The width of the peak reflects the limited resolution of the calorimeter.
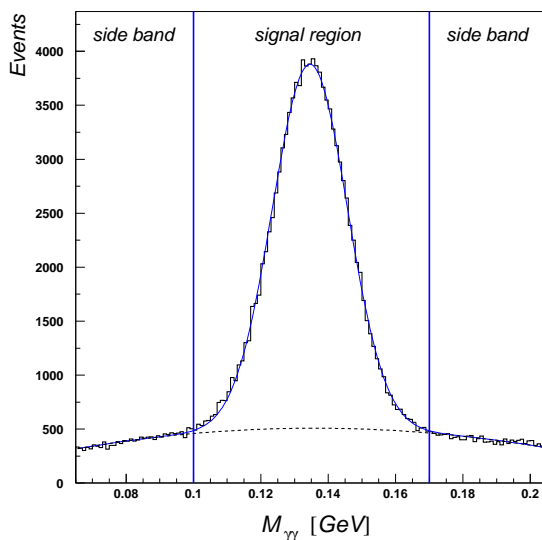
Figure 5.3: Invariant mass distribution of the photon pairs that have passed the geometric and the kinematic cuts. The solid line is a fit of the spectrum obtained using a Gaussian plus a modified second order polynomial. The latter, which parameterizes the combinatorial background, is also shown (dotted line). In order to facilitate the combinatorial background subtraction, the spectrum is divided into three distinct regions: the signal region (between 0.10 and 0.17 GeV) and the two side bands.

Fit parameters
M_{π^0} (mean value) $= 134.29 \pm 0.06$ MeV
σ (width) $= 11.26 \pm 0.06$ MeV
$N_{\text{background}}/N_{\text{signal}} = 0.373 \pm 0.008$
$R = N_{\text{background}}^{SR}/N_{\text{background}}^{SB} = 1.215$

Table 5.2: Invariant mass fit parameters. The last raw reports the ratio between the background events within the signal region (SR) and those in the side bands (SB).

As shown in Figure 5.3, the invariant mass spectrum has been divided into three mass regions: a *signal region*, between 0.100 and 0.170 GeV (corresponding to approximately $M_{\pi^0} \pm 3\sigma$), and the two *side bands*, from 0.065 to 0.100 and from 0.170 to 0.205, respectively. The signal region includes all the photon pairs which are decay products of neutral pions plus part of the combinatorial background, while the side bands only include uncorrelated photons, which only contribute to the background. The widths of the two side bands are chosen in such a way that their sum equals the width of the signal region ($0.070 \, \text{GeV}$). The ratio R between the number of background events within the signal region and those in the side bands (see Table 5.2), extracted from the fit, is used to subtract the combinatorial background within the signal region (see Section 5.4.2).

5.3.3 The kinematic cuts

The inclusive DIS events are needed in the present analysis since they provide a measure of the luminosity and can thus be used for the luminosity normalization, as explained below. Therefore, after the identification of the scattered lepton (electron or positron) and the produced hadrons, several cuts are applied on the kinematical variables in order to select inclusive and semi-inclusive deep inelastic scattering events.

A four-momentum transfer of more than $1\,\mathrm{GeV}^2$ is required to select the deep inelastic scattering regime, where perturbative QCD holds. The resonance region ($W \lesssim 2\,\mathrm{GeV}$) is excluded by a cut on the squared invariant mass of the final hadronic state: $W^2 > 4\,\mathrm{GeV}^2$ for the inclusive and $W^2 > 10\,\mathrm{GeV}^2$ for the semi-inclusive DIS events. The upper cut on the energy fraction y is meant to suppress higher order QED effects. The very low y region, which is affected by a poor resolution, is excluded by the cut $y > 0.1$. However, due to the restrictions on Q^2 and W^2, the lowest possible value of the fractional energy transfer in semi-inclusive events is $y \approx 0.18$. The range in the Bjørken scaling variable x is determined by the cuts on Q^2 and W^2 and by the HERMES acceptance.

	Inclusive DIS	Semi-Inclusive DIS
four momentum transfer	$Q^2 > 1\,\mathrm{GeV}^2$	$Q^2 > 1\,\mathrm{GeV}^2$
squared inv. mass of hadronic final state	$W^2 > 4\,\mathrm{GeV}^2$	$W^2 > 10\,\mathrm{GeV}^2$
fractional energy transfer	$0.1 < y < 0.95$	$y < 0.95$
Bjørken scaling variable	$0.023 < x < 0.4$	$0.23 < x < 0.4$
virtual photon - hadron angle		$\theta_{\gamma^*h} > 0.02\,\mathrm{rad}$
hadron momentum		$2\,\mathrm{GeV} < P_h < 15\,\mathrm{GeV}$
energy fraction (extended range)		$0.2 < z < 0.7$ $(0.2 < z < 1.2)$

Table 5.3: The kinematic cuts for the selection of inclusive and semi inclusive DIS events.

For those events in which more than one lepton (electron or positron) track remains after the geometry and kinematic cuts, the one with the highest momentum is identified as the DIS lepton. For the selection of the SIDIS hadrons, further cuts are applied on selected hadronic variables for those hadrons that are detected in coincidence with the identified DIS lepton. In particular, events with an angle θ_{γ^*h} between the virtual photon γ^* and the hadron h smaller that 0.02 rad are discarded in order to limit the uncertainty in the determination of the azimuthal angles ϕ and ϕ_S, defined in Figure 3.11. This constraint on θ_{γ^*h} reflects in a constraint on the final state hadron transverse momentum $P_{h\perp}$, e.g., for 2 GeV hadrons, transverse momenta below 0.05 GeV are excluded. In addition, for a reliable hadron identification with the RICH detector, the absolute momenta of the hadrons are restricted to a range between 2 GeV and 15 GeV. The upper limit of the energy fraction $z < 0.7$ rejects scattering events in a region which is dominated by exclusively produced vector mesons (cf. Section 5.7). Nevertheless, in order to investigate the z dependence of the azimuthal moments in the high z region, the range in z has been extended up to 1.2. On the other hand, the lower limit of 0.2 enhances the fraction of hadrons which

carry the information of the struck quark. A list of the kinematic cuts for inclusive and semi-inclusive DIS is reported in Table 5.3. The distributions of selected inclusive and semi-inclusive variables, subjected to the cuts discussed above, are plotted in Figure 5.4.
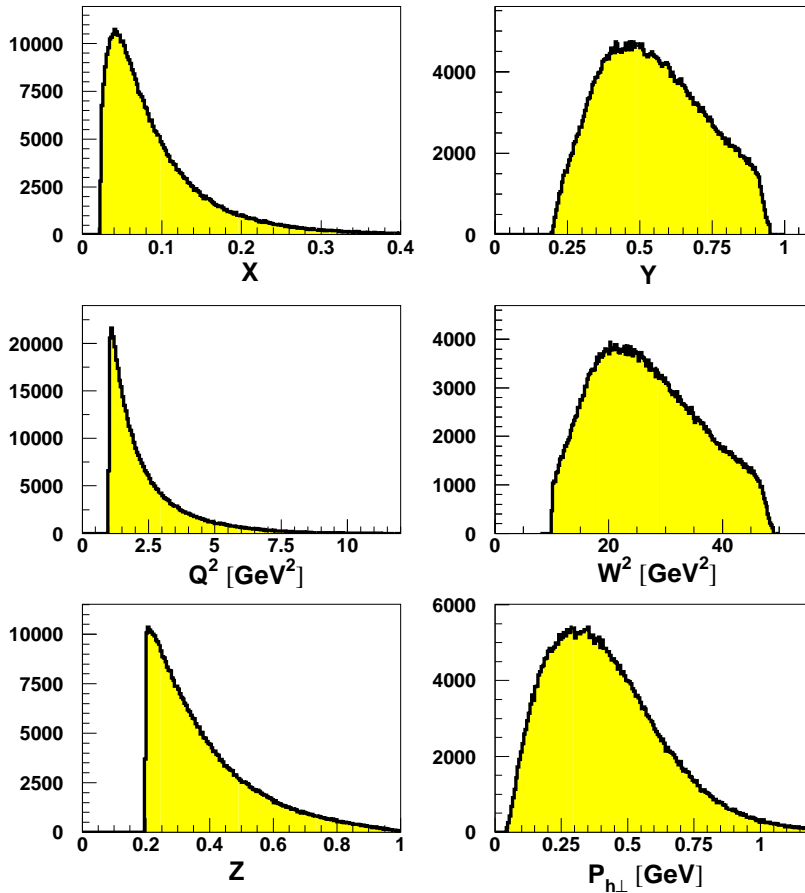
Figure 5.4: Selected DIS kinematic variables.

5.3.4 The charge symmetric background

A big fraction of the interactions that take place in the target region do not result in deep inelastic scattering processes. In addition, due to the limited geometric acceptance of the HERMES spectrometer, not all the DIS events result in a detected scattered lepton. Nevertheless, high energy leptons, produced in different processes such as electron-positron pair productions or Dalitz-like meson decays, might pass all the DIS cuts. These leptons can thus be misidentified as the scattered leptons, resulting in a wrong DIS and SIDIS count rate. Since, however, these leptons are produced in pairs (*charge symmetric background*), a same amount of leptons with the charge opposite to that of the beam particles is produced. These leptons were then used as a control sample to quantify the amount of charge symmetric background and to correct for it.

5.3.5 The DIS and SIDIS yields

After correcting for the charge symmetric background, all the DIS and SIDIS events which have passed both the geometric and the kinematic cuts contribute to the final DIS and SIDIS yields to be used for the extraction of the azimuthal asymmetries. The total DIS count rates and those relative to the two target transverse spin states are reported in Table 5.4 for all the data productions used in the present analysis (cf. Section 5.1). Table 5.4 also reports the corresponding values of the average target transverse polarization $\langle P_t \rangle$. The SIDIS yields, calculated for each hadron type h as the sum over the RICH event weights $w_{h,i}$ (cf. eqn. (5.14)), are reported in Table 5.5.

Data Production	$N_{DIS}^{\uparrow}$	$N_{DIS}^{\downarrow}$	N_{DIS}^{Tot}	$\langle P_t \rangle$
02c0	373386	380104	753490	0.783 ± 0.041
03c0	204562	206183	410745	0.795 ± 0.033
04c0	1136645	1139633	2276278	0.738 ± 0.030
05c0	2489996	2485988	4975984	0.706 ± 0.054
Total	4204589	4211908	8416497	0.726 ± 0.053

Table 5.4: The Inclusive DIS event yields.

Data Productions: $02c0 + 03c0 + 04c0 + 05c0$									
$N_{\pi+}^{\uparrow}$	$N_{\pi+}^{\downarrow}$	$N_{\pi-}^{\uparrow}$	$N_{\pi-}^{\downarrow}$	$N_{\pi0}^{\uparrow}$	$N_{\pi0}^{\downarrow}$	$N_{K+}^{\uparrow}$	$N_{K+}^{\downarrow}$	$N_{K-}^{\uparrow}$	$N_{K-}^{\downarrow}$
348433	348508	248375	250126	74341	74039	67171	67539	26905	27360
$N_{\pi+}^{Tot}$		$N_{\pi-}^{Tot}$		$N_{\pi0}^{Tot}$		N_{K+}^{Tot}		N_{K-}^{Tot}	
696941		498500		148380		134710		54265	
$N_{all\ hadrons}^{Tot} = 1532796$									

Table 5.5: The Inclusive SIDIS event yields for the full HERMES transverse data set. These values are evaluated according to eqn. (5.14).

5.4 The extraction of the azimuthal asymmetry moments

The extraction of the Collins and Sivers azimuthal amplitudes (cf. Section 3.7.5) has been carried out using two different approaches. The first one consists in a binned two-dimensional least square fit of the cross section asymmetries. The second one consists in a 'partially unbinned' Maximum Likelihood fit of the semi-inclusive events by means of a proper Probability Density Function (PDF). The two methods are discussed separately.

5.4.1 The least square fit approach

In this approach, each of the kinematic variables x, y, Q^2, z, $P_{h\perp}$ is binned, together with the azimuthal angles ϕ and ϕ_S (defined in Figure 3.11), according to the scheme reported in Table

5.6. Only the first four z bins are of interest for the extraction of the azimuthal moments. The kinematic region covered by the last two z bins is also investigated although it lies beyond the SIDIS range ($0.2 < z < 0.7$) and contains a large contamination from pions and kaons generated in the decay of exclusively produced vector mesons (cf. Section 5.7). As shown in Figure 5.5, the limited acceptance of the HERMES spectrometer causes a strong coupling of x and Q^2, resulting in an increase of Q^2 with x.

variable	# of bins	bin borders
x	5	[0.023, 0.05]]0.05, 0.09]]0.09, 0.15]]0.15, 0.22]]0.22, 0.4]
y	5	[0.1, 0.31]]0.31, 0.415]]0.415, 0.54]]0.54, 0.69]]0.69, 0.95]
Q^2	5	[1.0, 1.59]]1.59, 2.51]]2.51, 3.97]]3.97, 6.1]]6.3, 15.0]
z	4 (+2)	[0.2, 0.3]]0.3, 0.4]]0.4, 0.55]]0.55, 0.7] ( ]0.7, 0.85]]0.85, 1.2])
$P_{h\perp}$	5	[0.05, 0.25]]0.25, 0.40]]0.40, 0.55]]0.55, 0.8]]0.8, 2.0]
ϕ^π (ϕ^K)	12 (8)	$[0, \frac{\pi}{6}] \cdots]\frac{11\pi}{6}, 2\pi]$ $([0, \frac{\pi}{4}] \cdots]\frac{7\pi}{4}, 2\pi])$
ϕ_S^π (ϕ_S^K)	12 (8)	$[0, \frac{\pi}{6}] \cdots]\frac{11\pi}{6}, 2\pi]$ $([0, \frac{\pi}{4}] \cdots]\frac{7\pi}{4}, 2\pi])$

Table 5.6: Binning in the kinematic variables x, y, Q^2, z, $P_{h\perp}$. For the azimuthal angles ϕ and ϕ_S an equidistant 12×12 (8×8) binning is chosen for pions (kaons).

For the pions asymmetries each kinematic bin is split into 12×12 equidistant bins in the azimuthal angles ϕ and ϕ_S. Due to their lower statistics, a 8×8 binning is chosen for the kaons. The population of the $\phi - \phi_S$ plane is represented in Figure 5.6. The absence of events around $\phi_S = \pi/2$ and $\phi_S = 3\pi/2$ is a consequence of the gap between the top and bottom halves of the spectrometer.

In each azimuthal bin (ϕ, ϕ_S) and for each hadron type h, the asymmetry $A_{UT}^h(\phi, \phi_S)$ of the cross section between the two opposite target transverse spin states is derived as:

$$A_{UT}^h(\phi, \phi_S) \propto \frac{\sigma^\uparrow - \sigma^\downarrow}{\sigma^\uparrow + \sigma^\downarrow} = \frac{1}{\langle P_t \rangle} \frac{N_{h,norm}^\uparrow(\phi, \phi_S) - N_{h,norm}^\downarrow(\phi, \phi_S)}{N_{h,norm}^\uparrow(\phi, \phi_S) + N_{h,norm}^\downarrow(\phi, \phi_S)} . \tag{5.15}$$

This is done for each kinematic variable, while integrating over the other kinematic quantities. Here $N_{h,norm}^{\uparrow(\downarrow)}$ is the luminosity-normalized SIDIS event yield for hadron type h and spin state up ($down$), and $\langle P_t \rangle$ represents the total average target transverse polarization. Its value, $\langle P_t \rangle \approx 73\%$, was obtained by weighting the partial target polarization values measured for each data production with the corresponding integrated luminosities (cf. Table 5.4).

The luminosity normalization is performed by dividing the SIDIS event yield in each azimuthal bin by the total DIS yield $N_{DIS}^{\uparrow(\downarrow)}$ obtained with the same target spin state :

$$\frac{N_{h,norm}^\uparrow(\phi, \phi_S) - N_{h,norm}^\downarrow(\phi, \phi_S)}{N_{h,norm}^\uparrow(\phi, \phi_S) + N_{h,norm}^\downarrow(\phi, \phi_S)} = \frac{\frac{N_h^\uparrow(\phi, \phi_S)}{N_{DIS}^\uparrow} - \frac{N_h^\downarrow(\phi, \phi_S)}{N_{DIS}^\downarrow}}{\frac{N_h^\uparrow(\phi, \phi_S)}{N_{DIS}^\uparrow} + \frac{N_h^\downarrow(\phi, \phi_S)}{N_{DIS}^\downarrow}} . \tag{5.16}$$
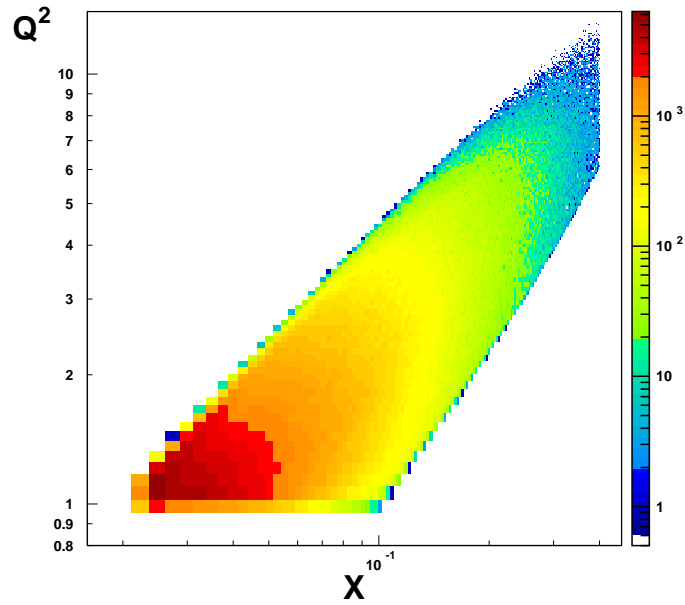
Figure 5.5: The kinematic plane covered. Q^2 and x are strongly correlated due to the acceptance of the spectrometer. Most of the statistics is concentrated in the low-x low-Q^2 region.
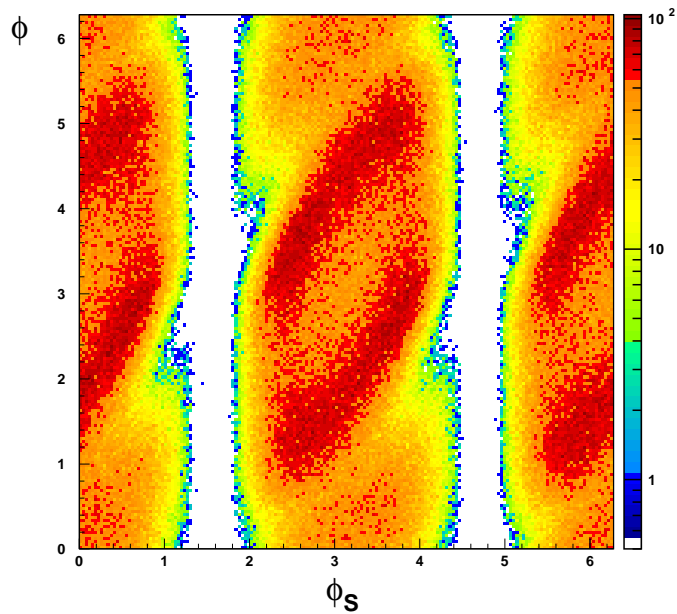

Figure 5.6: The ϕ - ϕ_S plane. The absence of events around $\phi_S = \pi/2$ and $\phi_S = 3\pi/2$ is a consequence of the gap between the top and bottom half of the spectrometer.

Plugging eqn. (5.16) into eqn. (5.17) and rearranging the terms, the latter can be rewritten in the form:

$$A^h_{UT}(\phi, \phi_S) = \frac{1}{\langle P_t \rangle} \frac{N^\uparrow_h(\phi, \phi_S) N^\downarrow_{DIS} - N^\downarrow_h(\phi, \phi_S) N^\uparrow_{DIS}}{N^\uparrow_h(\phi, \phi_S) N^\downarrow_{DIS} + N^\downarrow_h(\phi, \phi_S) N^\uparrow_{DIS}} . \tag{5.17}$$

The 144 (64) azimuthal asymmetries associated to each kinematic bin are fitted by a two-dimensional function whose parameters are the amplitudes $A^{\sin(n\phi \pm m\phi_S)}_{UT}$ of the different sine modulations ($m, n =$ integer number). The basic form of the fit function includes the Collins and Sivers azimuthal modulations plus a constant term C, which is expected to vanish for a correct luminosity normalization of the asymmetries:

$$A^h_{UT}(\phi, \phi_S) = A^{\sin(\phi + \phi_S)}_{UT} \sin(\phi + \phi_S) + A^{\sin(\phi - \phi_S)}_{UT} \sin(\phi - \phi_S) + C . \tag{5.18}$$

The parameters are extracted in a Least Square (LS) fit which makes use of the MIGRAD routine of the MINUIT program [Jam75] for the χ^2 minimization. The extracted amplitudes $A^{\sin(\phi \pm \phi_S)}_{UT}$ are related to the Collins and Sivers asymmetry moments $\langle \sin(\phi \pm \phi_S) \rangle^h_{UT}$, defined in Section 3.7.5, by

$$A^{\sin(\phi \pm \phi_S)}_{UT} = 2\langle \sin(\phi \pm \phi_S) \rangle^h_{UT} = 2\frac{\int d\phi_S d^2 P_{h\perp} \sin(\phi \pm \phi_S)(d^6\sigma_{U\uparrow} - d^6\sigma_{U\downarrow})}{\int d\phi_S d^2 P_{h\perp}(d^6\sigma_{U\uparrow} + d^6\sigma_{U\downarrow})} . \tag{5.19}$$

As discussed in Section 3.7.5, the $P_{h\perp}$-weighted Collins and Sivers asymmetries

$$\left\langle \frac{P_{h\perp}}{zM_h} \sin(\phi + \phi_S) \right\rangle^h_{UT} \quad \text{and} \quad \left\langle \frac{P_{h\perp}}{zM} \sin(\phi - \phi_S) \right\rangle^h_{UT}$$

are also of great interest as they can be interpreted in terms of distribution and fragmentation functions without the requirement of any assumption on the quark transverse momentum distribution. For their extraction an asymmetry is formed in which the events in the numerator are weighted by $P_{h\perp}/z$:

$$A^{P_{h\perp}/z}_{UT}(\phi, \phi_S) = \frac{1}{\langle P_t \rangle} \frac{N^\downarrow_{DIS} \sum_i w_{h,i}(P_{h\perp}/z)_i - N^\uparrow_{DIS} \sum_i w_{h,i}(P_{h\perp}/z)_i}{N^\uparrow_h(\phi, \phi_S) N^\downarrow_{DIS} + N^\downarrow_h(\phi, \phi_S) N^\uparrow_{DIS}} , \tag{5.20}$$

where $N^{\uparrow\downarrow}_h$ are given in Table 5.5 and, as usual, $w_{h,i}$ are the RICH event weights (cf. eqn. (5.14)). The $P_{h\perp}$-weighted asymmetry amplitudes are extracted in a two-dimensional fit based on the function:

$$A^{P_{h\perp}/z}_{UT}(\phi, \phi_S) = 2M_h \left\langle \frac{P_{h\perp}}{zM_h} \sin(\phi + \phi_S) \right\rangle^h_{UT} \cdot \sin(\phi + \phi_s) +$$

$$2M \left\langle \frac{P_{h\perp}}{zM} \sin(\phi - \phi_S) \right\rangle^h_{UT} \cdot \sin(\phi - \phi_s) + C . \tag{5.21}$$

5.4.2 The Maximum Likelihood fit approach

For a set of N independently measured quantities $\mathbf{x_i}$ following a Probability Density Function (PDF) $f(\mathbf{x}; \theta)$, where $\theta = (\theta_1, ..., \theta_m)$ is a set of n parameters whose values have to be determined, the method of Maximum Likelihood (ML) takes the estimators $\hat{\theta}$ to be those values of θ that maximize the *likelihood function*

$$\mathcal{L}(\theta) = \prod_{i=1}^{N} f(\mathbf{x}_i; \theta) \,, \tag{5.22}$$

which represents the joint PDF for the data. Since both $\mathcal{L}$ and $\log(\mathcal{L})$ are maximized for the same parameter values θ, it is usually preferable to work with $\log(\mathcal{L})$. The maximum likelihood estimators can then be found by solving the *likelihood equation*

$$\frac{\partial \log(\mathcal{L})}{\partial \theta_i} = 0, \quad i = 1, ..., m. \tag{5.23}$$

For the extraction of the Collins and Sivers amplitudes the following basic PDF was used:

$$f(\phi, \phi_S, P_t; A_{UT}^{\sin(\phi \pm \phi_S)}) = 1 + P_t \left[A_{UT}^{\sin(\phi + \phi_S)} \sin(\phi + \phi_S) + A_{UT}^{\sin(\phi - \phi_S)} \sin(\phi - \phi_S) \right], \tag{5.24}$$

where P_t is the target transverse polarization corresponding to each event. The product of the acceptance function $\epsilon(\phi, \phi_S)$ times the unpolarized cross section σ_{UU}, which should appear as a global factor in the r.h.s of eqn. (5.24), is dropped since it does not depend on the fit parameters and thus can not affect the fit results. The RICH event weights $w_{h,i}$ are taken into account, resulting in the following quantity to be maximized[1]:

$$\log(\mathcal{L}) = \sum_{i=1}^{N} w_{h,i} \log[f(\phi, \phi_S, P_t; A_{UT}^{\sin(\phi \pm \phi_S)})] \,. \tag{5.25}$$

As anticipated in Section 5.3.2, concerning the identification of the neutral pions, the ratio R between the number of background events within the signal region and those in the side bands (see Figure 5.3 and Table 5.2) is used to subtract the combinatorial background in the signal region. This is done by associating a weight $w_{\pi^0,i} = +1$ to all the events in the signal region and $w_{\pi^0,i} = -R$ to those in the side bands.

5.4.3 Comparing the two methods

Although the least square fit method is suitable for the pions, it was found to be unsuitable for the kaons, due to their limited statistics in certain azimuthal bins. The least squares, indeed, are not good maximum likelihood estimators in case of non-gaussian statistics. Since, in addition,

---

[1] In practice, the azimuthal moments $A_{UT}^{\sin(n\phi \pm m\phi_S)}$ are extracted in the minimization of the quantity $-2\log(\mathcal{L})$, operated through the MIGRAD routine of MINUIT.

binning in ϕ and ϕ_S results in a loss of information and hence in larger statistical errors for the parameter estimates, the method of (unbinned) maximum likelihood was adopted for both pions and kaons.

The unweighted Collins and Sivers amplitudes for pions and charged kaons, extracted from the full HERMES transverse-target data set, are reported as a function of x, z, $P_{h\perp}$, y and Q^2 in Figures 5.7 and 5.8, respectively. Here the results obtained with the two fit methods discussed above (least square and maximum likelihood), are compared. As expected, the two sets of results, obtained with the two different fit methods are compatible. Significant differences are observed only in correspondence of the kinematic bins with low statistics (high x, high z, high $P_{h\perp}$, low y and high Q^2). For these bins, the ML method is superior and provides the most reliable parameter estimates. In particular while the ML fit does not converge in the highest-z bins for charged kaons (no maximum is found for the likelihood function), the LS fit provides spurious solutions for these bins.

5.5   Systematic studies

In order to test the stability of the results and to estimate a systematic error which accounts for all the possible sources of biases, the Collins and Sivers amplitudes were extracted under different conditions. The systematic studies reported in the next sections of this chapter are based on the full HERMES data set with a transversely polarized target (data productions $02c0$, $03c0$, $04c0$ and $05c0$), while other studies, which are reported in the next chapter, rely on Monte Carlo simulations. A list of the systematic studies performed is reported below:

  - Contribution of other azimuthal moments (Section 5.5.1)

  - Compatibility of different data-taking periods (Section 5.5.2)

  - Hadron identification with the RICH (Section 5.5.3)

  - Effects of beam polarization (Section 5.5.4)

  - The Transverse Magnet Correction methods (Section 5.5.5)

  - Fake asymmetries (Section 5.5.6)

  - QED radiative effects (Section 5.5.7)

  - Detector acceptance and smearing effects (Chapter 6)

5.5.1   The contributions of other azimuthal moments

In the previous sections, very simple fit functions, including solely the Collins and the Sivers azimuthal modulations, were considered for both the fit methods (LS and ML) discussed. These modulations account for only two terms (3.68 and 3.69) of the SIDIS cross section (3.61). However, other terms of the cross section might contribute, which are associated to different

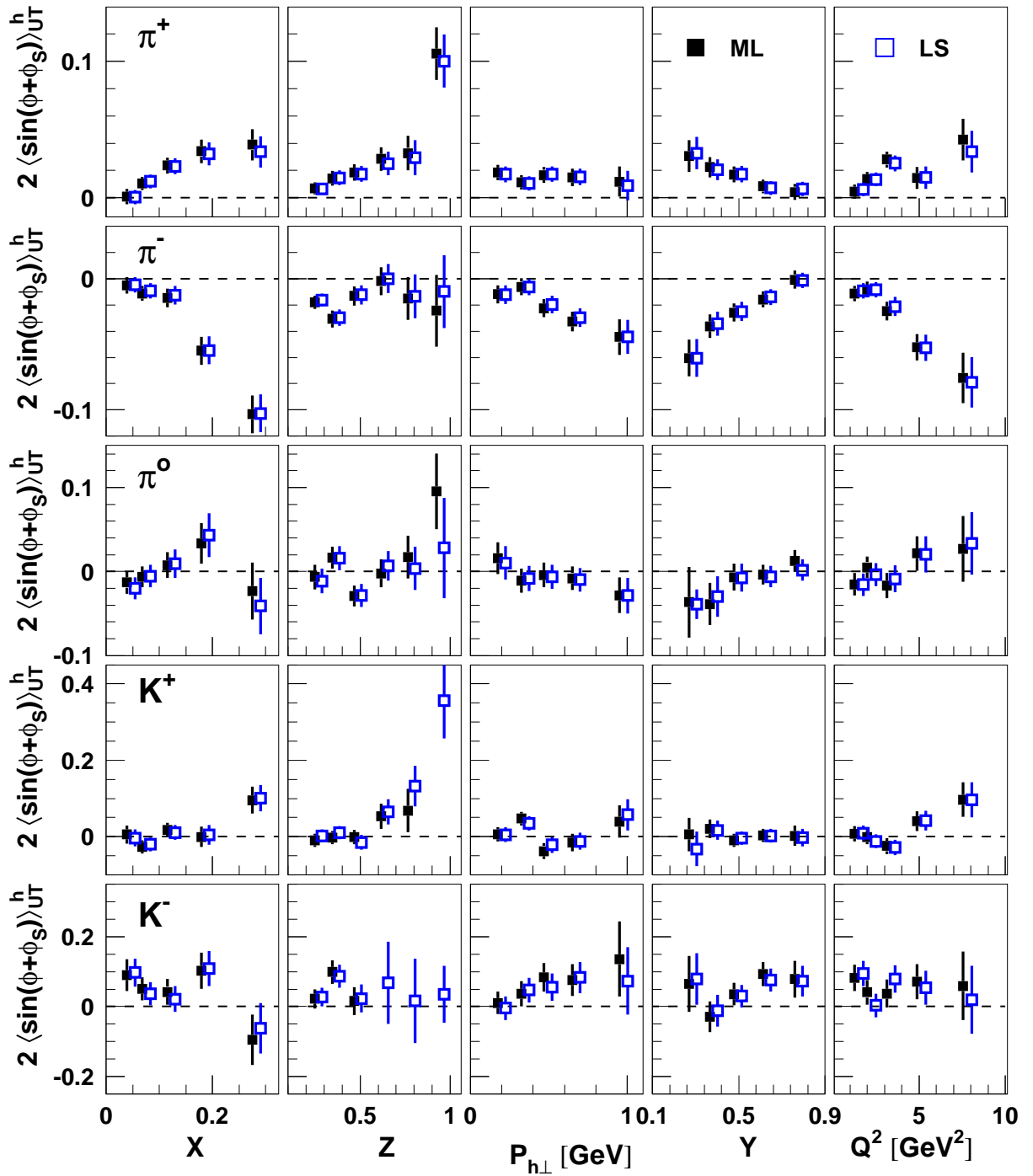Figure 5.7: Collins moments for pions and charged kaons as a function of x, z, $P_{h\perp}$, y and Q^2. The results obtained with the LS fit (open dots) and the ML fit (full dots) are compared.

Figure 5.8: Sivers moments for pions and charged kaons as a function of x, z, $P_{h\perp}$, y and Q^2. The results obtained with the LS fit (open dots) and the ML fit (full dots) are compared.
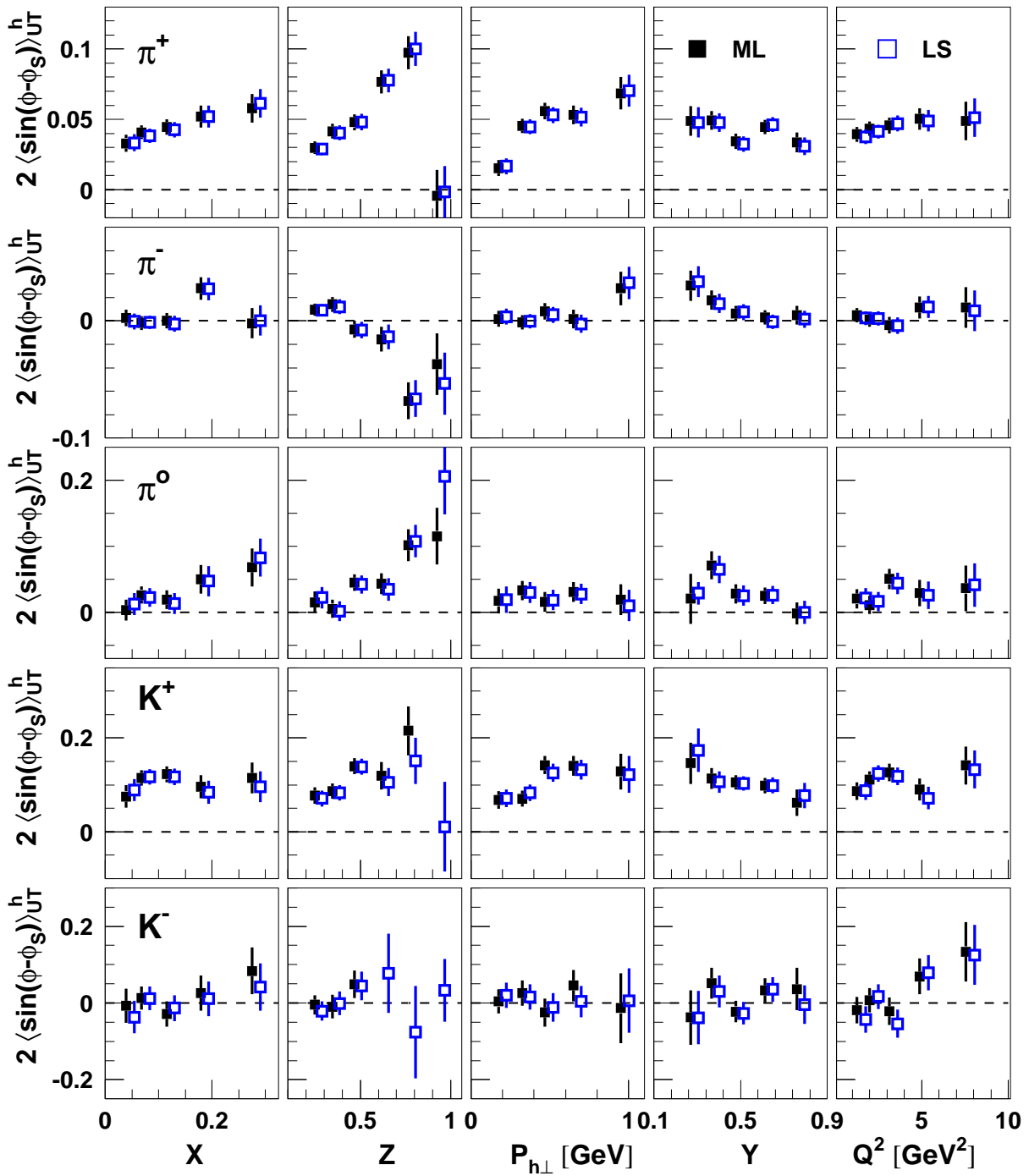
azimuthal modulations. The inclusion of such modulations in the fit function might then lead to slightly different amplitudes for the extracted Collins and Sivers moments.

In order to test the impact of selected additional azimuthal modulations on the extracted Collins and Sivers amplitudes, the latter were extracted in six different fits, each including a different additional azimuthal modulation (or combination of azimuthal modulations). The azimuthal modulations considered are summarized in Table 5.7. All of them arise from terms of the cross section which do not depend on the beam polarization, and are grouped according to the target polarization state.

Modulation	Beam pol.	Target pol.	Twist	Amplitude	Figure
$\sin(\phi_S)$	U	T	2	free	5.9
$\sin(2\phi - \phi_S)$	U	T	3	free	5.9
$\sin(3\phi - \phi_S)$	U	T	2	free	5.10
$\sin(2\phi + \phi_S)$	U	T	2	free	5.10
$\sin(2\phi)$	U	L	2	free	5.11
$\sin(\phi)$	U	L	3	free	5.11
$\cos(2\phi)$	U	U	2	fixed	5.11
$\cos(\phi)$	U	U	3	fixed	5.11

Table 5.7: Azimuthal modulations included in the fit functions for the extraction of the Collins and Sivers amplitudes. The fifth column specifies whether the corresponding amplitudes were kept fixed or left free in the fit. The last column indicates the Figure showing the corresponding comparison plots.

Similarly to the Collins and Sivers modulations, the $\sin(\phi_S)$, $\sin(2\phi - \phi_S)$, $\sin(3\phi - \phi_S)$ azimuthal modulations arise from the polarized part of the cross section dependent on the transverse polarization of the target. As a consequence, they are expected to contribute to the fit result for the Collins and Sivers amplitudes. These modulations have already been introduced in Section 3.7.4 and are included in the expression of the SIDIS cross section (3.61), which is referred to the direction of the virtual photon. Since, however, experimentally one can only measure the cross section with respect to the lepton beam direction, a new term has to be taken into account, which originates from the fact that lepton beam and virtual photon are not perfectly collinear. This term, which is related to the $\langle \sin(2\phi) \rangle_{UL}$ amplitude for unpolarized beam and longitudinally polarized nucleons, is modulated by $\sin(2\phi + \phi_S)$ [Die05].

In order to test the presence of further residual effects due to the non collinearity of lepton beam and virtual photon, the $\sin(2\phi)$ and $\sin(\phi)$ modulations (cf. eqn. (3.61)) are also regarded. The last two modulations, $\cos(2\phi)$ and $\cos(\phi)$, arise from the spin-independent part of the cross section (3.61). The latter four modulations are expected to provide a negligible contribution to the fit results of the Collins and Sivers amplitudes.

In Figure 5.9 the Collins and Sivers amplitudes extracted in a ML fit based on the 2-parameters PDF (eqn. (5.24)) are compared with those extracted using two different 3-parameters PDFs, including the $\sin(\phi_S)$ and the $\sin(2\phi - \phi_S)$ modulations, respectively. This comparison shows that while the inclusion of the $\sin(2\phi - \phi_S)$ modulation does not cause significant changes in

the extracted Collins and Sivers amplitudes, that of the $\sin(\phi_S)$ modulation produces sizeable shifts, especially visible in the Collins amplitudes for negative pions.

A similar comparison is shown in Figure 5.10. Here the Collins and Sivers amplitudes extracted with the 2-parameters PDF are compared with those extracted using two other 3-parameters PDFs, including the $\sin(3\phi - \phi_S)$ and the $\sin(2\phi + \phi_S)$ modulations, respectively. Only small shifts are observed when the latter is included in the PDF, while essentially no effects are observed when the former is included.

The last comparison, shown in Figure 5.11, involves the standard Collins and Sivers amplitudes (extracted with the 2-parameters PDF) and those extracted with a 2-parameters PDF, including also the $\cos(\phi)$ and $\cos(2\phi)$ modulations, and with a 4-parameters PDF, including also the $\sin(\phi)$ and $\sin(2\phi)$ modulations. While, similarly to the other cases discussed above, the amplitudes for these two sine modulations are extracted in the fit as free parameters, those for the $\cos(\phi)$ and $\cos(2\phi)$ modulations are kept fixed to the values of the $A_{UT}^{\cos(\phi)}$ and $A_{UT}^{\cos(2\phi)}$ moments extracted in [Gio08]. In both cases no significant effects in the extracted Collins and Sivers amplitudes are observed.

Despite only the $\sin(\phi_S)$ modulation produces sizeable effects on the extracted Collins and Sivers amplitudes, the four additional modulations dependent on the transverse target polarization (see first four rows in Table 5.7) were included, for completeness, in the PDF:

$$f(\phi, \phi_S, P_t; A_{UT}^{\sin(n\phi \pm m\phi_S)}) =$$

$$1 + P_t \Big[A_{UT}^{\sin(\phi + \phi_S)} \sin(\phi + \phi_S) + A_{UT}^{\sin(\phi - \phi_S)} \sin(\phi - \phi_S) + A_{UT}^{\sin(\phi_S)} \sin(\phi_S) +$$

$$A_{UT}^{\sin(2\phi - \phi_S)} \sin(2\phi - \phi_S) + A_{UT}^{\sin(3\phi - \phi_S)} \sin(3\phi - \phi_S) + A_{UT}^{\sin(2\phi + \phi_S)} \sin(2\phi + \phi_S) \Big]. \quad (5.26)$$

In the following, this PDF will be referred to as the 'standard 6-parameters PDF'. The tiny contributions due to the remaining four azimuthal modulations not included in eqn. (5.26) ($\cos(\phi)$, $\cos(2\phi)$, $\sin(\phi)$ and $\sin(2\phi)$) will be regarded as sources of systematic errors (see Section 5.5.8). Table 5.8 reports the values of the unweighted Collins and Sivers moments extracted at the average kinematics through the 'standard 6-parameters PDF' fit.

h	$\langle x \rangle$	$\langle z \rangle$	$\langle P_{h\perp} \rangle$	$\langle y \rangle$	$\langle Q^2 \rangle$	$2\langle sin(\phi + \phi_S) \rangle_{UT}$	$2\langle sin(\phi - \phi_S) \rangle_{UT}$
π^+	0.094	0.361	0.407	0.542	2.400	0.014 ± 0.003	0.044 ± 0.003
π^-	0.090	0.352	0.406	0.548	2.328	-0.023 ± 0.003	0.006 ± 0.003
π^0	0.087	0.394	0.458	0.589	2.440	-0.017 ± 0.009	0.032 ± 0.009
K^+	0.097	0.384	0.435	0.538	2.472	0.005 ± 0.009	0.093 ± 0.008
K^-	0.090	0.347	0.422	0.552	2.349	0.026 ± 0.014	0.006 ± 0.013

Table 5.8: Kinematic mean values and overall unweighted Collins and Sivers moments extracted with the standard 6-parameters PDF fit in the semi-inclusive range $0.2 < z < 0.7$. The average $P_{h\perp}$ and Q^2 are expressed in GeV and GeV^2, respectively. Only the statistical uncertainties are reported.

Figure 5.9: Unweighted Collins (upper half) and Sivers (lower half) moments for π^+ (upper panels) and π^- (lower panels) extracted with the basic 2-parameters PDF (full squares), compared with those extracted with two different 3-parameters PDFs including the $\sin(2\phi - \phi_S)$ (open triangles) and the $\sin(\phi_S)$ modulation (open circles), respectively.

Figure 5.10: Unweighted Collins (upper half) and Sivers (lower half) moments for π^+ (upper panels) and π^- (lower panels) extracted with the basic 2-parameters PDF (full squares), compared with those extracted with two different 3-parameters PDFs including the $\sin(2\phi + \phi_S)$ (open triangles) and the $\sin(3\phi - \phi_S)$ modulation (open circles), respectively.
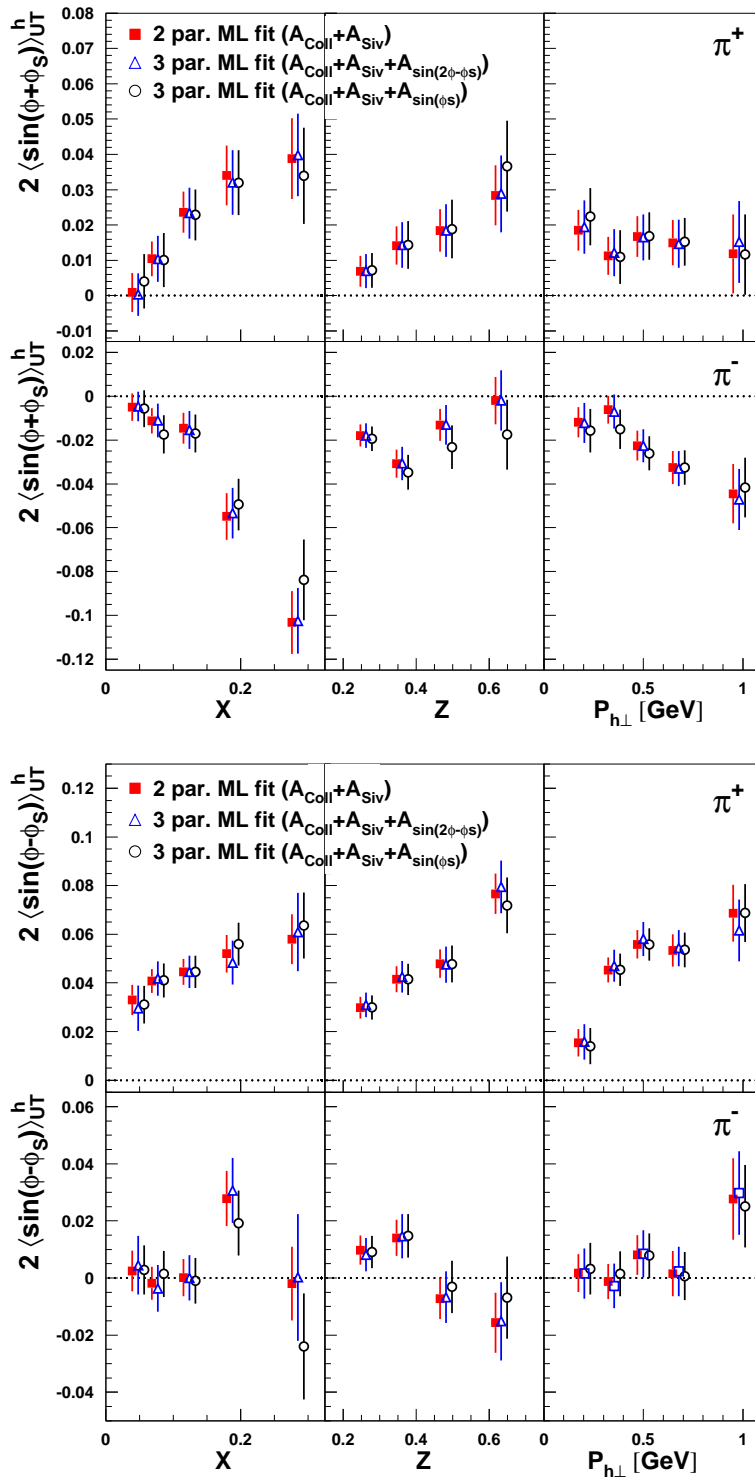
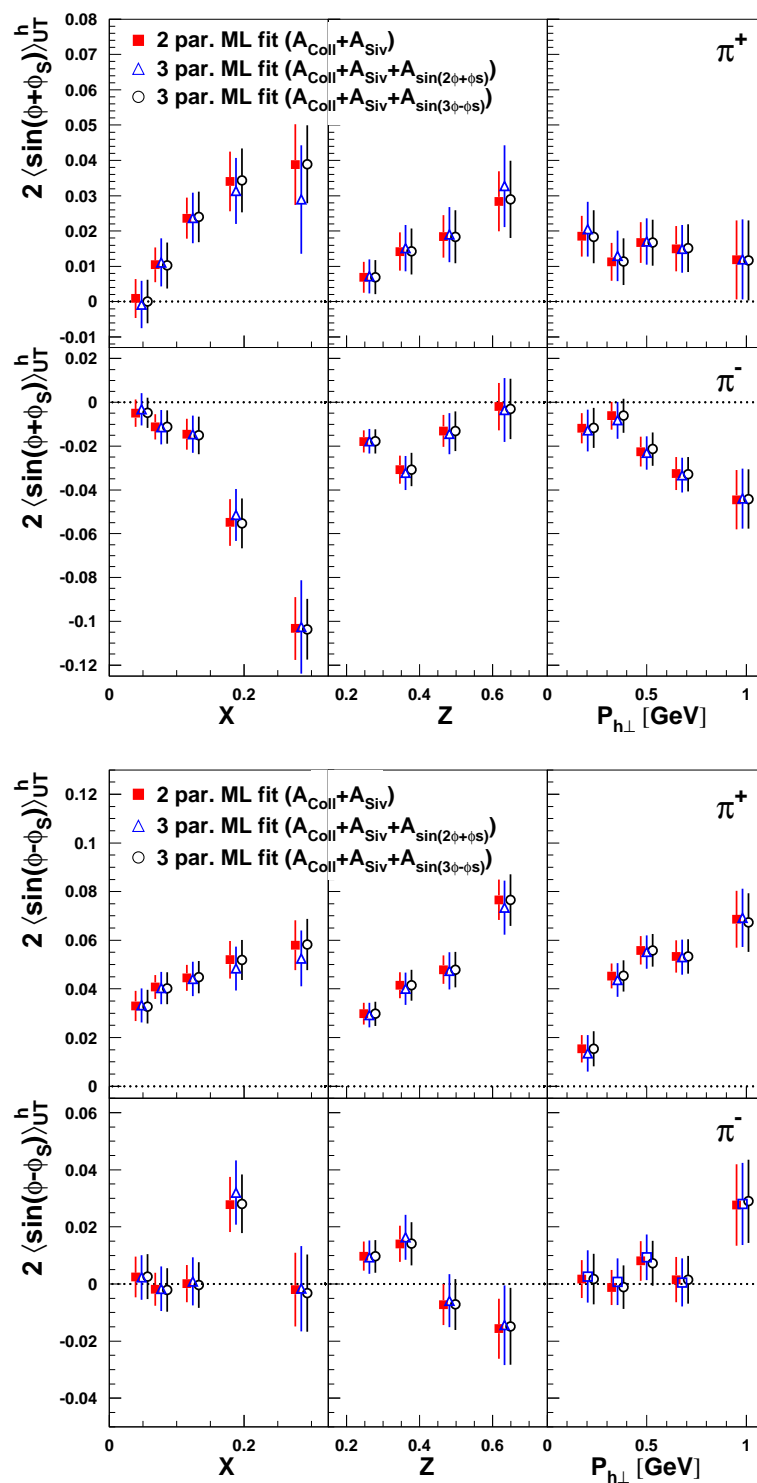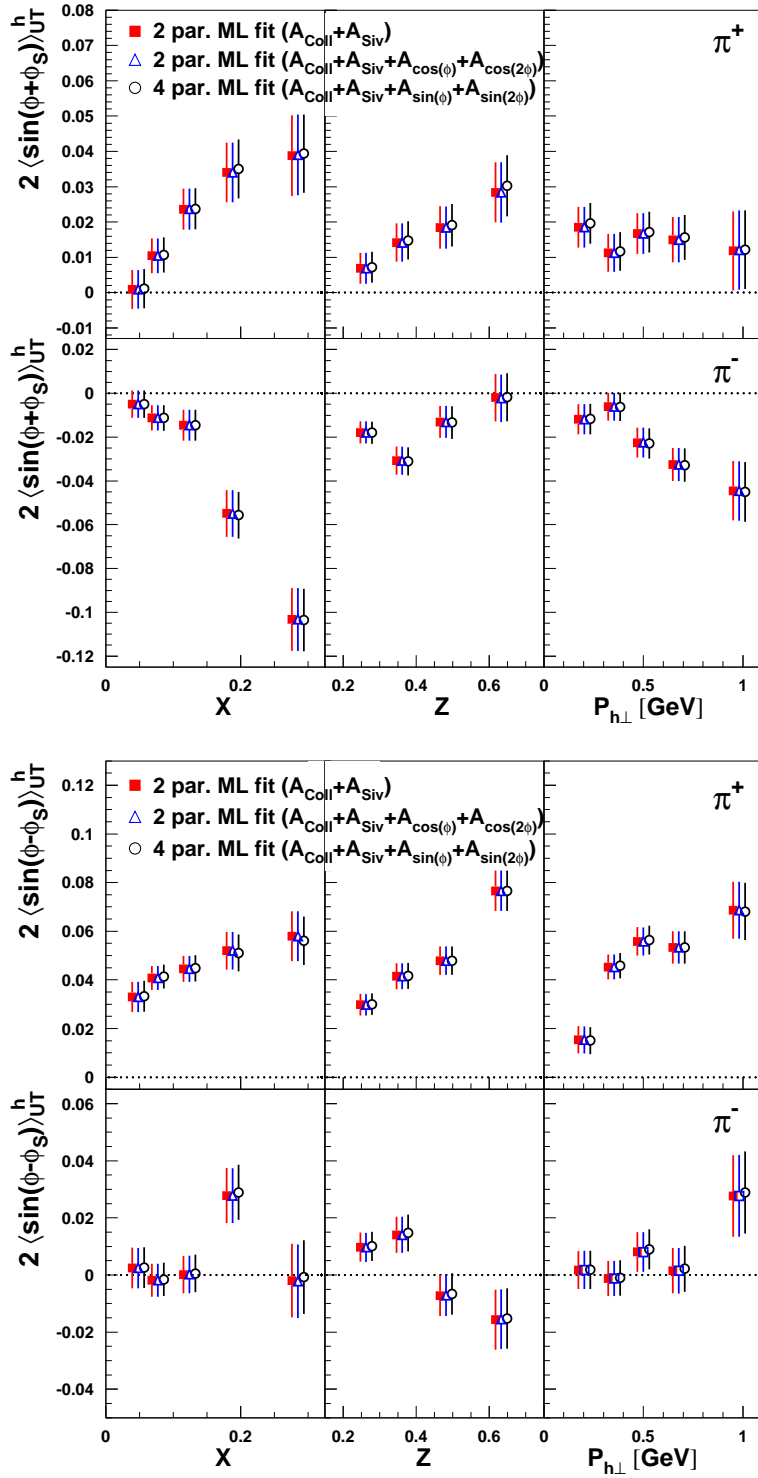Figure 5.11: Unweighted Collins (upper half) and Sivers (lower half) moments for π^+ (upper panels) and π^- (lower panels) extracted with the basic 2-parameters PDF (full squares), compared with those extracted with a 2-parameters PDF including the $\cos(\phi)$ and $\cos(2\phi)$ modulations (open triangles) and with a 4-parameters PDF including the $\sin(\phi)$ and $\sin(2\phi)$ modulations (open circles).

5.5.2 Compatibility of the different Data Taking periods

The Collins and Sivers moments extracted in the present analysis are based on the full transverse target data set, collected over a period of four years (2002-2005). During this long period, changes in the experimental apparatus, e.g. in the efficiencies or in the alignment of the detectors, might have occurred, resulting in a possible influence on the extracted azimuthal moments. The different data productions contain completely different amounts of data. For instance, the statistics collected during the 2005 more than doubles that collected during the previous three years all together (cf. Table 5.4). In addition, during the 2005 data taking, a different lepton beam charge (e^-) was used than in the previous three years (e^+). It is therefore natural to compare the results extracted during the 2002, 2003 and 2004 (data productions $02c0$, $03c0$ and $04c0$, respectively) with those extracted during the 2005 (data production $05c0$)[2].
In order to identify the presence of systematic discrepancies between the azimuthal moments extracted from two different data productions D_1 and D_2, the so-called *deviations* were calculated according to the general formula:

$$\text{Deviations} = \frac{A_{UT}^{sin(\phi \pm \phi_S)}(D_1) - A_{UT}^{sin(\phi \pm \phi_S)}(D_2)}{\sqrt{\sigma^2(D_1) + \sigma^2(D_2)}} \, , \qquad (5.27)$$

where $\sigma(D_i)$ denote the statistical uncertainties. Figures 5.12–5.14 show the deviations as a function of x between the Collins and Sivers moments extracted from the $05c0$ data production and those extracted from the $02c0$, $03c0$ and $04c0$ data productions, respectively.

Figure 5.12: Deviations for the Collins (upper panels) and the Sivers (lower panels) moments extracted from the $02c0$ and $05c0$ data productions.

---

[2]The compatibility among the 2002-2004 data productions was already checked in [Els06].
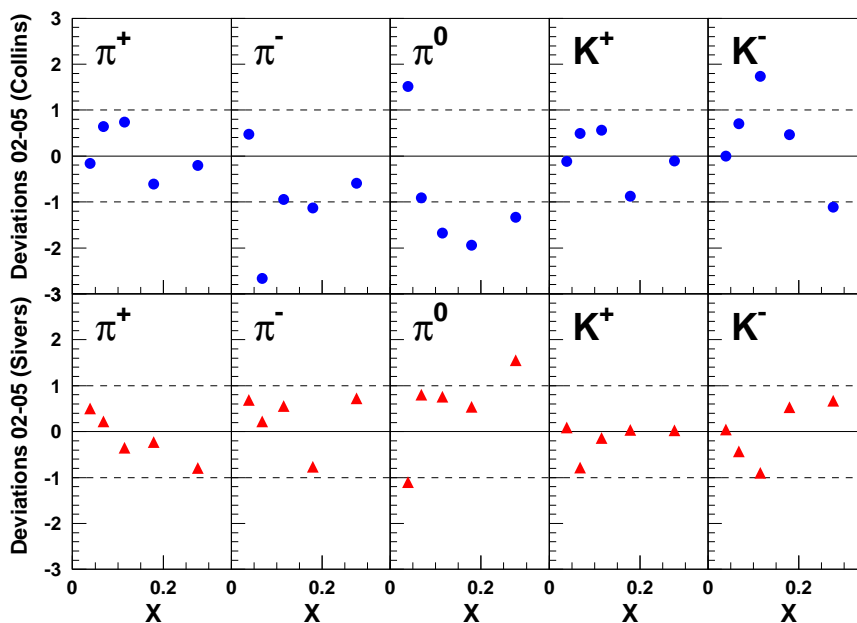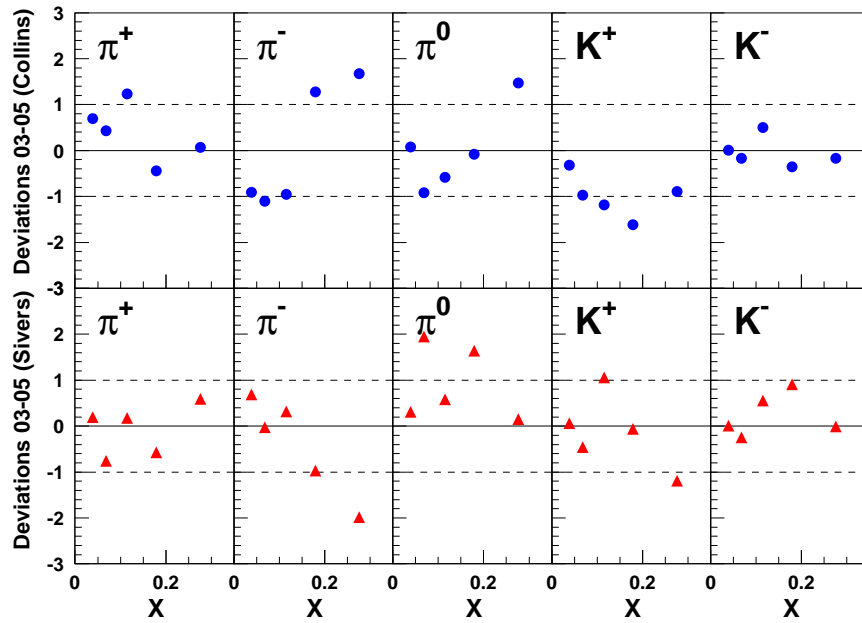
Figure 5.13: Deviations for the Collins (upper panels) and the Sivers (lower panels) moments extracted from the $03c0$ and $05c0$ data productions.
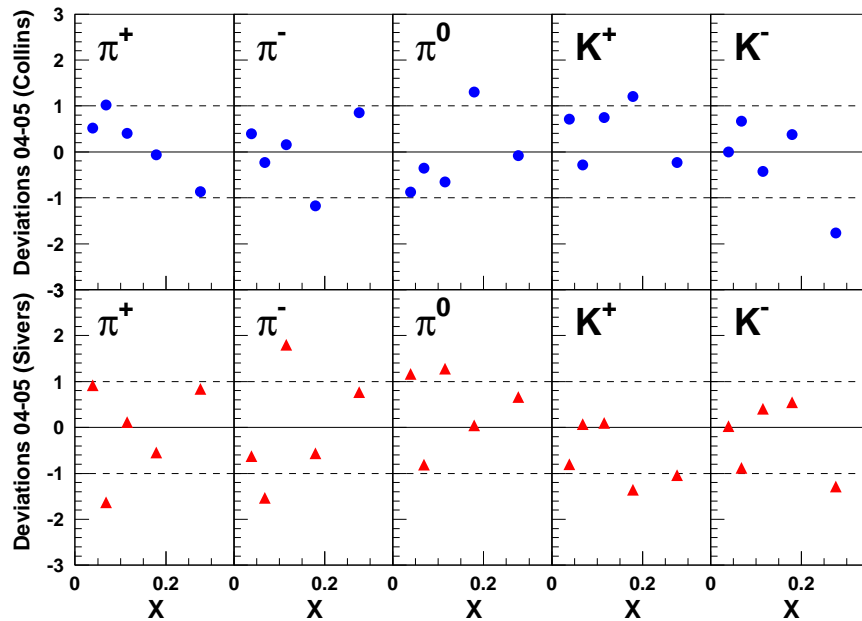

Figure 5.14: Deviations between the Collins and Sivers moments extracted from the two data productions $04c0$ and $05c0$.

In all of the three cases explored above, the deviations fluctuate around zero without showing any systematic shift. In addition, the amplitudes of such fluctuations are smaller than $|\pm 1|$ in most of the cases[3]. As a result, the four data sets considered are compatible within the statistical uncertainty and can be merged together without introducing any systematic bias.

5.5.3 Systematic uncertainties on the hadron identification with the RICH

As discussed in Section 5.3.2, the charged hadrons identification is performed through an unfolding procedure (RICH unfolding) which consists in the extraction of the fluxes of 'true' hadrons from those of the 'identified' hadrons. The extraction (eqn. (5.13)) is based on the use of the inverse $\mathcal{P}$-matrix (5.12), whose elements represent the conditional probabilities $P(h_{id}|h_{true})$ that a given hadron of the true type h_{true} is identified as particle of type h_{id}. It the analysis presented in this thesis, a weight $w_{i,h}$ dependent on the identified hadron type is assigned to each particle track according to the inverse $\mathcal{P}$-matrix (cf. eqn. (5.14)).

To estimate the systematic uncertainty in the true hadron numbers, the Collins and Sivers amplitudes were extracted using three different inverse $\mathcal{P}$-matrices [Hom04]. One is based on a full Monte Carlo simulation of the RICH detector and is considered as the standard choice. Another one is derived using identified hadron (e.g. Λ, ρ^0 and ϕ mesons) decays from the HERMES data[4]. The last is obtained by fitting a set of RICH operating parameters[5] generated by the lepton tracks.

Figures 5.15 and 5.16 show the Collins and Sivers amplitudes for charged pions and koans, respectively, extracted using the three different $\mathcal{P}$-matrices. While basically no differences are observed for the pions, differences are visible for the kaons. These differences will be accounted for as sources of systematic errors (see Section 5.5.8).

5.5.4 Effects of beam polarization

While in 2002 the polarization of the HERA lepton beam was very low, a beam polarization of the order of $30 - 40\%$ was measured in the following years (2003-2005) for both the positive ($\lambda = +1$) and negative ($\lambda = +1$) helicity states. The existence of a net beam polarization gives rise to additional cross section terms which result in additional azimuthal modulations. For instance, at leading twist, a contribution of the $\cos(\phi - \phi_S)$ modulation is expected from the combination of a longitudinally polarized beam and a transversely polarized target (cf. eqn. (3.61)). The asymmetry amplitudes $A_{LT}^{\cos(\phi-\phi_S)}$ of the two helicity states have opposite signs, thus leading to a non zero amplitude if the polarizations of the two beam spin states differ.

In order to study the influence of the beam polarization on the extracted Collins and Sivers moments, the 2003-2005 data sample was splitted into two independent data sets, according to the beam helicity state. The deviations

---

[3]By construction, a deviation of $|\pm 1|$ corresponds to a discrepancy of 1 standard deviation.

[4]This procedure, however, only relies on a limited topology of decay events.

[5]These parameters include the number of PMT hits and the average angles for both the aerogel and the gas rings for $\beta = 1$ particles.

Figure 5.15: Unweighted Collins (upper half) and Sivers (lower half) moments for positive (upper panels) and negative (lower panels) pions, extracted with the three different inverse $\mathcal{P}$-matrices.
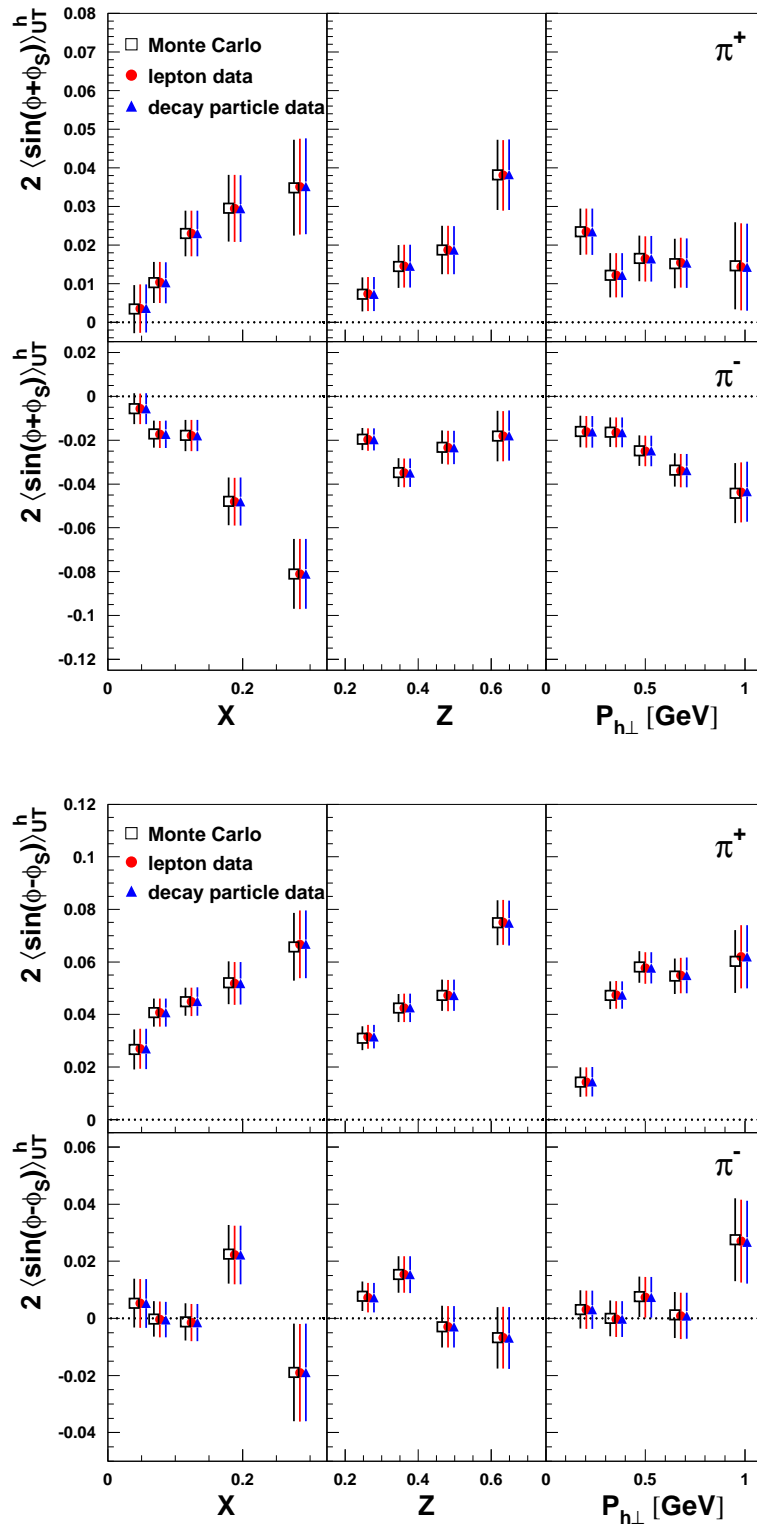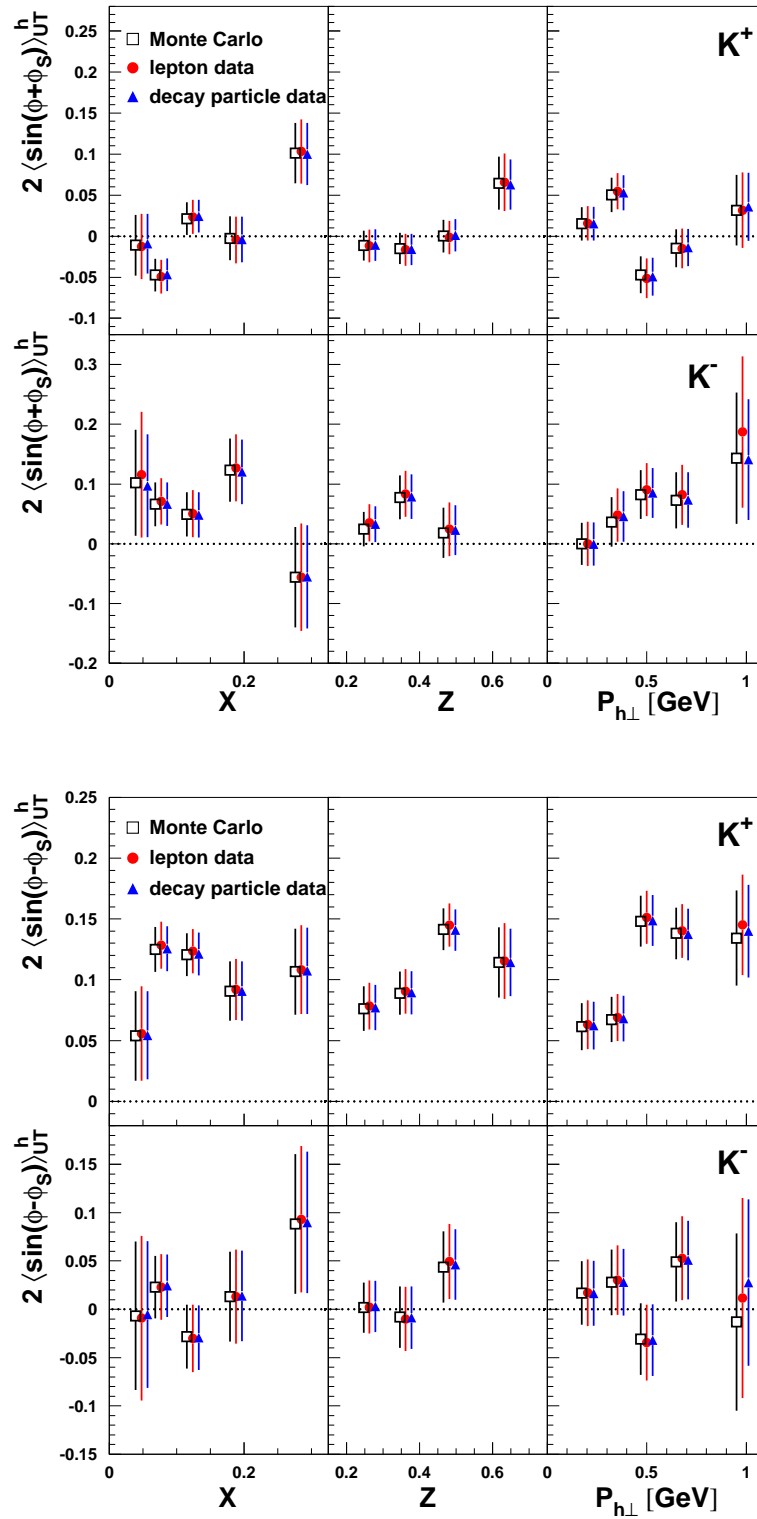
Figure 5.16: Unweighted Collins (upper half) and Sivers (lower half) moments for positive (upper panels) and negative (lower panels) kaons, extracted with the three different inverse $\mathcal{P}$-matrices.

$$\text{Deviations} = \frac{A_{UT}^{\sin(\phi\pm\phi_S)}(\lambda=+1) - A_{UT}^{\sin(\phi\pm\phi_S)}(\lambda=-1)}{\sqrt{\sigma^2(\lambda=+1) + \sigma^2(\lambda=-1)}} \ , \tag{5.28}$$

were calculated for each kinematic bin. As an example, the deviations for the Collins and Sivers moments are reported in Figure 5.17 as a function of x. Similarly to the comparison between the different data taking periods (cf. Section 5.5.2), the deviations fluctuate around zero without showing any systematic shift. This result is compatible with a vanishing net beam polarization. As a consequence, no effort was done to balance the helicity of the two data samples and no systematic error on the Collins and Sivers moments was assigned.
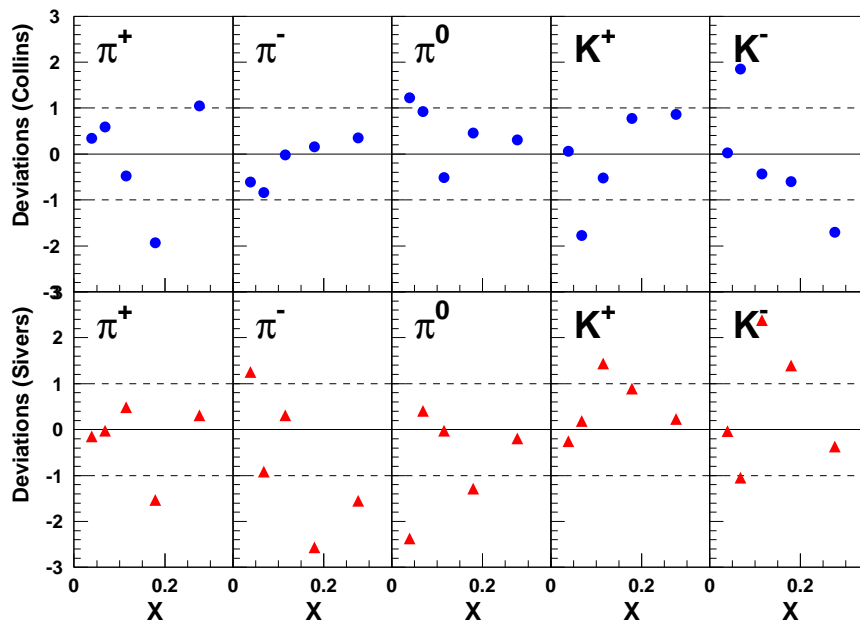
Figure 5.17: Deviations for the Collins (upper panels) and Sivers (lower panels) moments extracted for the two beam helicity states.

5.5.5 The Transverse Magnet Correction methods

As discussed in Section 4.2.5, the target magnet surrounding the storage cell provides a holding field which defines the polarization axis. While a holding field parallel to the lepton beam has no effect on the beam and a marginal effect on the scattered particle trajectories, for a transverse holding field different effects have to be taken into account. Since not only the beam but also the scattered particles are deflected, the reconstructed partial particle tracks in front of the spectrometer magnet do not yield the correct vertex positions and scattering angles when they are extrapolated into the target cell by a straight line.

As discussed in Section 4.3.2, at HERMES two alternative offline Transverse Magnet Correction (TMC) methods were developed [Aug07]. These methods, later referred to as TMC1 and TMC2, are not both available for all the data productions. In particular, concerning the data

productions used in the present analysis, only the TMC2 method is available for 02c0 and only the TMC1 is available for 03c0, while both methods are available for 04c0 and 05c0.

In order to test the compatibility of the two methods, the Collins and Sivers moments were extracted from the merged 04c0 and 05c0 data samples, analyzed with the two different correction methods. The comparison is shown in Figures 5.18 and 5.19 for the unweighted Collins and Sivers moments, respectively. No systematic shifts are observed between the two set of results. As a consequence no systematic error on the Collins and Sivers moments was assigned due to the choice of the transverse magnet correction method.

5.5.6   Fake asymmetries

In order to study the impact of other instrumental effects on the extracted azimuthal moments, fake asymmetry amplitudes were investigated. To this purpose, the data collected during the 2004 period with unpolarized deuterium target, corresponding to roughly one third of the statistics of the 2002-2005 transverse data set, was analyzed. The asymmetry amplitudes were then extracted by assigning the target spin polarization randomly in the interval $[-1; 1]$ and using the standard 6-parameters PDF maximum likelihood fit (cf. eqn. (5.26)).

The results are shown in Figures 5.20 and 5.21. As expected only statistical fluctuations around zero are found for both the $\sin(\phi + \phi_S)$ and $\sin(\phi - \phi_S)$ modulations. The overall amplitudes, obtained integrating over all kinematic variables, were found to be consistent with zero within the statistical uncertainty for both modulations. Therefore no systematic error originating from fake asymmetries was assigned to the Collins and Sivers moments.

5.5.7   Radiative effects

Real photons can be emitted in the scattering process either by the incoming lepton (initial state) or by the scattered lepton (final state). Since these photons carry a certain fraction of the lepton momentum, QED radiative effects influence the event kinematics. In particular, not only the x and Q^2 variables are affected, but also the azimuthal angles ϕ and ϕ_S, since the virtual photon momentum defines the z-axis of the coordinate system in which these angles are calculated (cf. Figure 3.11). As a consequence, in order to restore the correct event kinematics, the momentum of the lepton either before and after the scattering has to be corrected by the momentum of the real photon.

The PHYTIA Monte Carlo generator (cf. Section 6.2) allows to store, for each event, the four-momentum q_{real} of the radiated photon. One can then correct the four-momentum of the virtual photon using the relation: $q_{\mathrm{corr}} = k - k' - q_{\mathrm{real}}$, where k and k' are the four-momenta of the incoming and scattered lepton, respectively.

This approach was adopted in [Els06] to estimate the influence of the radiative effects on the extracted Collins and Sivers amplitudes for charged and neutral pions. Correction factors of the order of a few percent ($< 5\%$) were extracted for each kinematic bin [Els06].

Based on these results, a more conservative approach was used in the present analysis, which consisted in accounting for a global 5% systematic uncertainty due to the radiative effects.
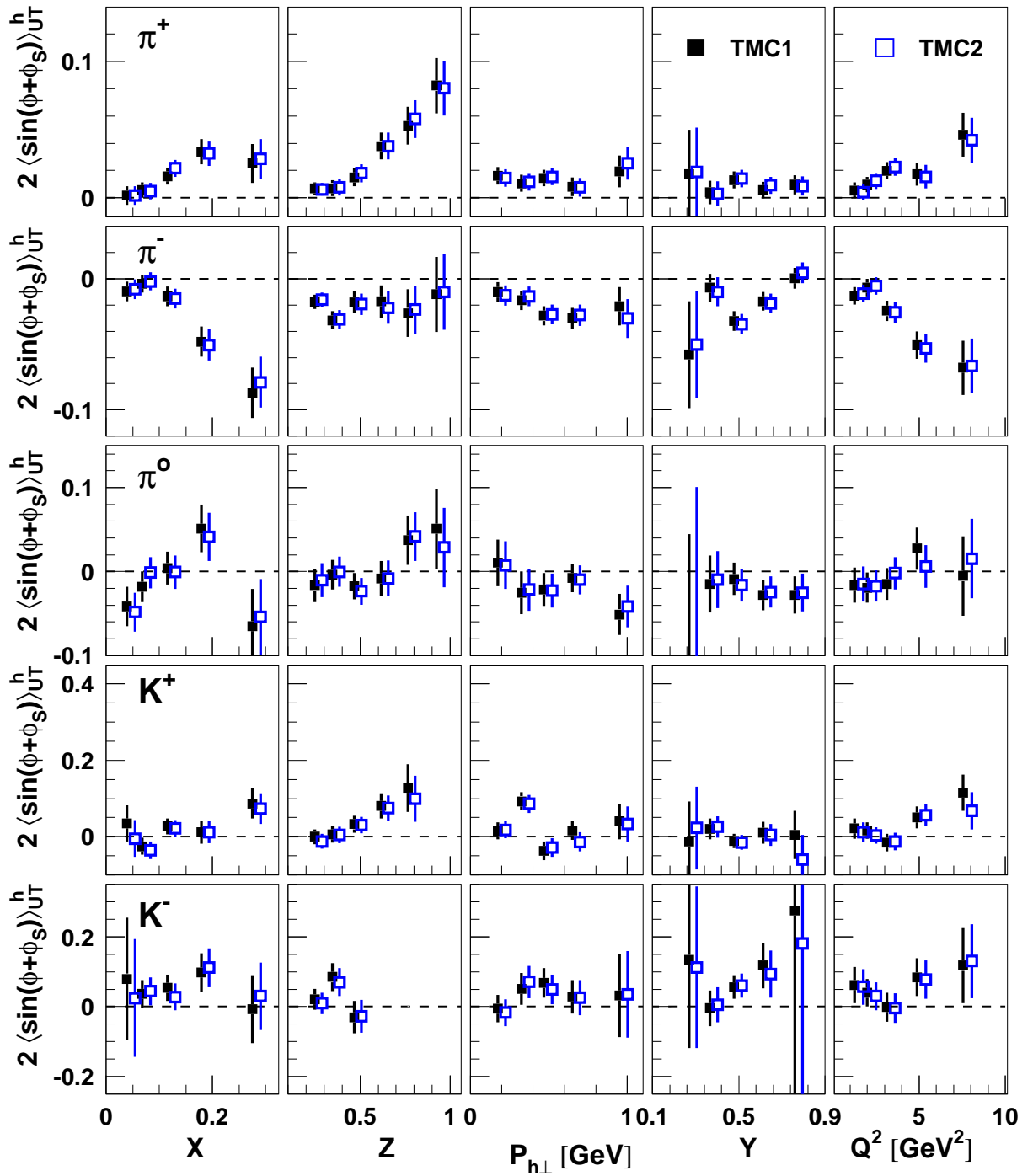
Figure 5.18: Unweighted Collins amplitudes extracted with the standard 6-parameters ML fit (eqn. (5.26)) from the 04c0 and 05c0 transverse data with the two transverse magnet correction methods TMC1 and TMC2.
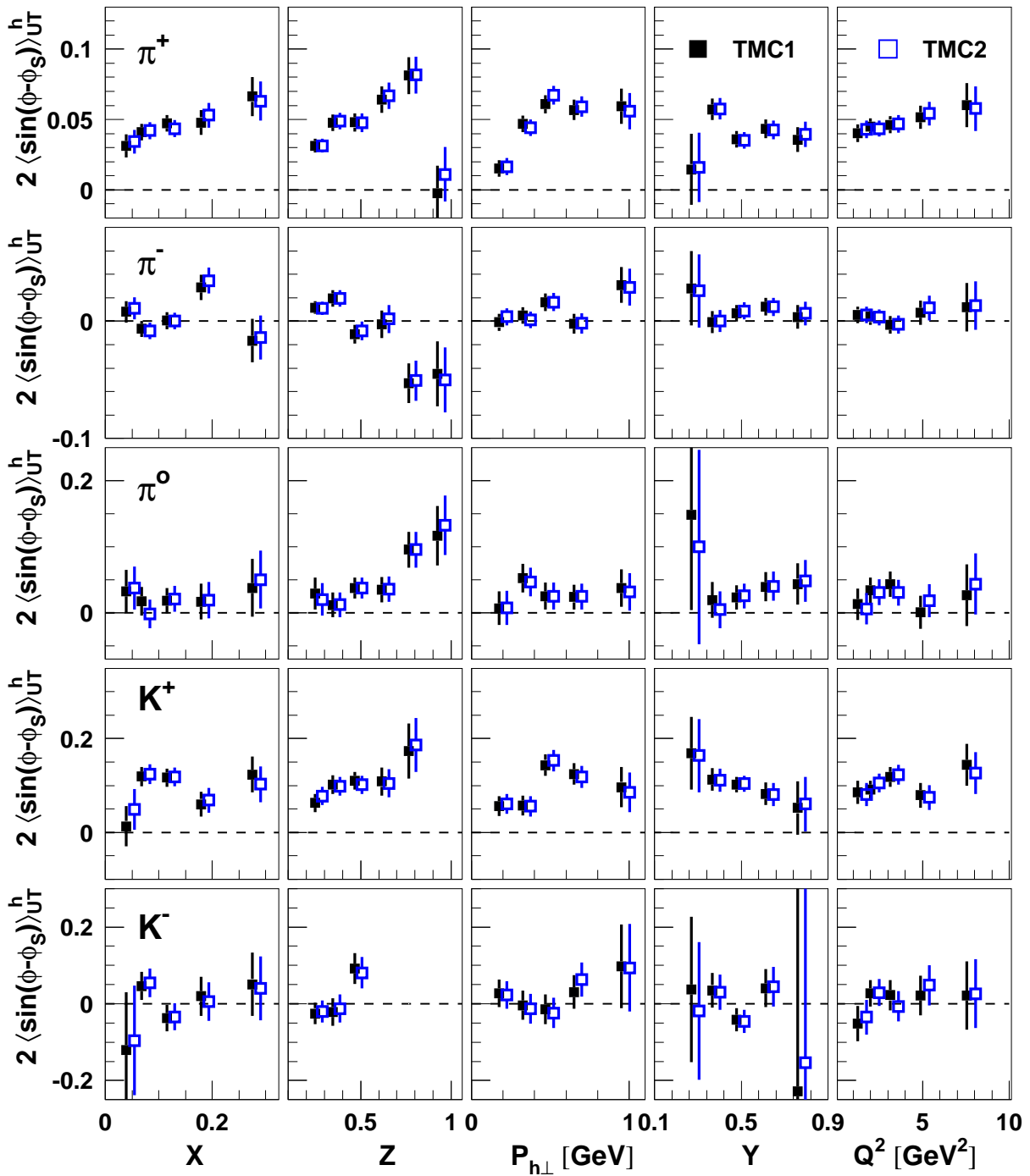
Figure 5.19: Unweighted Sivers amplitudes extracted with the standard 6-parameters ML fit (eqn. (5.26)) from the 04c0 and 05c0 transverse data with the two transverse magnet correction methods TMC1 and TMC2..
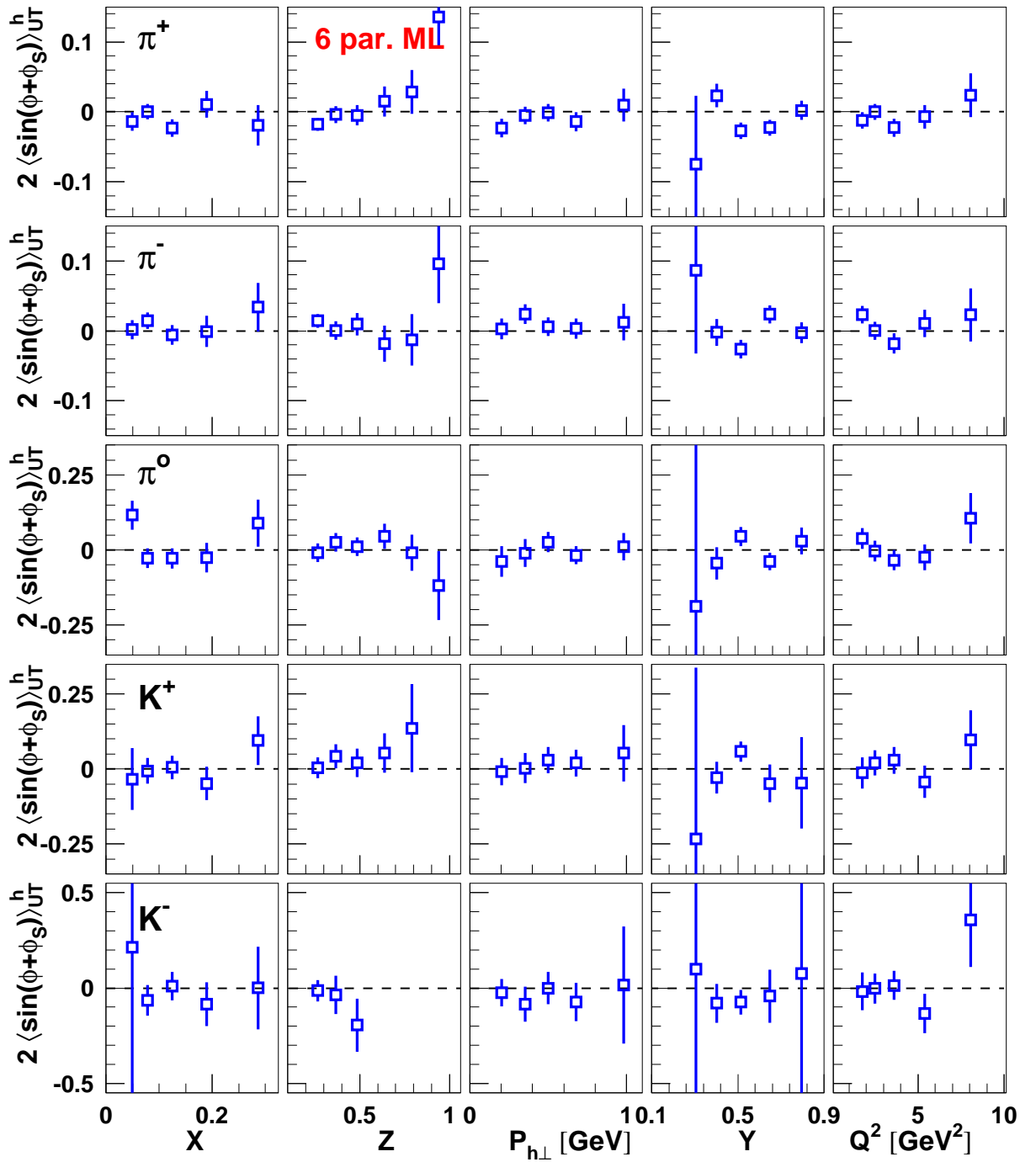
Figure 5.20: Fake Collins asymmetries extracted from the data collected in 2004 with an unpolarized deuterium target. The target polarization was assigned randomly between -1 and 1. The extraction was performed with the standard 6-parameters ML fit (eqn. (5.26)).
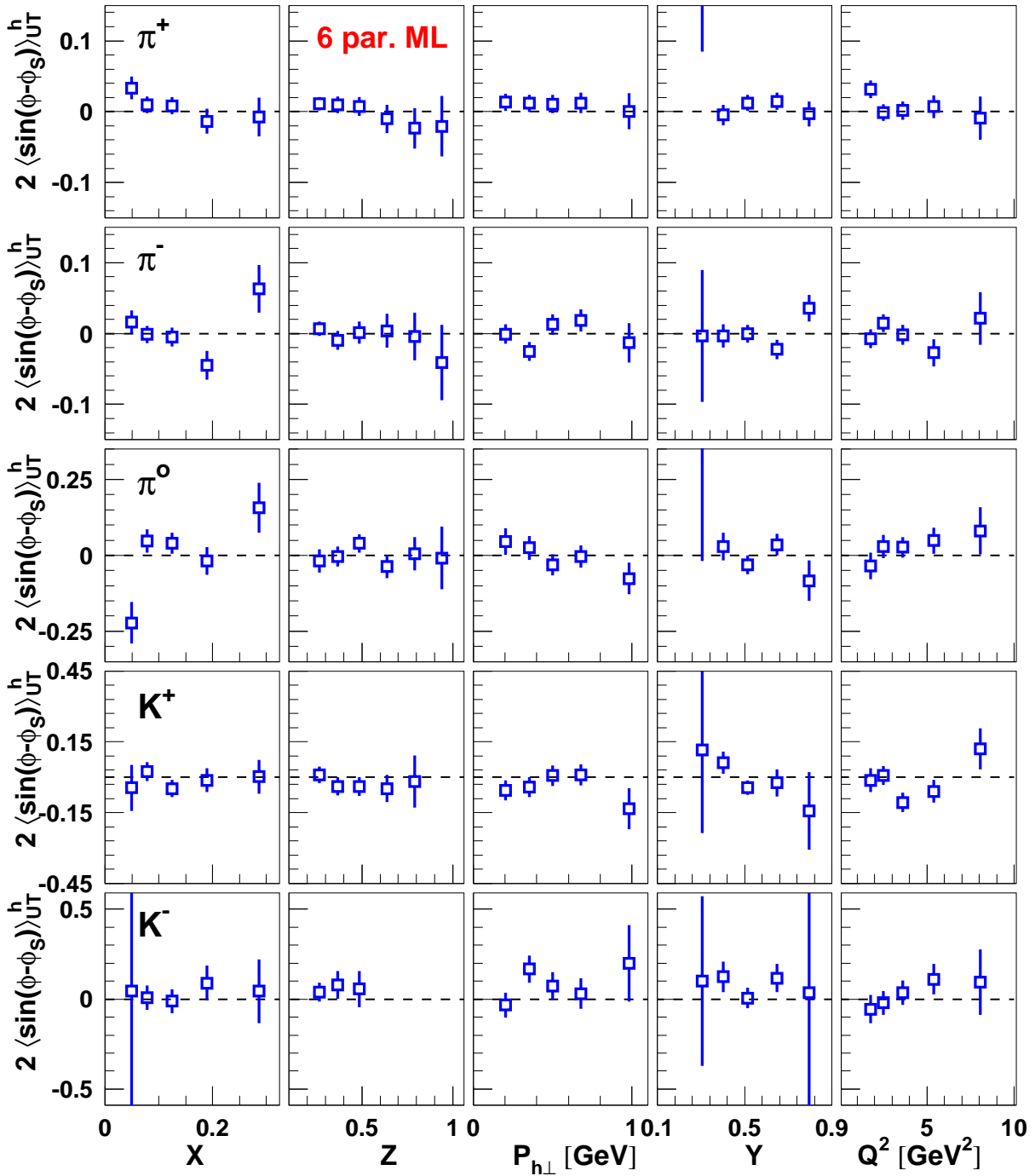
Figure 5.21: Fake Sivers asymmetries extracted from the data collected in 2004 with an unpolarized deuterium target. The target polarization was assigned randomly between -1 and 1. The extraction was performed with the standard 6-parameters ML fit (eqn. (5.26)).

.

5.5.8 Systematic uncertainties: a partial estimation

In the previous sections, three sources of systematic uncertainties were identified for the extracted Collins and Sivers moments:

- Contributions from the azimuthal modulations $\cos(\phi)$ and $\cos(2\phi)$ (from the unpolarized cross section) and $\sin(\phi)$ and $\sin(2\phi)$ (from the cross section terms arising from the longitudinally polarized target) (cf. Section 5.5.1)

- Contributions from the use of three different inverse $\mathcal{P}$-matrices for the hadron identification with the RICH (cf. Section 5.5.3)

- Contribution from QED radiative effects

The three contributions above were summed in quadrature to get an overall systematic uncertainty in each kinematic bin. Figures 5.22 and 5.23 show the Collins and Sivers moments together with the error bands representing the systematic uncertainties included so far. These systematic uncertainties are however only partial. An additional (dominant) contribution, arising form the acceptance studies reported in Chapter 6, has to be taken into account to get the total systematic uncertainty (cf. Section 6.9).

Besides the contributions listed above, another source of systematic error has to be taken into account which arises from the uncertainty in the measurement of the target polarization.
The average transverse target polarization for the data taking periods considered in the present analysis was estimated to be (cf. Table 5.4):

$$\langle P_t \rangle = 0.726 \pm 0.053 \ . \tag{5.29}$$

Since $\langle P_t \rangle$ enters as a global factor in the expression of the target spin asymmetry (cf. eqn. (5.15)), its error generates an overall scale uncertainty on the extracted asymmetries. The scale uncertainty was evaluated as:

$$\mathcal{S}_{Pol} = MAX \left\{ \frac{|A_{\min} - A_{\mathrm{mid}}|}{A_{\mathrm{mid}}} ; \frac{|A_{\max} - A_{\mathrm{mid}}|}{A_{\mathrm{mid}}} \right\} \approx 7.9\% \ , \tag{5.30}$$

where:

$$A_{\mathrm{mid}} = \frac{A}{\langle P_t \rangle} \ ; \qquad A_{\min} = \frac{A}{\langle P_t \rangle + \mathrm{error}} \ ; \qquad A_{\max} = \frac{A}{\langle P_t \rangle - \mathrm{error}} \ , \tag{5.31}$$

and A is the bare cross section asymmetry (eqn. (5.16)). Acting as a global scale uncertainty, i.e. with no kinematic dependence, this contribution was not included in the computation of the systematic errors discussed above.

Figure 5.22: Unweighted Collins amplitudes extracted from the full HERMES transverse data set with the standard 6-parameters ML fit (eqn. (5.26)). The yellow bands represent the systematic errors including the contributions of the $\cos(\phi)$, $\cos(2\phi)$, $\sin(\phi)$ and $\sin(2\phi)$ azimuthal modulations and those due to the choice of the inverse $\mathcal{P}$-matrix for the hadron identification with the RICH.

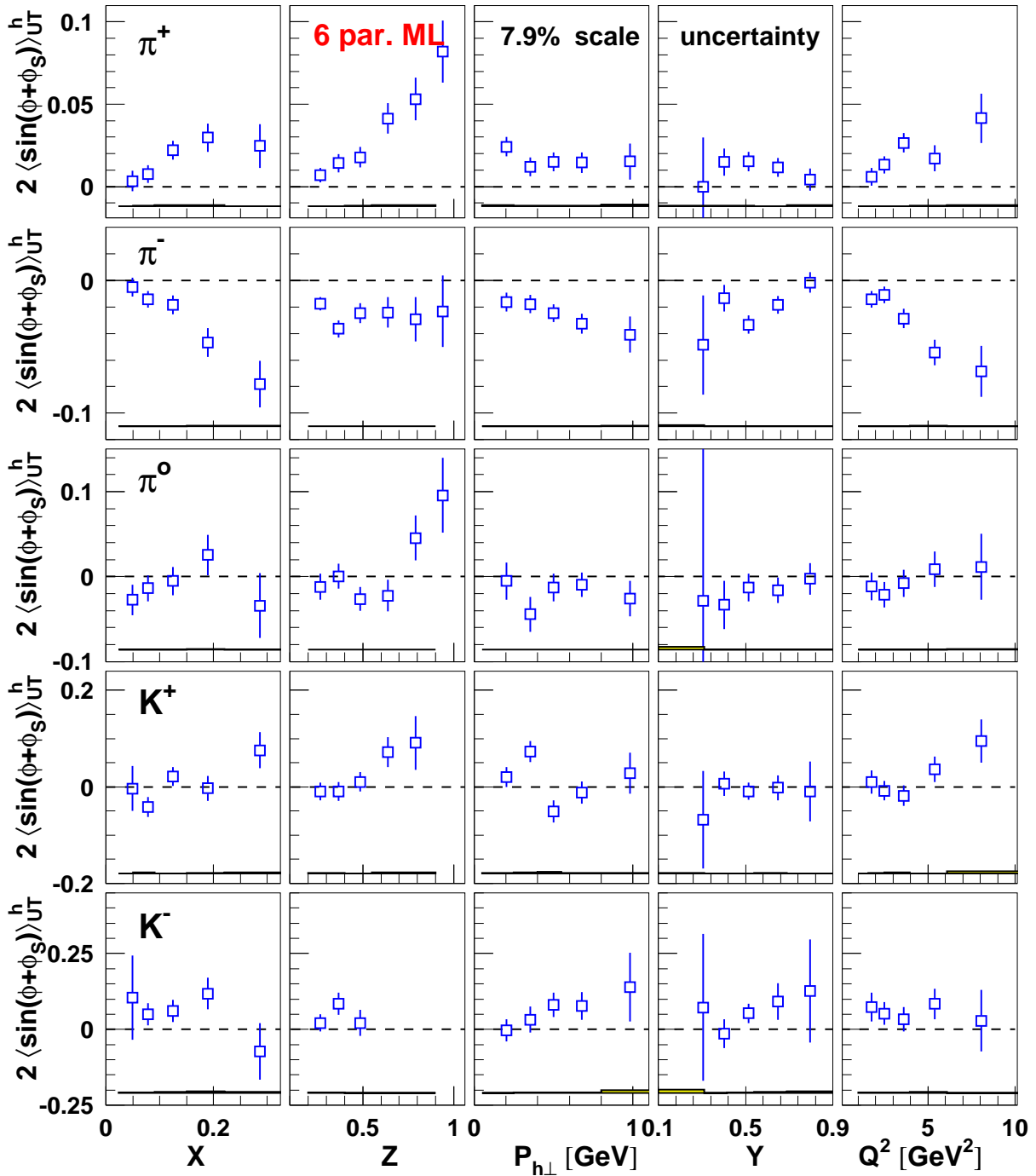Figure 5.23: Unweighted Sivers amplitudes extracted from the full HERMES transverse data set with the standard 6-parameters ML fit (eqn. (5.26)). The yellow bands represent the systematic errors including the contributions of the $\cos(\phi)$, $\cos(2\phi)$, $\sin(\phi)$ and $\sin(2\phi)$ azimuthal modulations and those due to the choice of the inverse $\mathcal{P}$-matrix for the hadron identification with the RICH.
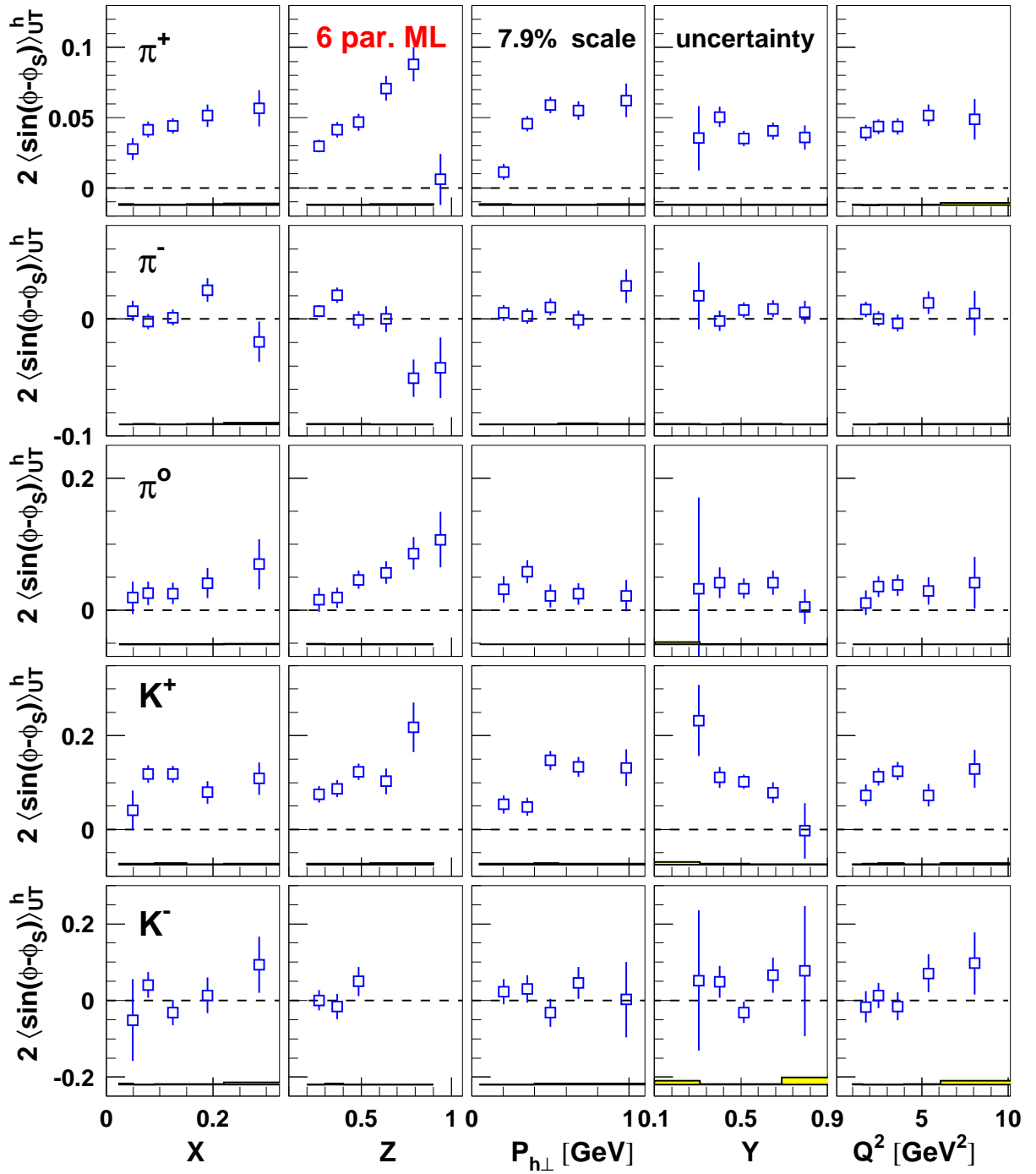
5.6 Isospin relation for the extracted azimuthal moments

An important consistency check for the extracted Collins and Sivers amplitudes consists in the fulfilment of a symmetry relation which reflects the isospin symmetry of the pions triplet. Besides the factorization of the semi-inclusive cross section, the derivation of this relation requires that isospin and charge conjugation symmetry hold in the fragmentation process. One thus only needs to consider the two independent *favored* and *unfavored* fragmentation functions (cf. eqns. (3.52–3.53)) and the following isospin relation between the fragmentation functions:

$$FF^{q\to\pi^0} = \frac{1}{2}(FF^{q\to\pi^+} + FF^{q\to\pi^-}) \,. \tag{5.32}$$

In addition, the reasonable assumption that contributions from the sea quarks are negligible at the HERMES kinematics is required. This assumption is supported by the HERMES results on the longitudinal polarizations for the sea quarks ($\Delta s/s$ and $\Delta\bar{s}/\bar{s}$) [Air05b]. Under these assumptions, the $P_{h\perp}$-weighted Collins and Sivers moments (3.92–3.93) for the three pion types can be written in the form:

$$\left\langle \frac{P_{h\perp}}{zM_{\pi^+}} \sin(\phi+\phi_S) \right\rangle_{UT}^{\pi^+} = \mathcal{K}_C \frac{(4\delta u + \delta\bar{d})H_{1,\text{fav}}^{\perp(1)} + (\delta d + 4\delta\bar{u})H_{1,\text{unfav}}^{\perp(1)}}{(4u+\bar{d})D_{1,\text{fav}} + (d+4\bar{u})D_{1,\text{unfav}}} \tag{5.33}$$

$$\left\langle \frac{P_{h\perp}}{zM_{\pi^-}} \sin(\phi+\phi_S) \right\rangle_{UT}^{\pi^-} = \mathcal{K}_C \frac{(4\delta u + \delta\bar{d})H_{1,\text{unfav}}^{\perp(1)} + (\delta d + 4\delta\bar{u})H_{1,\text{fav}}^{\perp(1)}}{(4u+\bar{d})D_{1,\text{unfav}} + (d+4\bar{u})D_{1,\text{fav}}} \,, \tag{5.34}$$

$$\left\langle \frac{P_{h\perp}}{zM_{\pi^0}} \sin(\phi+\phi_S) \right\rangle_{UT}^{\pi^0} = \mathcal{K}_C \frac{(4\delta u + \delta\bar{d} + \delta d + 4\delta\bar{u})(H_{1,\text{fav}}^{\perp(1)} + H_{1,\text{unfav}}^{\perp(1)})}{(4u+\bar{d}+d+4\bar{u})(D_{1,\text{fav}} + D_{1,\text{unfav}})} \,, \tag{5.35}$$

$$\left\langle \frac{P_{h\perp}}{zM} \sin(\phi-\phi_S) \right\rangle_{UT}^{\pi^+} = \mathcal{K}_S \frac{(4f_{1T}^{\perp(1)u} + f_{1T}^{\perp(1)\bar{d}})D_{1,\text{fav}} + (f_{1T}^{\perp(1)d} + 4f_{1T}^{\perp(1)\bar{u}})D_{1,\text{unfav}}}{(4u+\bar{d})D_{1,\text{fav}} + (d+4\bar{u})D_{1,\text{unfav}}} \,, \tag{5.36}$$

$$\left\langle \frac{P_{h\perp}}{zM} \sin(\phi-\phi_S) \right\rangle_{UT}^{\pi^-} = \mathcal{K}_S \frac{(4f_{1T}^{\perp(1)u} + f_{1T}^{\perp(1)\bar{d}})D_{1,\text{unfav}} + (f_{1T}^{\perp(1)d} + 4f_{1T}^{\perp(1)\bar{u}})D_{1,\text{fav}}}{(4u+\bar{d})D_{1,\text{unfav}} + (d+4\bar{u})D_{1,\text{fav}}} \,, \tag{5.37}$$

$$\left\langle \frac{P_{h\perp}}{zM} \sin(\phi-\phi_S) \right\rangle_{UT}^{\pi^0} = \mathcal{K}_S \frac{(4f_{1T}^{\perp(1)u} + f_{1T}^{\perp(1)\bar{d}} + f_{1T}^{\perp(1)d} + 4f_{1T}^{\perp(1)\bar{u}})(D_{1,\text{fav}} + D_{1,\text{unfav}})}{(4u+\bar{d}+d+4\bar{u})(D_{1,\text{fav}} + D_{1,\text{unfav}})} \,, \tag{5.38}$$

where $\mathcal{K}_C$ and $\mathcal{K}_S$ are kinematic factors common to all the Collins and Sivers moments, respectively. Combining eqns. (5.33–5.35), the following *Isospin Relation* (IR) results for the $P_{h\perp}$-weighted Collins moments [Mak03]:

$$IR^{P_{h\perp}/zM_h \cdot sin(\phi+\phi_S)} \equiv \left\langle \frac{P_{h\perp}}{zM_{\pi^+}} \sin(\phi+\phi_S) \right\rangle_{UT}^{\pi^+} + C \left\langle \frac{P_{h\perp}}{zM_{\pi^-}} \sin(\phi+\phi_S) \right\rangle_{UT}^{\pi^-} -$$

$$(1+C)\left\langle \frac{P_{h\perp}}{zM_{\pi^0}} \sin(\phi+\phi_S) \right\rangle_{UT}^{\pi^0} = 0 \, . \tag{5.39}$$

The coefficient C arises from the spin-independent distribution and fragmentation functions appearing in eqns. (5.33)–(5.35) and can be expressed in the compact form

$$C = \frac{4\eta+r}{4+r\eta} \, , \tag{5.40}$$

where

$$r = \frac{d+4\bar{u}}{u+\frac{1}{4}\bar{d}} \qquad \text{and} \qquad \eta = \frac{D_{1,\text{unfav}}}{D_{1,\text{fav}}} \, . \tag{5.41}$$

A similar IR exists for the Sivers moments, which can be derived combining eqns. (5.36)–(5.38):

$$IR^{P_{h\perp}/zM \cdot sin(\phi-\phi_S)} \equiv \left\langle \frac{P_{h\perp}}{zM} \sin(\phi-\phi_S) \right\rangle_{UT}^{\pi^+} + C \left\langle \frac{P_{h\perp}}{zM} \sin(\phi-\phi_S) \right\rangle_{UT}^{\pi^-} -$$

$$(1+C)\left\langle \frac{P_{h\perp}}{zM} \sin(\phi-\phi_S) \right\rangle_{UT}^{\pi^0} = 0 \, . \tag{5.42}$$

The validity of the IR is unaffected by a convolution integral over the transverse quark and pion momenta. As a consequence, it also holds for the unweighted Collins and Sivers moments:

$$IR^{sin(\phi\pm\phi_S)} \equiv \langle \sin(\phi\pm\phi_S) \rangle_{UT}^{\pi^+} + C \, \langle \sin(\phi\pm\phi_S) \rangle_{UT}^{\pi^-} - (1+C)\langle \sin(\phi\pm\phi_S) \rangle_{UT}^{\pi^0} = 0 \, . \tag{5.43}$$

More in general, it has been shown [Die05b] that the isospin symmetry relation is valid for any single-spin or double-spin asymmetry in semi-inclusive DIS at twist-two and twist-three and in leading and next-to-leading order in α_s when the coefficient C (5.40) is replaced by the unpolarized cross section ratio for semi-inclusive negative and positive pion production:

$$C = \sigma_{UU}^{\pi^-}/\sigma_{UU}^{\pi^+} \, . \tag{5.44}$$

In the present analysis the coefficient C was extracted using the mean values of the multiplicities M for positive and negative pions measured on a proton target at HERMES[6]:

$$C \approx \langle M \rangle^{\pi^-}/\langle M \rangle^{\pi^+} = 0.723 \pm 0.005 \, . \tag{5.45}$$

---

[6]These multiplicities are corrected for the smearing and radiative effects and for the contribution from exclusively produced vector mesons [Hil05].

For the calculation of the Isospin Relation, the averaged Collins and Sivers moments extracted with the 2-parameters ML fit (cf. eqn. (5.24)) were used, yielding:

$$IR^{\sin(\phi+\phi_S)} = 0.0045 \pm 0.0064 \,, \tag{5.46}$$

$$IR^{\sin(\phi-\phi_S)} = 0.0016 \pm 0.0066 \,, \tag{5.47}$$

where only statistical uncertainties were taken into account. As shown in Figure 5.24, the IR is fulfilled within the statistical uncertainty for both the Collins and Sivers moments.
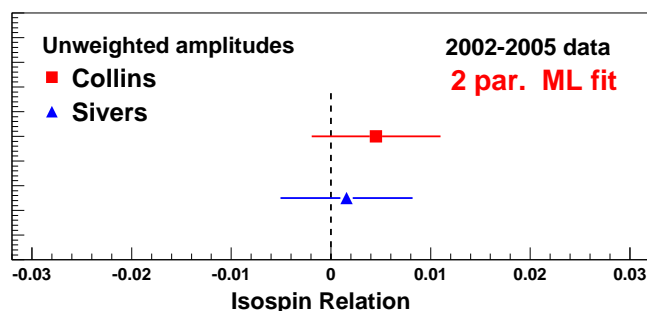
Figure 5.24: Isospin Relation for unweighted Collins and Sivers moments integrated over the full kinematic range.

The Isospin Relation can also be evaluated in the individual kinematic bins. The kinematic dependence of the IR for both the unweighted Collins and Sivers moments is shown in Figure 5.25. Reflecting the values obtained with the overall moments, the values of the Isospin Relation are compatible with zero for both the unweighted Collins and Sivers moments.
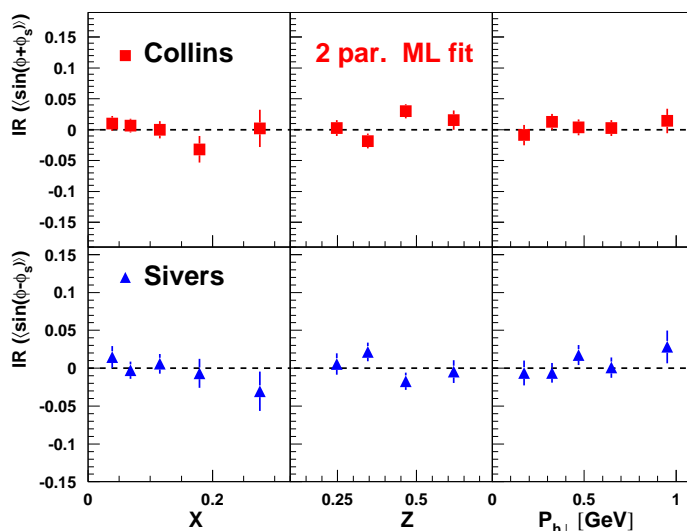
Figure 5.25: Isospin Relation for unweighted Collins and Sivers moments as a function of x, z and $P_{h\perp}$.

The IR was also studied for the $P_{h\perp}$-weighted moments (cf. eqns. (5.39) and (5.42)). The results for the Collins and Sivers moments integrated over the full kinematic range are listed below and shown in Figure 5.26):

$$IR^{P_{h\perp}/zM_h \sin(\phi+\phi_S)} = 0.0915 \pm 0.0494 \tag{5.48}$$

$$IR^{P_{h\perp}/zM \sin(\phi-\phi_S)} = 0.0018 \pm 0.0073 \; . \tag{5.49}$$

A fair fulfillment is obersved for the Sivers moments while a deviation of less than 2σ is observed for the Collins moments. The results in the different kinematic bins are shown in Figure 5.27.

Figure 5.26: Isospin Relation for the $P_{h\perp}$-weighted Collins and Sivers moments integrated over the full kinematic range.

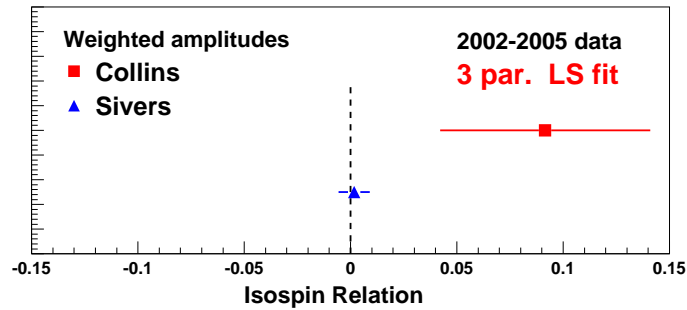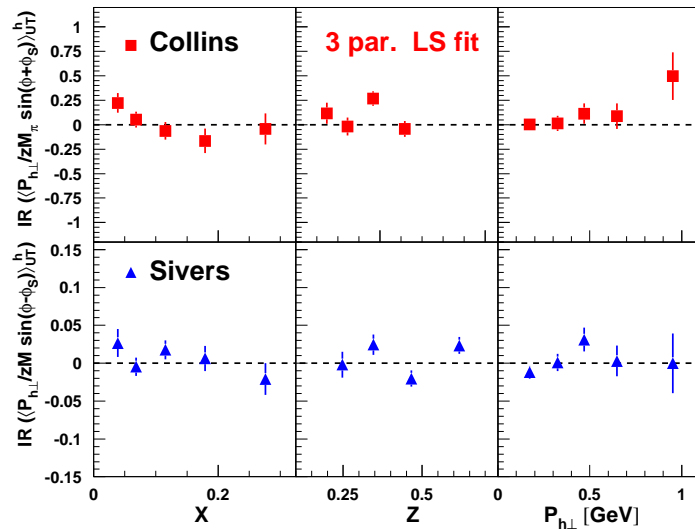
Figure 5.27: Isospin Relation for $P_{h\perp}$-weighted Collins and Sivers moments as a function of x, z and $P_{h\perp}$.

5.7 The contributions from exclusively produced vector mesons

In deep inelastic scattering, the incoming lepton interacts with a quark of the nucleon through a virtual photon exchange. The virtual photon, however, can also fluctuate into a quark-antiquark pair. This pair can live long enough to develop into a hadronic state which then interacts with the nucleon. This interaction between the hadronic component of the photon and the nucleon can only be described phenomenologically in terms of models for hadron-hadron interactions. One such model is the well known Vector Meson Dominance (VMD) model [Sak69], which describes successfully the experimental data over a wide energy range. In this model, the hadronic component of the photon is interpreted in terms of fluctuations into the vector mesons ρ^0, ω and ϕ, carrying the same quantum numbers as the photon. The scattering process then factorizes into the coupling of the virtual photon to the vector meson and the interaction of the vector meson with the nucleon. This model is implemented in the PYTHIA Monte Carlo generator (cf. Section 6.2).

The pion and the kaon samples of semi inclusive deep inelastic scattering events detected at HERMES contain decay particles of exclusively produced vector mesons. For the interpretation of the measured azimuthal moments in terms of quark distributions and fragmentation functions, these events might be considered as background contributions. These contributions, however, cannot be excluded entirely from the analysis since, due to the limited acceptance of the spectrometer, not all the decay particles produced in these events are observed.

Regarding the decay particles of exclusive vector mesons as background contributions to the semi inclusive DIS sample, one can, in principle, correct the measured asymmetry amplitudes A_{meas} using the relation:

$$A_{\text{corr}} = \frac{N_{\text{tot}}}{N_{\text{sig}}} A_{\text{meas}} - \frac{N_{VM}}{N_{\text{sig}}} A_{VM \to h} = \frac{1}{1 - f_{VM}} A_{\text{meas}} - \frac{f_{VM}}{1 - f_{VM}} A_{VM \to h} \ . \qquad (5.50)$$

Here f_{VM} is the vector meson fraction, defined as the ratio between the number of hadrons from vector meson decays N_{VM} and the total number of hadrons N_{tot}, and N_{sig} denotes the difference between N_{tot} and N_{VM}. Two different sources contribute to the amplitude $A_{VM \to h}$ of the decay particles: any Collins or Sivers like asymmetry amplitude A_{VM} in the vector mesons production partially transferred to the hadron, and a spurious asymmetry in the detected hadrons, introduced by the decay angular distributions. In general, the asymmetry amplitudes of the decay particles can be expressed as:

$$A_{VM \to h} = T \cdot A_{VM} + A_{\text{decay}} \ , \qquad (5.51)$$

where T denotes a transfer coefficient which describes how much of the vector meson asymmetry amplitude is transferred to its decay particles. For a correction of the measured asymmetries one thus needs four quantities: the vector meson fraction f_{VM}, the transfer coefficient T, the asymmetry amplitude A_{VM} of the exclusively produced vector mesons, and the asymmetry amplitude A_{decay} acquired in the decay process. An intense work has been done in [Els06] to extract these four quantities.

The total (i.e. including the contributions from ρ^0, ω and ϕ) fractions of pions and charged kaons produced in vector meson decays simulatated by the PYTHIA Monte Carlo tuned to the HERMES kinematics, are shown, as a function of x, z and $P_{h\perp}$, in Figure 5.28.
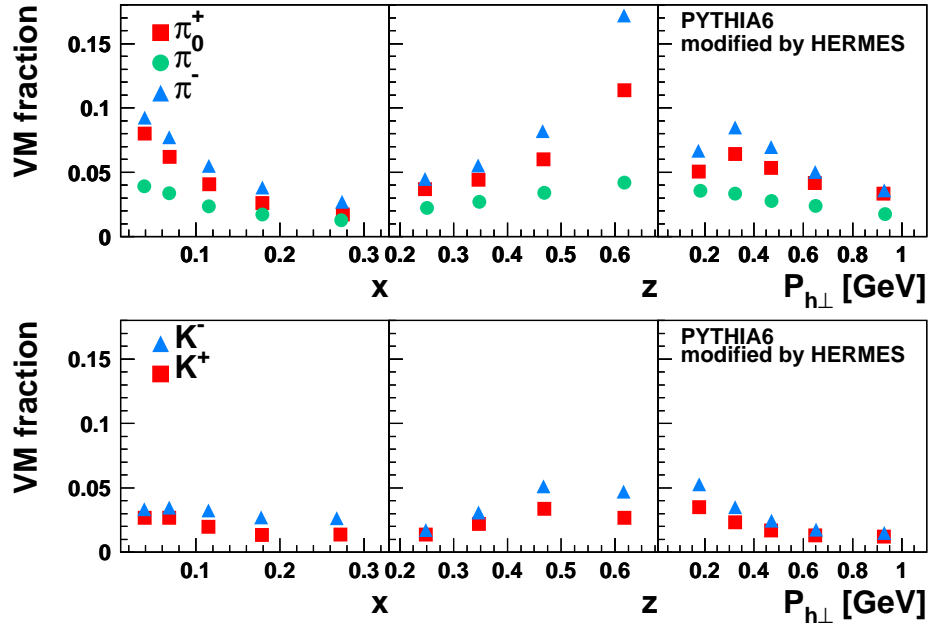
Figure 5.28: Fraction of pions (upper panel) and charged kaons (lower panel) produced in vector meson decays simulated by PYTHIA.

An increase of the vector meson fractions with decreasing x is observed for all hadron types. The fractions, which are dominated by exclusive ρ^0 decays, also increase with increasing z, reaching values of about 50% for $z > 0.7$. This is the reason why the higher z region was limited by the cut $0.2 < z < 0.7$ (cf. Section 5.3.3). Except for the higher z region, the fractions stay below 10% for charged pions, and below 5% for neutral pions and charged kaons.

The decay particles from exclusive vector mesons are expected to influence the extracted Collins and Sivers amplitudes. With the help of Monte Carlo simulations, the transfer coefficients T for charged pions coming from exclusive ρ^0 decays, and for neutral pions coming from exclusive ω decays, were determined in [Els06]. In addition, Collins and Sivers like asymmetries were extracted from the HERMES data for both exclusive ρ^0 mesons and their decay pions. In both cases the obtained amplitudes were found to be statistically consistent with zero. Furthermore, significantly positive amplitudes were extracted from azimuthal asymmetry in the yield difference of positive and negative pions, which has no contribution from exclusive vector mesons [Els06]. All these studies led to the conclusion that one can safely assume that exclusively produced vector mesons do not significantly affect the extracted Collins and Sivers amplitudes. This assumption is also supported by the fulfillment of the Isospin Relation, shown in Section 5.6.

Chapter 6

Monte Carlo studies

Due to the complexity of the experimental apparatus and of the physics processes involved, Monte Carlo simulations represent nowadays an indispensable tool in nuclear and high energy physics. Based on models and parameterizations, they allow to simulate, on a statistical basis, many aspects that can not be calculated in an analytical way and that are necessary for a complete understanding of the physical problems under study. For the analysis presented in this thesis, Monte Carlo simulations were used to estimate the impact of the limited resolution and geometrical acceptance of the HERMES detector on the measured asymmetry amplitudes.

6.1   The HERMES Monte Carlo Implementation

The HERMES Monte Carlo consists in a chain of programs that are operated in the order described in Figure 4.24. The chain starts with a physics generator, built within a general framework called GMC (Generator Monte Carlo). Several event generators are available which are suitable to simulate different aspects of the HERMES physics (exclusive processes, deeply virtual Compton scattering, transversity, etc). Usually, the generated events come with a weight W_j^{MC} which is needed to reproduce the cross section correctly. The effective number of events N_{MC} is then given by $N_{MC} = \sum_{j=1}^{N_{gen}} W_j^{MC}$, where N_{gen} is the number of generated events.

For a reasonable comparison with experimental data, further effects have to be simulated which are inevitably introduced by the measuring process. First of all, due to the limited acceptance of the spectrometer, only a fraction of the produced particles traverse the active area of the detector. These particles interact with the detector material before their kinematic properties are measured. As a result, the original energies and angles of the tracks are affected. In addition, one has also to take into account the intrinsic inefficiencies of the detector, like the limited detector resolution, misidentification of the different particle types, etc.

All these effects are simulated by a program called HERMES Monte Carlo (HMC), which contains a model of the HERMES apparatus based on GEANT3 [Bru84]. For each particle, the transition through the detector is simulated taking into account the interaction with the materials it traverses. The HMC produces a response function which is very similar to that for the real data, except that it contains additional Monte Carlo information such as the particle type and

the originally generated particle kinematics.

Alternatively, one can use the much faster HERMES Smearing Generator (HSG) [Hil05], which, being based on a parametrization of all smearing and acceptance effects of the detector, does not require the time consuming full track reconstruction through the detector materials. HSG makes use of the momentum resolution and of the resolution of the scattering angles θ_x and θ_y obtained from a fully tracked Monte Carlo production, to smear the kinematics of the generated tracks on a statistical basis. It also applies some acceptance cuts based on lookup tables for the bending into the magnet field. The HMC and HSG outputs are fed directly into the HERMES Reconstruction program (HRC), which determines the particle momenta from the bending in the magnet by matching the back and the front part of each track. It is important to note that this is exactly the same program used for the reconstruction of the real data. Since the event reconstruction is identical for both experiment and simulation, all possible biases introduced at this stage are automatically accounted for. Once the track information is available, a DST file very similar to that produced by the experimental data processing chain is written.

6.2 The PYTHIA Monte Carlo generator

PYTHIA [Sjo03] is a general purpose Monte Carlo generator for high energy physics. It contains a model of soft (non perturbative) as well as perturbative deeply inelastic scattering process and spans the whole region from real and quasi-real photoproduction (very low Q^2) to high Q^2 DIS. PYTHIA also includes a model for the semi-inclusive cross section. In particular, for the hadron fragmentation it makes use of the LUND string-fragmentation model [And83, And97] (cf. Section 3.7). The events generated by PYTHIA are processed by the HERMES Monte Carlo (HMC) for the track reconstruction. The PYTHIA default settings, mostly determined from e^+e^- data, do not describe the HERMES data sufficiently well. Therefore the parameters involved in the description of the cross sections implemented in PYTHIA were tuned to the HERMES kinematics to reproduce the measured multiplicities [Lie04]. Figure 6.1 shows the distributions of selected DIS and SIDIS kinematic variables obtained from real events and from events generated by PYTHIA. The comparison reveals a very good agreement.

In the present analysis, the PYTHIA generator was used to generate a sample of events according to the Born (spin-independent) cross section. As described in Section 6.5.1, the latter was used to project in 4π the Collins and Sivers moments extracted within the HERMES acceptance.

6.3 The GMC_TRANS Monte Carlo generator

Since HERMES is not a 4π detector, and thus can not cover the full $\phi - \phi_S$ plane (see Figure 5.6), acceptance effects might affect the extraction of the azimuthal (e.g. Collins and Sivers) moments. Moreover, in order to solve the convolution integrals in eqns. (3.86) and (3.87), one needs in principle to integrate over the whole range of transverse momentum. However this is experimentally not possible. A new Monte Carlo generator, called GMC_TRANS, was developed in order to simulate azimuthal distributions due to intrinsic transverse quark momenta and
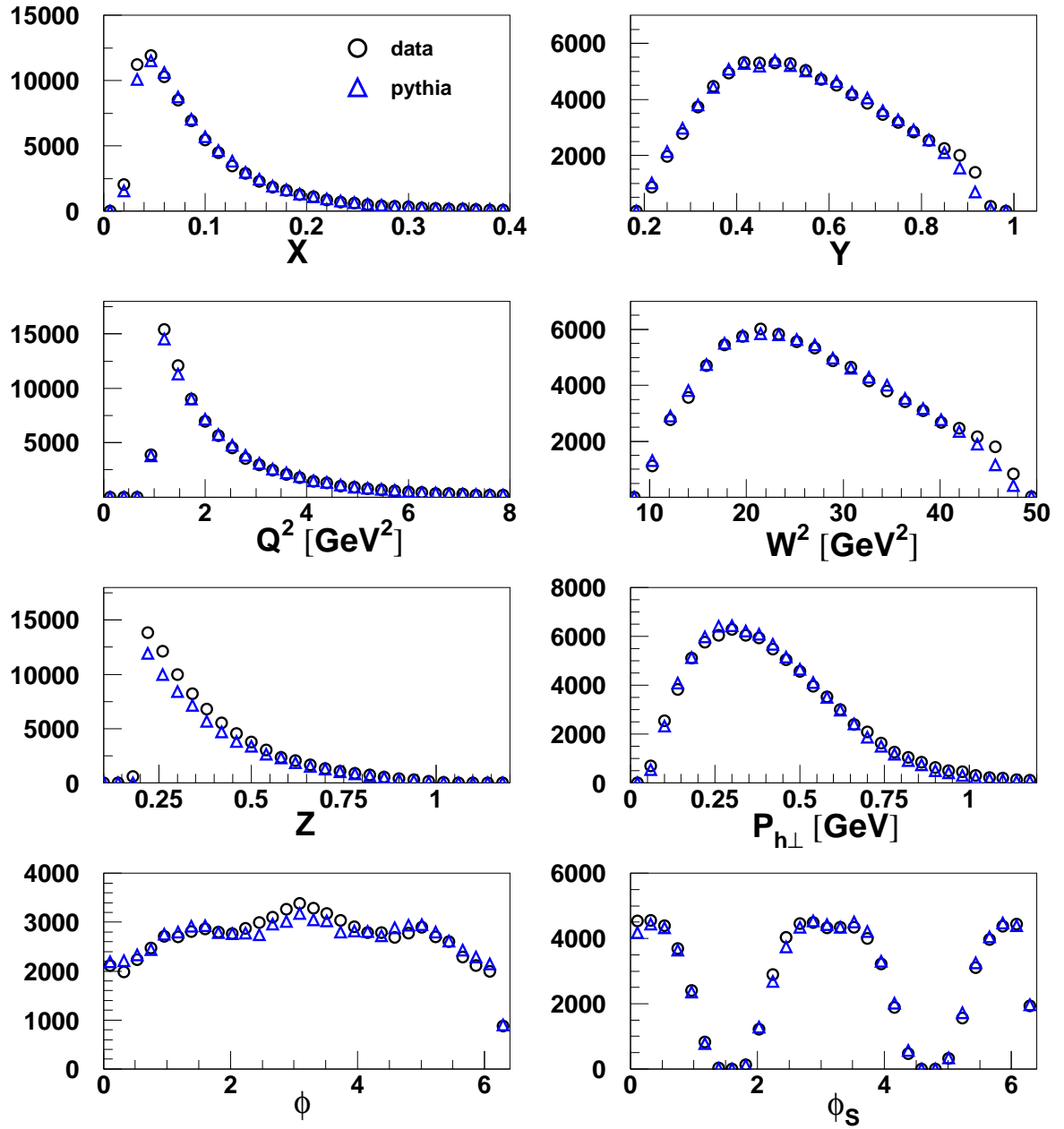
Figure 6.1: Comparison between the distributions of selected DIS and SIDIS kinematic variables obtained from real events and from events generated by PYTHIA.

to study such kind of effects.

To accomplish the demand of a fast Monte Carlo, the track reconstruction is performed through the HERMES Smearing Generator (HSG). The model parameters were tuned in such a way that the extracted asymmetry amplitudes are comparable to those extracted from experimental data.

6.3.1 The models

In GMC_TRANS, different models for the x and z dependencies of the transversity, Sivers and Collins functions are available [Mak03]. In these models, the first moments (i.e. integrals over the intrinsic transverse momenta) of the distribution or fragmentation functions are constructed proportional to the spin independent distribution of fragmentation functions $q(x)$, $\Delta q(x)$, or $D_1(z)$ (cf. Table 6.1). The latter, in turn, are based on leading order parameterizations based on fits to world data. It is worth noting that neither the unpolarized cosine moments (cf. eqs. (3.66) and (3.67)) nor the QED radiative effects (see Section 5.5.7) are implemented in GMC_TRANS. For the Monte Carlo studies reported in this section, two different versions (later referred to as GMCT1 and GMCT2) of the GMC_TRANS generator were used. These two versions have different ranges for the relevant kinematic variables and different models for the Sivers function. In particular, while the anti-quarks Sivers function is set equal to zero in one of the two versions, a non-vanishing Sivers function for the anti-quarks is implemented in the other. Furthermore, depending on the version used, the mean value $\langle K_T^2 \rangle$, which is always assumed to be independent of the quark flavours, is chosen to be dependent or independent of z. Table 6.1 summarizes the main settings of the two versions used. The parametrization of the spin independent fragmentation functions, taken from [Kre00], fulfil isospin and charge conjugation symmetry, leaving three independent fragmentation functions: favored (*fav*), unfavored (*unfav*) and strange (*s*) (cf. Section 3.7.1). In addition, unfavored and strange fragmentation functions are equal in the parametrization. The first moments of the Collins function are constructed proportional to the spin-independent fragmentation function with a coefficient for the unfavored fragmentation function twice as large as for the favoured one and with opposite sign (cf. Table 6.1). The current versions of GMC_TRANS allow to have only pions as final state hadrons. In the studies presented in the following sections, only the charged pions will be regarded.

6.3.2 The skewed Gaussian ansatz

In GMC_TRANS the p_T^2 (K_T^2) dependence in the quark distribution (fragmentation) functions is factorized and a Gaussian distribution for the transverse momenta is assumed (Gaussian ansatz). Under these assumptions the unpolarized distribution and fragmentation functions can be expressed as:

$$q(x, p_T^2) = q(x) \frac{1}{\pi \langle p_T^2(x) \rangle} e^{-\frac{p_T^2}{\langle p_T^2(x) \rangle}} \tag{6.1}$$

$$D_1(z, K_T^2) = D_1(z) \frac{1}{\pi \langle K_T^2(z) \rangle} e^{-\frac{K_T^2}{\langle K_T^2(z) \rangle}} \ , \tag{6.2}$$

GMC_TRANS settings	
Version **GMCT1**	Version **GMCT2**
Distribution Functions $\quad (q_{sea} = \bar{u}, \bar{d}, s, \bar{s})$	
$\delta u(x) = 0.7 \cdot \Delta u(x)$	$\delta u(x) = 0.7 \cdot \Delta u(x)$
$\delta d(x) = 0.7 \cdot \Delta d(x)$	$\delta d(x) = 0.7 \cdot \Delta d(x)$
$\delta q_{sea}(x) = 0.7 \cdot \Delta q_{sea}(x)$	$\delta q_{sea}(x) = 0.7 \cdot \Delta q_{sea}(x)$
$f_{1T}^{\perp u}(x) = -0.3 \cdot u(x)$	$f_{1T}^{\perp u}(x) = -0.6 \cdot u(x)$
$f_{1T}^{\perp d}(x) = 0.9 \cdot d(x)$	$f_{1T}^{\perp d}(x) = 1.05 \cdot d(x)$
$f_{1T}^{\perp q_{sea}}(x) = 0.0$	$f_{1T}^{\perp q_{sea}}(x) = 0.3 \cdot q_{sea}(x)$
Fragmentation Functions	
$H_{1,fav}^{\perp(1)}(z) = 0.65 \cdot D_{1,fav}(z)$	$H_{1,fav}^{\perp(1)}(z) = 0.65 \cdot D_{1,fav}(z)$
$H_{1,unfav}^{\perp(1)}(z) = -1.30 \cdot D_{1,unfav}(z)$	$H_{1,unfav}^{\perp(1)}(z) = -1.30 \cdot D_{1,unfav}(z)$
Transverse momentum mean values	
$\langle P_{h\perp}^2(z) \rangle = z^2 \langle p_T^2 \rangle + \langle K_T^2 \rangle$	$\langle P_{h\perp}^2(z) \rangle = z^2 \langle p_T^2 \rangle + \langle K_T^2(z) \rangle$
$(\langle p_T^2 \rangle = \langle K_T^2 \rangle = 0.18 \text{ GeV}^2$	$\langle K_T^2 \rangle$ z-dependent
kinematic ranges	
$Q^2 > 1 \text{ GeV}^2$	$Q^2 > 0.9 \text{ GeV}^2$
$0.023 < x_{Bj} < 0.4$	$0.02 < x_{Bj} < 0.5$
$y < 0.85$	$y < 0.99$
$W^2 > 10 \text{ GeV}^2$	$W^2 > 4 \text{ GeV}^2$
$z > 0.2$	$z > 0.18$

Table 6.1: The main settings of the two versions of the GMC_TRANS generator.

where $q(x)$ and $D_1(z)$ are the well known transverse momentum integrated spin-independent distribution and fragmentation functions and:

$$\langle p_T^2(x) \rangle = \frac{\int d^2 \vec{p}_T p_T^2 q(x, p_T^2)}{q(x)} \; , \qquad \langle K_T^2(x) \rangle = \frac{\int d^2 \vec{K}_T K_T^2 D_1(z, K_T^2)}{D_1(z)} \; . \qquad (6.3)$$

Similar expressions hold for the $1/2$-moments of the Sivers and the Collins function:

$$f_{1T}^{\perp(1/2)q}(x, p_T^2) \equiv \frac{|\vec{p}_T|}{2M} f_{1T}^{\perp q}(x, p_T^2) = \frac{|\vec{p}_T|}{2M} f_{1T}^{\perp q}(x) \frac{1}{\pi \langle p_T^2(x) \rangle} e^{-\frac{p_T^2}{\langle p_T^2(x) \rangle}} \qquad (6.4)$$

$$H_1^{\perp(1/2)}(z, z^2 k_T^2) \equiv \frac{|\vec{k}_T|}{2M_h} H_1^{\perp}(z, z^2 k_T^2) = \frac{|\vec{k}_T|}{2M_h} H_1^{\perp}(z) \frac{1}{\pi z^2 \langle k_T^2 \rangle} e^{-\frac{k_T^2}{\langle k_T^2 \rangle}} \; , \qquad (6.5)$$

where the usual relation $\vec{K}_T = -z \vec{k}_T$ was used.

However, when the eqs. (6.1)–(6.5) are inserted into the positivity constraints [Bac00, Bac04]

$$f_{1T}^{\perp(1/2)q}(x, p_T^2) \leq \frac{1}{2} q(x, p_T^2) \qquad (6.6)$$

$$H_1^{\perp(1/2)}(z, z^2 k_T^2) \leq \frac{1}{2} D_1(z, z^2 k_T^2) \; , \qquad (6.7)$$

one obtains:

$$\frac{|\vec{p}_T|}{M} f_{1T}^{\perp q}(x) < q(x) \qquad \frac{|\vec{k}_T|}{M_h} H_1^{\perp}(z) < D_1(z) \; , \qquad (6.8)$$

which, due to the explicit dependence on $|\vec{p}_T|$ and $|\vec{k}_T|$ of the left-hand sides, cannot ensure the fulfillment of the positivity bounds without applying unphysical cut-offs in $|\vec{p}_T|$ and $|\vec{k}_T|$.

This problem can be solved by using a modified version of eqs. (6.4) and (6.5), which allows for smaller widths of the quark transverse momentum distributions (*skewed gaussian ansatz*) [Bac04]:

$$f_{1T}^{\perp q}(x, p_T^2) = f_{1T}^{\perp q}(x) \frac{1}{\pi(1 - C_s)\langle p_T^2(x) \rangle} e^{-\frac{p_T^2}{(1 - C_s)\langle p_T^2(x) \rangle}} \qquad (6.9)$$

$$H_1^{\perp}(z, z^2 k_T^2) = H_1^{\perp}(z) \frac{1}{\pi z^2(1 - C_c)\langle k_T^2 \rangle} e^{-\frac{k_T^2}{(1 - C_c)\langle k_T^2 \rangle}} \; , \qquad (6.10)$$

where C_c and C_s are two *skewedness* parameters defined in the range $0 < C_c, C_s < 1$. In the limit $C \to 1$ the transverse momentum distributions reduce to a Dirac delta function, while in the limit $C \to 0$ one recovers the linear, i.e. unbound, p_T (k_T) dependence. With this new parametrization the positivity limits read:

$$f_{1T}^{\perp q}(x) \frac{|\vec{p}_T|}{2M} \frac{1}{\pi(1 - C_s)\langle p_T^2(x) \rangle} e^{-\frac{p_T^2}{(1 - C_s)\langle p_T^2(x) \rangle}} \leq \frac{1}{2} q(x) \frac{1}{\pi \langle p_T^2(x) \rangle} e^{-\frac{p_T^2}{\langle p_T^2(x) \rangle}} \qquad (6.11)$$

$$H_1^\perp(z)\frac{|\vec{k}_T|}{2M_h}\frac{1}{\pi z^2(1-C_c)\langle k_T^2\rangle}e^{-\frac{k_T^2}{(1-C_c)\langle k_T^2\rangle}} \le \frac{1}{2}D_1(z)\frac{1}{\pi z^2\langle k_T^2\rangle}e^{-\frac{k_T^2}{\langle k_T^2\rangle}} \qquad (6.12)$$

whence

$$\frac{|\vec{p}_T|}{1-C_s}e^{-\frac{C_s}{(1-C_s)}\frac{p_T^2}{\langle p_T^2(x)\rangle}} \le M\frac{q(x)}{f_{1T}^{\perp q}(x)} \qquad\text{and}\qquad \frac{|\vec{k}_T|}{1-C_c}e^{-\frac{C_c}{(1-C_c)}\frac{k_T^2}{\langle k_T^2\rangle}} \le M_h\frac{D_1(z)}{H_1^\perp(z)} \cdot \qquad (6.13)$$

These inequalities can easily be fulfilled for a reasonable choice of the skewedness parameters C_s and C_c. In particular, it has been shown [Bac04] that small skewedness parameters ($C_c = C_s = 0.25$) are sufficient to bound the functions. Very large values of these skewedness parameters would limit the range of the intrinsic momentum dependent functions to quite unphysical values.

With the skewed Gaussian ansatz for the p_T (k_T) dependence of the Sivers (Collins) function, one can solve analytically the convolution integral involved in the Sivers (Collins) term of the cross section (cf. eqs. (3.79) and (3.80)), yielding respectively [Bac04]:

$$\mathcal{I}\left[f_{1T}^{\perp q}(x,p_T^2)D_1(z,z^2k_T^2)\frac{\vec{p}_T\cdot\hat{P}_{h\perp}}{M}\right] =$$

$$f_{1T}^{\perp q}(x)\cdot D_1(z)\cdot\frac{|\vec{P}_{h\perp}|}{M\pi z^3}\cdot\frac{(1-C_s)\langle p_T^2\rangle}{[\langle k_T^2\rangle+(1-C_s)\langle p_T^2\rangle]^2}\cdot exp\left[-\frac{P_{h\perp}^2/z^2}{\langle k_T^2\rangle+(1-C_s)\langle p_T^2\rangle}\right], \qquad (6.14)$$

$$\mathcal{I}\left[\delta q(x,p_T^2)H_1^\perp(z,z^2k_T^2)\frac{\vec{k}_T\cdot\hat{P}_{h\perp}}{M_h}\right] =$$

$$-\delta q(x)\cdot H_1^\perp(z)\cdot\frac{|\vec{P}_{h\perp}|}{M_h\pi z^3}\cdot\frac{(1-C_c)\langle k_T^2\rangle}{[\langle p_T^2\rangle+(1-C_c)\langle k_T^2\rangle]^2}\cdot exp\left[-\frac{P_{h\perp}^2/z^2}{\langle p_T^2\rangle+(1-C_c)\langle k_T^2\rangle}\right]. \qquad (6.15)$$

6.3.3   The implemented asymmetries

The main advantage of using the Gaussian ansatz is that it allows to calculate the asymmetry amplitudes analytically for all the generated events. These values, which we call *implemented asymmetries*, can then be compared with the *extracted asymmetries*, obtained applying the standard fit procedure described in Section 5.4 to the MC events selected by the analysis program (see Sections 6.4.3 and 6.4.4).

The unweighted and $P_{h\perp}$-weighted *implemented asymmetries* are calculated according to

$$2\langle\sin(\phi+\phi_S)\rangle_{UT}^{h,\text{implem}} = \frac{1}{M_h}\frac{\sqrt{\pi}}{2}\frac{(1-C_c)\langle k_T^2\rangle}{\sqrt{(1-C_c)\langle k_T^2\rangle+\langle p_T^2\rangle}}\cdot\frac{\frac{1}{xy^2}B(y)\sum_q e_q^2\delta q(x)H_1^{\perp(1/2)q}(z)}{\frac{1}{xy^2}A(y)\sum_q e_q^2 q(x)D_1^q(z)},$$

$$(6.16)$$

$$2\langle\sin(\phi-\phi_S)\rangle_{UT}^{h,\text{implem}} = -\frac{1}{M}\frac{\sqrt{\pi}}{2}\frac{(1-C_s)\langle p_T^2\rangle}{\sqrt{(1-C_s)\langle p_T^2\rangle + \langle k_T^2\rangle}} \cdot \frac{\frac{1}{xy^2}A(y)\sum_q e_q^2 f_{1T}^{\perp(1/2),q}(x)D_1^q(z)}{\frac{1}{xy^2}A(y)\sum_q e_q^2 q(x)D_1^q(z)} \,,$$
(6.17)

$$2\left\langle\frac{|P_{h\perp}|}{zM_h}\sin(\phi+\phi_S)\right\rangle_{UT}^{h,\text{implem}} = \frac{(1-C_c)\langle k_T^2\rangle}{M_h^2} \cdot \frac{\frac{1}{xy^2}B(y)\sum_q e_q^2\delta q(x)H_1^{\perp(1)q}(z)}{\frac{1}{xy^2}A(y)\sum_q e_q^2 q(x)D_1^q(z)} \,,$$
(6.18)

$$2\left\langle\frac{|P_{h\perp}|}{zM}\sin(\phi-\phi_S)\right\rangle_{UT}^{h,\text{implem}} = -\frac{(1-C_s)\langle p_T^2\rangle}{M^2} \cdot \frac{\frac{1}{xy^2}A(y)\sum_q e_q^2 f_{1T}^{\perp(1),q}(x)D_1^q(z)}{\frac{1}{xy^2}A(y)\sum_q e_q^2 q(x)D_1^q(z)} \,,$$
(6.19)

and stored for each event j. In order to compare them with the corresponding *extracted asymmetries* in a given kinematic bin, the *implemented asymmetries* have to be averaged over all the events (N_{ev}) in that bin:

$$2\langle\sin(\phi\pm\phi_S)\rangle_{UT}^{h,\text{implem}} = \frac{\sum_j^{N_{ev}} 2\langle\sin(\phi\pm\phi_S)\rangle_{UT,j}^{h,\text{implem}}}{N_{ev}} \,.$$
(6.20)

Similar expressions hold for the $P_{h\perp}$-weighted asymmetries. The *implemented asymmetries* are integrated over $P_{h\perp}$ and therefore can not be compared to the *extracted asymmetries* in the individual $P_{h\perp}$ bins. To this purpose the $P_{h\perp}$-dependent cross section ratios have to be used instead.

6.3.4 The comparison Data-GMC_TRANS

In order to test the reliability of the GMC_TRANS Monte Carlo in reproducing the experimental results, the asymmetry amplitudes extracted from the GMC_TRANS events generated within the HERMES acceptance were compared with those extracted from the experimental data. The comparison plots are shown in Figure 6.2. Here the Collins and the Sivers moments extracted from the experimental data are reported together with those extracted from the two versions of GMC_TRANS. For this comparison the same number (2) of fit parameters has been used for the three cases. Although the Collins amplitudes extracted from GMCT1 (open triangles) and GMCT2 (open circles) are substantially different (those extracted from GMCT2 are systematically lower than the others), they are both reasonably compatible with the experimental ones (full squares) for both positive and negative pions. In contrast, none of the two GMC_TRANS versions reproduces the experimental Sivers amplitudes for positive pions. Both the simulated Sivers amplitudes are indeed systematically smaller than the experimental ones. This is especially true for those extracted from GMCT1, where a zero Sivers function for the sea quarks is implemented. All the Sivers amplitudes for the negative pions are compatible with zero.
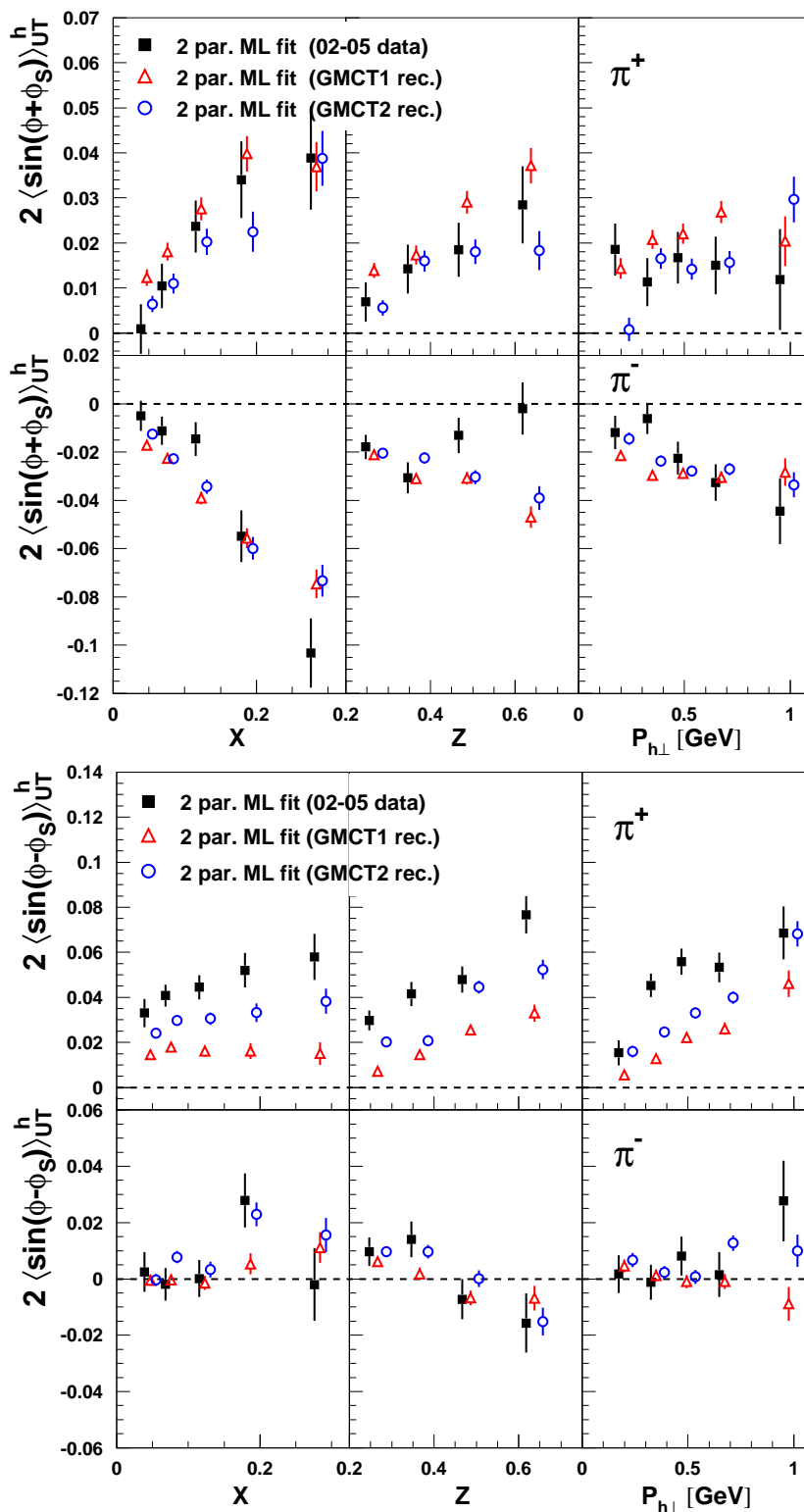
Figure 6.2: Unweighted Collins (upper half) and Sivers (lower half) moments for π^+ (upper panels) and π^- (lower panels) extracted from the full HERMES transverse data set (full squares), and from the two GMC_TRANS versions GMCT1 (open triangles) and GMCT2 (open circles). The average kinematics of the bins has been slightly shifted to accommodate the three sets of results.

6.4 Study of acceptance and smearing effects: a qualitative approach

The studies presented in the following sections were performed in order to estimate the impact of the acceptance and smearing effects on the extracted Collins and Sivers moments. To this purpose, different categories of Collins and Sivers asymmetries were extracted and compared for both the unweighted and the $P_{h\perp}$-weighted cases. These categories originate from the combinations of three different Monte Carlo event samples and two different extraction methods:

MC event samples:

- *generated events*: GMC_TRANS events generated in 4π with the original (i.e. unsmeared) kinematics;

- *generated events in acceptance*: GMC_TRANS events generated within the HERMES acceptance with the original (i.e. unsmeared) kinematics;

- *reconstructed events*: GMC_TRANS events generated within the HERMES acceptance with smeared (HSG) kinematics.

Extraction methods:

- *implemented asymmetries*: asymmetries implemented in GMC_TRANS, calculated and stored for each event (see Section 6.3.3);

- *extracted asymmetries*: asymmetries extracted from the GMC_TRANS events with the 'standard fit method' (see Section 6.4.1);

The comparison between the asymmetries obtained from *reconstructed* and *generated events* allows to study the impact of the instrumental (detector acceptance and smearing) effects, while that between *implemented* and *extracted asymmetries* allows to test the extraction method.

6.4.1 Fit methods comparison

The comparison studies mentioned above were repeated for both the GMC_TRANS versions (GMCT1 and GMCT2) described in Section 6.3.1 and making use of both the fit methods (LS and ML) described in Section 5.4. In particular, since only the Collins and the Sivers effects are implemented in the GMC_TRANS generator, there is no need to include in the fit the four additional sine moments appearing in eqn. (5.26). As a result only two parameters, corresponding to the Collins and the Sivers amplitudes, are used in the ML fit, while an additional constant term is included in the LS fit. Since no implementation exists at the moment for the $P_{h\perp}$-weighted asymmetries in the maximum likelihood fit, these have only been extracted with the least square fit. The unweighted Collins and Sivers asymmetry amplitudes extracted with the two different fit methods from the GMCT2 *generated* (*reconstructed*) events are compared in Figure 6.3 (6.4). The two sets of results are in a very good agreement. A similar agreement is observed using GMCT1.

Figure 6.3: Unweighted Collins (upper half) and Sivers (lower half) moments for π^+ (upper panels) and π^- (lower panels) extracted from the GMCT2 *generated events* with ML fit (open squares) and LS fit (full triangles).
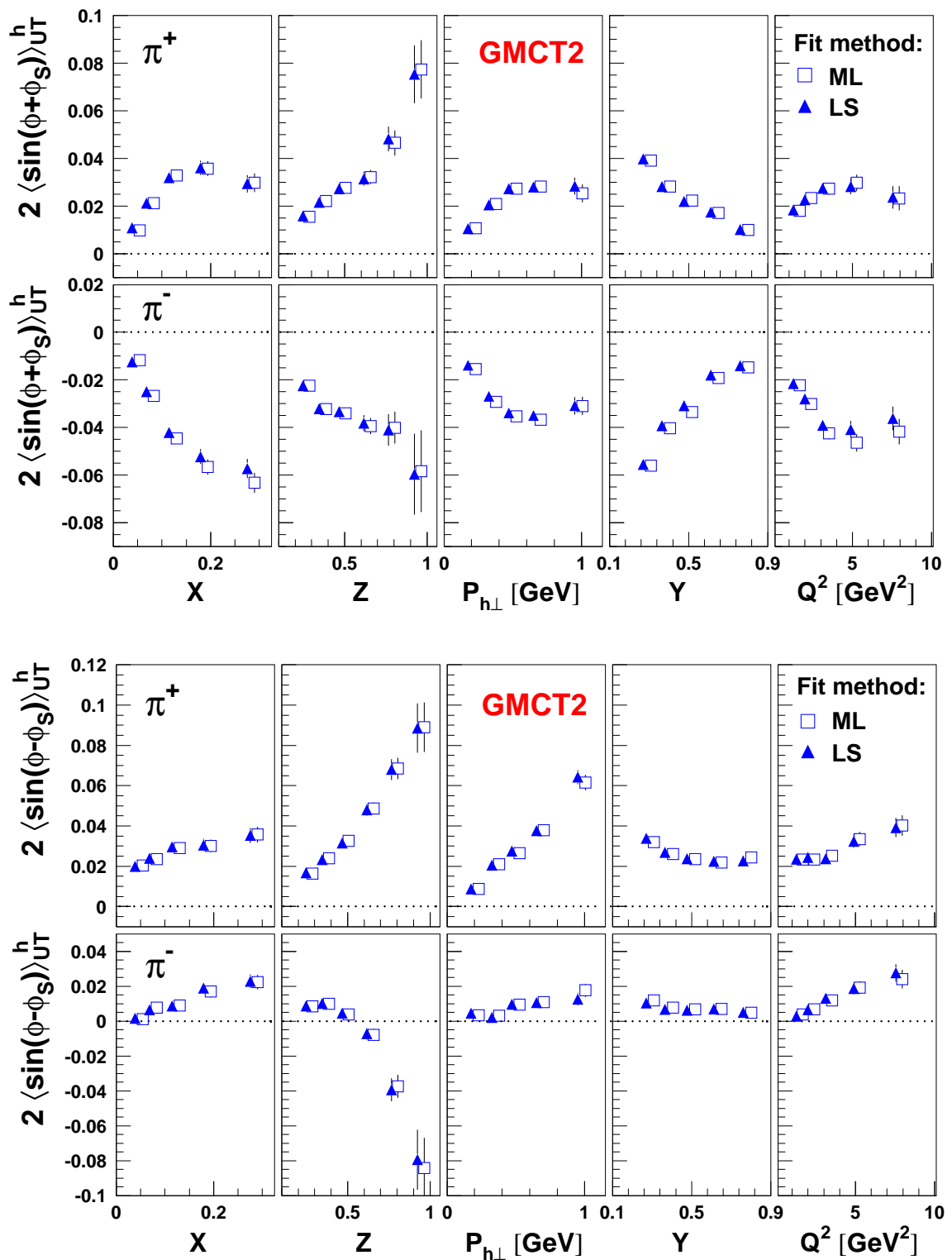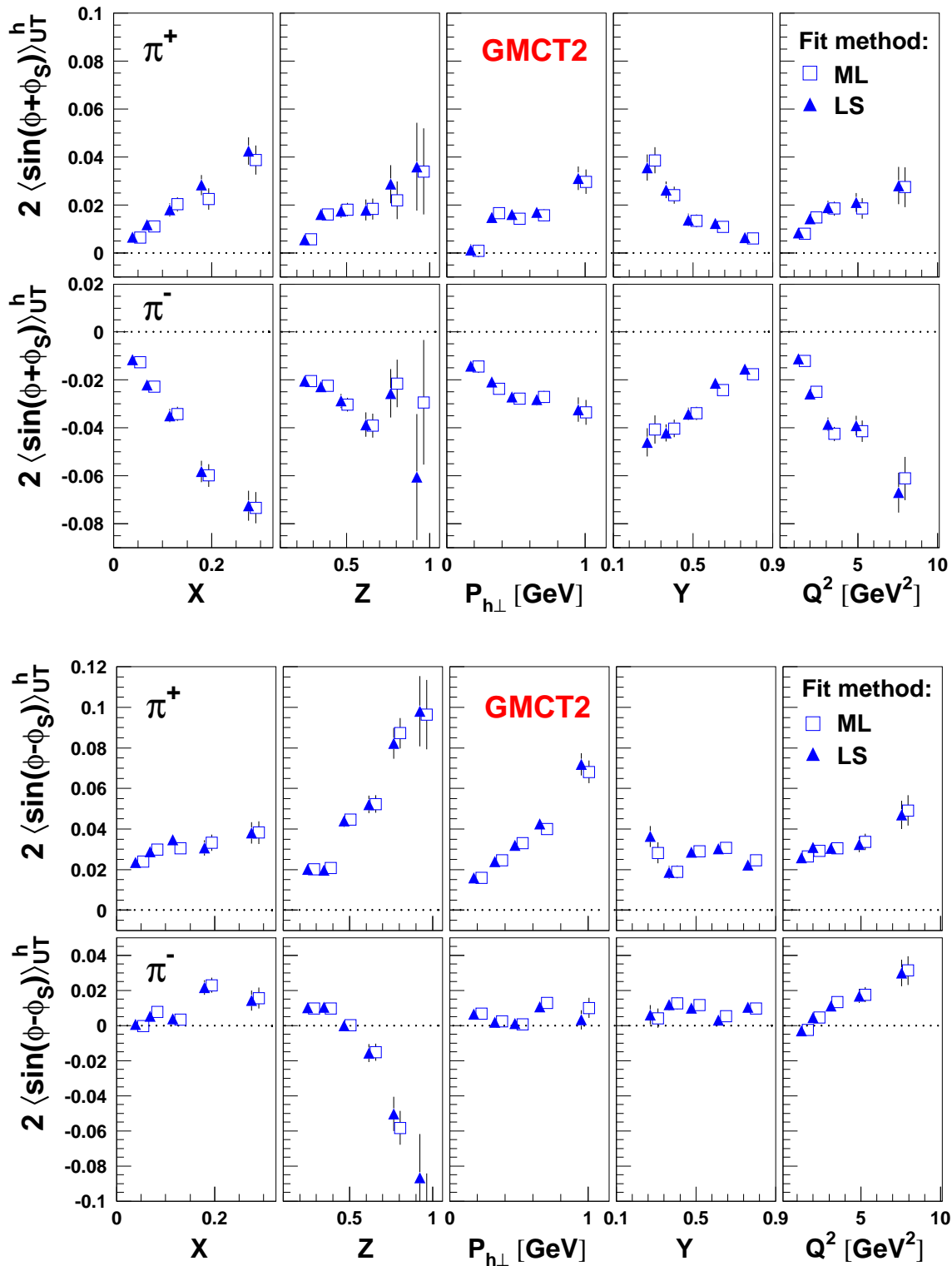
Figure 6.4: Unweighted Collins (upper half) and Sivers (lower half) moments for π^+ (upper panels) and π^- (lower panels) extracted from the GMCT2 *reconstructed events* with ML fit (open squares) and LS fit (full triangles).

In the studies reported in the next sections, the ML fit will always be used for the extraction of the unweighted asymmetries and the LS fit for the extraction of the $P_{h\perp}$-weighted asymmetries.

6.4.2 The smearing effects

The contribution due to the smearing effects can be evaluated by comparing the asymmetry amplitudes obtained from the *reconstructed events* with those obtained from the *generated events in acceptance*. Any difference between the two sets of results can only be attributed to the action of the detector smearing on the event kinematics. For this comparison, the GMCT2 version of GMC_TRANS was used. The results for the Collins and Sivers moments are shown in Figures 6.5 and 6.6 (upper plots), respectively, together with the corresponding differences (lower plots). Except for the highest z-bins, whose events are not accounted for while projecting onto the other variables (cf. Section 5.3.3), the differences are relatively small in the whole kinematic range. These differences are considered as a source of systematic uncertainty and are accounted for in the evaluation of the global systematic error (see Section 6.9).

6.4.3 Acceptance effects: the unweighted asymmetries

As discussed in Section 6.4, the differences between *generated* and *reconstructed events* originate from both the acceptance and the smearing effects. Figure 6.7 reports the comparison between the unweighted Collins and Sivers moments extracted from the GMCT1 *generated* and *reconstructed events*. The plots show a relatively good agreement in most of the kinematic bins, thus leading to the conclusion that acceptance and smearing effects are relatively small ($< 10\%$). Significant differences are only observed as a function of $P_{h\perp}$ for both π^+ and π^-. This result fully agrees with that of an equivalent study reported in [Els06], where the same version of GMC_TRANS was used. These figures also show the corresponding *implemented asymmetries*. The differences between *implemented* and *extracted asymmetries* are relatively small for both *generated* and *reconstructed events*. The latter result ensures that the extraction method has been implemented correctly and does not introduce any significant bias.

A similar comparison study was performed for the first time using the GMCT2 version of GMC_TRANS. As discussed in Section 6.3.1, this version is expected to be more reliable since it not only uses a non-zero Sivers function for the sea quarks, but also includes the z-dependence of $\langle K_T^2 \rangle$. The comparison plots for GMCT2 are shown in Figure 6.8. Contrarily to the previous comparison (based on GMCT1), this comparison shows unexpectedly large differences between the asymmetries extracted from *generated events* and those extracted from *reconstructed events*. These differences are particularly pronounced for the Collins moments for π^+, for which they are estimated to be, in the average, of the order of 40%. Significant differences are also observed between *implemented* and *extracted* asymmetries for the *reconstructed events*.
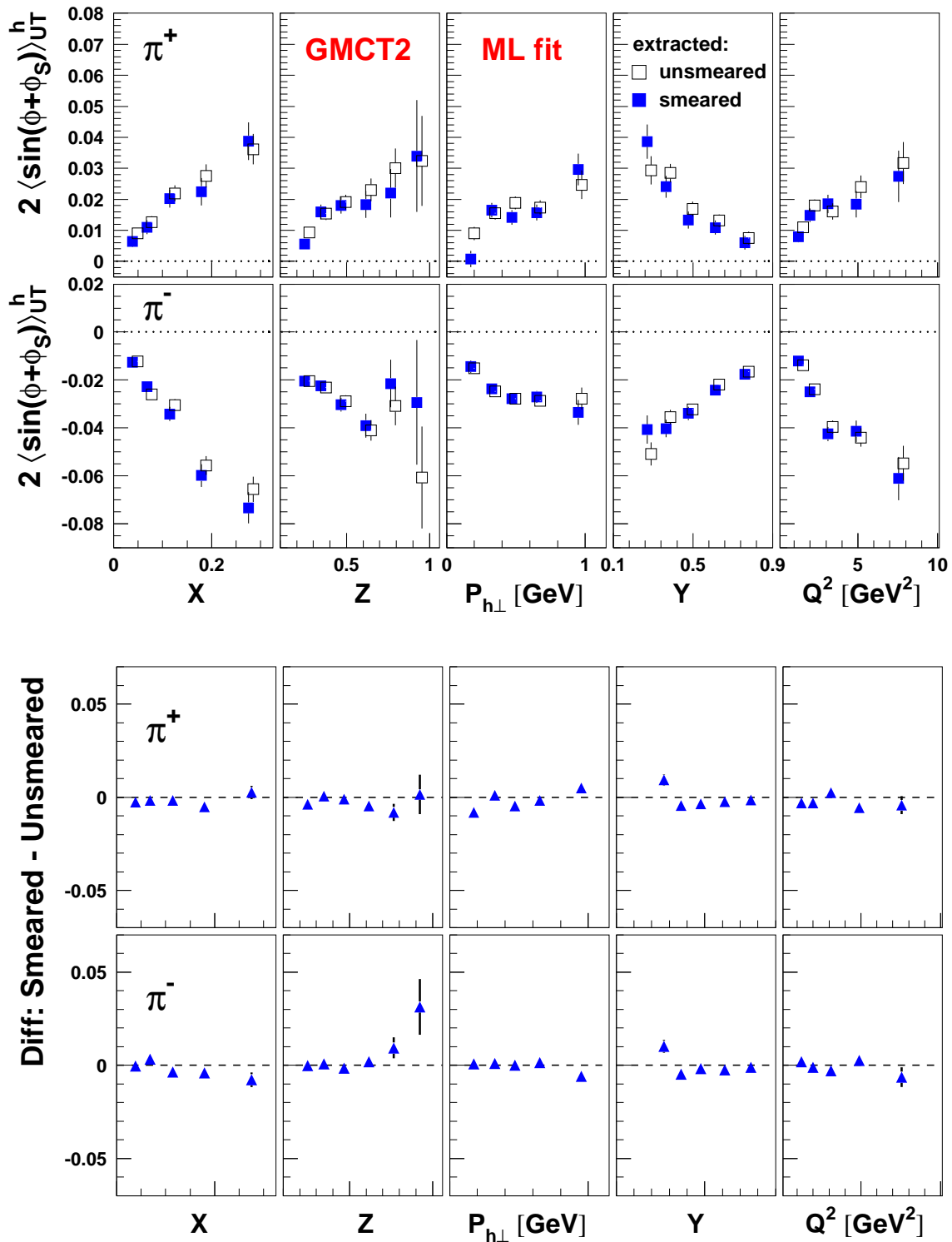
Figure 6.5: Upper half: Collins moments for π^+ and π^- extracted from GMCT2 smeared (full dots) and unsmeared (open dots) events reconstructed within the HERMES acceptance. Lower half: differences between the amplitudes extracted from smeared and unsmeared events.
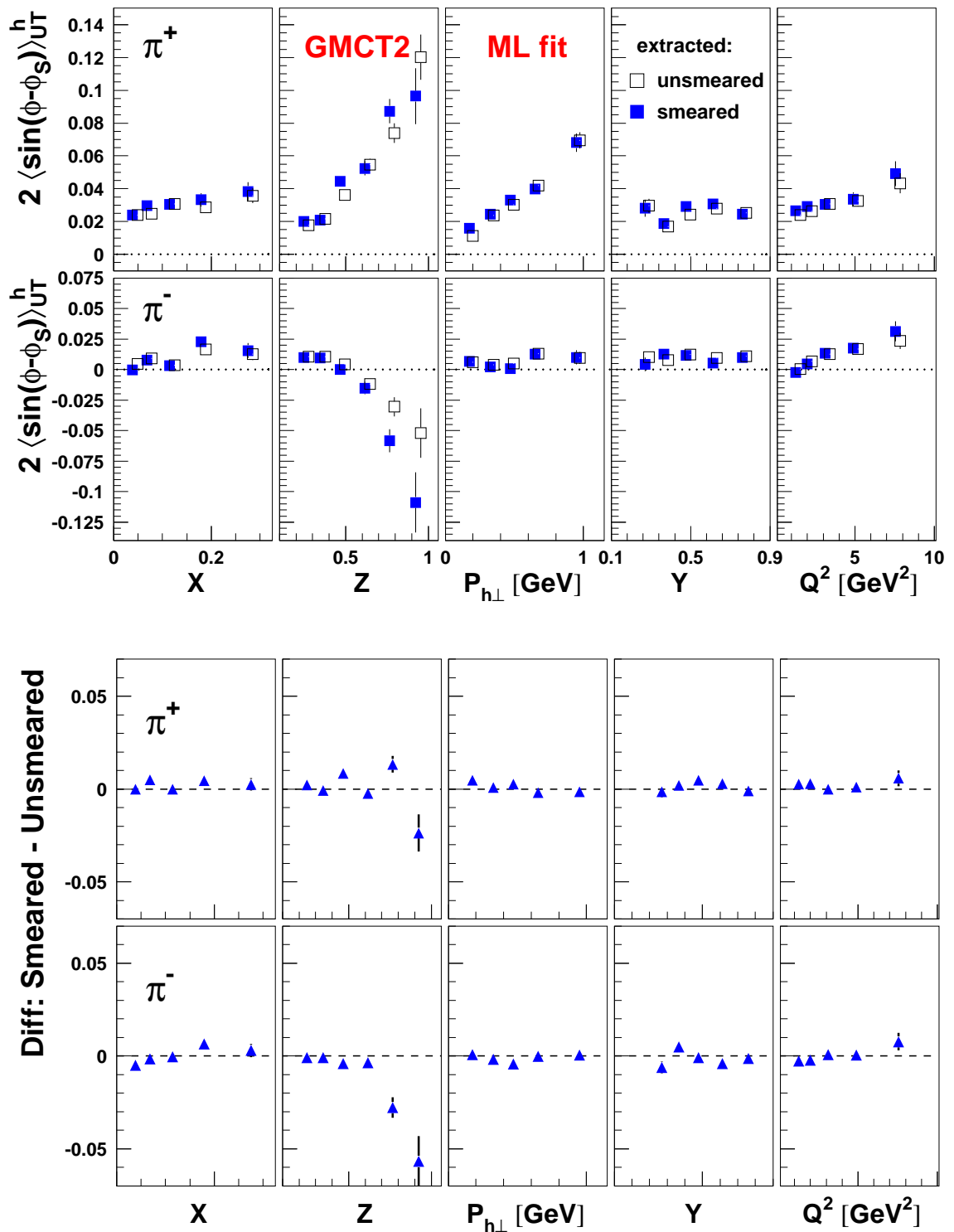
Figure 6.6: Upper half: Sivers moments for π^+ and π^- extracted from GMCT2 smeared (full dots) and unsmeared (open dots) events reconstructed within the HERMES acceptance. Lower half: differences between the amplitudes extracted from smeared and unsmeared events.
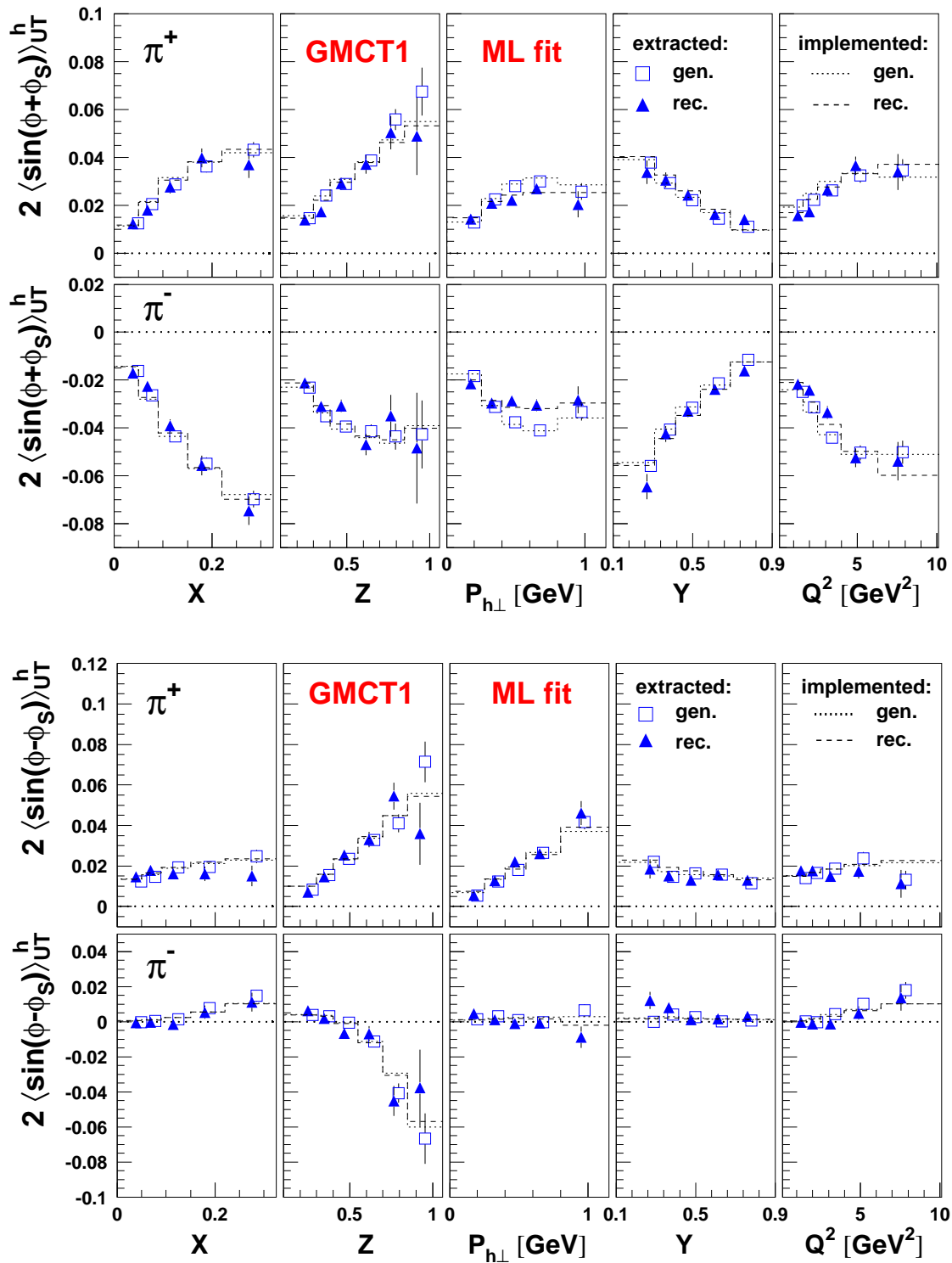
Figure 6.7: Unweighted Collins (upper half) and Sivers (lower half) moments for π^+ (upper panels) and π^- (lower panels) extracted with ML fit from the GMCT1 *generated events* (open squares) and *reconstructed events* (full triangles). The reconstructed and generated implemented asymmetries are also shown for comparison.
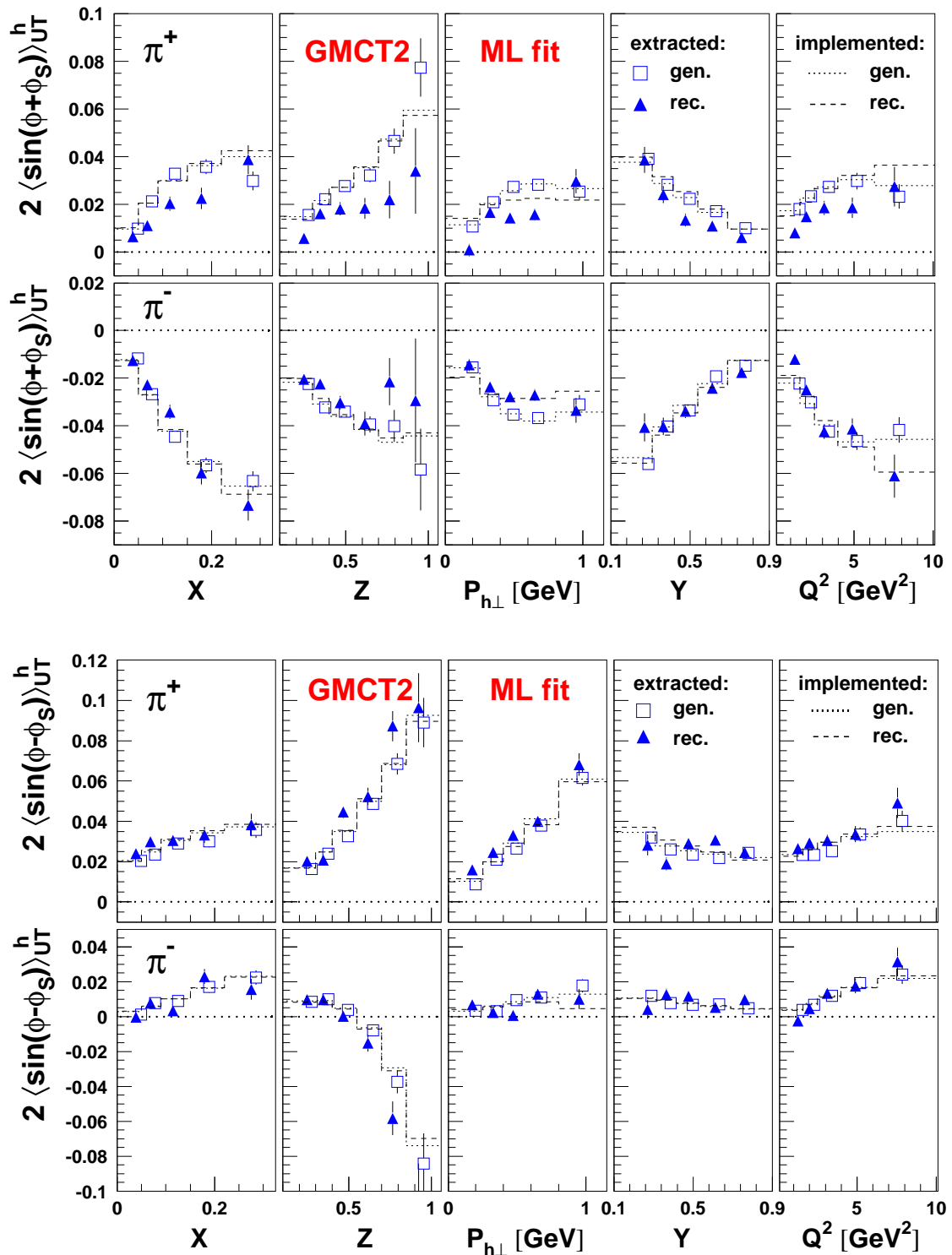
Figure 6.8: Unweighted Collins (upper half) and Sivers (lower half) moments for π^+ (upper panels) and π^- (lower panels) extracted with ML fit from the GMCT2 *generated events* (open squares) and *reconstructed events* (full triangles). The reconstructed and generated implemented asymmetries are also shown for comparison.

6.4.4 Acceptance effects: the $P_{h\perp}$-weighted asymmetries

A similar study was done for the $P_{h\perp}$-weighted asymmetry amplitudes. The *implemented* and the *extracted asymmetries* obtained from *generated* and *reconstructed events* are compared for both the GMC_TRANS versions in Figures 6.9 and 6.10, respectively. As already found in [Els06] with GMCT1, large differences are observed for the Collins moments. Even larger differences are observed when GMCT2 is used. In both cases (GMCT1 and GMCT2) the absolute values of the Collins and Sivers amplitudes extracted from the *reconstructed events* are systematically lower than those extracted from the *generated events* in most of the kinematic bins.
Big differences are also observed between the *extracted* and the *implemented asymmetries* for *reconstructed events*. An exception is represented, in both cases, by the $P_{h\perp}$ bins, where a relatively better agreement is observed. The contrast between the relatively good reproduction of the amplitudes in the individual $P_{h\perp}$ bins and the large deviations observed as a function of the other kinematic variables suggests that an insufficient integration over $P_{h\perp}$ causes the problem. Indeed, in the former case, the integration of the $P_{h\perp}$-dependent cross section is restricted to the rather small range within each bin. However, it is difficult to interpret the results since the deconvolution of distribution and fragmentation functions is not achieved with an incomplete integration over $P_{h\perp}$.

The studies discussed above show that an estimation of the acceptance and smearing effects on the extracted asymmetry amplitudes based on this method is strongly model dependent. The comparisons above were only meant to estimate qualitatively the impact of acceptance and smearing effects on the extracted asymmetry amplitudes. A different and more sophisticated approach, aimed to extract a quantitative estimate of these effects, was subsequently adopted, as discussed in Section 6.5.

6.5 Acceptance studies: a more sophisticated approach

The large deviations observed between the asymmetry amplitudes extracted from *generated* and *reconstructed* Monte Carlo events, suggest that the effects of the HERMES acceptance have a substantial impact on our results. In order to avoid this problem, two alternative approaches can, in principle, be adopted: A different extraction method which is not influenced by the HERMES acceptance and smearing, or an a-posteriori correction for these effects. The first approach, which basically consists in a multi-dimensional unfolding of the radiative and experimental effects, has already been intensively adopted in different analyses at HERMES [Hil05, Mai06, Air07]. This method requires a multi-dimensional binning of the selected events. In the present analysis, however, this method would be prohibitive due to the much lower statistics available for the transversely polarized target data in combination with the relatively high number of independent variables[1]. The second approach, based on an innovative method, was then adopted, as reported in the following sections.

---

[1]The SIDIS cross section depends on six independent variables (cf. Section 3.7.4)).

Figure 6.9: $P_{h\perp}$-weighted Collins (upper half) and Sivers (lower half) moments for π^+ (upper panels) and π^- (lower panels) extracted with LS fit from the GMCT1 *generated events* (open squares) and *reconstructed events* (full triangles). The reconstructed and generated implemented asymmetries are also shown for comparison.
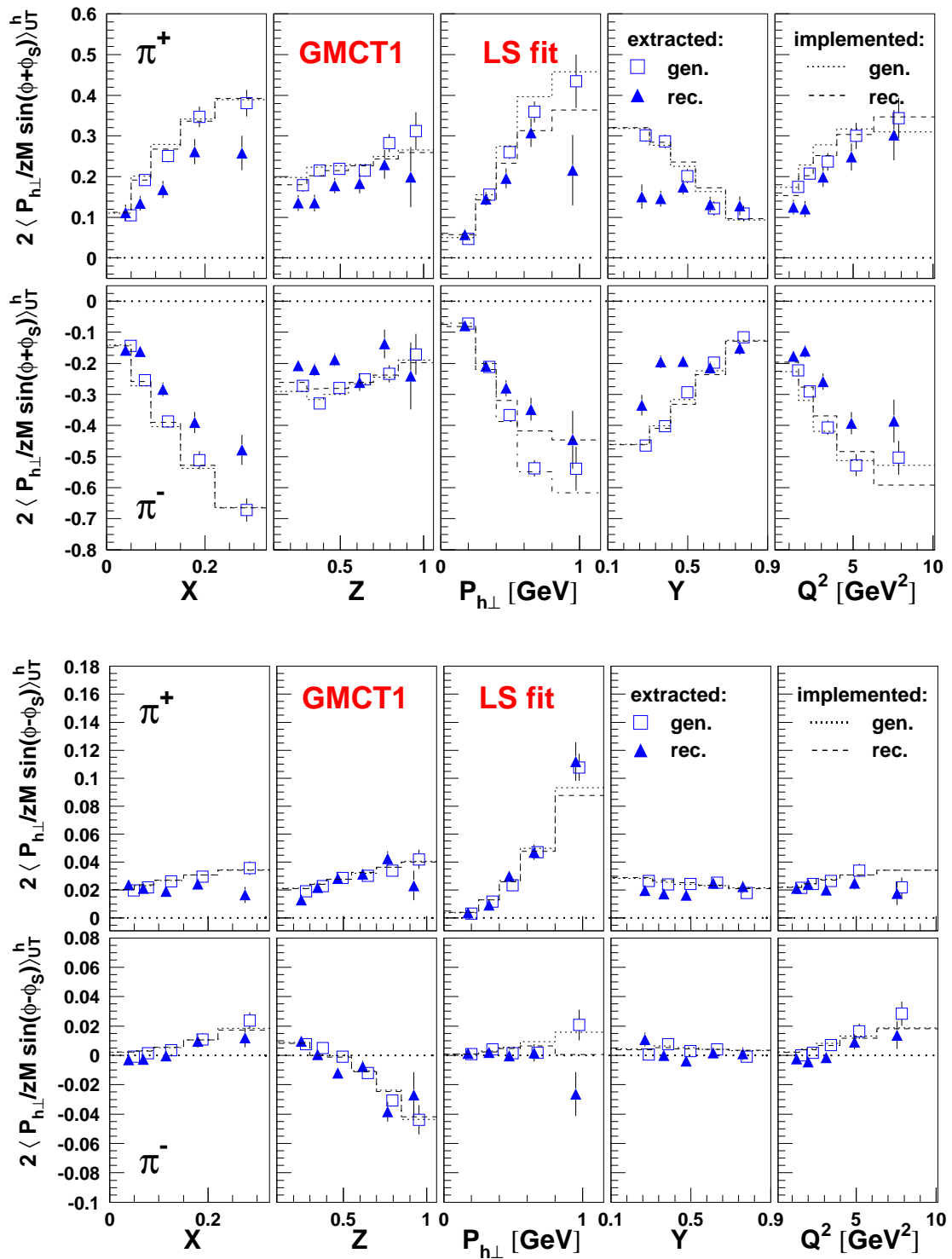
Figure 6.10: $P_{h\perp}$-weighted Collins (upper half) and Sivers (lower half) moments for π^+ (upper panels) and π^- (lower panels) extracted with LS fit from the GMCT2 *generated events* (open squares) and *reconstructed events* (full triangles). The reconstructed and generated implemented asymmetries are also shown for comparison.
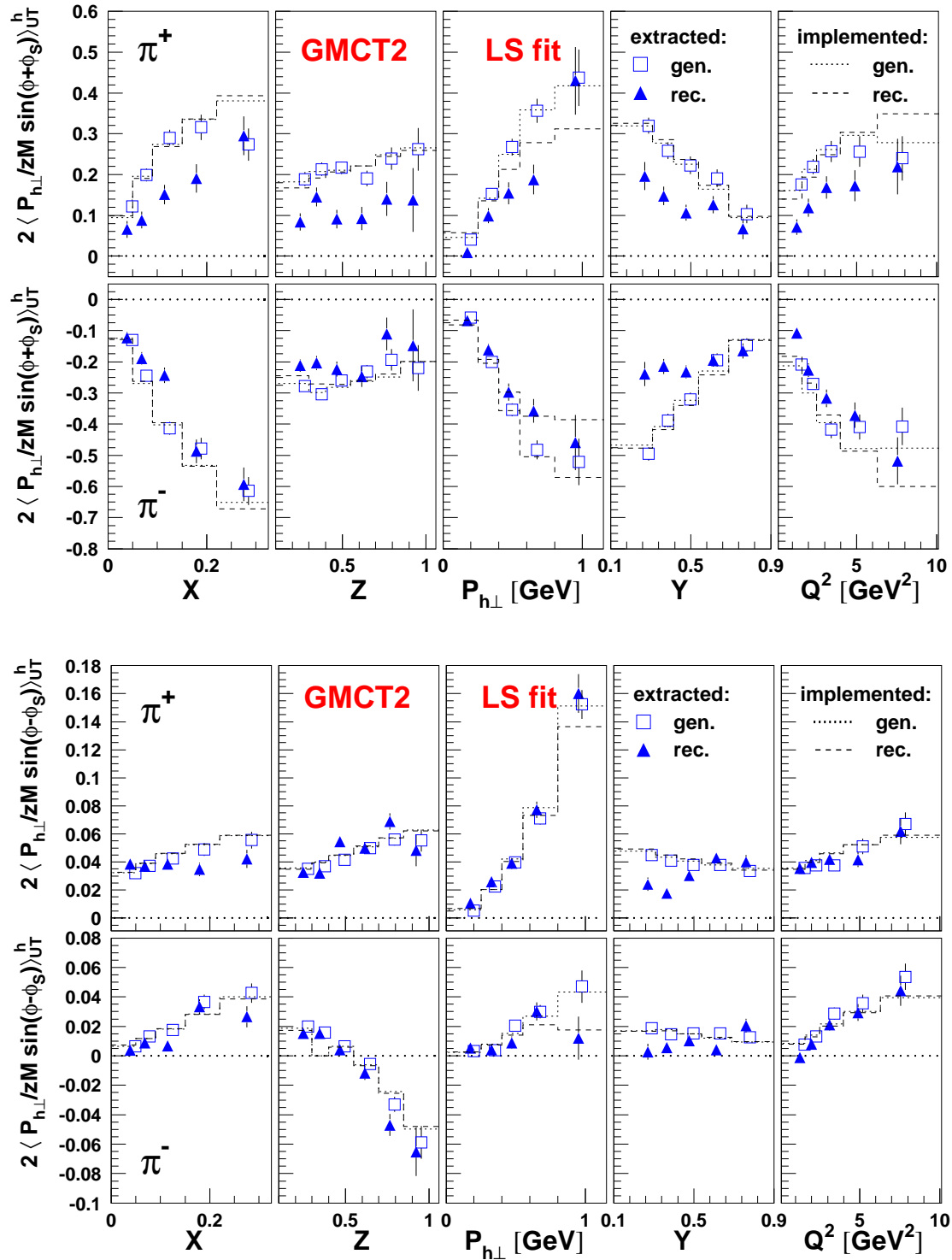
6.5.1 The idea underneath the method

This new method [Mil06] is based on two major steps. In the first step, the full kinematic dependence of the Collins and Sivers moments on x, Q^2, z and $P_{h\perp}$ is extracted from the real data through a fit based on a fully differential Probability Density Function (PDF):

$$f(x, Q^2, z, P_{h\perp}, \phi, \phi_S, P_t; a_C, a_S, ...) =$$

$$1 + P_t \cdot \left[A_{\text{Collins}}(x, Q^2, z, P_{h\perp}; a_C) \cdot \sin(\phi + \phi_S) + \right.$$

$$\left. A_{\text{Sivers}}(x, Q^2, z, P_{h\perp}; a_S) \cdot \sin(\phi - \phi_S) + ... \right] . \qquad (6.21)$$

Here P_t denotes the target transverse polarization and $A_{\text{Collins(Sivers)}}(x, Q^2, z, P_{h\perp}; a_{C(S)})$ the Collins (Sivers) asymmetry amplitudes, dependent on the four kinematic variables x, Q^2, z and $P_{h\perp}$. A set $a_{C(S)}$ of parameters constitute the coefficients of a four-dimensional Taylor expansion in the four kinematic variables (see an example in the next section).

The second step then consists in folding these parameterizations with the known Born (spin-independent) cross section $\sigma_{Born} = \sigma_{UU}^{4\pi}(x, Q^2, z, P_{h\perp})$, according to the following general relation:

$$\langle \sin(\phi \pm \phi_S) \rangle_{UT}^{h,4\pi}(x) = \frac{\int dy dz dP_{h\perp} \, \sigma_{UU}^{4\pi}(x, Q^2, z, P_{h\perp}) \cdot A_{\text{Collins(Sivers)}}(x, Q^2, z, P_{h\perp}; a_{C(S)})}{\int dy dz dP_{h\perp} \sigma_{UU}^{4\pi}(x, Q^2, z, P_{h\perp})} .$$
$$(6.22)$$

In practice, the GMC_TRANS events generated in 4π summed over the two target spin states are used to reproduce the Born cross section. The folding is then effectively performed using the formulae:

$$\langle \sin(\phi \pm \phi_S) \rangle_{UT}^{h,4\pi}(x) = \frac{\sum_{j=1}^{N_{MC}} W_j^{MC} \cdot A_{\text{Collins(Sivers)}}(x, Q^2, z, P_{h\perp}; a_{C(S)})}{\sum_{j=1}^{N_{MC}} W_j^{MC}} \qquad (6.23)$$

and

$$\left\langle \frac{P_{h\perp}}{zM} \sin(\phi \pm \phi_S) \right\rangle_{UT}^{h,4\pi}(x) = \frac{\sum_{j=1}^{N_{MC}} W_j^{MC} \cdot \frac{P_{h\perp}}{zM} \cdot A_{\text{Collins(Sivers)}}(x, Q^2, z, P_{h\perp}; a_{C(S)})}{\sum_{j=1}^{N_{MC}} W_j^{MC}} \qquad (6.24)$$

to get, respectively, the unweighted and the $P_{h\perp}$-weighted Collins and Sivers moments projected in 4π. Here W_j^{MC} denote the Monte Carlo event-weights[2] (cf. Section 6.1). If the method works correctly, these asymmetry amplitudes should correspond to those that one would measure with an ideal 4π detector, i.e. a detector with a full coverage of the solid angle. Similar relations can be used to project the extracted Collins and Sivers amplitudes within the HERMES acceptance itself. In this case the spin-independent cross section within the acceptance can be obtained from the GMC_TRANS *reconstructed events* summed over the two target spin states.

---

[2]In the current versions of GMC_TRANS all the event-weights are equal to 1.

It is important to stress that this method represents a real improvement with respect to the standard method discussed in the previous sections. In this case, indeed, one does not need anymore to rely on a model (e.g. the GMC_TRANS model) for the kinematic dependence of the Collins and Sivers moments. On the contrary, such a dependence is extracted from the real data through a Taylor expansion, which does not imply any physical assumption. The limits of the method are represented by the choice of the truncation of the Taylor expansion (see Section 6.6.2), the use of a model for the Born cross section (see Section 6.6.1) and the assumption that the kinematic dependence of the azimuthal moments outside the acceptance is the same as inside.

Before applying this method to the experimental data, for which no information outside the HERMES acceptance is available, a preliminary test was done using the GMC_TRANS data. The use of the Monte Carlo, indeed, allows to test the method by checking that the asymmetry amplitudes extracted from the *reconstructed* events and folded with the unpolarized cross section in 4π, corresponds to those extracted directly from the *generated events*. A good agreement between the two would, in principle, imply that the method works correctly and can thus be applied to the real data to make an estimate of the acceptance effects.

6.5.2 A first attempt: the 44-parameters fit

In a first attempt, the GMC_TRANS *reconstructed events* were fitted by a ML fit based on a 44-parameters PDF where the Collins and Sivers kinematic dependencies are parameterized as:

$$A_{\text{Collins(Sivers)}}(x, Q^2, z, P_{h\perp}; a_{C(S)}) = a_1 + a_2 \cdot x' + a_3 \cdot Q'^2 + a_4 \cdot z' + a_5 \cdot P'_{h\perp} +$$

$$a_6 \cdot x'^2 + a_7 \cdot z'^2 + a_8 \cdot P'^2_{h\perp} + a_9 \cdot x' \cdot z' +$$

$$a_{10} \cdot x' \cdot P'_{h\perp} + a_{11} \cdot z' \cdot P'_{h\perp} + a_{12} \cdot x'^3 + a_{13} \cdot x' \cdot z'^2 +$$

$$a_{14} \cdot x'^2 \cdot z' + a_{15} \cdot x'^2 \cdot P'_{h\perp} + a_{16} \cdot x' \cdot P'^2_{h\perp} +$$

$$a_{17} \cdot z'^2 \cdot P'_{h\perp} + a_{18} \cdot z' \cdot P'^2_{h\perp} + a_{19} \cdot x'^2 \cdot P'^2_{h\perp} +$$

$$a_{20} \cdot z'^2 \cdot P'^2_{h\perp} + a_{21} \cdot x' \cdot z' \cdot P'_{h\perp} + a_{22} \cdot x'^2 \cdot z' \cdot P'_{h\perp} , \qquad (6.25)$$

where:

$$x' = x - \langle x \rangle \qquad Q'^2 = Q^2 - \langle Q^2 \rangle \qquad z' = z - \langle z \rangle \qquad P'_{h\perp} = P_{h\perp} - \langle P_{h\perp} \rangle .$$

This PDF, proposed in [Mil06], consists of a Taylor expansion of the Collins and Sivers moments performed around the average values $\langle x \rangle$, $\langle Q^2 \rangle$, $\langle z \rangle$ and $\langle P_{h\perp} \rangle$. Its peculiar functional form, which includes all first order terms plus a selection of second, third and fourth order terms, was originally derived in such a way to reproduce the full kinematic dependence of the GMC_TRANS *implemented* Collins and Sivers asymmetry amplitudes.

As an example, the correlation matrix for the Collins set of parameters for positive pions is shown in Figure 6.11. Except for a few cases, the correlations among the 22 parameters are relatively small. It is worth noting that a very similar pattern is observed for the negative pions and for Sivers case (not shown).
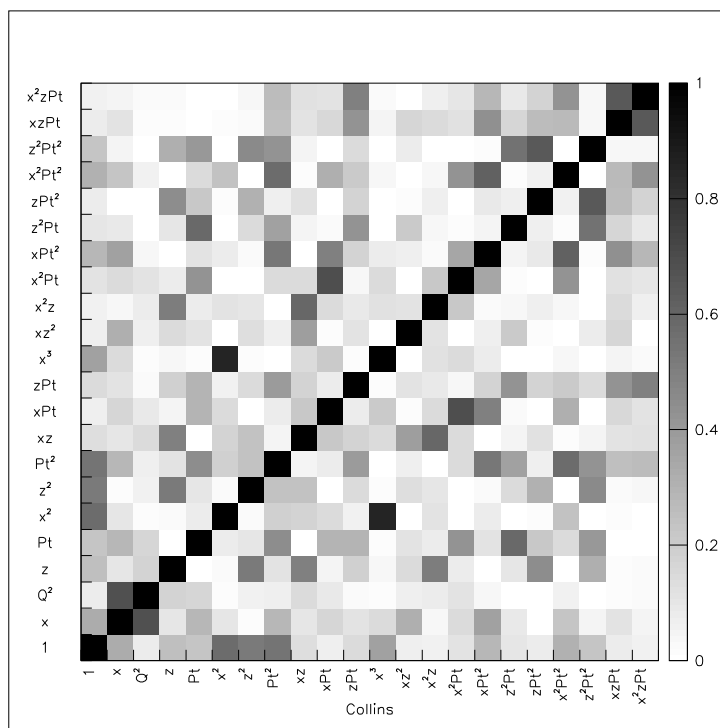
Figure 6.11: Correlation matrix for the 22 Collins parameters for π^+ (GMCT2 events).

The fitted asymmetry amplitudes $A_{Collins(Sivers)}(x, Q^2, z, P_{h\perp}; a_{C(S)})$ were then folded with the Born cross section according to eqn. (6.23). The unweighted Collins and Sivers moments, extracted with the standard method described in Sections 6.4.3 for both the *generated* and *reconstructed* GMCT2 events (cf. Figure 6.8), are compared in Figure 6.12 with those obtained with the new method described above (44-parameters fit plus folding with the Born cross section). The Collins and Sivers moments projected within the acceptance (i.e. folded with the spin-independent cross section restricted to the HERMES acceptance) are also shown in the plots. As expected, these amplitudes (open triangles) approach those extracted from the *reconstructed events* (full triangles). Similarly, the asymmetry amplitudes folded with the spin-independent cross section in 4π (open squares) approach those extracted from the *generated events* (full squares). This is particularly visible in the Collins moments for π^+, where the largest differences between the asymmetry amplitudes extracted from *generated* and *reconstructed events* are observed. Similar conclusions can be drawn for the $P_{h\perp}$-weighted asymmetries, shown in Figure 6.13. It is important to note, however, that the error bars of the asymmetry amplitudes extracted with the two different methods are not comparable. While the amplitudes extracted with the standard method are obtained by fitting the events in each kinematic bin, those extracted with the new method are obtained from a fit of the full event sample (the kinematic dependence of the azimuthal amplitudes being accounted for through the fully differential PDF) and projected in the various kinematic bins afterwards, when folding with the spin-independent cross section. As a consequence, the errors of the amplitudes extracted with the new method in the various kinematic bins are fully correlated.

Figure 6.12: Unweighted Collins (upper half) and Sivers (lower half) moments for π^+ (upper panels) and π^- (lower panels) extracted from GMCT2 events. The amplitudes folded with the spin-independent cross section in 4π (open squares) approach those extracted from the events generated in 4π (full squares). The average kinematics of the bins has been slightly shifted to accommodate the four sets of results.

Figure 6.13: $P_{h\perp}$-weighted Collins (upper half) and Sivers (lower half) moments for π^+ (upper panels) and π^- (lower panels) extracted from GMCT2 events. The amplitudes folded with the spin-indep. cross section in 4π (open squares) approach those extracted from the events generated in 4π (full squares). The average kinematics of the bins has been slightly shifted to accommodate the four sets of results.

The comparison studies discussed above lead to the conclusion that the asymmetry amplitudes extracted from the events reconstructed within the HERMES acceptance and folded with the Born cross section reproduce, to a reasonable extent, those extracted from Monte Carlo events in 4π. This method, thus, allows to recover most of the acceptance effects that affect the Collins and Sivers moments extracted inside the HERMES acceptance.

These studies, performed at the Monte Carlo level, were meant to test the reliability of the method before applying it to the experimental data (see next section).

6.5.3 Applying the method to the experimental data

The studies discussed above show that the new method introduced in Section 6.5.1 works nicely at the Monte Carlo level. The method can therefore be safely applied to the experimental data in order to estimate the real acceptance effects.

As a first attempt, the same 44-parameters PDF (6.25), optimized for the GMC_TRANS data, was used to fit the real data. Since, however, the asymmetry amplitudes extracted from the *reconstructed* events generated by GMC_TRANS do not fully reproduce the experimental ones (cf. Figure 6.2), the latter might be better described by a different functional form. In particular, the 44-parameters fit does not account for the additional sine moments (cf. eqn. 5.26) that were found to influence the fit results (especially the $\langle \sin(\phi_S) \rangle^h_{UT}$ moment). This point is discussed in detail in Section 6.6.2.

Figure 6.14 shows the comparison between the Collins and Sivers moments extracted with the standard 2-parameter ML fit (cf. Section 5.4.2) (full squares) and those obtained with the new method in the acceptance (open triangles) and in 4π (open squares). Here the GMCT2 version of GMC_TRANS was used to calculate the Born cross section for the folding procedure.

Differently from the case of GMC_TRANS, only relatively small differences are observed in the data between the asymmetry amplitudes in the acceptance and those extrapolated in 4π. A similar result is observed for the $P_{h\perp}$-weighted asymmetries for positive pions, while relatively bigger effects are observed for the negative pions (see Figure 6.15).

Although very preliminar, this study already suggests that the real acceptance and smearing effects are less dramatic than those predicted by the Monte Carlo simulation.

6.6 Testing the stability of the method

The extrapolation in 4π of the experimental Collins and Sivers amplitudes, described in the previous section, was achieved under two very specific conditions: The fit was based on the 44-parameter PDF, optimized for the GMC_TRANS model but not necessarily for the experimental data, and the folding procedure was performed using the Born cross section derived from one of the two versions of the GMC_TRANS Monte Carlo.

To test the stability of these results, the method was applied under different conditions. In particular, a variety of PDFs were explored, based on different truncations of the Taylor expansion, and three different models for the Born cross section were compared. For the latter test, which is discussed first, the 44-parameter fit was used as a first guess.
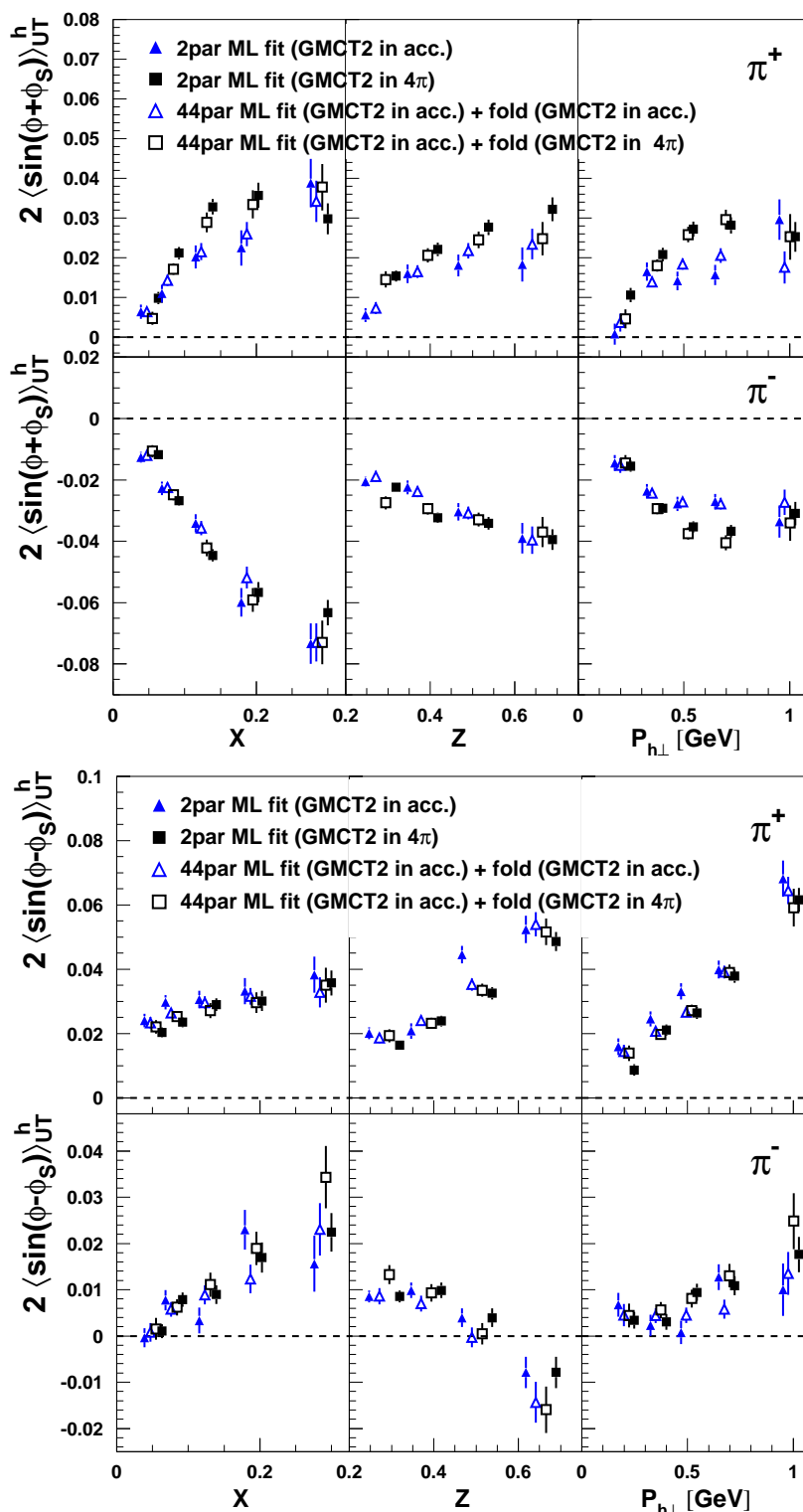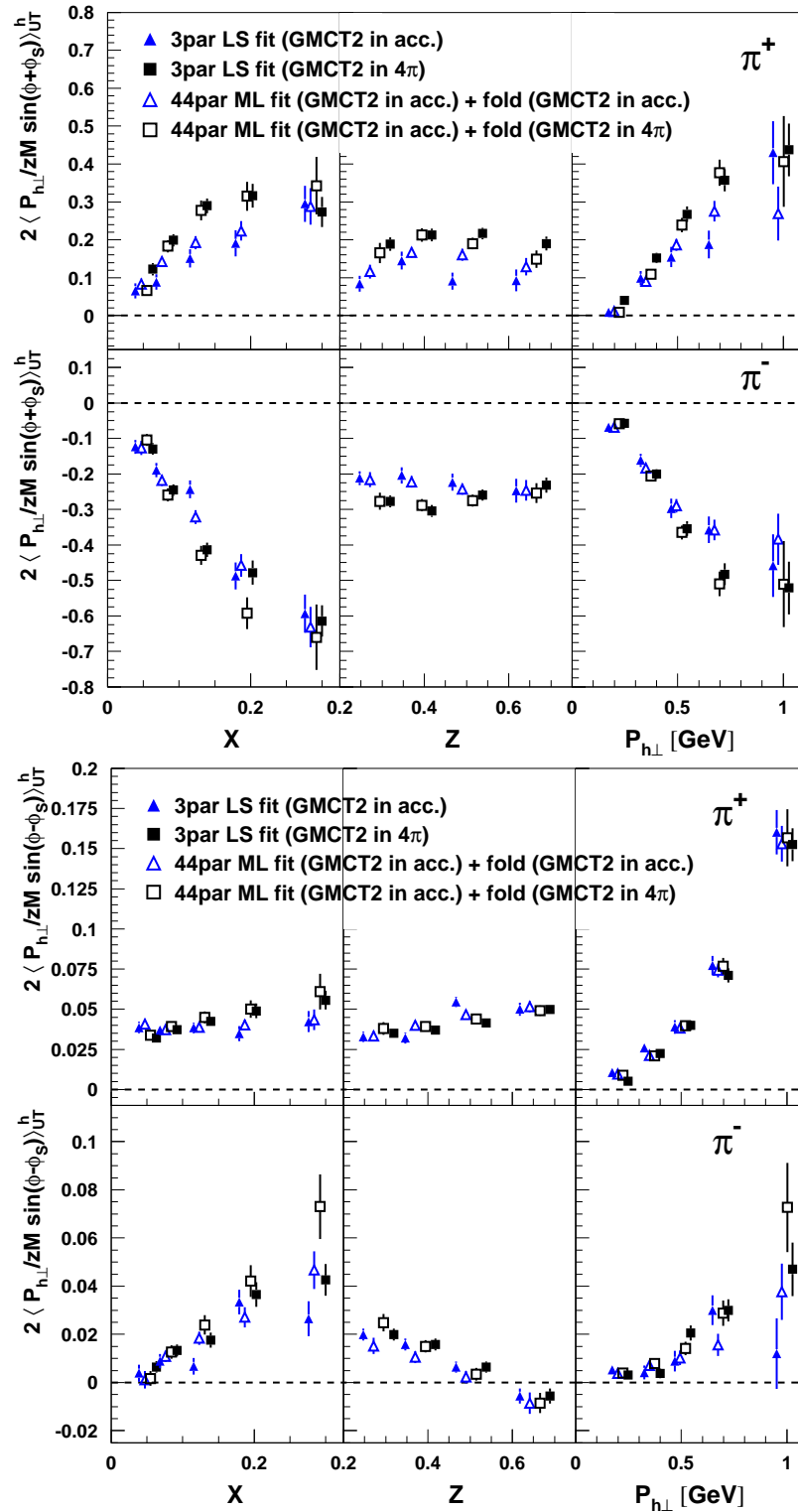
Figure 6.14: Unweighted Collins (upper half) and Sivers (lower half) moments for π^+ (upper panels) and π^- (lower panels) extracted from the full transverse data set (full squares). The amplitudes folded with the spin-independent cross section in the acceptance (open triangles) and in 4π (open circles) are also shown.

Figure 6.15: $P_{h\perp}$-weighted Collins (upper half) and Sivers (lower half) moments for π^+ (upper panels) and π^- (lower panels) extracted from the full transverse data set (full squares). The amplitudes folded with the spin-independent cross section in the acceptance (open triangles) and in 4π (open circles) are also shown.

6.6.1 Three models for the Born cross section

The folding procedure is dependent on the model for the SIDIS Born cross section. In order to test the sensibility of this procedure upon the choice of the model, the Born cross section was extracted from three different models: the two versions of GMC_TRANS, GMCT1 and GMCT2, which are based on different models for the Sivers function and on a different dependence of $\langle K_T^2 \rangle$ (cf. Section 6.3), and PYTHIA.

The projected (in 4π) Collins and the Sivers moments, obtained using the three different models mentioned above, are compared in Figure 6.16. The comparison shows that the Collins amplitudes folded with the Born cross section extracted from GMCT1 and GMCT2 are compatible in all kinematic bins, while systematic deviations are observed for those based on the PYTHIA generator. These deviations become significant in the intermediate to high z region (for both π^+ and π^-) and in the low $P_{h\perp}$ region (for π^+). No significant deviations are observed for the Sivers amplitudes. The differences on the extracted amplitudes obtained with the three different models for the Born cross section are regarded as a source of systematic uncertainty and are accounted for in the evaluation of the global systematic error (see Section 6.9).

6.6.2 The choice of the PDF

So far, the 44-parameter PDF displayed in eqn. (6.25) was used, as a first guess, to fit the selected events. The peculiar functional form of this PDF, which includes all first order terms plus a selection of second, third and fourth order terms, is motivated by the fact that it allows to reproduce satisfactorily the full kinematic dependence of the Collins and the Sivers amplitudes implemented in GMC_TRANS. Since, however, the asymmetry amplitudes extracted from the GMC_TRANS *reconstructed events* do not fully reproduce the experimental ones (cf. Figure 6.2), the latter might be better described by a different functional form based on a different truncation of the Taylor expansion and/or on the involvement of additional azimuthal amplitudes besides the Collins and Sivers ones. In particular, as discussed in Section 5.5.1, the $\langle \sin(\phi_S) \rangle_{UT}^h$ moment was found to significantly contribute to the Collins and Sivers fit results, while the other three sine moments ($\langle \sin(2\phi - \phi_S) \rangle_{UT}^h$, $\langle \sin(3\phi - \phi_S) \rangle_{UT}^h$ and $\langle \sin(2\phi + \phi_S) \rangle_{UT}^h$) were found to barely influence the results.

Since a virtually infinite number of possible combinations exists, only the most relevant cases were considered, as reported in Table 6.2. These cases include the basic 2-parameters PDF, with constant Collins and Sivers terms, the 5-parameters PDF, which, apart for the lack of the $\sin(2\phi + \phi_S) \rangle_{UT}^h$ moment, corresponds to the standard 6-parameters PDF (5.26), PDFs with Taylor expansions of increasing order (from 1st to 3rd), the 'standard' 44-parameters PDF and a 48-parameters PDF which also includes the $\langle \sin(\phi_S) \rangle_{UT}^h$ moment.

Although limited to the eight scenarios listed above, the choice of the "best" PDF requires a measure of the *goodness* of the maximum likelihood fit. Such a measure would be highly desirable since, similarly to the χ^2 in the standard χ^2-fits, it would provide a powerful tool to discriminate among the various PDFs. Only recently a general theory of goodness for unbinned maximum likelihood fits was developed, as reported in [Raj06]. According to this theory, in
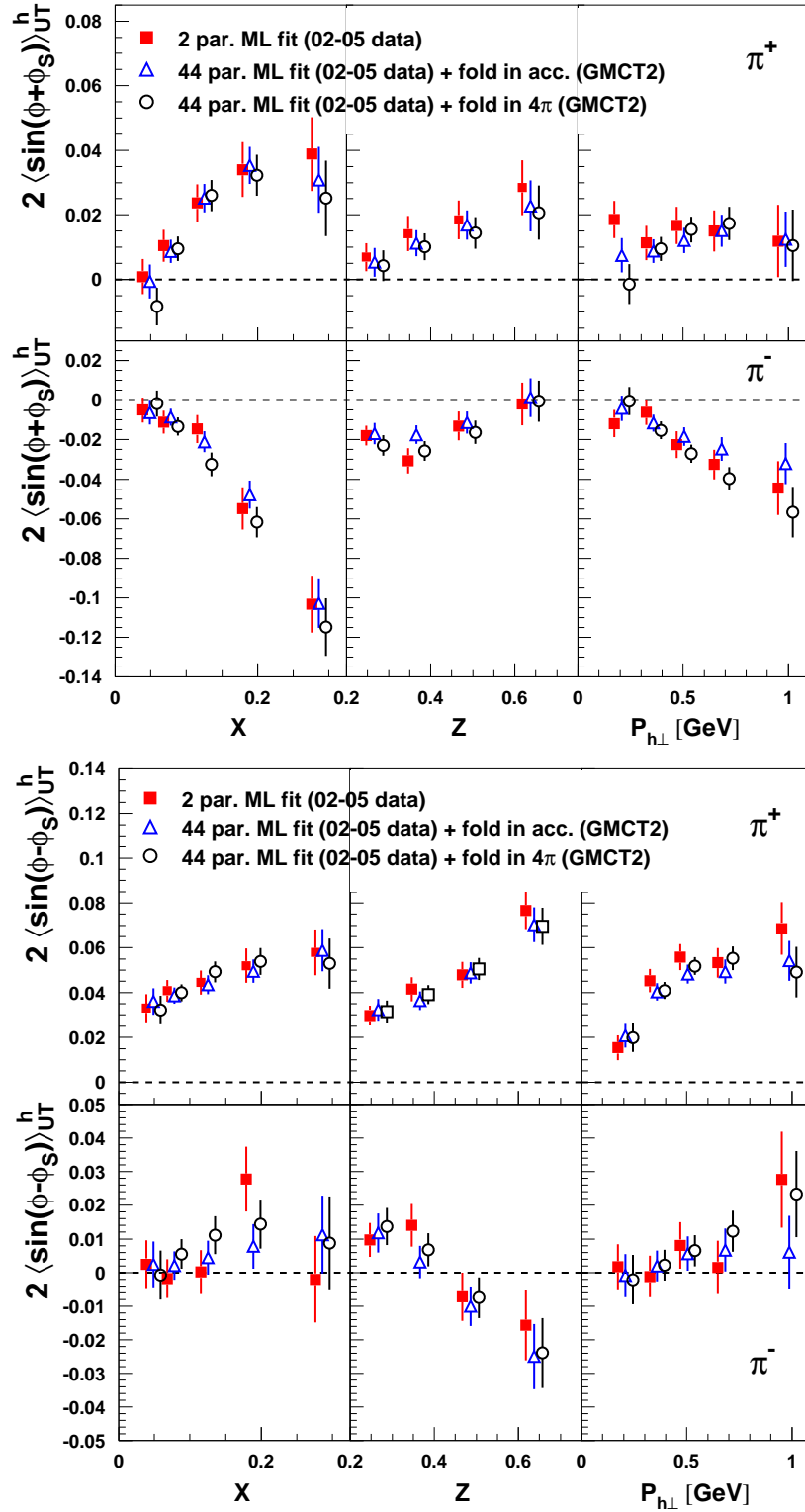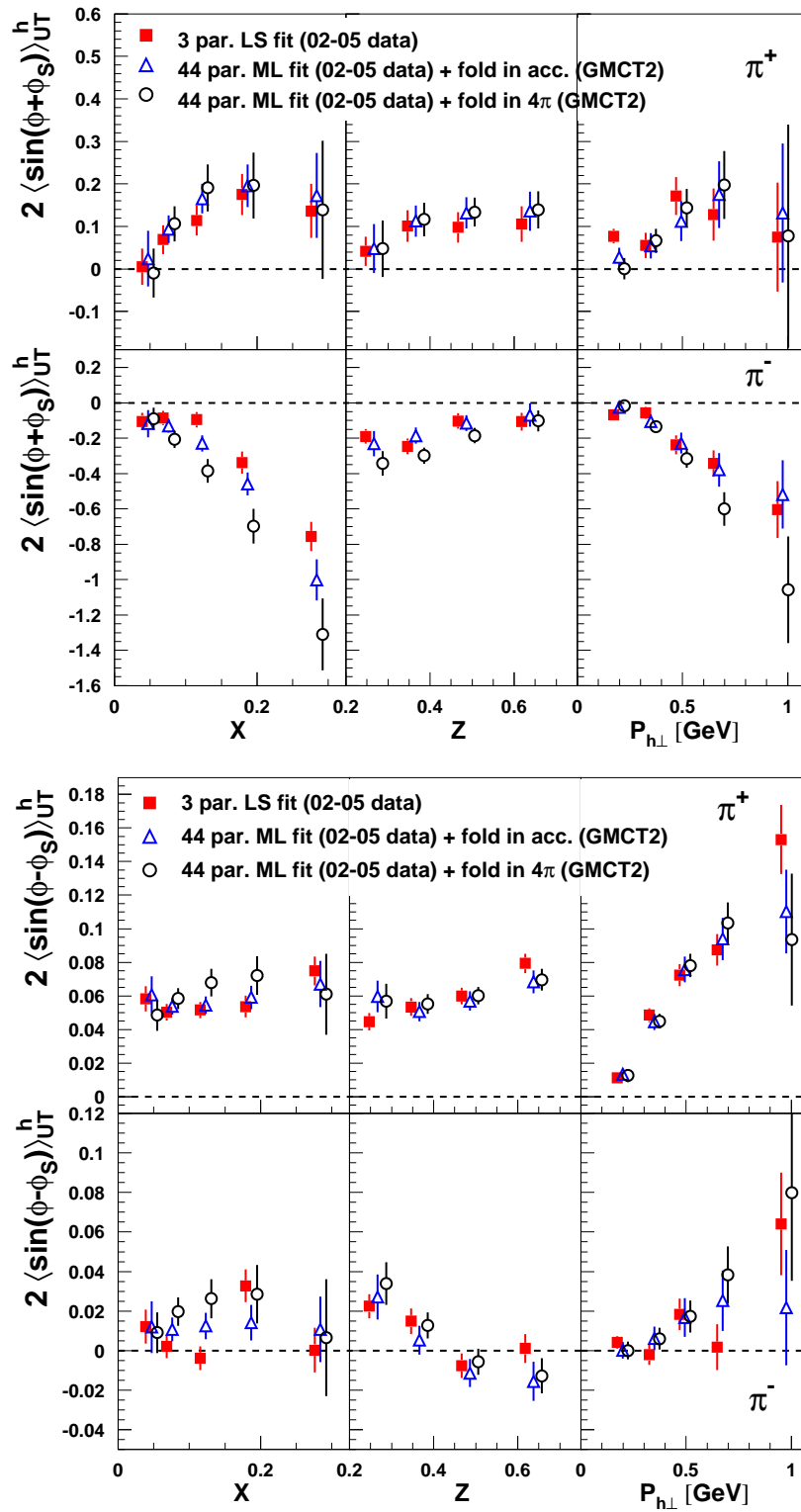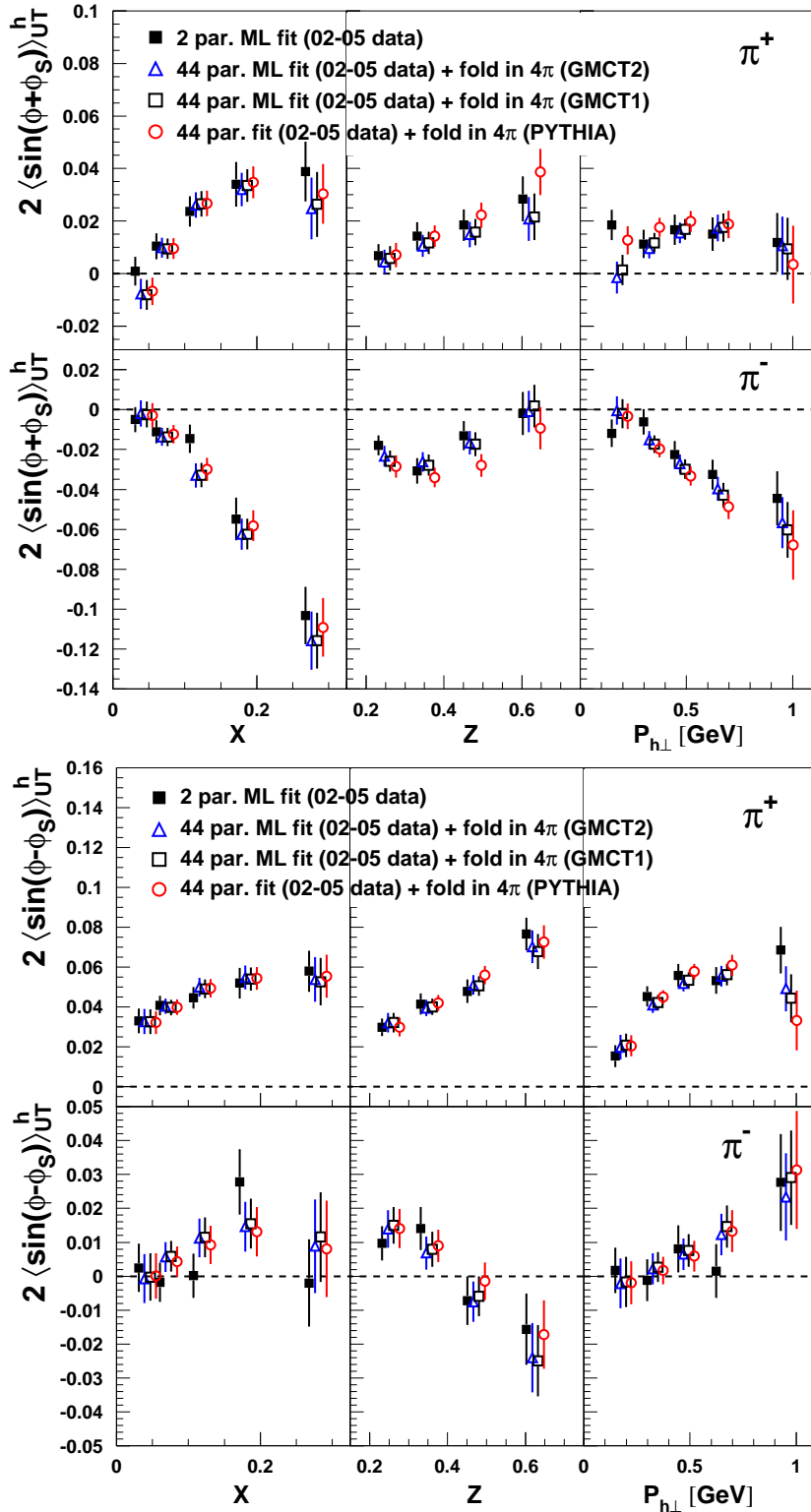
Figure 6.16: Unweighted Collins (upper half) and Sivers (lower half) moments for π^+ (upper panels) and π^- (lower panels) extracted from the full transverse data set (full squares) and their projections in 4π obtained with three different models for the Born cross section. The average kinematics of the bins has been slightly shifted to accommodate the three sets of results.

# par.	$\langle\sin(\phi + \phi_S)\rangle$	$\langle\sin(\phi - \phi_S)\rangle$	$\langle\sin(\phi_S)\rangle$
2	constant	constant	0
5*	constant	constant	constant
10	constant + 1st order	constant + 1st order	0
22	constant + 1st and 2nd order	constant + 1st and 2nd order	0
32	constant + 1st and 2nd order + selection of 3rd order	constant + 1st and 2nd order + selection of 3rd order	0
42	constant + 1st, 2nd and 3rd order	constant + 1st, 2nd and 3rd order	0
44	constant + 1st and 2nd order + selection of 3rd and 4th order	constant + 1st and 2nd order + selection of 3rd and 4th order	0
48	constant + 1st and 2nd order + selection of 3rd order	constant + 1st and 2nd order + selection of 3rd order	constant + 1st and 2nd order + selection of 3rd order

Table 6.2: The PDFs analyzed. The first column reports the number of parameters. The second, third and fourth columns report the terms included in the Taylor expansion for each of the three relevant azimuthal moments. The order refers to the powers of the kinematic variables x, z and $P_{h\perp}$ included in the Taylor expansion (Q^2 only appears at 1st order). The same functional form holds for all the azimuthal moments involved. * The 5-par. PDF also includes the $\langle\sin(2\phi - \phi_S)\rangle$ and the $\langle\sin(3\phi - \phi_S)\rangle$ sine moments.

order to measure the goodness of the ML fit for a set of N independently measured quantities $\mathbf{x}_i$, one should consider the *likelihood ratio*

$$\mathcal{L}_{\mathcal{R}} = \prod_{i=1}^{N} \frac{f(\mathbf{x}_i; \theta)}{f(\mathbf{x}_i)} \tag{6.26}$$

of the theoretically predicted probability density function $f(\mathbf{x}_i; \theta)$ to that of the a-priori *data probability density function* $f(\mathbf{x}_i)$. Unlike the standard likelihood function, the likelihood ratio is invariant under change of variable. This condition is necessary to allow for a measure of the goodness of the fit [Raj06]. In addiction, since the *data probability density* $f(\mathbf{x}_i)$ is constant with respect to the fit parameters θ, one needs to solve the same set of equations that one gets when maximizing the standard likelihood function (cf. eqn. (5.23)), thus resulting in the same parameter values at the maximum.

In order to evaluate the likelihood ratio $\mathcal{L}_{\mathcal{R}}$, one needs to evaluate the function $f(\mathbf{x}_i)$ at the observed event configurations $x_1, x_2, ..., x_N$. In statistics this problem is generally solved with the method of the Probability Density Estimators (PDE). In our contest the PDE was calculated using an approximated version of the approach described in [Raj06]. The details of the method are discussed in Appendix E.

The Negative Log-Likelihood Ratio $\mathcal{NLLR} \equiv -log_e \mathcal{L_R}$ at the maximum of the likelihood function provides a measure of the goodness of the fit. If, indeed, the functional form of the theoretically predicted probability density function $f(\mathbf{x}; \theta)$, expressed in terms of the fit parameters θ, reproduces the a-priori *data probability density function* $f(\mathbf{x}_i)$, one would have:

$$f_{optimal}(\mathbf{x}_i; \theta) \approx f(\mathbf{x}_i) \quad \Rightarrow \quad \mathcal{L_R} \approx 1 \quad \Rightarrow \quad \mathcal{NLLR} \approx 0 \; ; \tag{6.27}$$

if, on the other hand, the PDF is not adequate to reproduce the data, one would get $\mathcal{NLLR} \neq 0$. In particular, the worse the PDF is, the more the $\mathcal{NLLR}$ would differ from zero.

In order to use this technique efficiently, one needs to compare, for each PDF, the value of the negative log-likelihood ratio obtained in the fit of the real data, with that obtained in the fit of a similar amount of events generated by a Monte Carlo simulation in which the same PDF is implemented for the event generation. For the choice of the best PDF one should then consider non only the absolute value of $\mathcal{NLLR}_{Data}$ (i.e. its distance from 0), but also the relative distance between $\mathcal{NLLR}_{Data}$ and $\mathcal{NLLR}_{MC}$. The smaller this distance is, the more appropriate the PDF is for the description of the data.

To avoid the introduction of biases due to the use of specific models for the spin-dependent part of the cross section, the PYTHIA generator was used to generate events (within the HERMES acceptance) according to the spin-independent cross section. The azimuthal dependence of the cross section, due to the target transverse polarization, was then implemented a-posteriori. To this purpose, the azimuthal asymmetries were extracted from the experimental data for each of the PDFs tested, and used to create two Monte Carlo data sets with opposite transverse spin states. For instance, given a generic PDF

$$f(x, Q^2, z, P_{h\perp}, \phi, \phi_S, P_t; \theta) = 1 + P_t \cdot A(x, Q^2, z, P_{h\perp}; \theta) \cdot \sin(m\phi \pm n\phi_S) , \tag{6.28}$$

in which the asymmetry A is expressed in terms of a set of parameters θ, previously extracted in a fit of the experimental data, the spin-up and spin-down normalized cross sections were built up from the PYTHIA events according to:

$$\sigma^\uparrow(x, Q^2, z, P_{h\perp}, \phi, \phi_S, P_t; \theta) = \frac{1}{2}\left[1 + |P_t| \cdot A(x, Q^2, z, P_{h\perp}; \theta)\right] \cdot \sin(m\phi \pm n\phi_S) , \tag{6.29}$$

$$\sigma^\downarrow(x, Q^2, z, P_{h\perp}, \phi, \phi_S, P_t; \theta) = \frac{1}{2}\left[1 - |P_t| \cdot A(x, Q^2, z, P_{h\perp}; \theta)\right] \cdot \sin(m\phi \pm n\phi_S) . \tag{6.30}$$

Since, by construction, $\sigma^\uparrow + \sigma^\downarrow = 1 \quad \Rightarrow \quad 0 < \sigma^\uparrow < 1$, a random number extraction between 0 and 1, modulated by $\sigma^\uparrow$, allowed to associate to each PYTHIA event the sign of the target polarization according to the real (experimental) spin-dependent cross section. In particular the experimental average value $|P_t| = 0.73$ was used (cf. Section 5.4.1).

Since the Monte Carlo events are generated on a statistic basis, one may obtain different maxima of the likelihood ratio for different, although statistically equivalent, Monte Carlo data sets, all based on the same model. For this reason, for each of the PDFs tested, 48 such Monte Carlo data sets were produced, each time resulting in a distribution of the $\mathcal{NLLR}_{MC_j}^{PDF}$ ($j = 1, 48$)

values. The mean values of such distributions, $\langle \mathcal{NLLR}_{MC}^{PDF} \rangle$, were then compared with the corresponding values of the $\mathcal{NLLR}_{Data}^{PDF}$, obtained with the use of the same PDF.

As an example, the results obtained with the 44-parameters PDF are shown in Figure 6.18 for both positive and negative pions. Here the distribution of the negative log likelihood ratios $\mathcal{NLLR}_{MC_j}^{44Par}$ is shown together with the corresponding value from the data, $\mathcal{NLLR}_{Data}^{44Par}$ (blue boxes). For the positive (negative) pions case, the distribution of $\mathcal{NLLR}_{MC_j}^{44Par}$ is centered at 124.4 (184.4) with a RMS of 26 (22) and $\mathcal{NLLR}_{Data}^{44Par}$ equals 47 (124). As a result, the distance between the mean value $\langle \mathcal{NLLR}_{MC}^{44Par} \rangle$ and $\mathcal{NLLR}_{Data}^{44Par}$ is $3.0 \times RMS$ ($2.7 \times RMS$). These numbers allow to identify the best PDF among those tested. According to this method, indeed, the best PDF is the one which results in the smallest value for $\mathcal{NLLR}_{Data}^{PDF}$ and in the smallest relative distance (in RMS) between $\mathcal{NLLR}_{Data}^{PDF}$ and $\langle \mathcal{NLLR}_{MC}^{PDF} \rangle$.

The results for all the PDFs tested are reported in Table 6.3 and shown in Figure 6.17. As expected, both the negative log likelihood ratios and the relative distances between Data and MC decrease for PDFs with higher number of parameters. This trend is faster for the PDFs with a smaller number of parameters ($2 \rightarrow 5 \rightarrow 10$), and becomes slower and slower for the those with a larger number of parameters ($10 \rightarrow ... \rightarrow 48$). These results indicate that the more terms are included in the Taylor expansion, the more adequate the PDF is. The improvement, however, saturates beyond a certain number of parameters.

Although in the saturation region, an inversion of the trend is observed from 44 to 48 parameters for positive pions. This leads to the conclusion that, although the 48-parameters PDF includes the $\langle \sin(\phi_S) \rangle$ modulation, a higher number of parameters would be desirable. The 48-parameters PDF is anyway considered the best choice since the $\langle \sin(\phi_S) \rangle$ modulation is highly recommended to be taken into account (cf. Section 5.5.1). This conclusion is anyway supported by the monotonically decreasing values of the $\mathcal{NLLR}_{Data}^{PDF}$ with increasing number of terms involved in the PDF (cf. Figure 6.17). It is important to note, however, that, although monotonically decreasing, the $\mathcal{NLLR}_{Data}^{PDF}$ never reaches 0. This is due to the fact that all the PDFs used are based on a truncation of the Taylor expansion, and are thus only approximations of the 'true' *data probability density function*.

As a consistency check for the method, the deviations

$$\Delta_{i,j} = \frac{\text{Par}(i)_{Data} - \text{Par}(i)_{MC_j}}{\sigma_{\text{Par}(i)_{Data}}} \qquad (i = 1, \# \text{ par. } ; \ j = 1, 48) \qquad (6.31)$$

were calculated. Here the index i spans the values $\text{Par}(i)$ of the parameters of the PDF and the index j the 48 MC data sets. As expected, the mean values $\text{Diff} = \Delta_i = \langle \Delta_{i,j} \rangle$ fluctuate around 0 and the RMSs around 1, indicating that no significant biases are introduced in the method. As an example, the results relative to the 48-parameters PDF are shown in Figure 6.19 for positive pions. For sake of clarity, the 16 parameters for Collins and the 16 for Sivers are shown separately. Similar results are obtained for the negative pions and for all the other PDFs tested.

Positive pions			
PDF (# of par.)	$\mathcal{NLLR}_{Data}$	$\langle\mathcal{NLLR}_{MC}\rangle$ (RMS)	$\Delta\,[n\times\text{RMS}]$
2	156	382 (18)	12.8
5	150	309 (22)	7.1
10	88	196 (26)	4.1
22	62	150 (24)	3.7
32	55	139 (25)	3.4
42	49	127 (25)	3.1
44	47	124 (26)	3.0
48	44	131 (27)	3.2
Negative pions			
PDF (# of par.)	$\mathcal{NLLR}_{Data}$	$\langle\mathcal{NLLR}_{MC}\rangle$ (RMS)	$\Delta\,[n\times\text{RMS}]$
2	198	300 (19)	5.3
5	168	272 (20)	5.1
10	144	223 (23)	3.5
22	134	202 (22)	3.0
32	130	194 (23)	2.8
42	122	184 (22)	2.8
44	124	184 (22)	2.7
48	106	170 (24)	2.7

Table 6.3: The values of $\mathcal{NLLR}_{Data}$ and $\langle\mathcal{NLLR}_{MC}\rangle$ are reported, for all the PDFs tested, for positive (upper table) and negative (lower table) pions. The last column reports the distance between $\mathcal{NLLR}_{Data}$ and $\langle\mathcal{NLLR}_{MC}\rangle$, expressed in units of the RMS.
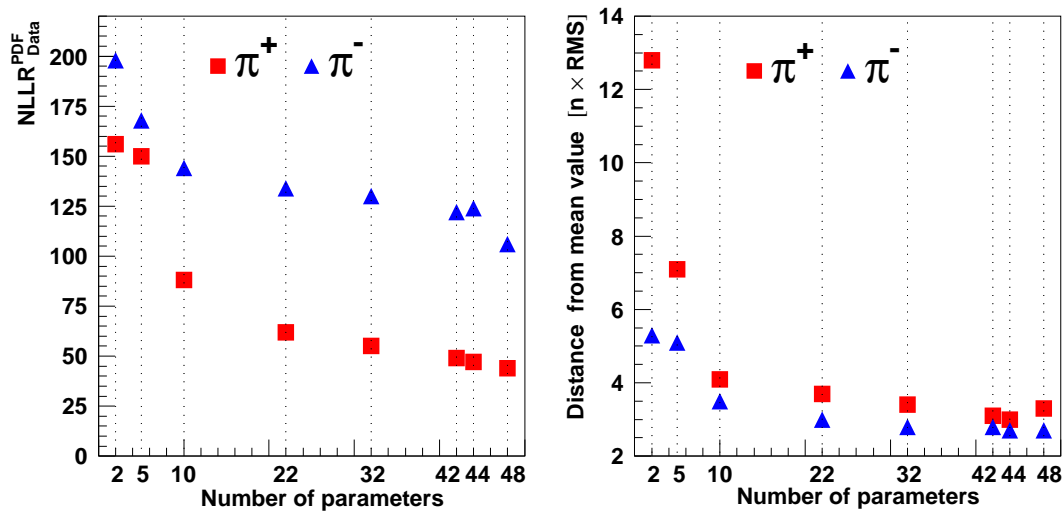
Figure 6.17: Values of $\mathcal{NLLR}_{Data}$ (left panel) and distance between $\mathcal{NLLR}_{Data}$ and $\langle\mathcal{NLLR}_{MC}\rangle$, expressed in units of RMS (right panel), as a function of the number of parameters involved in the PDF.
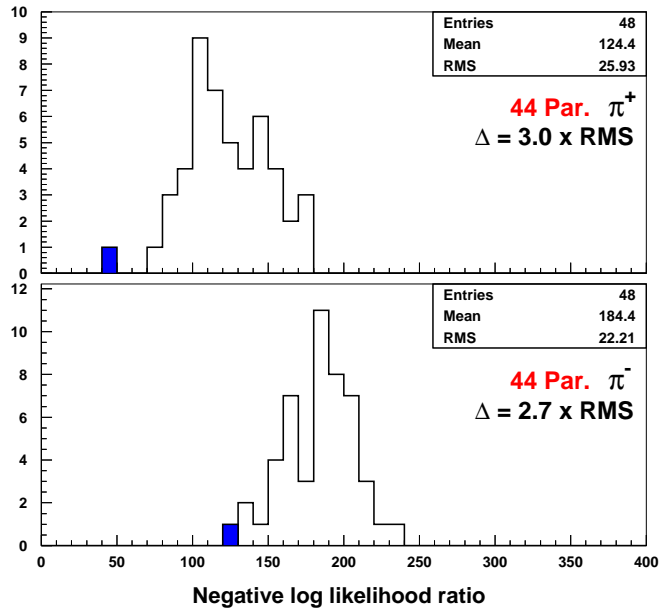
Figure 6.18: The negative log-likelihood ratio for the data (blue box), obtained with the 44-parameters PDF, is reported together with the distribution of the 48 Monte Carlo negative log-likelihood ratios $\mathcal{NLLR}_{MC_j}$ obtained with the same PDF for positive (upper panel) and negative (lower panel) pions.
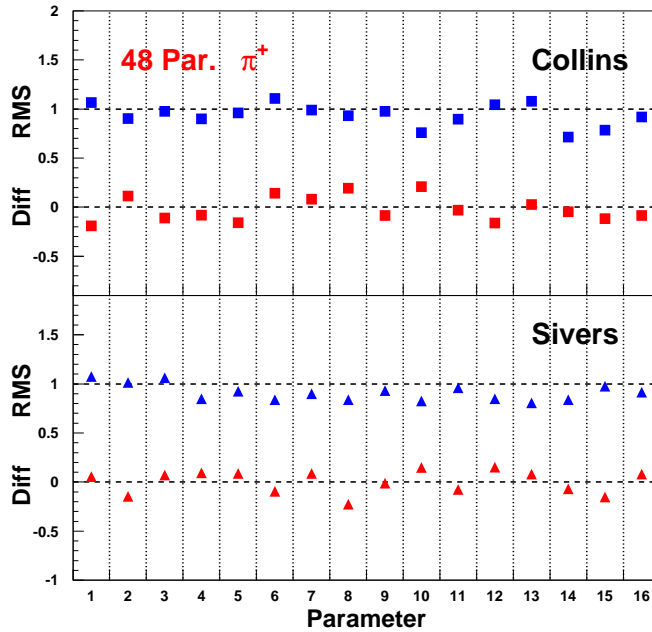
Figure 6.19: The mean values (Diff) and the RMSs of the deviations calculated, for each parameter, according to eqn. (6.31) for the 48-parameters PDF for positive pions. The 16 parameters for Collins and the 16 for Sivers are shown separately.

6.7 The PDFs for the five hadron types

The choice of the 48-parameters PDF was possible for the charged pions, thanks to their relatively high statistics. Instead, a smaller number of terms in the Taylor expansion was required for the convergence of the fit for the other three hadron types (π^0, K^+ and K^-) due to their much smaller statistics (cf. Table 5.5).

As a criterion for the choice of the corresponding PDFs, the $\langle \sin(\phi_S) \rangle$ modulation was included and the higher order terms of the Taylor expansion were reduced until the fit converged. As a result, a 45-parameters (15 parameters $\times$ 3 moments) PDF was selected for the K^+ and a 18-parameters (6 parameters $\times$ 3 moments) PDF was selected for both the K^+ and π^0. In summary, the three PDFs selected are of the form:

$$f_h(x, Q^2, z, P_{h\perp}, \phi, \phi_S, P_t; \alpha_1, \alpha_2, \alpha_3) =$$

$$1 + P_t \cdot \left[A_1^h(x, Q^2, z, P_{h\perp}; \alpha_1) \cdot \sin(\phi + \phi_S) + \right.$$

$$A_2^h(x, Q^2, z, P_{h\perp}; \alpha_2) \cdot \sin(\phi - \phi_S)$$

$$\left. A_3^h(x, Q^2, z, P_{h\perp}; \alpha_3) \cdot \sin(\phi_S) \right] , \tag{6.32}$$

where, for each of the three azimuthal moments ($i = 1, 2, 3$),:

$$A_i^{\pi^+, \pi^-}(x, Q^2, z, P_{h\perp}; \alpha_i) = a_i(1) + a_i(2) \cdot x' + a_i(3) \cdot Q'^2 + a_i(4) \cdot z' +$$

$$a_i(5) \cdot P'_{h\perp} + a_i(6) \cdot x'^2 + a_i(7) \cdot z'^2 + a_i(8) \cdot P'^2_{h\perp} +$$

$$a_i(9) \cdot x' \cdot z' + a_i(10) \cdot x' \cdot P'_{h\perp} + a_i(11) \cdot z' \cdot P'_{h\perp} +$$

$$a_i(12) \cdot x'^3 + a_i(13) \cdot x' \cdot z'^2 + a_i(14) \cdot x'^2 \cdot z' +$$

$$a_i(15) \cdot x'^2 \cdot P'_{h\perp} + a_i(16) \cdot x' \cdot P'^2_{h\perp} , \tag{6.33}$$

$$A_i^{K^+}(x, Q^2, z, P_{h\perp}; \alpha_i) = a_i(1) + a_i(2) \cdot x' + a_i(3) \cdot Q'^2 + a_i(4) \cdot z' +$$

$$a_i(5) \cdot P'_{h\perp} + a_i(6) \cdot x'^2 + a_i(7) \cdot z'^2 + a_i(8) \cdot P'^2_{h\perp} +$$

$$a_i(9) \cdot x' \cdot z' + a_i(10) \cdot x' \cdot P'_{h\perp} + a_i(11) \cdot z' \cdot P'_{h\perp} +$$

$$a_i(12) \cdot x'^3 + a_i(13) \cdot x' \cdot z'^2 + a_i(14) \cdot x'^2 \cdot z' +$$

$$a_i(15) \cdot x'^2 \cdot P'_{h\perp} , \tag{6.34}$$

$$A_i^{K^-, \pi^0}(x, Q^2, z, P_{h\perp}; \alpha_i) = a_i(1) + a_i(2) \cdot x' + a_i(3) \cdot Q'^2 + a_i(4) \cdot z' +$$

$$a_i(5) \cdot P'_{h\perp} + a_i(6) \cdot x'^2 , \tag{6.35}$$

and:

$$x' = x - \langle x \rangle \quad Q'^2 = Q^2 - \langle Q^2 \rangle \quad z' = z - \langle z \rangle \quad P'_{h\perp} = P_{h\perp} - \langle P_{h\perp} \rangle .$$

6.8 Correcting for the acceptance effects

The PDFs showed in the previous section were used to fit the data relative to the five hadron types analyzed. The extracted Collins and Sivers amplitudes, expressed in terms of the corresponding sets of parameters, where then folded, according to the procedure discussed in Section 6.5.1, with the spin-independent cross section provided by the PYTHIA generator. As a result, the Collins and Sivers amplitudes projected in 4π and inside the acceptance itself were obtained for the five hadron types.

The difference, in each kinematic bin, between the Collins and Sivers moments projected in 4π and those projected within the acceptance, was then used to correct for the acceptance effects. The final results for the Collins and Sivers moments, presented in Chapter 7, are in fact obtained by correcting for this difference the amplitudes extracted in each bin with the 'standard 6-parameters PDF' (5.26). This correction introduces an extrapolation error which was taken into account in the estimation of the global systematic error (cf. Section 6.9).

6.9 The contributions to the systematic error

In Section 5.5.8 a partial estimation of the systematic error affecting the extracted Collins and Sivers amplitudes was discussed. Here three additional contributions are taken into account.

The first one accounts for the smearing effects, estimated in Section 6.4.2. The differences between 'smeared' and 'unsmeared' amplitudes were regarded as a systematic error due to the detector smearing of the event kinematics. In particular, in order to get rid of the fluctuations observed in the lower halves of Figures 6.5 – 6.6, which are of statistical nature, the average values of the differences for each kinematic variable were considered.

The second one arises from the choice of the Monte Carlo generator for the extraction of the spin-independent cross section to be used in the folding procedure. As discussed in Section 6.6.1, the spin-independent cross section was extracted with three different MC generators: the two versions (GMCT1 and GMCT2) of GMC_TRANS and PYTHIA. For the final results, the PYTHIA generator was chosen since, unlike GMC_TRANS, it also generates charged kaons tracks. Since, however, systematic deviations were observed between the moments folded with the three different Born cross sections (cf. Figure 6.16), a systematic error was assigned accordingly.

The third contribution accounts for the uncertainty that affects the correction for the acceptance effects (cf. Section 6.8). This uncertainty arises from the errors of the original fit parameters. These errors, which are of statistical nature, are propagated, through the folding procedure, to get the errors of the projected (in 4π and inside the acceptance) Collins and Sivers amplitudes. These final errors then reflect the precision of the correction for the acceptance and are thus regarded as systematic errors. In particular, this uncertainty was found to represent the dominant contribution to the total systematic error.

To summarize, the three sources of systematic errors related to the acceptance studies reported in this chapter are:

- Contribution due to the detector smearing

- Contribution due to the choice of the Monte Carlo generator for the extraction of the spin-independent cross section

- Contribution due to the correction for the acceptance effects

As an example, Figures 6.20 – 6.21 show the unweighted (upper halves) and the $P_{h\perp}$-weighted (lower halves) Collins and Sivers moments for the charged pions. In each plot the amplitudes extracted with the standard extraction method[3], not corrected for the acceptance effects, are compared with those extracted with the 48-parameters PDF (cf. eqns. (6.32-6.33)) and folded with the PYTHIA spin-independent cross section in 4π and within the HERMES acceptance. The yellow bands represent the systematic errors obtained adding in quadrature the three contributions listed above.

The total systematic errors, to be associated to the Collins and Sivers amplitudes corrected for the acceptance effects (see Chapter 7), was then obtained adding in quadrature all the contributions, included those reported in Section 5.5.8.

---

[3]For consistency, the 3-parameters ML fit for unweighted and 4-parameters LS fit for $P_{h\perp}$-weighted amplitudes were used.
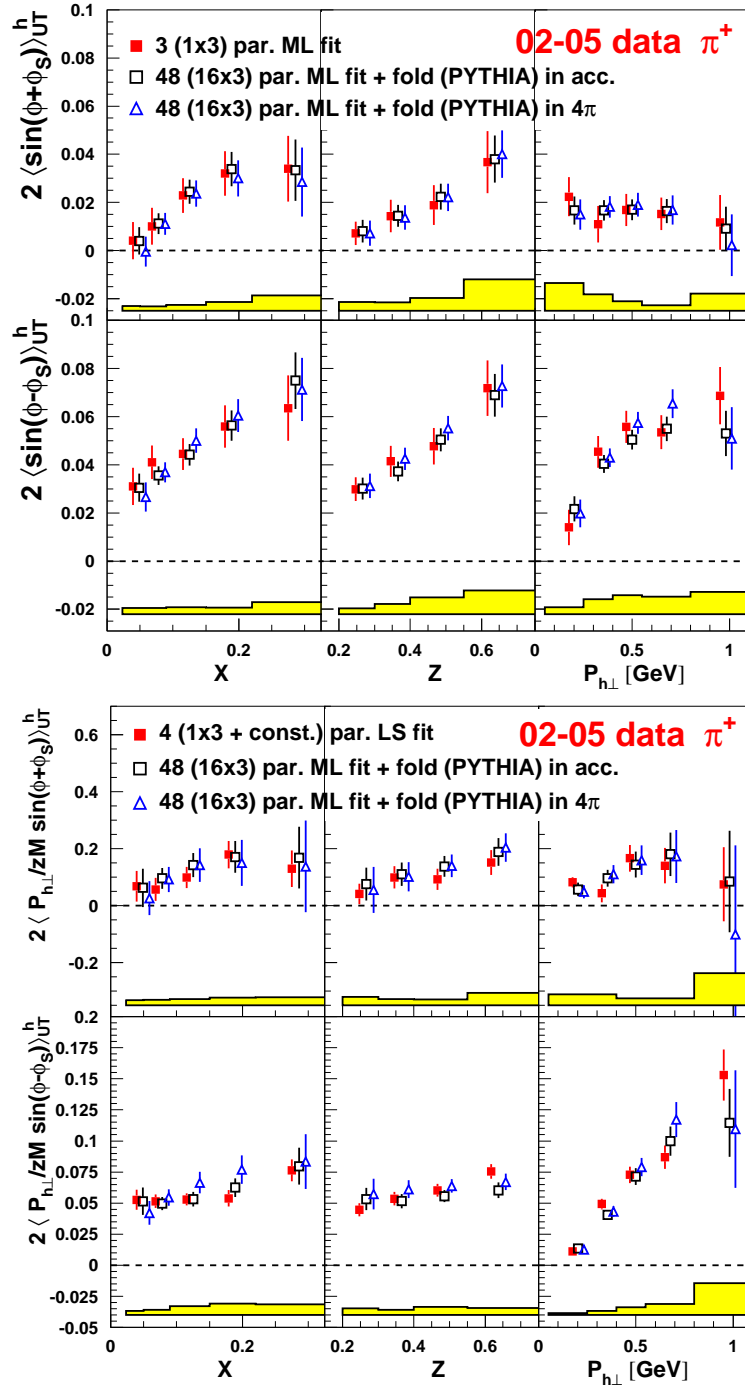
Figure 6.20: Unweighted (upper half) and $P_{h\perp}$-weighted (lower half) Collins (upper panels) and Sivers (lower panels) amplitudes for positive pions. The full squares represent the unweighted ($P_{h\perp}$-weighted) amplitudes extracted with a 3-par. (4-par.) fit (i.e. including also the $\sin(\phi_s)$ modulation) based on the standard method outlined in Chapter 5. Open triangles and open squares represent the amplitudes extracted with the 48-parameters fit and folded with the spin-independent cross section in 4π and within the acceptance, respectively. The yellow bands represent the systematic errors as estimated in Section 6.9.
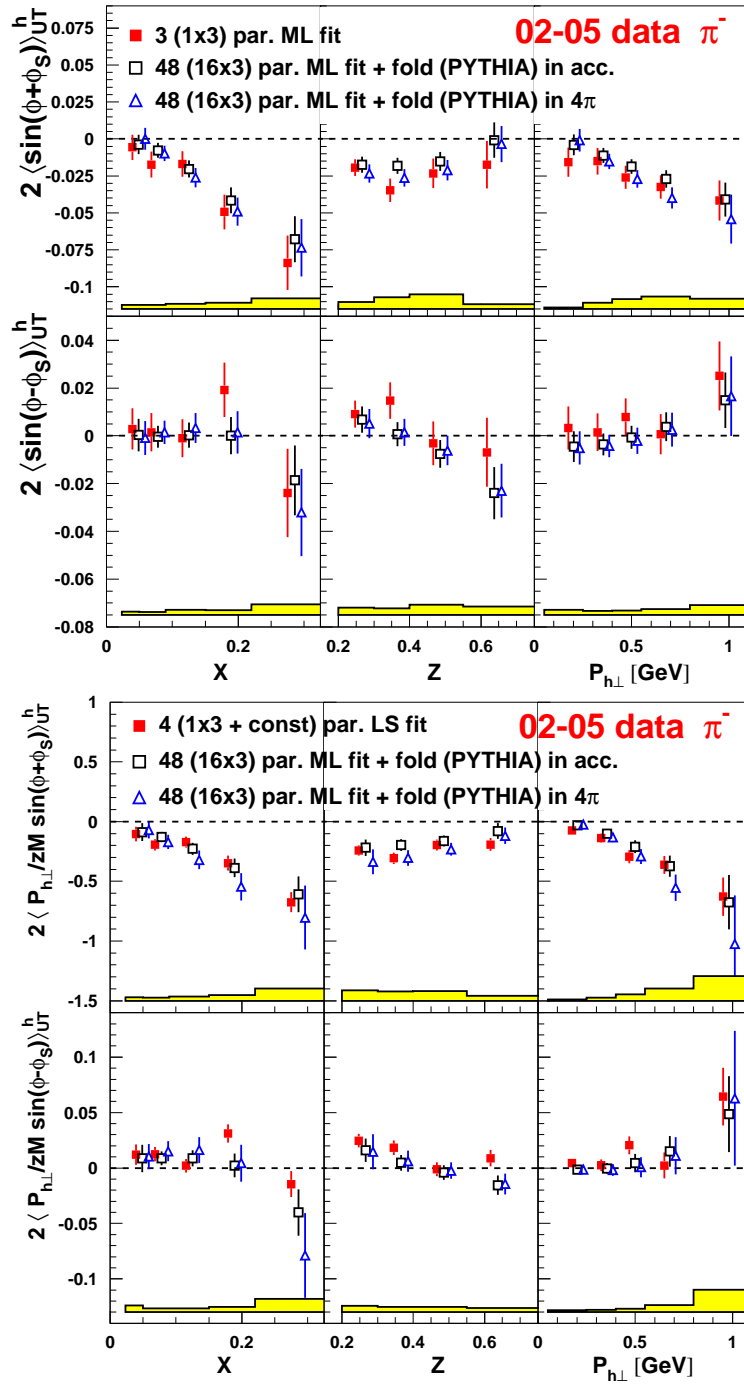
Figure 6.21: Unweighted (upper half) and $P_{h\perp}$-weighted (lower half) Collins (upper panels) and Sivers (lower panels) amplitudes for negative pions. The full squares represent the unweighted ($P_{h\perp}$-weighted) amplitudes extracted with a 3-par. (4-par.) fit (i.e. including also the $\sin(\phi_s)$ modulation) based on the standard method outlined in Chapter 5. Open triangles and open squares represent the amplitudes extracted with the 48-parameters fit and folded with the spin-independent cross section in 4π and within the acceptance, respectively. The yellow bands represent the systematic errors as estimated in Section 6.9.

Chapter 7

Results and interpretation

As discussed in Chapter 5, the Collins and Sivers moments were extracted simultaneously through a 6-parameters maximum likelihood fit based on the PDF (5.26). The results are shown in Figures 5.22–5.23. Similarly, the $P_{h\perp}$-weighted Collins and Sivers amplitudes (not shown) were extracted with a 7-parameters fit based on the least square method[1]. This fit includes the same six azimuthal moments used for the ML fit plus a constant term. The correlations between the extracted Collins and the Sivers amplitudes vary over the different kinematic bins and are in the order of -0.5.

In Chapter 6, an innovative method for the estimation of the effects due to the limited acceptance of the HERMES spectrometer was introduced. This method allowed to fold the extracted Collins and Sivers moments with the spin-independent cross section to get their projections in 4π and within the acceptance itself. The acceptance effects were then estimated as the difference between the amplitudes projected in 4π and those projected within the acceptance (see Figures $6.20 - 6.21$).

The results of the studies presented in Chapters 5 and 6 were combined to get the final results presented here. As discussed in Section 6.8, the final results for the Collins and Sivers moments were obtained by correcting for the acceptance effects the amplitudes obtained with the standard extraction method. These corrected amplitudes then represent the results that one would obtain with an ideal detector with a full coverage of the solid angle.

7.1 The Collins moments

The unweighted and $P_{h\perp}$-weighted Collins moments for pions and charged kaons, corrected for acceptance, are shown as a function of x, z, $P_{h\perp}$, y and Q^2 in Figures 7.1 and 7.2, respectively. The yellow bands, obtained by adding in quadrature all the contributions discussed in Sections 5.5.8 and 6.9, represent the total systematic errors. The amplitudes are affected by an overall 7.9% scale uncertainty, associated to the measure of the target polarization (cf. Section 5.5.8).

---

[1]As discussed in Section 6.4.1, no implementation exists at the moment for the $P_{h\perp}$-weighted asymmetries in the maximum likelihood fit.

Figure 7.1: Unweighted Collins amplitudes extracted from the full HERMES transverse data set with the standard 6-parameters ML fit. The amplitudes are corrected for the acceptance effects. The yellow bands represent the total systematic errors.
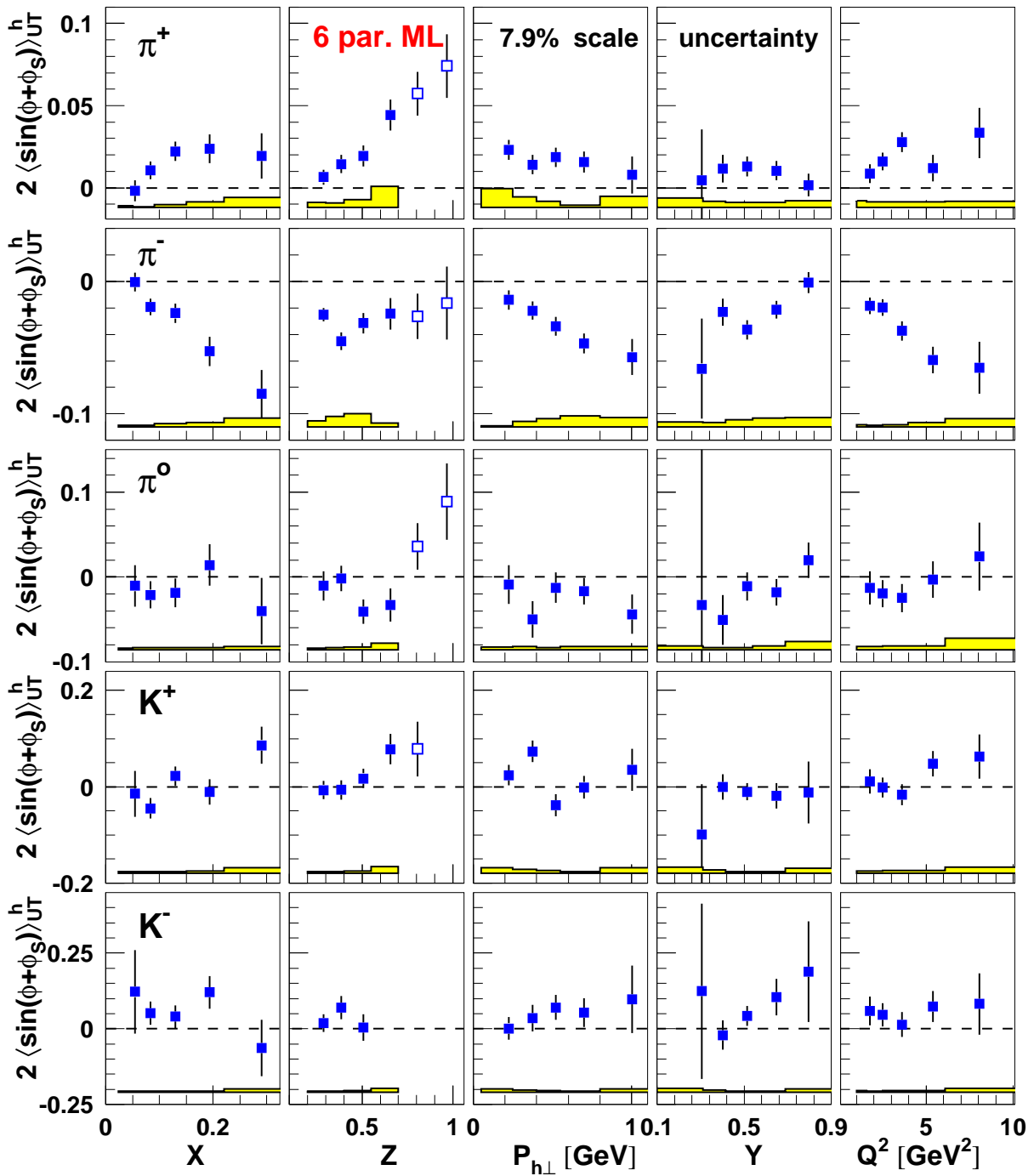
Figure 7.2: $P_{h\perp}$-weighted Collins amplitudes extracted from the full HERMES transverse data set with the standard 6-parameters ML fit. The amplitudes are corrected for the acceptance effects. The yellow bands represent the total systematic errors.
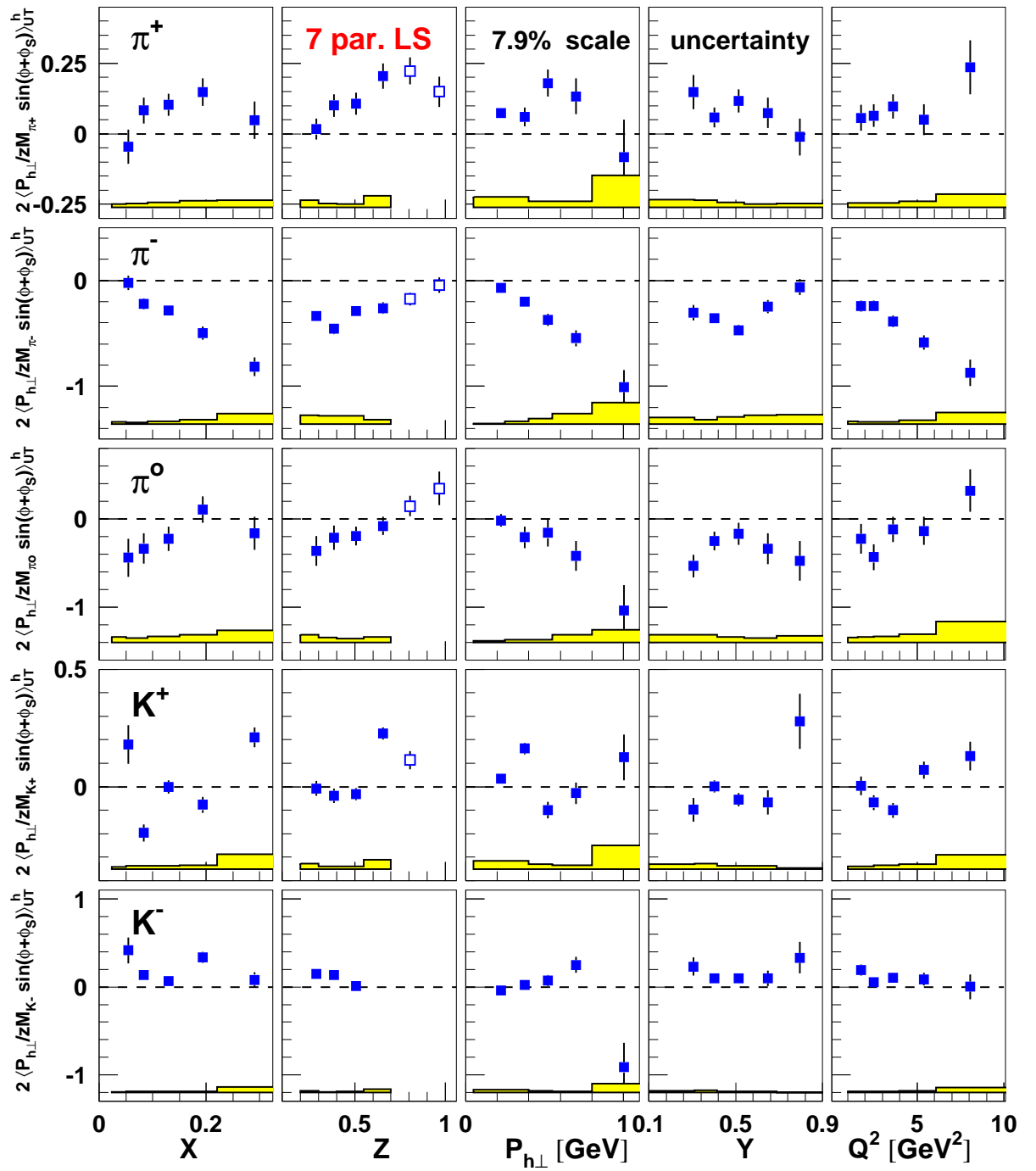
The results show a significantly positive amplitude for π^+ and a significantly negative amplitude for π^-. Because of the u quark dominance in DIS, due to the quark charge factor e_q^2 weighting the contribution of the different quark flavours in the cross section, both π^+ and π^- are likely generated in the fragmentation an u quark. Thus, the Collins moments of both π^+ and π^- receive a dominant contribution from the u quarks of the proton. As a consequence, the different sign between the Collins amplitudes for π^+ and π^- can only arise from the different fragmentation functions involved. While the fragmentation of an u quark into a π^+ is favoured, since the π^+ contains a valence u quark, the fragmentation of an u quark into a π^- is unfavored (cf. eqns. (3.52-3.53)). The Collins amplitudes for π^- thus suggests that the unfavored Collins function is of roughly the same magnitude of the favoured one, but with opposite sign:

$$H_{1,\mathrm{unfav}}^{\perp,u\to\pi^-}(z,z^2 k_T^2) \approx -H_{1,\mathrm{fav}}^{\perp,u\to\pi^+}(z,z^2 k_T^2) \, . \tag{7.1}$$

Since no gluon transversity can exist in a proton (cf. Section 3.2), the transversity distribution of the sea quarks, which are produced in pairs in the gluon splitting, is expected to be small. The increase of the Collins amplitudes with increasing x, observed for both π^+ and π^-, can then be interpreted as the evidence that the transversity is a pure valence object (cf. Section 3.2), and thus dominates the high x region. Since no Q^2 dependence is expected for leading-twist cross section terms, the observed Q^2 dependence of the Collins moments for the charged pions can only be attributed to the strong correlation between x and Q^2 (cf. Figure 5.5).

The Collins amplitude for π^0, which is consistent with zero, is in agreement with the expectations based on the Isospin Relation (cf. Section 5.6), which predicts, for the π^0, an amplitude intermediate between those of π^+ and π^-.

Due to the u quark dominance, one would naïvely expect similar Collins amplitudes for pions and kaons. However, the amplitudes for K^+ are systematically smaller that those for π^+ in the full kinematic range, even though they are compatible within the statistical uncertainty[2]. This difference might be due to the fact that, like in the case of the spin-independent fragmentation functions, the Collins function may differ for fragmentation of a u quark into a π^+ or into a K^+. On the other hand, the Collins amplitudes for π^- and K^- are not expected to be similar, not only because of a different Collins fragmentation function, but also because the K^- is a purely sea object, i.e. it contains only sea-quark flavours of the proton ($\bar{u}, s$).

A phenomenological explanation of the Collins effect based on the string-fragmentation model (cf. Section 3.7) is presented in [Art93] and illustrated in Figure 7.3. Chart (a) shows the absorption of the virtual photon by the struck quark which reverses the quark polarization component in the lepton scattering plane. When the string that connects the struck quark and the nucleon remnant breaks, chart (b), a quark-antiquark pair is produced with vacuum quantum numbers $J^P = 0^+$. Since the positive parity of this state requires aligned spins of quarks and antiquarks, an orbital angular momentum of $L = 1$ has to compensate the spins. This angular momentum then creates a transverse momentum of the produced pseudo-scalar meson. As a result, the outgoing meson is deflected with respect to the virtual-photon direction, indicated by an open arrow in chart (c).

---

[2]This can be inferred from Figures 7.1, paying attention to the fact that a different vertical scale is used for pions and kaons.

$\phi_S = 0$

(a)

$\phi_S = \pi/2$

(d)

(b) $L = 1$

(e) $L = 1$

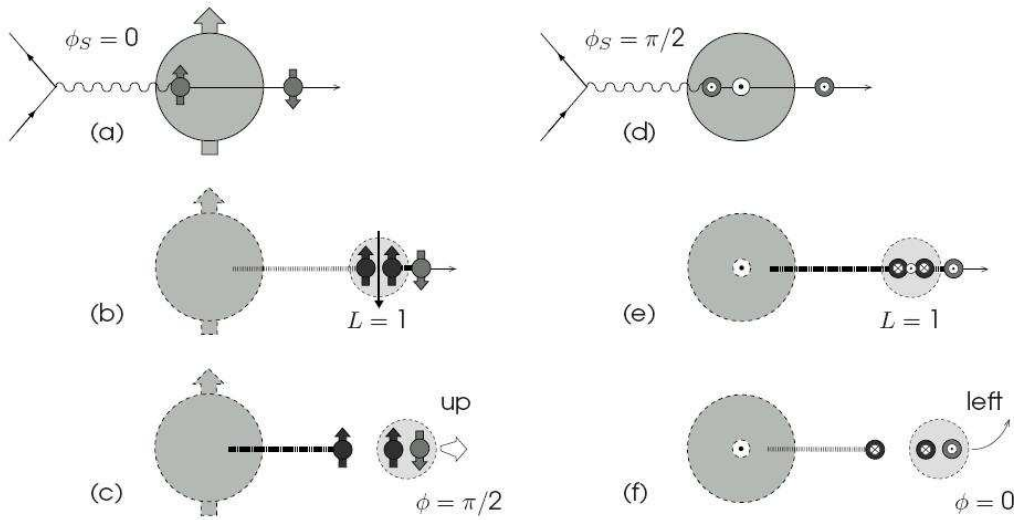(c) up $\phi = \pi/2$

(f) left $\phi = 0$

Figure 7.3: Collins effect in the string fragmentation model [Art93] for a transversely polarized nucleon with its spin orientation in (left panels) and perpendicular (right panel) to the lepton scattering plane (source [Els06]).

Let us now assume a positive transversity distribution function for the u quarks in the proton ($\delta u > 0$). In this hypothesis, the spin of the u quarks are predominantly orientated parallel to the (transverse) spin of the proton. This assumption is in agreement with all models for transversity, e.g. with the chiral quark soliton model [Wak01, Efr05] and the light-cone quark-spectator-diquark model [Ma02], and supported by lattice QCD calculations of the tensor charge [Aok97] and by the recent extraction of the transversity reported in [Ans07]. If, as depicted in chart (a), the azimuthal angle of the target spin with respect to the scattering plane is zero ($\phi_S = 0$), the spin of the u quark is reversed by the absorption of the virtual photon. The creation of a $d\bar{d}$ pair from the vacuum then yields a π^+ meson which is deflected upwards with respect to the plane of the page, i.e. at $\phi = \pi/2$ (chart (c)). If, on the other hand, the target spin is oriented perpendicularly to the scattering plane, as in chart (d), then $\phi_S = \pi/2$ and the virtual photon does not flip the spin of the u quark. The orbital angular momentum then deflects the produced π^+ meson towards the left-hand side of the target spin, resulting in $\phi = 0$ (chart (e)). For both target spin orientations one has $\sin(\phi + \phi_S) = \sin(\pi/2) > 0$, which is in fair agreement with the sign of the measured Collins moments for positive pions.

Relation (7.1), which allows to interpret the negative Collins amplitudes observed for π^-, is in fair agreement with the extractions of the Collins function reported in [Vog05, Efr06, Bac07b]. These extractions are based on the Collins moments measured at the HERMES and COMPASS experiments, and on model calculations for the trasversity distribution function[3]. This interpretation is also in agreement with the recent results reported in [Ans07]. In this work, the favoured and unfavored Collins fragmentation functions were extracted based on a global analysis of the world data. In particular, the Collins moments measured at HERMES, with a transversely

---

[3] In particular [Bac07b] reports the first estimates of the Collins function for kaons.

polarized hydrogen target, and at COMPASS, with a transversely polarized deuterium target [Age07], were fitted together with the BELLE data. BELLE measured the combined effects of two Collins mechanisms, obtained by looking at azimuthal correlations between hadrons in opposite jets in $e^+e^- \rightarrow h_1 h_2 X$ unpolarized processes [Sei06]. As a result, a positive (negative) favoured (unfavored) Collins function was extracted. The same global analysis allowed the first extraction of the transversity distribution for u and d quarks [Ans07]. In particular a positive (negative) transversity distribution for u (d) quarks was obtained. The magnitude of $\delta u(x)$ was found to be larger than that of $\delta d(x)$, and both $\delta u(x)$ and $\delta d(x)$ were found to be significantly smaller than the corresponding Soffer bound (cf. eqn. (3.34)). This result represents a milestone in hadron physics as it constitutes the first glimpse on the last missing piece of the (transverse momentum independent) nucleon structure at leading-twist (cf. Section 3.1)).

7.2 The Sivers moments

As displayed in eqn. (3.87), the Sivers moments can be expressed in terms of the convolution of the Sivers function times the spin-independent fragmentation function. The importance of measuring the Sivers moments is twofold: from one side, being the spin-independent fragmentation function well know, it allows to extract the Sivers function (see Section 7.3), which is a leading-twist unmeasured distribution function; from the other side it provides indirect information on the quark orbital angular momentum and has been linked to the spatial distribution of the partons inside the nucleon [Bro02, Bur02].

The unweighted and $P_{h\perp}$-weighted Sivers moments for pions and charged kaons, corrected for acceptance, are shown as a function of x, z, $P_{h\perp}$, y and Q^2 in Figures 7.4 and 7.5, respectively. The yellow bands, obtained by adding in quadrature all the contributions discussed in Sections 5.5.8 and 6.9, represent the total systematic errors. Similarly to the Collins case, the amplitudes are affected by an overall 7.9% scale uncertainty, associated to the measure of the target polarization (cf. Section 5.5.8).

A significantly positive Sivers amplitude is observed for positive pions and kaons. This important result proves the existence of a non-zero Sivers function and, indirectly, of a non-zero orbital angular momentum of the quarks in the nucleon.

Similarly to the case of the Collins amplitudes, the u quark dominance in DIS would lead to the naïve expectation of similar Sivers amplitudes for pions and kaons. In contrast, a Sivers amplitude for the positive kaons which is roughly twice as large as that for the positive pions is observed. The difference in the spin-independent fragmentation functions $D_1^{u\rightarrow\pi^+}$ and $D_1^{u\rightarrow K^+}$ can not account for such a large discrepancy. Therefore, since the valence content of these two mesons differs only in the anti-quark involved, this observation suggests a significant Sivers function for the proton sea quarks.

An amplitude consistent with zero is observed for the negative pions[4] and kaons, while, as predicted by the Isospin Relation (cf. Section 5.6), an intermediate amplitude between those of π^+ and π^- is observed for the π^0.

---

[4]An interpretation of the zero-amplitude for the π^- in discussed in Section 7.3.

Figure 7.4: Unweighted Sivers amplitudes extracted from the full HERMES transverse data set with the standard 6-parameters ML fit. The amplitudes are corrected for the acceptance effects. The yellow bands represent the systematic errors.

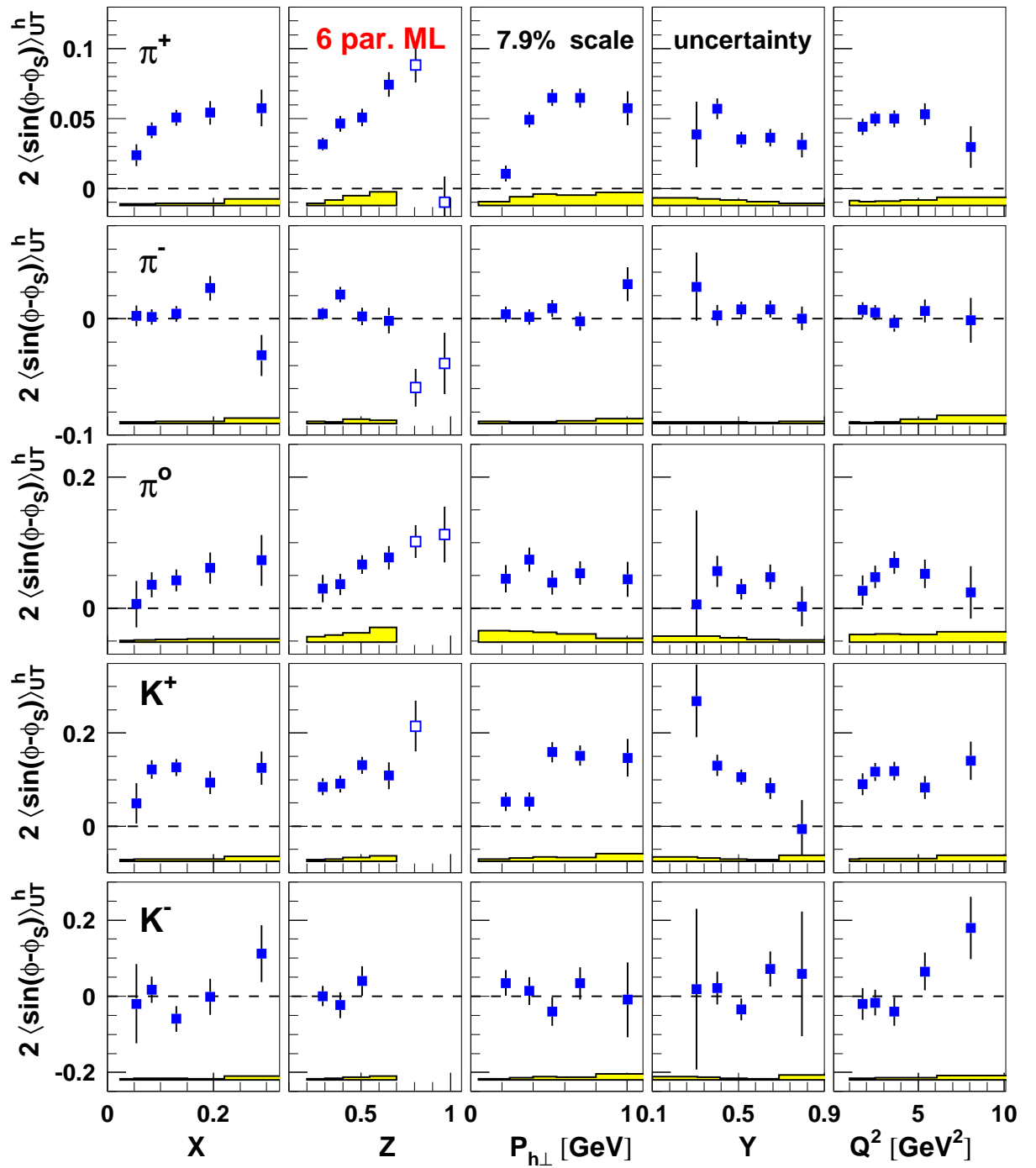Figure 7.5: $P_{h\perp}$-weighted Collins amplitudes extracted from the full HERMES transverse data set with the standard 6-parameters ML fit. The amplitudes are corrected for the acceptance effects. The yellow bands represent the systematic errors.
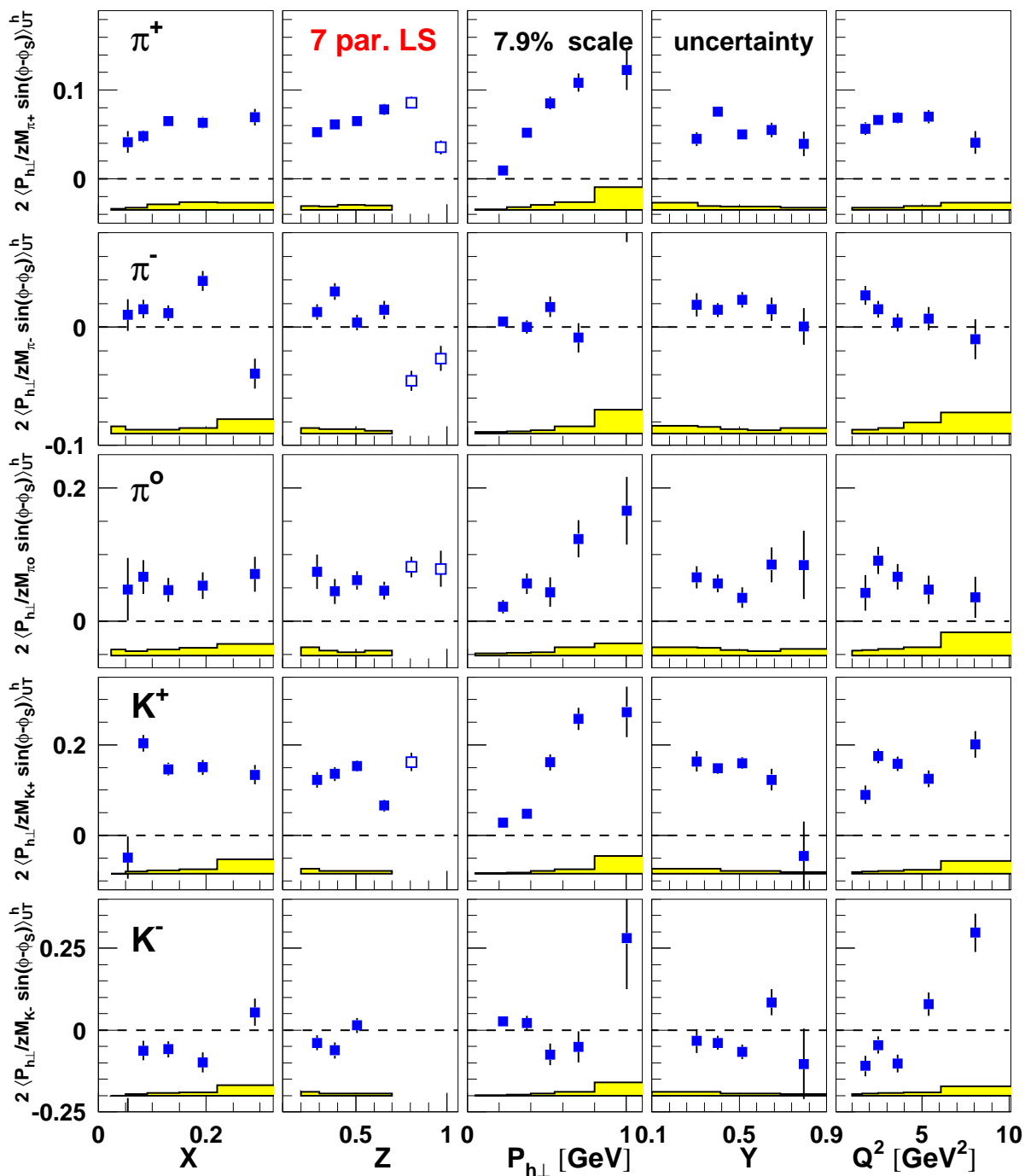
An intuitive phenomenological interpretation of the relation between the orbital angular momentum of the quarks and the Sivers effect is based on a description of the parton distribution functions in terms of the impact parameter $\vec{b}_T \equiv (b_x, b_y)$ [Bur02]. In the impact parameter space, the spin-independent distribution function can be written as:

$$q(x) = \int d^2\vec{b}_T \, q(x, \vec{b}_T) \,, \tag{7.2}$$

where the reference point for the impact parameter is given by the sum over the transverse positions $\vec{r}_{T,i}$ of all quarks, antiquarks and gluons of the nucleon, weighted by their momentum fractions x_i:

$$\vec{R}_T = \sum_{q,\bar{q},g} x_i \, \vec{r}_{T,i} \,. \tag{7.3}$$

The impact parameter spin-independent distribution function $q(x, \vec{b}_T)$ is axial symmetric for unpolarized or longitudinally (i.e. along the z-direction) polarized nucleons. In case of transversely polarized nucleon, the distribution of unpolarized quarks is distorted in the direction perpendicular to the spin and the momentum of the nucleon. This distortion vanishes when there is no quark orbital angular momentum parallel to the nucleon spin. Figure 7.6 shows a model calculation of the distribution of unpolarized u and d quarks with momentum fraction $x = 0.3$ in a transversely polarized nucleon. The nucleon spin points to the right (x-direction) and the virtual photon points into the plane of the page (negative z-axis).
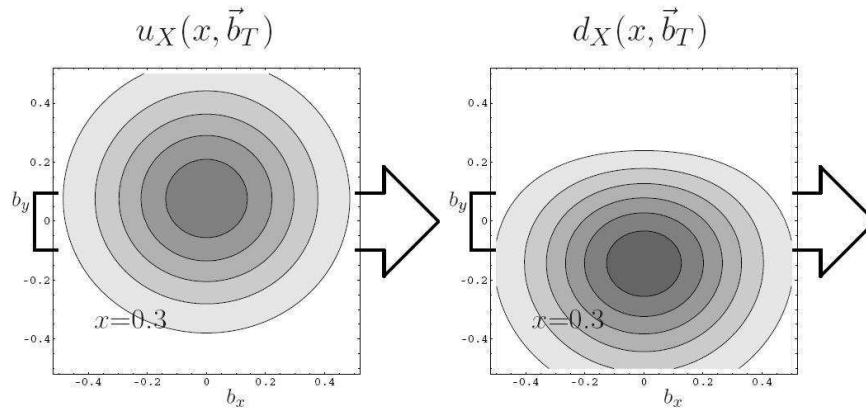
Figure 7.6: Impact parameter distribution function of unpolarized u and d quarks in a transversely polarized nucleon for $x = 0.3$. The virtual photon points into the plane of the page (negative z-axis).

The cause of the distortion can be understood, with semi-classical arguments, as the result of the superposition of translational and orbital motion of the quarks within the nucleon. Indeed, when viewed in the Breit frame (see Figure 2.6), quarks with orbital angular momentum in the transverse direction (i.e. parallel to the nucleon spin) move towards the virtual photon on one

side of the nucleon and away from it on the other side. Therefore, the quarks on one side of the nucleon are probed by the virtual photon at larger momentum fractions, while those on the other side are probed at smaller momentum fractions. As a consequence, the spin-independent distribution function is shifted towards higher x values in one side of the nucleon, and towards smaller x values in the other side.

Since, in the valence region, the spin-independent distribution function decreases rapidly with increasing values of x, the decrease of the momentum on one side of the nucleon spin results in a larger number density of quarks at this side and in a corresponding smaller number density in the opposite side. This mechanism thus results in a distortion of the distribution function, as shown in Figure 7.6.

As depicted in Figure 7.7, according to this semi-classical picture, u quarks with positive orbital angular momentum have a higher probability to absorb the incoming virtual photon in the top hemisphere of a transversely polarized nucleon (i.e. the left side hemisphere with respect to the virtual photon direction). After the absorption, attractive final state interactions (FSI), arising from the fact that the struck quark and the nucleon remnant constitute a color antisymmetric state, bend the quark towards the center of the nucleon.
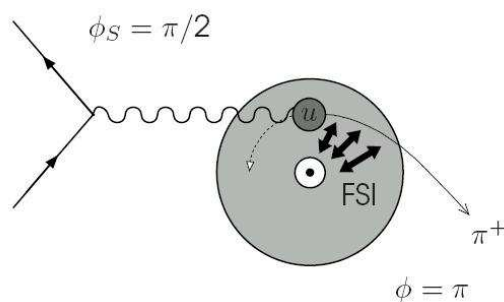
Figure 7.7: Semi-classical view of the scattering off a u quark with the production of a positive pion. Attractive final state interactions (FSI) bend the struck quark towards the center of the nucleon. (Sorce [Els06]).

The outgoing π^+, generated in the fragmentation of the struck quark, is therefore observed on the right-hand side of the nucleon spin direction, i.e. $\phi = \pi$. This is consistent with the observed positive Sivers amplitude for π^+ in the HERMES data: $\sin(\phi - \phi_S) = \sin(\pi - \pi/2) = \sin(\pi/2) > 0$.

In case of π^- production, due to the u quark dominance, both u and d quarks have to be taken into account. Thus, the results can not be interpreted exclusively in terms of scattering off a d quark alone, which would result in a negative Sivers moment. Our measured amplitudes, which are consistent with zero, can then be explained as the result of a cancelation of the contributions from the two quark flavours in combination with the different values of the favoured and the unfavored spin-independent fragmentation functions.

7.3 The extraction of the Sivers Polarization

The formalism of the *purities*, introduced in Section 3.7.5, allows to express explicitly the Sivers moments in terms of the so-called *Sivers polarization* (cf. eqn. (3.96)):

$$\widetilde{\mathcal{S}}(x) \equiv \frac{f_{1T}^{\perp(1/2)q}(x)}{q(x)} , \qquad (7.4)$$

which represents the ratio between the Sivers function (unmeasured) and the well known spin-independent quark distribution function.

The purities used in the present analysis are based on the parameterizations of the spin-independent distribution function $q(x, Q^2)$ implemented in the CTEQ4LQ (low Q^2) data base [Lai97]. Technically, the LO parameterizations are obtained by fits of the expression

$$F_2(x, Q^2) = \sum_q x \, e_q^2 \, q(x, Q^2) \qquad (7.5)$$

to world data on $F_2(x, Q^2)$. Owing to eqn. (2.46), the parton distributions $q(x, Q^2)$ can be related to the structure function $F_1(x, Q^2)$:

$$F_1(x, Q^2) = \frac{1 + \gamma^2}{1 + R(x, Q^2)} \frac{1}{2} \sum_q e_q^2 \, q(x, Q^2) . \qquad (7.6)$$

This allows to rewrite eqn. (3.96) in the compact form:

$$\langle \sin(\phi - \phi_S) \rangle_{UT}^h \equiv -\mathcal{C}_T(z)\mathcal{C}_i \sum_{q,\bar{q}} \mathcal{P}_q^h(x, z) \frac{f_{1T}^{\perp(1/2)q}(x)}{q(x)} , \qquad (7.7)$$

where $\mathcal{C}_i = (1 + R(x, Q^2))/(1 + \gamma^2)$. The kinematic factor

$$\mathcal{C}_T(z) = \frac{1}{\sqrt{1 + \langle K_T^2 \rangle / (z^2 \langle p_T^2 \rangle)}} , \qquad (7.8)$$

which originates from the Gaussian ansatz, introduces a big uncertainty since neither the z-dependence nor the quark flavour dependence of $\langle K_T^2 \rangle$ are known. As a consequence this factor is assumed to be identical for the different hadron types. Using the approximate relation

$$\langle P_{h\perp}^2 \rangle = \langle K_T^2 \rangle + z^2 \langle p_T^2 \rangle \qquad (7.9)$$

which can be found (with a different notation) in [Ans05b], $C_T(z)$ can be rewritten in the form:

$$C_T(z) \approx z \sqrt{\langle p_T^2 \rangle / \langle P_{h\perp}^2 \rangle} . \qquad (7.10)$$

Therefore, since $\langle p_T^2 \rangle$ and $\langle P_{h\perp}^2 \rangle$ are of the same order of magnitude, it follows that C_T is of the order of z. This has to be taken into account in the interpretation of the Sivers polarization extracted from unweighted Sivers moments.

Eqn. (7.7) can be expressed as a matrix equation for m hadron types and n quark flavours:

$$\vec{A}(x_i) = -\mathcal{C}_i \cdot \mathbf{P}(x_i)\, \vec{Q}(x_i)\,. \tag{7.11}$$

Here $\vec{A}(x_i)$ contains the Sivers moments extracted for the various hadron types, $\mathbf{P}(x_i)$ denotes the so-called purity matrix, and $\vec{Q}(x_i)$ contains the Sivers polarizations for the different quark flavours:

$$\vec{A}(x_i) = \begin{pmatrix} \langle sin(\phi - \phi_S) \rangle^{h_1}_{UT}(x_i) \\ \vdots \\ \langle sin(\phi - \phi_S) \rangle^{h_m}_{UT}(x_i) \end{pmatrix}, \qquad \vec{Q}(x_i) = \begin{pmatrix} \widetilde{\mathcal{C}}_T \dfrac{f^{\perp(1/2)q_1}_{1T}}{q_1}(x_i) \\ \vdots \\ \widetilde{\mathcal{C}}_T \dfrac{f^{\perp(1/2)q_n}_{1T}}{q_n}(x_i) \end{pmatrix}^{,} \tag{7.12}$$

$$\mathbf{P}(x_i) = \begin{pmatrix} \mathcal{P}^{h_1}_{q_1}(x_i) & \ldots & \mathcal{P}^{h_1}_{q_n}(x_i) \\ \vdots & \ddots & \vdots \\ \mathcal{P}^{h_m}_{q_1}(x_i) & \ldots & \mathcal{P}^{h_m}_{q_n}(x_i) \end{pmatrix}. \tag{7.13}$$

Since the purities are evaluated in bins of x, they are integrated over z. As a consequence the symbol $\widetilde{C}_T$ was used in eqn. (7.12) to denote the C_T kinematic factor averaged over z.

The purities used in the present analysis were extracted through a Monte Carlo generator called LEPTO. Similarly to PYTHIA, LEPTO generates events in 4π according to the spin-independent (Born) cross section. LEPTO, however, has the additional advantage that the flavours of the struck quarks are tagged and stored for each event. This allowed to separate the generated events according to the struck quark flavour q and to the produced hadron type h, thus enabling the construction of the purity matrix elements $\mathcal{P}^{h_k}_{q_j}$. Figure 7.8 shows the purities for the six quark flavours u, d, s, $\bar{u}$, $\bar{d}$, $\bar{s}$ and for the five hadron types π^+, π^-, π^0, K^+ and K^- as a function of x.

The Sivers polarization (7.4), multiplied by the kinematic factors $\widetilde{C}_T$ (vector $\vec{Q}(x_i)$) was obtained for $n \leq m$ by minimizing the figure-of-merit function:

$$\chi^2 = (\vec{A} + \mathcal{C}_i \cdot \mathbf{P}\, \vec{Q})^T \mathbf{\Gamma}^{-1}_A (\vec{A} + \mathcal{C}_i \cdot \mathbf{P}\, \vec{Q})\,, \tag{7.14}$$

where $\mathbf{\Gamma}_A$ denotes the covariance matrix of the set of asymmetry moments. In the present extraction of the Sivers polarization the correlations between the Sivers moments obtained for the different hadron types were not accounted for. The covariance matrix used has therefore vanishing off-diagonal elements and diagonal elements given by the squared statistical uncertainties of the Sivers moments.

Since the Sivers moments are measured for only five hadron types, an independent extraction of the Sivers polarization for the six quark flavours u, d, s, $\bar{u}$, $\bar{d}$, $\bar{s}$ is not possible. Therefore, a fully symmetric Sivers polarization was initially imposed for the sea quarks:

$$\frac{f^{\perp(1/2)q_{sea}}_{1T}}{q_{sea}} \equiv \frac{f^{\perp(1/2)u_s}_{1T}}{u_s} = \frac{f^{\perp(1/2)\bar{u}}_{1T}}{\bar{u}} = \frac{f^{\perp(1/2)d_s}_{1T}}{d_s} = \frac{f^{\perp(1/2)\bar{d}}_{1T}}{\bar{d}} = \frac{f^{\perp(1/2)s}_{1T}}{s} = \frac{f^{\perp(1/2)\bar{s}}_{1T}}{\bar{s}}\,. \tag{7.15}$$
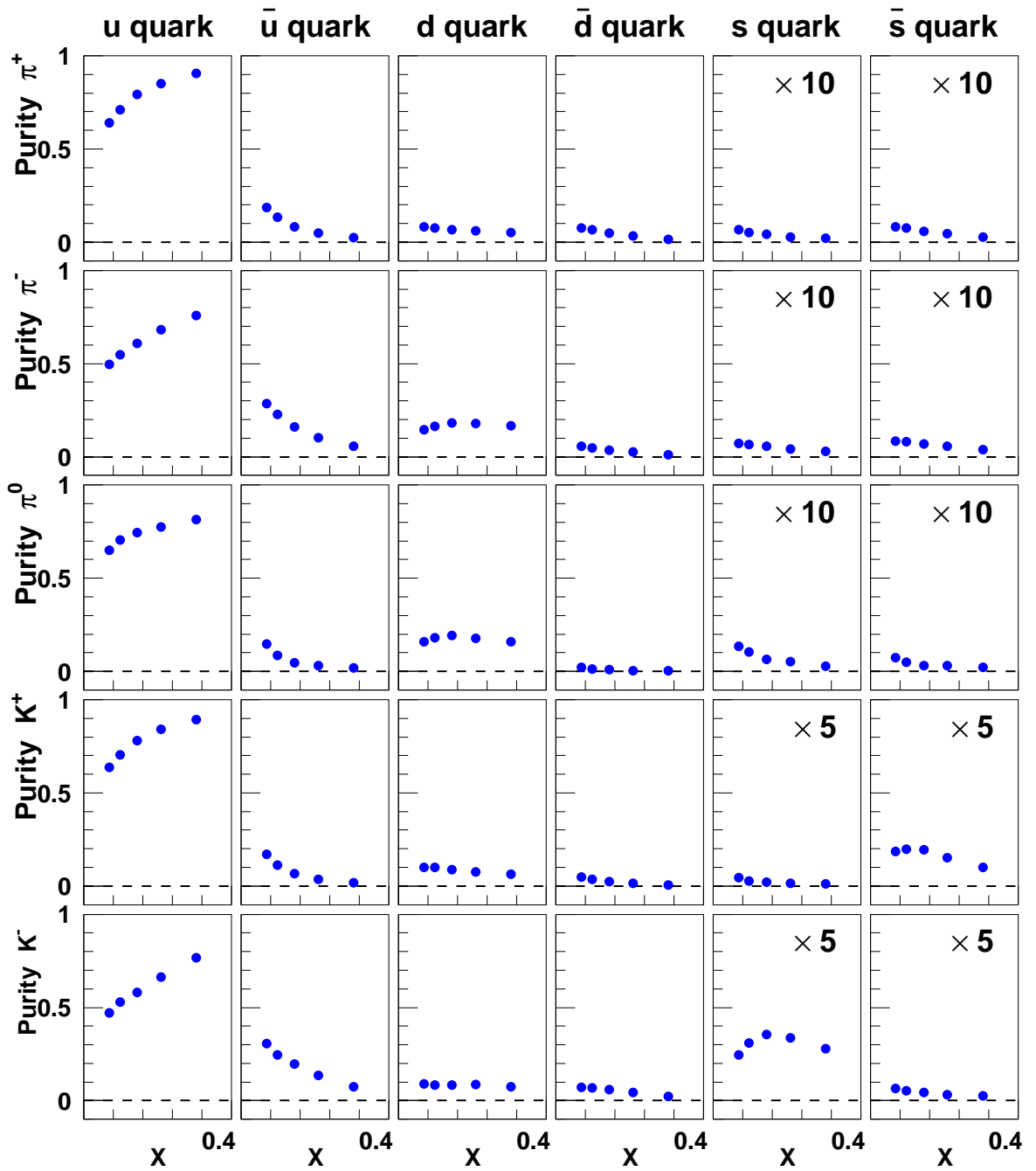
Figure 7.8: Purities for pions and kaons and the three lightest quarks and antiquarks. The purities of the s and $\bar{s}$ quarks are scaled for better visibility.

Here u_v and d_v denote the valence u and d quarks and u_s and d_s the sea u and d quarks.

Two different combinations of quarks were considered: the *Flavour Decomposition* (FD), in which the Sivers polarizations are extracted for sets of quarks and antiquarks of the same flavour

$$\widetilde{C}_T \frac{f_{1T}^{\perp(1/2)u}}{u}\bigg|_{FD} = \widetilde{C}_T \frac{f_{1T}^{\perp(1/2)u} + f_{1T}^{\perp(1/2)\bar{u}}}{u + \bar{u}} \ ,$$

$$\widetilde{C}_T \frac{f_{1T}^{\perp(1/2)d}}{d}\bigg|_{FD} = \widetilde{C}_T \frac{f_{1T}^{\perp(1/2)d} + f_{1T}^{\perp(1/2)\bar{d}}}{d + \bar{d}} \ ,$$

$$\widetilde{C}_T \frac{f_{1T}^{\perp(1/2)s}}{s}\bigg|_{FD} = \widetilde{C}_T \frac{f_{1T}^{\perp(1/2)s} + f_{1T}^{\perp(1/2)\bar{s}}}{s + \bar{s}} \equiv \widetilde{C}_T \frac{f_{1T}^{\perp(1/2)q_{sea}}}{q_{sea}} \ , \tag{7.16}$$

and the *Valence Decomposition* (VD), in which the Sivers polarizations are separated into contributions from valence and from sea quarks:

$$\widetilde{C}_T \frac{f_{1T}^{\perp(1/2)u}}{u}\bigg|_{VD} = \widetilde{C}_T \frac{f_{1T}^{\perp(1/2)u} - f_{1T}^{\perp(1/2)\bar{u}}}{u - \bar{u}} \ ,$$

$$\widetilde{C}_T \frac{f_{1T}^{\perp(1/2)d}}{d}\bigg|_{VD} = \widetilde{C}_T \frac{f_{1T}^{\perp(1/2)d} - f_{1T}^{\perp(1/2)\bar{d}}}{d - \bar{d}} \ ,$$

$$\widetilde{C}_T \frac{f_{1T}^{\perp(1/2)q_{sea}}}{q_{sea}}\bigg|_{VD} \equiv \widetilde{C}_T \frac{f_{1T}^{\perp(1/2)q_{sea}}}{q_{sea}} \ . \tag{7.17}$$

The formalism above was derived for the extraction of the Sivers polarization from the unweighted Sivers moments. The same formalism holds for the extraction from the $P_{h\perp}$-weighted Sivers moments. In this case, however, one gets rid of the coefficient $\widetilde{C}_T$, which introduces a big uncertainty due to our poor knowledge of the quark transverse momentum distribution. The components of $\vec{Q}(x_i)$ thus represent, in this case, the bare Sivers polarizations, with no assumptions on the quark transverse momentum. In addition, the 1-moment instead of the $1/2$-moment of the Sivers function is involved (cf. eqns. (3.95))

The elements of the two purity matrices to be used for the two quark decompositions are obtained from linear combinations of the standard purity matrix elements. For the *flavour decomposition* one obtains:

$$\widetilde{P}_u^{FD} = P_u \cdot \frac{u + \bar{u}}{u} \ , \tag{7.18}$$

$$\widetilde{P}_d^{FD} = P_d \cdot \frac{d + \bar{d}}{d} \ , \tag{7.19}$$

$$\widetilde{P}_{sea}^{FD} = -P_u \cdot \frac{\bar{u}}{u} + P_{\bar{u}} - P_d \cdot \frac{\bar{d}}{d} + P_{\bar{d}} + P_s + P_{\bar{s}} \ , \tag{7.20}$$

while for the *valence decomposition* one obtains:

$$\widetilde{P}_u^{VD} = P_u \cdot \frac{u - \bar{u}}{u} \,, \tag{7.21}$$

$$\widetilde{P}_d^{VD} = P_d \cdot \frac{d - \bar{d}}{d} \,, \tag{7.22}$$

$$\widetilde{P}_{sea}^{VD} = P_u \cdot \frac{\bar{u}}{u} + P_{\bar{u}} + P_d \cdot \frac{\bar{d}}{d} + P_{\bar{d}} + P_s + P_{\bar{s}} \,. \tag{7.23}$$

The derivation of the combinations above can be found in [Bec00].

The minimization of the figure-of-merit function (7.14), performed with MINUIT, was affected by strong correlations between u, d and sea quarks, especially for the flavour decomposition. As a consequence, the additional constraint of a null Sivers polarization for the sea quarks was adopted:

$$\frac{f_{1T}^{\perp(1/2)q_{sea}}}{q_{sea}} = 0 \,. \tag{7.24}$$

Figure 7.9 shows the Sivers polarizations for the flavour and the valence decomposition extracted from the unweighted Sivers moments corrected for the acceptance effects. The Sivers polarization extracted from the $P_{h\perp}$-weighted Sivers moments is shown in Figure 7.10. At the present stage, no statistical correlations nor systematic uncertainties are taken into account in the extraction. The parametrization of the Sivers function used in [Ans05] to fit the Sivers moments extracted from the HERMES data collected during the 2002-2004 period [Dief05] are also shown for comparison in Figure 7.10 for both the valence (blue line) and the flavour (red line) decompositions. A similar comparison is not possible for the Sivers polarizations extracted from the unweighted moments due to the unknown contribution of the $\widetilde{C}_T$ factor.

A negative (positive) Sivers polarization is observed for the u (d) quarks for both the quark decompositions although, similarly to the case of the helicity distribution function [Dur98], a larger sensitivity is obtained for the *flavour decomposition*.

The average magnitude of the Sivers polarization for the d quarks is, in absolute value, roughly twice as big as that for the u quarks. Since, however, the spin-independent distribution function, appearing in the denominator of the Sivers polarization, is for u quarks about twice as large as for d quarks, the Sivers functions for u and d quarks are of similar size:

$$f_{1T}^{\perp,u}(x) \approx -f_{1T}^{\perp,d}(x) \,. \tag{7.25}$$

The result above is in fair agreement with previous extractions based on earlier HERMES data and on the Gaussian ansatz (cf. Section 3.7.5) [Vog05, Ans05, Col06]. It was also proven, in a model independent way, to be valid in the large-N_c limit of QCD [Efr06, Pob03].

According to the semi-classical picture described in Section 7.2, a negative (positive) Sivers function would result in a net motion of the struck quark to the right (left) with respect to the virtual photon direction if the nucleon spin is oriented perpendicular to the scattering plane

Figure 7.9: Sivers polarizations for flavour and valence decomposition extracted from the unweighted Sivers moments (corrected for the acceptance) under the assumption of a null sea polarization.

Figure 7.10: Sivers polarizations for flavour and valence decomposition extracted from the $P_{h\perp}$-weighted Sivers moments (corrected for the acceptance) under the assumption of a null sea polarization. Also shown are the theoretical curves obtained form the fit reported in [Ans05].

($\phi_S = \pi/2$). This scenario would be compatible with a positive (negative) orbital angular momentum for the u (d).

The relation (7.25) allows to interpret the smallness of the Sivers amplitudes for π^- observed (cf. Figure 7.4). As discussed in [Col06], combining eqn. (7.25) with the expression of the Sivers moment (3.91) yields:

$$\langle \sin(\phi - \phi_S) \rangle_{UT}^{\pi^-} \propto \left(\frac{4}{9} D_{1,unfav} - \frac{1}{9} D_{1,fav} \right) , \qquad (7.26)$$

where $D_{1,fav}$ and $D_{1,unfav}$ denote the spin-independent *favoured* and *unfavoured* fragmentation functions. Although $D_{1,unfav}(z) < D_{1,fav}(z)$ at any z, due to the weighting by the square of the quark electric charges, the effects of smaller *unfavoured* and larger *favoured* fragmentation functions become comparable and tend to cancel each other. As a result the Sivers moments for π^- appear consistent with zero.

Results form the COMPASS experiment [Age07], which show a Sivers effect from deuterium target compatible with zero for both positively and negatively charged hadrons, can also be interpreted in terms of relation (7.25). In the COMPASS experiment a solid transversely polarized ^6LiD target was used. Neglecting nuclear binding effects and using isospin symmetry arguments, one expects for a deuterium target:

$$f_{1T}^{u/D} \approx f_{1T}^{u/p} + f_{1T}^{u/n} \approx f_{1T}^{u} + f_{1T}^{d} , \qquad (7.27)$$

and analogously for d and for the antiquarks. Therefore, the deuterium target is sensitive to the flavour combination which is suppressed by relation (7.25), and this explains the COMPASS results. The new results from COMPASS, obtained with a transversely polarized proton target, are expected to exhibit non zero Sivers amplitudes. The much higher (with respect to HERMES) average Q^2 would also help in confirming the leading-twist nature of the Sivers (and Collins) asymmetries.

In order to check the Sivers polarization for the sea quarks, under the assumption (7.15) of a fully symmetric sea, the constraint (7.24) was relaxed and the condition (7.25), which is supported by the COMPASS results and by predictions based on the large-N_c limit of QCD [Efr06, Pob03], was imposed. The results for unweighted and $P_{h\perp}$-weighted Sivers moments are shown in Figures 7.11 and 7.12, respectively. A significantly positive sea quarks polarization is observed in both cases. This result is compatible with the expectation of a large Sivers function for the proton sea quarks, as suggested by the significantly larger Sivers moments extracted for K^+ than for π^+ (cf. Section 7.2).

A particularly interesting feature of the Sivers function concerns its universality property. This property ensures that one deals with the same parton distribution in SIDIS and in Drell-Yan process (DY) (cf. Section 3.6). In the case of the Sivers function (and other T-odd distributions) the universality property takes a different form. Indeed, on the basis of time-reversal arguments, it was predicted [Col02] that $f_{1T}^{\perp}$ have opposite sign in SIDIS and DY:

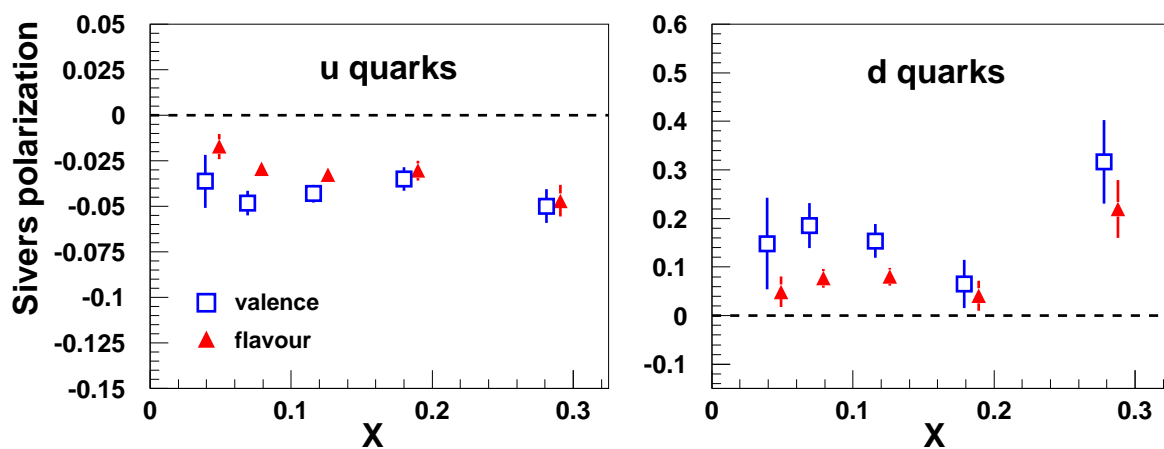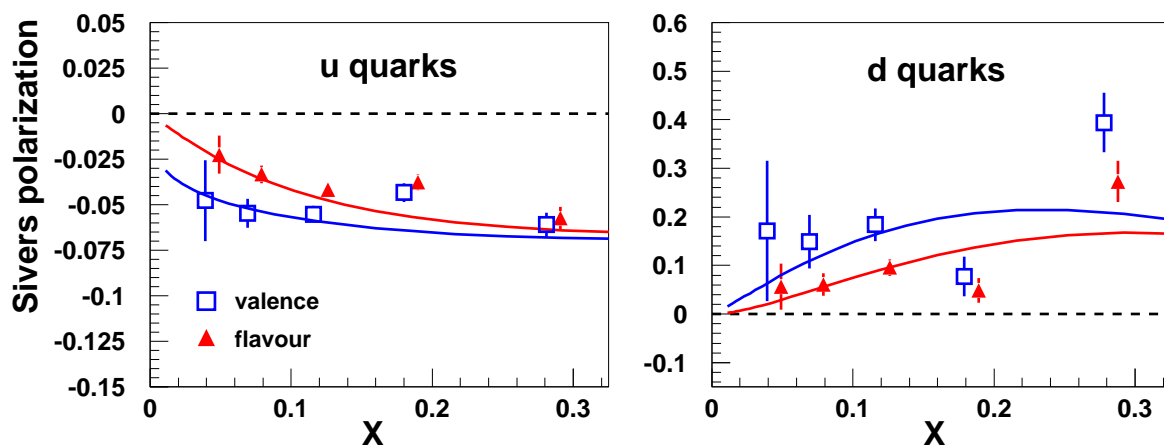$$f_{1T}^{\perp}(x, p_T^2)\big|_{SIDIS} = -f_{1T}^{\perp}(x, p_T^2)\big|_{DY} . \qquad (7.28)$$
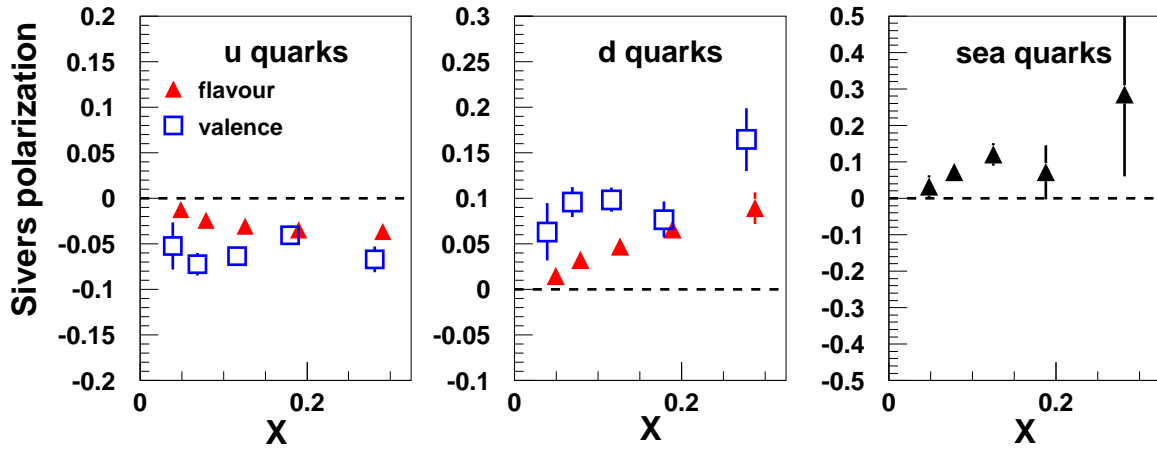
Figure 7.11: Sivers polarizations for flavour and valence decomposition extracted from the unweighted Sivers moments (corrected for the acceptance) under the assumptions (7.15) and (7.25).
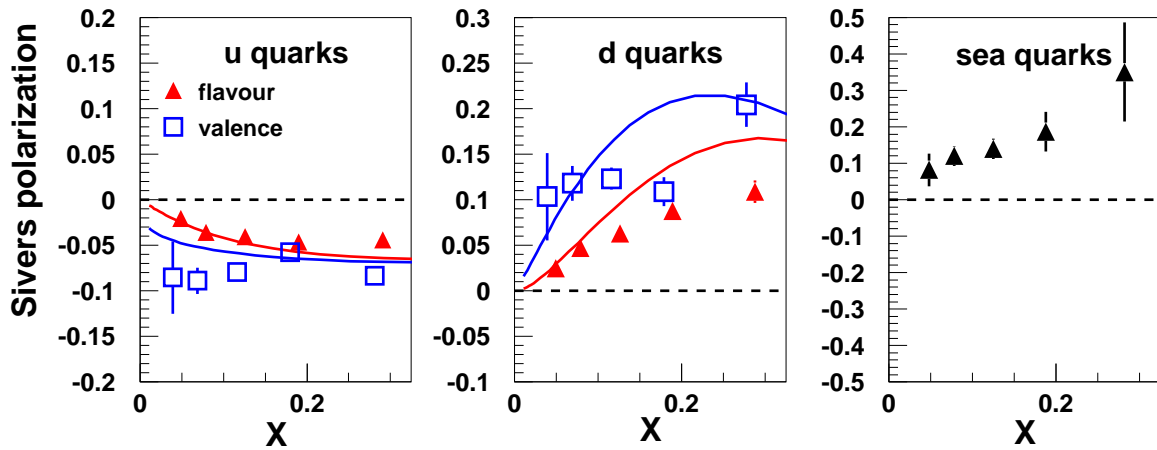
Figure 7.12: Sivers polarizations for flavour and valence decomposition extracted from the $P_{h\perp}$-weighted Sivers moments (corrected for the acceptance) under the assumptions (7.15) and (7.25). Also shown are the theoretical curves obtained form the fit reported in [Ans05].

The experimental check of relation (7.28) would provide a crucial test of the current understanding of the Sivers effect within the QCD framework and, more in general, of the single spin asymmetries. It would also represent an important test for the factorization approach to the description of the non-collinear processes, i.e. sensitive to the quark transverse momentum.

Chapter 8

Conclusions

The data collected by the HERMES experiment during the 2002-2005 period, with a transversely polarized hydrogen target, was analyzed in this work to extract the so-called Collins and Sivers moments. The extraction of these moment is of great importance since they provide information on barely known distribution and fragmentation functions. In particular, the Collins moments can be expressed as the convolution of the transversity distribution function times the Collins fragmentation function. The transversity is a leading-twist chiral-odd function describing the probability to find, in a transversely polarized nucleon, quarks with their spin oriented parallel or antiparallel to the spin of the nucleon. It is one of the three fundamental parton distribution functions and, together with the momentum (spin-independent) and the helicity distribution functions, provides a complete description of the nucleon structure at leading twist, if the transverse quark momentum is integrated over. The Collins function represents the correlation between the transverse spin of the quarks and the transverse momentum of the produced hadron. It can thus be viewed as a quark spin analyzer. This correlation produces left right (azimuthal) asymmetries in the direction of the outgoing hadrons, thus providing a clear experimental observable in semi-inclusive DIS. Transversity and Collins function, combined together in the so-called Collins moments, are indeed accessible at HERMES in Single (transverse target) Spin Asymmetries. These two quantities were recently extracted for the first time in a global analysis of the HERMES, COMPASS and BELLE data [Ans07].

If one does not integrate over the transverse quark momentum, a variety of new (transverse momentum dependent) distribution functions arise, which contain a wide spectrum of information on the nucleon structure. These functions, which have recently experienced a rapidly increasing interest form both the theoretical and the experimental communities, represent a new frontier in hadron physics. Among these functions, the Sivers function, which describes the correlation between the transverse momentum of the quarks and the transverse spin of the nucleon, is of particular importance since its existence requires a non-zero orbital angular momentum of the quarks. This function appears in the semi-inclusive DIS cross section in combination with the known spin independent fragmentation function, generating the so-called Sivers moments. Similarly to the Collins moments, the Sivers moments can be accessed at HERMES in Single (transverse-target) Spin Asymmetries.

In the present work the HERMES data was analyzed and selected according to kinematic and geometric cuts. Particular attention was devoted to the particle identification in order to allow for a correct separation between leptons and hadrons and between the various hadron types. The selected semi-inclusive DIS events were used to extract the 'unweighted' Collins and Sivers moments with a 6-parameters maximum likelihood fit. Similarly, the so-called 'P$_{h\perp}$-weighted' Collins and Sivers moments were extracted in a 7-parameters least-square fit. Differently from the unweighted moments, the P$_{h\perp}$-weighted moments allow, in principle, to extract the relevant distribution functions (transversity and Sivers function, in this case) without any assumption (model) on the quark transverse momentum distribution. This represents a great advantage with respect to the unweighted moments. However, Monte Carlo studies showed that the P$_{h\perp}$-weighted moments are heavily affected by acceptance effects introduced by the detector. For this reason the P$_{h\perp}$-weighted moments could not be used in previous analyses to extract the Sivers function.

In the present work, an innovative technique was adopted to correct for the acceptance effects. As a result the unweighted and P$_{h\perp}$-weighted Collins and Sivers in 4π were extracted for the first time. Significant positive (negative) Collins moments were found for π^+ (π^-), thus indicating that both the transversity and the Collins function are non-zero. Similarly, significantly positive Sivers amplitudes were observed for both positive pions and kaons. This result clearly indicates that the Sivers function is non-zero and, indirectly, that also the quark orbital angular momentum, which is still an unmeasured quantity, is non-zero. In particular, the amplitude for the K^+ was found to be twice as large as that for the π^+, thus suggesting a significant Sivers function for the sea quarks.

The extraction of the P$_{h\perp}$-weighted Sivers moments corrected for acceptance allowed, for the first time, an extraction of the Sivers function free from assumptions on the quark transverse momentum distribution. Under the assumption of a null Siver polarization for the sea quarks, a negative (positive) Sivers polarization was found for u (d) quarks. This result is in agreement with the assumption of a Sivers function of opposite sign for u and d quarks, which is supported by the COMPASS null results on the Sivers moments and by predictions based on the large-N_c limit of QCD [Efr06, Pob03]. When this condition is imposed, together with a symmetric sea Sivers polarization, a significantly positive sea Sivers polarization is found. This result is compatible with the expectation of a large Sivers function for the proton sea quarks, as suggested by the significantly larger Sivers moments extracted for K^+ than for π^+.

Appendix A

QCD: general concepts

Quantum Chromo Dynamics (QCD) is the gauge theory of the strong interactions, i.e. those occurring among objects which carry color charge, such as the quarks.

The Lagrangian of QCD

$$\mathcal{L}_{QCD} = \sum_f \overline{\psi}_f(x)(i\not{D} - m_f)\psi_f(x) - \frac{1}{4}F_{\mu\nu}^\alpha(x)F_\alpha^{\mu\nu}(x) \tag{A.1}$$

is invariant under the $SU(3)_C$ local transformations

$$\psi_f(x) \rightarrow U\psi_f(x) \equiv e^{i\theta^\alpha(x)\frac{\lambda_\alpha}{2}}\psi_f(x) \qquad \alpha = 1,...,8\,, \tag{A.2}$$

where $\psi(x)_f$ are the 4-component Dirac spinors associated with each quark field of flavor f[1] and mass m_f, $\frac{\lambda_\alpha}{2}$ are the 8 generators of the transformation, given in terms of the so-called Gell-Mann matrices λ_α, and $\theta^\alpha(x)$ are the 8 parameters of the transformation, which are functions of the space-time coordinate x.

$SU(3)_C$ is a group of 3×3 unitary matrices with unit determinant. The subscript C refers to the Color charge and 3 reflects the dimensionality of the space: 3 possible color states exist for the quarks (red (r), blue (b) and green (g)) and, correspondingly, 3 anti-color states exist for the antiquarks (anti-red ($\overline{r}$), anti-blue ($\overline{b}$) and anti-green ($\overline{g}$)).

According to the group properties of $SU(3)_C$, the $3 \times \overline{3}$ combinations of colors and anti-colors can be combined into two multiplets of states: a color octet, made by 8 different combinations of colors and anti-colors, such as:

$$r\overline{g},\ r\overline{b},\ g\overline{b},\ g\overline{r},\ b\overline{r},\ b\overline{g},\ \sqrt{\frac{1}{2}}(r\overline{r} - g\overline{g}),\ \sqrt{\frac{1}{3}}(r\overline{r} + g\overline{g} - 2b\overline{b}) \tag{A.3}$$

and a color singlet:

$$\sqrt{\frac{1}{3}}(r\overline{r} + g\overline{g} + b\overline{b})\,. \tag{A.4}$$

---

[1] $f = u, d, s, c, b, t.$

185

Being the color singlet totally symmetric under exchange of colors, it owes a null net color charge. As a consequence it cannot be exchanged between colored particles and thus cannot exist as a physical mediator of the strong interaction. On the contrary, the states of the octet are physical and correspond to the 8 gauge boson fields $A_\mu^\alpha(x)$ of the theory. These fields, called gluons, act as the mediators of the strong interactions among quarks.

Similarly to the QED, the covariant derivatives

$$D = \partial_\mu - ig_s\frac{\lambda_\alpha}{2}A_\mu^\alpha(x) \, , \tag{A.5}$$

which have been introduced in eqn. (A.1) in order to ensure the local gauge invariance of the theory, provide the gauge interactions between quarks and gluons through the term $\overline{\psi}(i\not{D})\psi$ of the Lagrangian. In addition, since gluons carry color (and anti-color) they can interact not only with the quarks but also among themselves, as depicted in Figure A.1. This fact, which represents a major difference with respect to QED, where the photons cannot interact among themselves since they do not carry electric charge, is a direct consequence of the fact that $SU(3)_C$ is a non-abelian group, i.e. such that the product of two transformations $e^{i\theta^\alpha(x)\frac{\lambda_\alpha}{2}}$ and $e^{i\theta^\beta(x)\frac{\lambda_\beta}{2}}$ depends in general on the order in which these transformations are operated. As a consequence the field strength tensor

$$F_{\mu\nu}^\alpha(x) = \partial_\mu A_\nu^\alpha(x) - \partial_\nu A_\mu^\alpha(x) + g_s f^{\alpha,\beta,\gamma} A_{\mu\beta} A_{\nu\gamma} \qquad (\alpha,\beta,\gamma = 1,...,8) \, , \tag{A.6}$$

which appears in the last term of the Lagrangian (A.1), contains an additional term which is bilinear in the gluon fields. This term is responsible for the 3-gluon and 4-gluon vertices (see Figure A.1). The quantities $f^{\alpha,\beta,\gamma}$ and g_s, which multiply the bilinear term in eqn. (A.6), represent the structure constants of the $SU(3)$ algebra and the strong coupling constant, respectively.
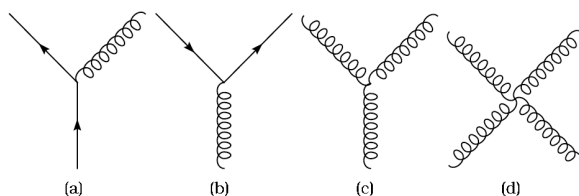
Figure A.1: The four basic gluon interactions. (a) gluon radiation by a quark, (b) splitting of a gluon in a quark - antiquark pair, (c) splitting of a gluon in two gluons and (d) a gluon four - vertex.

As in QED, the strength of the color interaction is measured by a coupling constant which depends on the momentum transfer (running constant). More specifically, it can be shown that the strong coupling constant is given to a good approximation by:

$$\alpha_s(|q^2|) = \frac{12\pi}{(11N_c - 2f)\,ln(|q^2|/\Lambda_{QCD}^2)} \, , \tag{A.7}$$

where N_c is the number of colors ($N_c = 3$ in QCD), f is the number of quark flavors involved and Λ_{QCD} is the QCD scale parameter, which represents the only free parameter of the theory.

The approximate value of $\Lambda_{QCD} \approx 250 \; MeV$ has been determined experimentally by measuring the strong coupling constant in a variety of processes.

While the electromagnetic coupling constant α is reduced at large distances due to the effect of the vacuum polarization, which is responsible for a *screening* of the bare electric charge, the strong coupling constant is reduced at short distances. Indeed, the interactions among the gluons induces an *anti-screening* of the color charge or, equivalently, an enhancement of the color charge at large distances. This effect, which is a consequence of the non-commutativity of $SU(3)_C$, is responsible for the so-called *asymptotic freedom*. In this regime, that corresponds to high momentum transfers ($|q|^2 \gg \Lambda_{QCD}^2$), the coupling constant becomes weak ($\alpha_s \ll 1$) and can be used as a perturbative expansion parameter. This is the domain of the perturbative QCD (pQCD) in which quarks can be treated essentially as non-interacting particles. Perturbative QCD is considered a relatively well established theory. It is highly predictive and reliable in its range of validity and, similarly to QED, it is based on the Feynman-diagram approach [2].

On the other hand one immediately sees from eqn. (A.7) that at low momentum transfers the coupling becomes large and a perturbative approach is no longer practicable. This is the regime of *confinement*, where the color interaction only allows color-singlet states to exists and forces quarks and gluons to be confined within the colorless bound states that we observe in nature: the mesons and the baryons.

---

[2]Although it often requires the inclusion of higher order processes in order to obtain the desired accuracy.

Appendix B

Light-cone variables

A four-vector A^μ with Cartesian contravariant components is represented as

$$A^\mu = (A^0, A^1, A^2, A^3) = (A^0, \vec{A}). \tag{B.1}$$

In the light-cone frame (cf. Figure B.1), the components of A^μ are defined as:

$$A^\pm = \frac{1}{\sqrt{2}}(A^0 \pm A^3). \tag{B.2}$$

In these components A^μ and its norm are written respectively as

$$A^\mu = (A^+, A^-, \vec{A}_\perp). \tag{B.3}$$

$$A^2 = (A^0)^2 - \vec{A}^2 = 2A^+A^- - \vec{A}_\perp^2 \tag{B.4}$$

and the scalar product of two four-vectors A^μ and B^μ is

$$A \cdot B = A^0 B^0 - \vec{A} \cdot \vec{B} = A^+ B^- + A^- B^+ - \vec{A}_\perp \cdot \vec{B}_\perp. \tag{B.5}$$
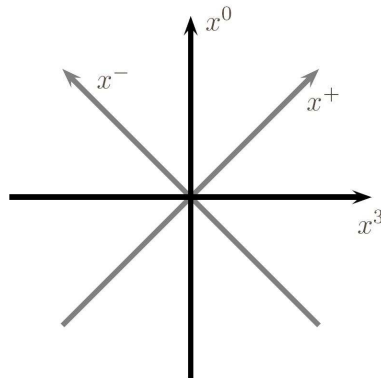
Figure B.1: The light-cone axes $x^\pm$

In the Bjørken limit ($Q^2 \to \infty, \nu \to \infty, x$ const) the four-momentum vectors of the proton and the virtual photon can be parameterized in light-cone coordinates as:

$$P^\mu = \left(\frac{M^2}{2P^+}, P^+, \vec{0} \right) \tag{B.6}$$

$$q^\mu = \left(\frac{Q^2}{2xP^+}, -xP^+, \vec{0} \right) . \tag{B.7}$$

This parametrization is valid in any collinear frame, i.e., in any frame of reference in which the virtual photon direction is antiparallel to the x^3 axis. For all collinear frames P^+ is the dominant variable in a $1/Q$ expansion. In the infinite momentum frame P^+ is of the order of Q.

Appendix C

The optical theorem

The *optical theorem*, which is a very general law of wave scattering theory, relates the forward scattering amplitude to the total cross section of the scatterer:

$$\sigma_{tot} = \frac{4\pi}{q}\mathcal{I}mf(0) \ . \tag{C.1}$$

Here $f(0)$ is the forward ($\theta_{CM} = 0$) scattering amplitude, q is the center-of-mass momentum and σ_{tot} is the total cross section, including the elastic and the inelastic contributions.

In the framework of the deep inelastic scattering, the optical theorem relates the hadronic tensor $W_{\mu\nu}$ to the imaginary part of the forward virtual Compton scattering amplitude $\mathcal{T}$ (see Figure C.1):

$$W_{\mu\nu} \sim \mathcal{I}m(\mathcal{T}^{\mu\nu}) \tag{C.2}$$

where:

$$\mathcal{T}^{\mu\nu} = i \int d\xi^4 e^{iq\cdot\xi}\langle P, S|T(J^\mu(\xi)J_\nu(0))|P, S\rangle \ . \tag{C.3}$$

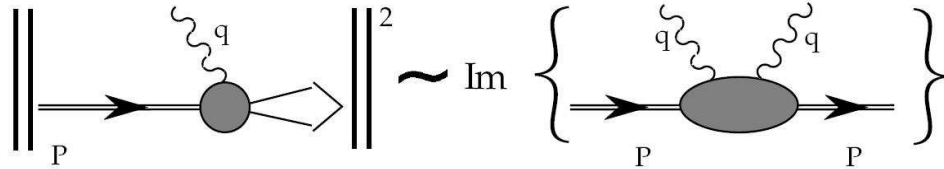Here $T()$ represents the time-ordered product.

Figure C.1: The optical theorem relates the hadronic tensor $W_{\mu\nu}$ to the imaginary part of the forward virtual Compton scattering.

The optical theorem allows to express the three leading-twist quark distribution functions $q(x)$, $\Delta q(x)$ and $\delta q(x)$ in terms of quark-nucleon forward amplitudes.

191

Appendix D

The gauge link operator

The quark-quark correlation matrix Φ, defined in Section 3.1, relates a quark and an antiquark at two different space-time points 0 and ξ. As quark fields are colored objects, two quarks separated by a distance ξ must have a gauge link, eg. a gluon field connecting them to become colorless. Therefore, a path-dependent link operator $\mathcal{L}$ must be inserted between the quark fields to obtain a gauge invariant quark-quark correlatator [Boe00, Ell83]:

$$\Phi_{i,j}(p, P, S) = \frac{1}{(2\pi)^4} \int d\xi^4 e^{ip\cdot\xi} \langle P, S | \bar{\psi}_j(0) \mathcal{L}(0, \xi) \psi_i(\xi) | P, S \rangle \ . \tag{D.1}$$

The gauge link $\mathcal{L}$, also known as *Wilson line*, is a bilocal operator connecting the quark fields ψ in two different space-time points 0 and ξ and is given by

$$\mathcal{L}(0, \xi) = \mathcal{P} \ exp \left(-i\sqrt{4\pi\alpha_s} \int_0^\xi ds^\mu A_\mu(s) \right) \ . \tag{D.2}$$

Here $\mathcal{P}$ indicates the path-ordering of the integral over the gauge field A_μ. The link operator corresponds to the summation of all diagrams with a soft gluon exchange. Figure D.1 reports, as an example, the handbag diagram for one-gluon exchange.
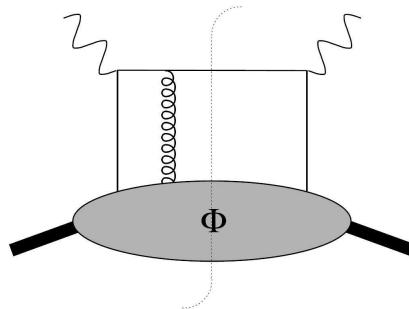

Figure D.1: The one-gluon gauge link. A soft gluon is exchanged between the quark line and the nucleon remnant.

Appendix E

The Probability Density Estimator

The method of the Probability Density Estimator (PDE) was used for the calculation of the a-priori *data probability density function* $f(\mathbf{x}_i)$, to be implemented in the so-called *likelihood ratio* (cf. eqn. (6.26)). Unlike the standard likelihood function, the latter allows for a measure of the goodness of the fit for unbinned maximum likelihood fits.

For the implementation of this method, the same philosophy adopted in [Raj06] was used. However, in order to substantially reduce the computation time, a multidimensional binning was used instead of the original unbinned approach.

As a first step, all the events selected according to the standard kinematic and geometrical cuts (cf. Section 5.3) were grouped into 28800 multidimensional bins. The binning adopted is summarized in Table E.1.

variable	# of bins	bin borders
x	5	[0.023, 0.10]]0.10, 0.17]]0.17, 0.25]]0.25, 0.32]]0.32, 0.4]
Q^2	2	[1.0, 5.5]]5.5, 10]
z	4	[0.20, 0.33]]0.33, 0.45]]0.45, 0.58]]0.58, 0.7]
$P_{h\perp}$	5	[0.05, 0.44]]0.44, 0.83]]0.83, 1.22]]1.22, 1.61]]1.61, 2.0]
ϕ	12	$[0, \frac{\pi}{6}] \cdots]\frac{11\pi}{6}, 2\pi]$
ϕ_S	12	$[0, \frac{\pi}{6}] \cdots]\frac{11\pi}{6}, 2\pi]$

Table E.1: Binning in the kinematic variables x, Q^2, z, $P_{h\perp}$, ϕ and ϕ_S used for the PDE.

For each of those multidimensional bins $i \equiv (x_\alpha, Q^2_\beta, z_\gamma, P_{h\perp,\delta}, \phi_\varepsilon, \phi_{S,\eta})$ with a sufficiently high statistics (e.g. containing more than 100 events), the asymmetries

$$A_i = \frac{Y_i^\uparrow - Y_i^\downarrow}{Y_i^\uparrow + Y_i^\downarrow} \tag{E.1}$$

were calculated from the yields $Y_i^{\uparrow(\downarrow)}$ of the events corresponding to each of the two target spin states

$$Y_i^{\uparrow(\downarrow)} = \sum_{j=1}^{N_{ev}^{\uparrow(\downarrow)}} w_{i,j} \; , \tag{E.2}$$

where $w_{i,j}$ are the event-weights.

As a last step the a-priori Probability Density Estimator (PDE) was evaluated as:

$$f(\mathbf{x}_i) = 1 + P_t \cdot A_i \; , \tag{E.3}$$

where, as usual, P_z indicates the target polarization. This quantity has the same structure of the PDF (cf. eqn. (6.7)) but does not depend on the fit (i.e. theoretical) parameters. In contrast, it depends on an asymmetry A_i directly extracted from the data, thus representing the a-priori *data probability density function*.

Bibliography

[Abe98] K. Abe *et al.* (E143 Collaboration), "Measurements of the proton and deuteron spin structure functions g1 and g2", Phys. Rev. **D58**, 112003 (1998).

[Abe97] K. Abe *et al.* (E154 Collaboration), "Precision Determination of the Neutron Spin Structure Function g_1^n ", Phys. Rev. Lett.**79**, 26 (1997).

[Ack97] K. Ackerstaff *et al.* (HERMES Collaboration), "Measurement of the Neutron Spin Structure Function g_1^n with a Polarized ^{3}He Target", Phys. Lett. **B404**, 383 (1997).

[Ack98] K. Ackerstaff *et al.* (HERMES), "The HERMES Spectrometer", Nucl. Inst. & Meth. **A 417**, 230 (1998).

[Ada94] D. Adams *et al.* (SMC Collaboration), "Measurement of the spin-dependent structure function $g_1(x)$ of the proton", Phys. Lett. **B329**, 399 (1994).

[Ada95] D. Adams *et al.* (SMC Collaboration), "A new measurement of the spin-dependent structure function $g_1(x)$ of the deuteron", Phys. Lett. **B357**, 248 (1995).

[Ada04] J. Adams *et al.* (STAR Collaboration), "Cross Sections and Transverse Single-Spin Asymmetries in Forward Neutral-Pion Production from Proton Collisions at $\sqrt{(s)} = 200$ GeV", Phys. Rev. Lett.**92** Num 17, 171801 (2004).

[Ade93] B. Adeva *et al.* (SMC Collaboration), "Measurement of the spin-dependent structure function $g_1(x)$ of the deuteron", Phys. Lett. **B302**, 533 (1993).

[Ade97] B. Adeva *et al.* (SMC Collaboration), "The spin-dependent structure function g1(x) of the proton from polarized deep-inelastic muon scattering", Phys. Lett. **B412**, 414 (1997).

[Ade98] B. Adeva *et al.* (SMC Collaboration), "Polarized Quark distributions in the nucleon from semi-inclusive spin asymmetries", Phys. Lett. **B420**, 180 (1998), arXiv:hep-ex/9711008.

[Adl04] S.S. Adler *et al.* (PHENIX Collaboration), "Double Helicity Asymmetry in Inclusive Midrapidity π^0 Production for Polarized p+p Collisions at $\sqrt{(s)} = 200$ GeV ", Phys. Rev. Lett.**93** Num 20, 202002 (2004).

[Adl06] S.S. Adler *et al.* (PHENIX Collaboration), "Improved measurement of double helicity asymmetry in inclulsive midrapidity π^0 production for polarized p+p collisions at $\sqrt{(s)} = 200$ GeV", Phys. Rev. **D73**, 091102 (2006).

[Age05] E.S. Ageev *et al.* (COMPASS Collaboration), "Measurement of the spin structure of the deuteron in the DIS region", Phys. Lett. **B612**, 154 (2005).

[Age07] E.S. Ageev *et al.* (COMPASS Collaboration), "A new measurement of the Collins and Sivers asymmetries on a transversely polarized deuteron target", Nucl. Phys. **B765**, 31 (2007).

[Air98] A. Airpetian *et al.* (HERMES Collaboration), "Measurement of the proton spin structure function g_1^p with a pure hydrogen target", Phys. Lett. **B442**, 484 (1998).

[Air03] A. Airpetian *et al.* (HERMES Collaboration), "Measurement of single-spin azimuthal asymmetries in semi-inclusive electroproduction of pions and kaons on a longitudinally polarised deuterium target", Phys. Lett. **B562**, 182 (2003).

[Air05] A. Airapetian *et al.* (HERMES Collaboration), "Single-Spin Asymmetries in Semi-Inclusive Deep-Inelastic Scattering on a Transversely Polarized Hydrogen Target", Phys. Rev. Lett. **94**, 012002 (2005) Eprint numbers: arXiv:hep-ex/0408013 and DESY-04-141.

[Air05b] A. Airapetian *et al.* (HERMES Collaboration), "Quark Helicity Distributions in the Nucleon for Up, Down, and Strange Quarks from Semi-Inclusive Deep-Inelastic Scattering", Phys.Rev. **D71**, 012003 (2005), arXiv:hep-ex/0407032, DESY-04-107.

[Air05c] A. Airapetian *et al.* (HERMES Collaboration), "The HERMES polarized hydrogen and deuterium gas target in the HERA electron storage ring", Nucl. Instr. Meth. **A540**, 68 (2005)

[Air07] A. Airapetian *et al.* (HERMES Collaboration), "Precise determination of the spin structure function $g1$ of the proton, deuteron and neutron", Phys. Rev. **D75**, 012007 (2007). Eprint numbers: arXiv:hep-ex/0609039 and DESY-06-142

[Ako02] N. Akopov *et al.*, "The HERMES Dual-Radiator Ring Imaging Cerenkov Detector", Nucl. Instrum. Meth. **A479**, 511 (2002)

[Alg76] M.J. Alguard *et al.* (E80 Collaboration), "Deep Inelastic Scattering of Polarized Electrons by Polarized Protons", Phys. Rev. Lett. **37** Num.19, 1261 (1976).

[Alg78] M.J. Alguard *et al.* (E80 Collaboration), Phys. Rev. Lett. **41** Num.2, 71 (1978).

[Alt77] G. Altarelli and G. Parisi, "Asymptotic Freedom in Parton Language" Nucl. Phys. **B126** 298 (1977).

[Ama02] M. Amarian *et al.* (E94-101 Collaboration), "Q^2 Evolution of the Generalized Gerasimov-Drell-Hearn Integral for the Neutron using a ^{3}He Target ", Phys. Rev. Lett.**89** Num 24, 242301 (1997).

[And83] B. Anderson *et al.*, "Parton Fragmentation and String Dynamics", Phys. Rept. **97** 31, (1983).

[And97] B. Anderson, "The Lund model", Camb. Monogr. Part. Phys. Nucl. Phys. Cosmol. **7** 1, (1997).

[And01] A. Andreev *et al.*, "Multiwire Proportional Chambers in the HERMES Experiment", Nucl. Instru. Meth. **A465** 482 (2001).

[Ans95] M. Anselmino, A. Efremov and E. Leader, "The theory and penomenology of polarized deep inelastic scattering", Phys. Rept. **261**, 1-124 (1995).

[Ans95] M. Anselmino, A. Efremov and E. Leader, "The theory and penomenology of polarized deep inelastic scattering", Phys. Rept. **261**, 1-124 (1995).

[Ans99] M. Anselmino, M. Boglione and F. Murgia, "Phenomenology of single spin asymmetries in p↑p$\longrightarrow \pi$ X ", Phys. Rev. **D60**, 054027 (1999).

[Ans05] M. Anselmino *et al.*, "Extracting the Sivers function from polarized SIDIS data and making predictions", Phys. Rev. **D72**, 094007 (2005), arXiv:hep-ph/0507181v2

[Ans05b] M. Anselmino *et al.*, "The role of Cahn and Sivers effects in Deep Inelastic Scattering", Phys. Rev. **D71**, 074006 (2005), arXiv:hep-ph/0501196v2

[Ans07] M. Anselmino *et al.*, "Transversity and Collins functions from SIDIS and e+e-data",arXiv:hep-ph/0701006 (2007), Revised version to appear in Phys. Rev D.

[Ant96] P.L. Anthony *et al.* (E142 Collaboration), "Deep inelastic scattering of polarized electrons by polarized ^{3}He and the study of the neutron spin structure", Phys. Rev. **D54**, 6620 (1996).

[Ant00] P.L. Anthony *et al.* (E155 Collaboration), "Measurements of the Q2-dependence of the proton and neutron spin structure functions g_1^p and g_1^n", Phys. Lett. **B493**, 19 (2000).

[Ant02] P.L. Anthony *et al.* (E155x Collaboration),"Precision measurement of the proton and deuteron spin structure functions g_2 and asymmetries A_2", Phys. Lett. **B553**, 18 (2003).

[Ant99] P.L. Anthony *et al.* (E155 Collaboration), "Measurement of the deuteron spin structure function g_1^d(x) for 1 (GeV/c)^2¡Q^2¡40 (GeV/c)^2", Phys. Lett. **B463**, 339 (1999).

[Aok97] S. Aoki, M. Doui, T. Hatsuada and Y. Kuramashi, "Tensor charge of the nucleon in lattice QCD", Phys. Rev. **D56**, 433 (1997)

[Arr04] E.R. Arriola and W. Broniowski, "Solution of the Kwiecinski ecolution equations for unintegrated parton distributions using the Mellin transform", Phys. Rev. **D70**, 034012 (2004), arXiv:hep-ph/0404008.

[Art90] X. Artru and M. Mekhfi, "Transversely polarized parton densities, their evolution and their measurement", Z. Phys. C **45**, 669 (1990).

[Art93] X. Artru,"Proposal for measuring transversity distributions in deep inelastic electron scattering and a model for E-704 asymmetries", Prepared for the 5th International Workshop on High-energy Spin Physics, Protvino,Russia Sep 20-24 1993, arXiv:hep-ph/9310323.

[Ash88] EMC, J.Ashman *et al.*, "A measurement of the spin asymmetry and determination of the structure function g_1 in deep inelastic muon-proton scattering", Phys. Lett. **B206**, 364 (1988).

[Ash89] J. Ashman *et al.* (EMC Collaboration), "An investigation of the spin structure of the proton in deep inelastic scattering of polarised muons on polarised protons", Nucl. Phys. **B328**, 1 (1989).

[Aug07] W. Augusyniac, A. Miller, G. Shnell, S. Yen, P. Zupransky, "TMC - Vertex Reconstruction in the Presence of the HERMES Transverse Target Magnet", HERMES Internal Report 07-008

[Ava96] H. Avakian *et al.*, "Performance of $F101$ Radiation Resistant Lead Glass Shower Counters", Nucl. Instrum. Meth. **A378**, 155 (1996)

[Ava98] H. Avakian *et al.*, "Performance of the Electromagnetic Calorimeter of the HERMES experiment", Nucl. Instrum. Meth. **A417**, 69 (1998)

[Bac00] A. Bacchetta, M. Boglione, A. Henneman and P.J. Mulders, "Bounds on transverse momentum dependent distribution and fragmentation functions", Phys. Rev. Lett. **85**, 712 (2000).

[Bac01] A. Bacchetta, R. Kundu, A. Metz and P.J. Mulders, "The Collins fragmentation function: A simple model calculation", Phys. Lett. **B506**, 155 (2001).

[Bac02a] A. Bacchetta, R. Kundu, A. Metz and P.J. Mulders, "Estimate of the Collins fragmentation function in a chiral invariant approach", Phys. Rev. **D65**, 094021 (2002).

[Bac02b] A. Bacchetta, "Probing the transverse spin of quarks in deep inelastic scattering", PhD thesis (2002). arXiv:hep-ph/0212025.

[Bac04] A. Bacchetta *et al.* "On the way to a decomposition of the flavor dependent Sivers functions: Transverse asymmetries, the decomposition and the transverse MC generator GMC_TRANS", Hermes Internal Report 04-039 (2004).

[Bac07] A. Bacchetta, M. Diehl, K. Goeke, A. Metz, P.J. Mulders, M. Schlegel, "Semi-inclusive deep inelastic scattering at small transverse momentum', JHEP 0702 (2007) 093, arXiv:hep-ph/0611265

[Bac07b] A. Bacchetta *et al.*, "Collins fragmentation function for pions and kaons in a spectator model', aiXiv:hep-ph/0707.3372v1 (2007)

[Bar79] D.P. Barber *et al.*, "Discovery of Three-Jet Events and a Test of Quantum Chromodynamics at PETRA", Phys. Rev. Lett. **43**, 830 (1979).

[Bar93] D.P. Barber *et al.*, "The HERA polarimeter and the first observation of electron spin polarization at HERA", Nucl. Instrum. Meth. **A329**, 79 (1993).

[Bau83] G. Baum *et al.* (E130 Collaboration), "New Measurement of Deep-Inelastic e-p Asymmetries", Phys. Rev. Lett. **51** Num.13, 1135 (1983).

[Bau02] Ch. Baumgarten *et al.*, "An Atomic Beam Polarimeter to Measure the Nuclear Polarization in the HERMES Gaseous Polarized Hydrogen and Deuterium Target", Nucl. Instrum. Meth. **A482**, 606 (2002).

[Bau03a] Ch. Baumgarten *et al.*, "Measurement of the atomic recombinationin the HERMES polarized hydrogen and deuterium storage cel target", Nucl. Instrum. Meth. **A496**, 263 (2003).

[Bau03b] Ch. Baumgarten *et al.*, "The storage cell of the polarized internal H/D gas target of the HERMES experiment at HERA", Nucl. Instrum. Meth. **A496**, 277 (2003).

[Bru84] R. Brun, F. Bruyant, A.C. McPherson, and P. Zanarini, "GEANT3", CERN-DD/EE/84-1

[Ben01] T. Benisch *et al.*, "The Luminosity Monitor of the HERMES Experiment at DESY", Nucl. Instrum. Meth. **A471**, 314 (2001).

[BDR02] V. Barone, A. Drago and P.G. Ratcliffe, "Transverse polarisation of quarks in hadrons", Phys. Rep. **359**, 1-168 (2002).

[Bec00] M. Beckmann, "Extraction of polarised quark distributions of the nucleon from deep inelastic scattering at the HERMES experiment", PhD. Thesis, Albert-Ludwigs-Universitat Freiburg, DESY-THESIS-2000-029 (2000).

[Bec02] M. Beckmann *et al.*, "The longitudinal polarimeter at HERA", Nucl. Instrum. Meth. **A479**, 334 (2002).

[Ber98] S. Bernreuther *et al.*, "The HERMES Back Drift Chambers", Nucl. Instrum. Meth., **A416**, 45 (1998).

[Bha88] R.K. Bhaduri, "Models of the Nucleon", Addison Wesley, Reading, MA, (1988).

[Bjo69a] J.D. Bjørken, "Asymptptic sum rules at infinite momentum", Phys. Rev. **179**, 1547 (1969).

[Bjo69b] J.D. Bjørken and E.A. Paschos, "Inelastic electron-proton and γ-proton scattering and the structure of the nucleon", Phys. Rev. **185**, 1975 (1969).

[Boe00] D. Boer and P.J. Mulders, "Color gauge invariance in the Drell-Yan process", Nucl. Phys. **B569**, 505 (2000).

[Bra01] J.T. Brack *et al.*, "The HERMES Forward Tracking Chambers: Construction, Operation, and Aging Effects"Nucl. Instrum. Meth. **A469**, 47 (2001).

[Bra06] F. Bradamante, "The COMPASS Experiment at CERN: present and future", Nucl. Phys. **B154** (Proc. Suppl.), 86 (2006).

[Bro02] S.J. Brodsky, D.S. Hwang and I. Schmidt, "Final-state interactions and single-spin asymmetries in semi-inclusive deep inelastic scattering", Phys. Lett. **B530**, 99 (2002).

[Bur02] M. Burkardt, "Impact parameter dependent parton distributions and transverse single spin asymmetries", Phys. Rev. **D66**, 114005 (2002)

[Cal69] C.G. Callan and D.J. Gross, "High-energy electroproduction and the constitution of the electric curent", Phys. Rev. Lett. **33**, 156 (1969).

[Cer93] CERN Programming Techniques Group, ADAMO-Entity-Relationship Programming System, (1993), User Guide, Version 3.3

[Cho74a] A. Chodos *et al.*, "New extended model of hadrons", Phys. Rev. **D9** Num.12, 3471 (1974).

[Cho74b] A. Chodos *et al.*, "Baryon structure in the bag theory", Phys. Rev. **D10** Num.8, 2599 (1974).

[Chr96] C.V. Christov *et al.*, "Baryons as non-topological chiral solitons", Prog. Part. Nucl. Phys. **37**, (1996). arXiv:hep-ph/9604441

[Col93] J.C. Collins, "Fragmentation of transversely polarized quarks probed in transverse momentum distributions", Nucl. Phys. **B396**, 161 (1993).

[Col02] J.C. Collins, "Leading-twist single-transverse spin asymmetries: Drell-Yan and deep-inelastic scattering", Phys. Lett. **B536**, 43 (2002). arXiv:hep-ph/0204004

[Col06] J.C. Collins *et al.*, "Sivers effect in semi-inclusive deeply inelastic scattering", Phys. Rev. **D73**, 014021 (2006). arXiv:hep-ph/0509076

[Dia98] D. Diakonov, "Chiral Quark-Soliton Model", World Scientific in School proceedings Report-no: NORDITA-98/14 (1998). arXiv:hep-ph/9802298

[Die05] M. Diehl and S.Sapeta, "On the analysis of lepton scattering on longitudinally or trasversely polarized protons", Eur.Phys.J. C41, 515-533 (2005), aiXiv:hep-ph/0503023v1

[Die05b] M. Diehl A. Bacchetta, "Question: semi-inclusive isospin symmetry", Mailing list: draft_61@hermes.le.desy.de, January 27, 2005

[Dief05] M. Diefenthaler, "Transversity measurements at HERMES", Conference proceeding of DIS 2005, Madison, Wisconsin (USA), April 27 - May 1 (2005), arXiv:hep-ex/05507013

[Dok77] Y.L. Dokshitzer, "Calculation of the Structure Functions for Deep Inelastic Scattering and e^+e^- Annihilation by Perturbation Theory in Quantum Chromodynamics", Sov. Phys JETP **46**, 641 (1977)

[Dur95] M. Duren, "The HERMES experiment: from the design to the first results", Habilitation Thesis, Friedrich-Alexander-Universitaet Erlangen-Nurnberg (1995) HERMES 95-002.

[Dur98] M. Duren, "Quark Spin Flavour Decomposition - Cross Checks and First Moments", HERMES Internal Report (1998) HERMES 98-018.

[Efr05] A.V. Efremov, K. Goeke and P.Schweitzer, "Transversity distribution in spin asymmetries in semi-inclusive DIS and in the Drell-Yann process", Czech. J. Phys.**55**, A189 (2005).

[Efr06] A.V. Efremov, K. Goeke and P.Schweitzer, "Collins effect in semi-inclusive deeply inelastic scattering and in e^+e^--annihilation", Phys. Rev. **D73** 094025 (2006).

[Ell74] J. Ellis and R.L. Jaffe, "Sum rule for deep-inelastic electroproduction from polarized protons", Phys. Rev. **D9** 1444 (1974); "Erratum: Sum rule for deep-inelastic electroproduction from polarized protons", Phys. Rev **D10**, 1669 (1974).

[Ell83] R.K. Ellis, W. Furmanski and R. Petronzio, "Unraveiling Higher twist", Nucl. Phys. **B212**, 29 (1983).

[Els06] U. Elschenbroich, PhD Thesis "Transverse Spin Structure of the Proton Studied in Semi-Inclusive DIS", DESY-THESIS-2006-004, (2006).

[Fat03] R. Fatemi *et al.* (CLAS Collaboration), "Measurement of the Proton Spin Structure Function $g_1(x,Q^2)$ for Q^2 from 0.15 to 1.6 GeV^2 with CLAS ", Phys. Rev. Lett.**91**, Num 22, 222002 (1997).

[Fey69] R. Feynman, "Very high-energy collisions of hadrons", Phys. Rev. Lett. **23**, 1415 (1969).

[Flo07] D. de Florian, R. Sassot and M. Stratmann, "Global Analysis of Fragmentation Functions for Protons and Charged Hadrons", arXiv:hep-ph/007.1506v1 (2007).

[Gei09] H. Geiger and E. Marsden, "On a diffuse reflection of the α particles", Pro. Roy. Soc. **A82**, 495 (1909).

[Gel64] M. Gell-Mann,"A schematic model of baryons and mesons", Phys. Lett. **8**, 214 (1964).

[Ger21] W. Gerlach and O. Stern, Z. Physik **8**, 110 (1921)

[Gio08] F. Giordano, "The role of transverse momentum and spin in unpolarized semi-inclusive deep inelastic scattering", PhD Thesis, University of Ferrara (2008)

[Gri72] V.N. Gribov and L.N. Lipatov ,"e^+e^- pair annihilation and deep inelastic $e\,p$ scattering in perturbation theory", Sov. J. Nucl. Phys. **15**, 675 (1972).

[Glu96] M. Glück, E. Reya, M. Stratmann and W. Vogelsang, "Next-to-leading order radiative parton model analysis of polarized deep inelastic lepton-nucleon scattering", Phys. Rev. **D53**, 4775 (1996)

[Has03] D. Hash, "Effect of a dead calo block in the analysis of semi-inclusive asymmetries...", Mailing list: offline-list@hermes.le.desy.de, Apr. 24 (2003)

[HDQa] , HERMES data quality group, "DIS Statistics of Different Years", http://www-hermes.desy.de/groups/daqlgrp/OFFLINE_DQ/uDST/general/docu/DISstats.html

[HDQb] , HERMES data quality group, "Offline Data Quality - μDST Productions", http://www-hermes.desy.de/groups/daqlgrp/OFFLINE_DQ/uDST/index.html

[Hil05] , A. Hillenbrand, "Measurement and Simulationof the Fragmentation Process at HERMES", PhD thesis, Friedrich-Alexander-Universitaet Erlangen-Nurnberg, HERMES-THESIS-2005-035 (2005).

[Hom03] , B. Hommez, "Hadron Identification with the HERMES RICH", Nucl. Instrum. Meth. **A502**, 294 (2003).

[Hom04] , B. Hommez, H. Jackson, R. Kaiser and Y. Miyachi, "Using the RICH detector for Physics Analysis", December 2004, http://www-hermes.desy.de7groups/richgrp/rich/richanalysis/index.html

[Ier97] G. Ingelman, A. Edin, and J. Rathsman, "LEPTO 6.5 - A Monte Carlo Generator for Deep Inelastic Lepton-Nucleon Scattering", Comput. Phys. Commun. **101**, 108 (1997)

[Jaf92] R.L. Jaffe and X. Ji, "Chiral-odd parton distributions and Drell-Yan processes", Nucl. Phys. **B375**, 527 (1992).

[Jaf96] R.L. Jaffe, "Spin, Twist and Hadron Structure in Deep Inelastic Processes", arXiv:hep-ph/9602236 (1996).

[Jam75] F. James and M. Roos, "'MINUIT' A System for Function Minimization and Analysis of the Parameter Errors and Correlations", Comput. Phys. Commun. **10**, 343 (1975).

[Jun00] P. Jung, "Pion-Kaon separation with the HERMES RICH detector", Diploma thesis, Humboldt Universitaet Berlin (2000), HERMES-01-025

[Kow87] S.B. Kowalski and H.A. Enge, "The ion-optical program raytrace", Nucl. Instrum. Meth **A258**, 407 (1987).

[Kre00] S. Kretzer, "Fragmentation functions from flavour-inclusive and flavour-tagged e^+e^- annihilations", Phys. Rev **D62**, 054001 (2000).

[Lai97] H.L. Lai *et al.*, "Improved parton distributions from global analysis of recent deep inelastic scattering and inclusive jet data", Phys. Rev. **D55**, 1280 (1997).

[Lam00] B. Lampe and E. Reya, "Spin physics and polarized structure functions", Phys. Rep. **332**, 1 (2000).

[Lie04] P. Liebing, "Can the gluon polarization in the nucleon be extracted from HERMES data on single high-p_T hadrons?", PhD thesis, Univsersitaet Hamburg (2004), DESY-THESIS-2004-036

[Lip75] L.N. Lipatov, "The parton model and the perturbation theory", Sov. J. Nucl. Phys. **20**, 94 (1975).

[Ma02] B.Q. Ma, I. Schmidt and J.-J. Yang, "Azimuthal spin asymmetries of pion electroproduction", Phys. Rev. **D65**, 034010 (2002).

[Mak03] N. Makins, "GMC_TRANS Manual", Hermes Internal Report, HERMES-03-060 (2003).

[Mak03b] N. Makins, "Back-of-the-Envelope interpretation of our First Transversity Data", Hermes Internal Report, HERMES-03-010 (2003).

[Mai06] B. Maiheu, "Hadronization in electron-proton scattering at HERMES", PhD Thesis, Universiteit Gent (2006) HERMES-06-061

[Mck02] P. M. Mckee (E01-006 Collaboration),www.jlab.org/ jones/rss/mckee-proc.pdf (2002).

[Mil06] A. Miller, "Extracting azimuthal Fourier moments from sparse data", talk given at HERMES Transversity Week, Gent, (2006)

[Miy03] Y. Miyachi, "The HERMES RICH Aerogle Radiator", Nucl. Instrum. Meth. **A502**, 222 (2003).

[Mul96] P.J. Mulders and R.D. Tangerman, "The complete tree-level result up to order $1/Q$ for polarized deep-inelastic leptoproduction", Nucl. Phys. **B461**, 197 (1996).

[Mur74] J.J. Murphi *et al.*, "Proton form factor from 0.15 to 0.79 fm^{-2}", Phys. Rev C **9**, 2125 (1974).

[Nas03] A. Nass *et al.* "The HERMES polarized atomic beam source", Nucl. Intrum. Meth. **A505**, 633 (2003).

[PAX05] PAX Collaboration, "Technical Proposal for Antiproton-Proton Scattering Experiments with Polarization" arXiv:hep-ex/0505054 (2005)

[Per72] D.H. Perkins, Proc. of the 16th Int. Conf. on High Energy Physics, Batavia,Vol.4 (1972).

[Pob03] P.V. Pobylitsa, "Transverse-momentum dependent parton distributions in large-N_c QCD", arXiv:hep-ph/0301236

[Raj06] Rajendran Raja, "A General Theory of Goodness of Fit in Liekilhood Fits", arXiv:physics/0509008 v2 (2006) (preprint submitted to Elsevier Science).

[Ral79] J.P. Ralston and D.E. Soper, "Production of dimuons from high-energy polarized proton-proton collisions", Nucl. Phys. **B152**, 109 (1979).

[Ron03] O. A. Ron (E01-006 Collaboration),Proceedings of NAPP03, Dubrovnik, Croatia (2003).

[Ros50] M.N. Rosenbluth, "High Energy Elastic Scattering of Electrons on Protons", Phys. Rev. **79**, 615 (1950)

[Rut11] E. Rutherford, "The scattering of α and β particles by matter and the structure of the atoms", Phil. Mag. **21**, 669 (1911).

[Sak69] J.J. Sakurai,"Vector meson dominance and high-energy electron proton inelastic scattering", Phys. Rev. Lett. **22**, 981 (1969)

[Sei06] R.C. Seidl, "Spin dependent fragmentation function at Belle" (Results presented at the DIS 2006 conference in Tsukuba, Japan), arXiv:hep-ex/0607014 (2006)

[Siv90] D.W. Sivers, "Single Spin Production Asymmetries from the Hard Scattering of Point-like Constituents", Phys. Rev D **41**, 83 (1990).

[Sjo95] T. Sjostrand, "PYTHIA 5.7 and JETSET 7.4: Physics and manual", arXiv:hep-ph/9508391 (1995)

[Sjo03] T. Sjostrand, L.Lonnblad, S. Mrenna and P.Skands "PYTHIA 6.3: Physics and manual", arXiv:hep-ph/0308153

[Sof95] J. Soffer, "Positivity constraints for spin dependent parton distributions", Phys. Rev Let. **74**, 1292 (1995).

[Sol64] A.A. Sokolov and I.M. Ternov "On POlarization and Spin Effects in the Theory of Synchrotron Radiation", Sov. Phys. Doklady. **8**, 1203 (1964).

[Ste00] J.J.M. Steijger, "The HERMES Silicon Project" Nucl. Inst. & Meth. **A447**, 55 (2000).

[Vog05] W. Volgelsang and F. Yuan, "Single-Transverse Spin Asymmetries: From DIS to Hafronic Collisions", Phys. Rev. **D72** 054028 (2995), arXiv:hep-ph/0507266v2.

[Wak99] M. Wakamatsu and T. Kubota, "Chiral symmetry and the nucleon spin structure functions", Phys. Rev. DG **60**, 034020 (1999)

[Wak01] M. Wakamatsu,"Chiral-odd distribution functions in the chiral quark soliton model", Phys. Lett. **B509**, 59 (2001)

[Wan04] S. Wang, "Improvements of the HERMES Transverse Polarized Hydrogen Target and Calculations of the Sextupole Magnet", PhD Thesis, China Institute of Atomic Energy (2004) HERMES-04-056

[Wei97] T. Weiland textitet al., "MAFIA Version 4, AIP Conf. Proc. **391**, 65 (1997), Prepared for CAP 96: The 1996 Computational Accelerator Physics Conference, Williamsburg, Virginia, USA 24-27 Sep 1996

[Wen03] J. Wendland, "Polarized parton distributions measured at the HERMES experiment", PhD Thesis, Simon Fraser University (2003), DESY-THESIS-2003-032

[Yao06] W.-M. Yao *et al.* (PDG), Phys. G. **33**, 1 (2006)

[Yun03] J. Yun *et al.* (CLAS Collaboration), "Measurement of inclusive spin structure functions of the deuteron", Phys. Rev. C **67**, 055204 (2003).

[Zhe04] X. Zheng *et al.* (E99-117 Collaboration), "Precision measurement of the neutron spin asymmetries and spin-dependent structure functions in the valence quark region", Phys.Rev. **C70**, 065207(2004).

[Zwe64] G. Zweig, "An SU(3) model for strong interaction symmetry and its breaking", CERN preprints **TH-401, TH-412** (1964).

Acknowledgements

Now that my thesis is over, I urge to thank all the people whose help was indispensable during the period of my PhD.

First of all, I would like to thank my tutor, Prof. Paola Ferretti Dalpiaz, for accepting me as a part of the 'Ferrara group' and for transmitting me her experience and enthusiasm in hadron physics. Since the very beginning of my PhD, she involved me in a rich and interesting research program, giving me the opportunity to learn a lot of new concepts and techniques. But, most importantly, she gave me the opportunity to join an exciting experiment such as HERMES!

A special thank goes to Marco C., for his constant and distinguished guidance throughout the whole PhD period. He was always present for suggestions and discussions and for pushing me, day after day, towards the extraction of the final results. I am indebted with him for his extraordinary efforts to make this analysis successful.

Thanks also to Paolo and Michelle, for the interesting and pleasing discussions and for their support. And thanks to Marco S., for sharing with me his knowledge on superconducting magnets and swagelok stuff!

Thanks Delia, Gunar, Naomi, Andy, Alessandro and Riccardo, for your contagious enthusiasm in physics and for your precious advices, and, of course, thanks Markus, for sharing with me so many cross checks and interesting discussions (not just on analysis!!!).

Thanks Francesca, for our daily coffee breaks and our discussions on physics, future plans, vacations, new houses and cats! Thanks for sharing with me the stress and the excitement (...maybe a little bit more stress than excitement) of the last months.

Finally, thanks to Professors Moskow Amarian and Mauro Anselmino, for accepting to be referees of this thesis.

Tutto il mio affetto va alla mia famiglia, per il costante sostegno e gli incoraggiamenti che non mi avete mai fatto mancare e a Carmen, che ho sposato durante il dottorato, per la gioia e l'amore che ogni giorno sei capace di trasmettermi.